MODELING AND CONTROL OF
BACKDRIVABLE FLEXIBLE SYSTEMS

A Dissertation
Presented to
The Academic Faculty

by

Christopher James Adams

In Partial Fulfillment
of the Requirements for the Degree
Doctor of Philosophy in the
School of Mechanical Engineering

Georgia Institute of Technology
December 2018

MODELING AND CONTROL OF
BACKDRIVABLE FLEXIBLE SYSTEMS

Approved by:

Dr. William Singhose, Advisor
School of Mechanical Engineering
Georgia Institute of Technology

Dr. Thomas Kurfess
School of Mechanical Engineering
Georgia Institute of Technology

Dr. Jonathan Rogers
School of Mechanical Engineering
Georgia Institute of Technology

Dr. Eric Feron
School of Aerospace Engineering
Georgia Institute of Technology

Dr. Khalid Sorensen
PaR Systems

Date Approved: 6 November 2018

ACKNOWLEDGEMENTS

This work would have taken even longer to complete without the help, guidance, and support of my advisors, collaborators, friends, and family. I would like to thank and acknowledge the following:

- My advisor, Dr. William Singhose, for his guidance, patience, and tolerating my procrastination. His constant support and boundless enthusiasm have helped and inspired me greatly. I am also grateful for all of the opportunities to work on and learn from challenging and interesting projects.

- My committee members, Dr. Eric Feron, Dr. Thomas Kurfess, Dr. Jonathan Rogers, and Dr. Khalid Sorensen, for their thoughtful feedback and support of this work.

- The research group members I have worked with over the years. I feel privileged for the opportunities I had working with and learning from all of you. In particular, I would like to acknowledge Ali AlSaibie, Arnoldo Castro, Arto Kivila, John Harber, Ehsan Maleki, Alex Miller, Kelvin Peng, Jackson Potter, and Joshua Vaughan for their advice, help, thoughtful questions, encouragement, and putting up with all of my questions.

- The many faculty and teaching assistants I worked with during my time serving as a teaching assistant for ME 2110. In particular, I would like to thank Jacob Kunz, Aaron Howell, Gina Sforzo, Hannes Daepp, Daniel Moreno, Steven Bohlemann, Patrick Caudill, Yash Chitalia, Vanessa Wei, and Inseung Kang for all of their hard work and dedication.

- The Vertical Lift Consortium, Space Systems/Loral, and Boeing for supporting me with research assistantships, and The George W. Woodruff School of Mechanical Engineering for giving me the opportunity to serve as a teaching assistant for numerous semesters.

- My parents for their love, encouragement, and unquestioning support, without which I would not be where I am today. They have made many sacrifices to provide me with opportunities in life and to ensure that I have received a good education. Also, I would like to thank my extended family members for their interest in my research and frequently asking when I was planning to graduate.

TABLE OF CONTENTS

LIST OF TABLES

LIST OF FIGURES

SUMMARY

Flexible systems deflect, vibrate, or oscillate when moved. This behavior results in decreased performance in the form of inaccurate positioning, stress loading, transient deflection, and residual vibration. In a backdrivable flexible system, coupling between flexible and rigid-body modes also leads to degraded performance of the rigid-body motion. For example, sway of a massive payload can backdrive the position of a crane trolley, forcing it to move in unintended ways. Other examples of backdrivable flexible systems include helicopters carrying suspended loads and spacecraft with large flexible appendages.

This thesis investigates dynamic models that capture the fundamental behavior of a variety of backdrivable flexible systems. These models are used to understand and illustrate the conditions under which a system can be classified as backdrivable. Then, the models are studied to identify the range of system parameters that can lead to significant backdrivability and degraded performance. Performance metrics are defined based on analysis of mode shapes and system poles and zeros to quantify the level of backdrivability resulting from a given set of system parameters.

The fundamental models are then used to develop and analyze control methods that can mitigate or suppress the performance degradation seen in both the flexible mode(s) and the backdriven rigid-body mode(s). The proposed control methods are illustrated through two demonstrative applications: experiments and simulations of helicopters carrying suspended loads, and as part of an attitude control system for a spacecraft with flexible appendages driven by stepper motors.

CHAPTER I

INTRODUCTION

Flexible systems deflect, vibrate, or oscillate when moved. This behavior results in decreased performance in the form of inaccurate positioning, transient deflection, internal stress, and residual vibration. A backdrivable flexible system exists when there is significant coupling between flexible and rigid-body modes, and this coupling leads to degraded performance of the rigid-body motion.

For example, sway of a massive payload as shown in Figure 1(a) affects the position of the crane trolley. Motion of the trolley excites the flexible pendulum mode, leading to swing. The swinging payload will then apply horizontal forces to the trolley through the suspension cables, leading to a backdriving effect on the trolley. This effect can be significant when the payload mass is large relative to the trolley mass. Figures 1(b), (c), and (d) are other backdrivable systems that will be discussed below.

Figure 2 demonstrates coupling between a pendulum and cart. The solid arrow in the schematic shown in Figure 2(a) illustrates swinging of the pendulum. As the pendulum swings, it applies horizontal forces to the cart that lead to a backdriving effect illustrated by the dashed arrow. Figure 2(b) shows a free response of the system for an initial pendulum angle of 5 degrees. The swing of the pendulum causes coupled motion of the cart. Note that while the system states appear to be in phase, the definition of positive x and θ in Figure 2(a) show they are actually moving in opposite directions. This is typical for flexible backdriving effects if the mass center remains in a fixed location.

The state of the main body or base, for example the position x of the cart in Figure 2, is often referred to as the rigid body state throughout this thesis. The flexible element, such as the pendulum in Figure 2, is referred to as the flexible mode and its angle θ is referred to as the flexible state. This is despite the fact that the cart itself experiences oscillation under normal circumstances due to its coupled backdriving effect with the pendulum swing.
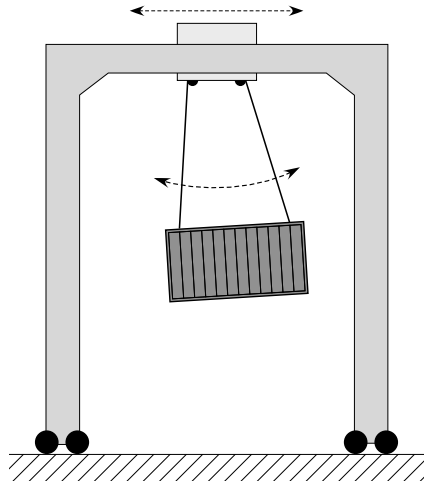
(a) Container crane unloading massive cargo container.
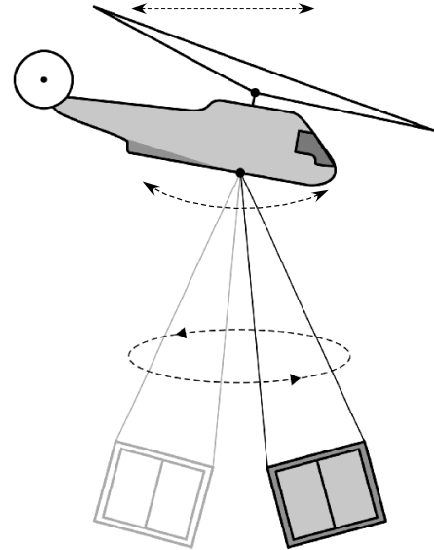
(b) Helicopter carrying a suspended load.

(c) Spacecraft with flexible appendages[1].

(d) Inverted-pendulum transporter[2].

Figure 1: Examples of backdrivable flexible systems.

---

[1]Image Source: SSL. (2014). "DIRECTV 14", Date Accessed: March 5, 2014, Available: `http://sslmda.com/html/satexp/directv14.html`.

[2]Photo Source: JP Wallet, Shutterstock.com, Royalty-free stock photo ID: 300086114, Date Accessed: December 14, 2015, Available: `https://www.shutterstock.com/image-photo/handsome-young-man-riding-segway-gyropode-300086114?src=aqBH2ffJOT8LDJxu0uqByg-1-51`.
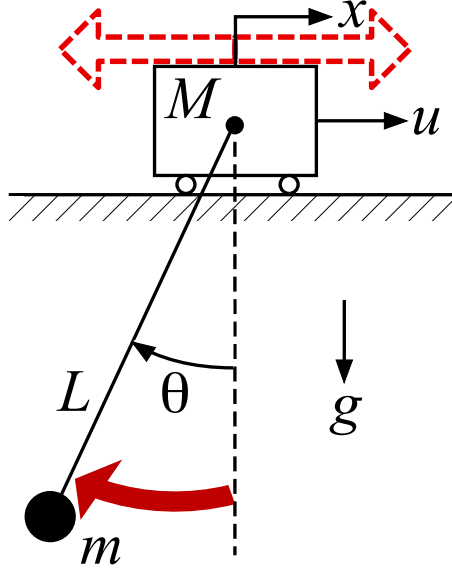
(a) Schematic diagram.
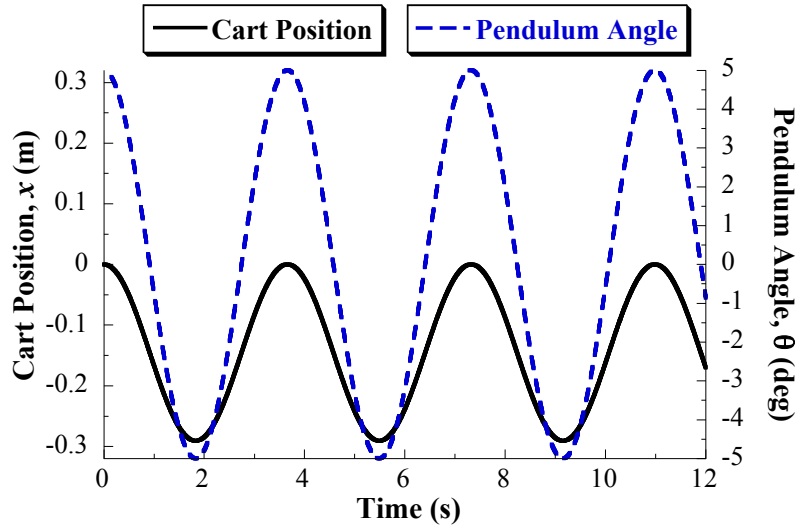
(b) Example free response to pendulum angle initial condition of 5 degrees.

Figure 2: Example of coupling between rigid and flexible modes for a planar cart with pendulum.

However, without the flexible element or mode present, or if the backdriving effect is mitigated through control, then the main body or state would undergo rigid body motion in response to system inputs.

While coupling between system modes is a well-studied dynamic behavior, this thesis seeks to explore these effects from new perspectives by studying the coupling dynamics and

mode shapes, classifying systems that can be described as backdrivable, and using understanding of the dynamics to develop control systems that mitigate performance degradation due to backdriving effects. Systems with flexibility where the main body or base can be described as "freely floating" are particularly susceptible to backdriving effects. Some examples include helicopters carrying suspended loads and spacecraft with flexible appendages, as were shown in Figure 1.

An example of a helicopter carrying a suspended load was shown in Figure 1(b). These "flying cranes" are extremely versatile. For example, they can be used to transport timber during remote logging operations, deliver power transmission towers to their installation locations, and rescue people stranded in otherwise inaccessible areas. These are just a few examples of tasks that are too expensive, too slow, or physically impossible to perform with other types of vehicles. In a flying crane, both the helicopter position and attitude may be affected by the swinging load. The load suspension point is typically below the helicopter's center of gravity, so tension in the suspension cable produces an oscillating torque about the helicopter's center of gravity as the load swings. The backdrivability may be significant depending on the helicopter-load mass ratio, helicopter inertia, suspension point offset distance, and other factors.

A third example of backdrivability is a spacecraft with flexible appendages. Figure 1(c) shows a commercial communications satellite which includes flexible solar arrays and parabolic reflectors. In such spacecraft, the significance of the backdrivability depends on the relative inertias of the appendages and main spacecraft body, and appendage stiffnesses and mounting locations. In addition, the presence of multiple flexible appendages and other sources of flexibility such as fuel sloshing can complicate the dynamics and lead to additional backdriving effects. Also, the mass and inertia of a spacecraft will change over time as fuel is expended. This can lead to increased backdriving effects as the main body inertia decreases while appendages likely have fixed masses.

As the system complexity increases, so too do the factors and combinations of system parameters that may lead to significant backdrivability. Therefore, it is beneficial to study these systems to better understand the dynamic effects and parameter combinations that

lead to significant backdrivability.

A backdrivable flexible system may arise naturally through mechanical flexible elements. Another source of flexibility is feedback control systems. For example, in a PD feedback controller for rigid-body motion, the proportional gain control element acts as stiffness while the derivative gain control element acts as damping. This can introduce flexibility to the closed-loop behavior of systems that consist of only rigid body elements.

As an example of the latter case, consider inverted-pendulum human transporters such as the Ninebot Personal Transporter shown in Figure 1(d). These transporters consist of two wheels placed side-by-side along the same axis of rotation, and a platform for the rider. With this wheel configuration, the mechanical design of the transporter is unstable about the pitch (forward/backward) axis. A feedback controller is utilized to adjust the wheel torques and maintain the pitch motion within an acceptable envelope so that the device and rider do not fall over. Because the unstable pitch motion of the transporter is mitigated with a feedback controller, there is possibility for flexible poles to be introduced by the stabilized closed-loop control system. This flexibility can lead to so-called "rider-induced" oscillations that backdrive the transporter base [101]. If these oscillations continue without intervention by the rider, then they may cause actuator saturation where the motors are unable to supply the necessary torque to balance the device and rider.

Figure 3 depicts the sequence of events in a practical situation where this oscillation can be dangerous. The image sequence is captured from a YouTube video showing a Segway crash with over 1,000,000 views, as of September 2018 [60]. The following describes the sequence of events pictured in the video frames:

Frame 1 - Starting from rest, the rider starts leaning forward to begin accelerating the Segway forward.

Frame 2 - The rider has leaned far forward, and the Segway wheels have moved backward to keep the center of mass in the same position due to linear momentum conservation. This behavior is a consequence of the non-minimum phase dynamics of two-wheeled inverted pendulum transporters transporters.

Frame 3 - The Segway and rider move forward.

Figure 3: Sequence of video frames showing Segway rider oscillation and crash [60].

Frame 4 - The rider begins initiating a stop by leaning back.

Frame 5 - The wheels accelerate in front of rider to slow down the rider. This requirement for the wheels to accelerate to begin decelerating the system is another consequence of the non-minimum phase behavior of these transporters.

Frame 6 - Now that the rider and Segway have slowed down, the wheels race back under the rider to recover from the backward pitch angle caused by the wheels racing forwards during the deceleration process.

Frame 7 - The wheels overshoot behind the rider, continuing the base oscillation about the rider's stopped position. This base oscillation causes the transporter's pitch angle to change rapidly.

Frame 8 - In this case, the base oscillation has caused the motors to reach their performance limit and the transporter can no longer recover balance from the steep pitch angle. This results in the machine turning itself off and the rider falling on his face.

There are many other examples of this type of oscillation during stops in inverted-pendulum transporter crash videos on the Internet. In some cases, this type of base and pitch oscillation can occur for several cycles before the device recovers, the rider gets thrown off, or the motor performance limits are reached and the rider falls. Falls of this type often result in the rider being dangerously thrown to the ground as the device rolls backwards out from under him/her. In addition, many riders do not release the handlebars quickly enough and so do not get their hands up to protect their face.

The dynamic hazards of inverted-pendulum transporters are discussed in more detail in Appendix A and [101]. The existence of these hazards warrants studying the dynamics of these devices in more detail in an effort to understand device and rider configurations that may make them more likely to occur.

1.1 Contributions

1.1.1 Explanation of Backdrivable Flexible Dynamics

This thesis presents dynamic models that capture the fundamental behavior of backdrivable flexible systems, such as the example systems shown in Figure 1. These models are then

used to understand and illustrate the conditions and range of system parameters that lead to significant backdrivability and degraded performance.

As an illustration of the analysis methods, Figure 4 shows a plot of system *response ratio*. The response ratio is defined as the ratio of rigid to flexible response amplitude. The mass ratio shown on the horizontal axis is the mass of the flexible element relative to the rigid body mass. As the relative mass of the flexible element increases, it has a larger effect on the rigid body motion and the response ratio increases. As the response ratio increases, the system is said to be more backdrivable. However, for low mass ratios, the flexible element will have little effect on the rigid body motion, and the system can be considered as not backdrivable.

While mass ratio was used here as an example, other system parameter combinations including relative inertias and geometry may have similar relationships with the response ratio. This thesis introduces two performance metrics for quantitatively analyzing response ratio as a function of system parameters. The performance metrics are applied to the fundamental models to examine how their parameters influence the system backdrivability. Also, a threshold can be used to identify when a given system will experience significant levels of backdrivability. However, its numerical value will be application-dependent in many cases. This ambiguity is conceptually represented by the shaded region in Figure 4.
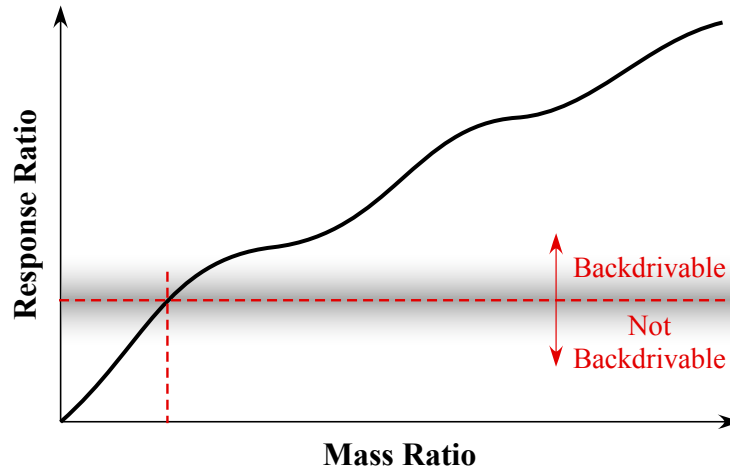
Figure 4: Example response ratio for a backdrivable system as the relative mass of the flexible element changes.

1.1.2   Control of Backdrivable Flexible Dynamics

The fundamental models are also used to analyze control methods that can mitigate or suppress the performance degradation seen in both the flexible mode(s) and the backdriven rigid-body mode(s).

One effective technique for controlling flexible systems is input shaping. Input shaping has proven effective on many kinds of machines, including cranes [112], robotic arms [9, 27, 67, 83], coordinate measuring machines [49, 106], and satellites [33, 93, 94, 104, 102, 120, 128]. The performance of many of these flexible systems can suffer due to backdrivability. Because input shaping eliminates residual vibration, it also reduces the backdriving effect of the flexible mode on the rigid body. In addition, input shaping does not require measurements of the flexible system states. These properties make it well-suited for controlling backdrivable flexible systems.

Input shaping is also compatible with feedback controllers that only use partial state feedback of rigid body motion. Such controller architectures are investigated in this research, and applied to example systems including helicopters with suspended loads and spacecraft with flexible appendages. The goal of the controller design is to improve the response characteristics of both the flexible element and backdrivable rigid body, such as residual vibration, settling time, and overshoot.

1.1.3   Demonstrative Applications

Two demonstrative applications are presented to illustrate how the backdrivable system principles may be applied to more sophisticated models and systems, and to demonstrate the effectiveness of the input shaping method for backdrivable flexible systems. The first application considers a spacecraft with flexible appendages driven by stepper motors along with the attitude control system for the spacecraft. The second application addresses challenges with helicopters carrying suspended loads using experiments and simulations.

1.2 Thesis Outline

Chapter II presents three fundamental dynamic models of backdrivable flexible systems. The models include a planar Cart with Pendulum, planar Rotary Hub with Flexible Arm, and a planar Cart with Inverted Pendulum. The models are linearized to facilitate studying their modes shapes and for control design in later chapters. The validity of studying the linear model over the nonlinear model for effects important to backdrivable systems is verified using the Cart with Pendulum model. Also, an example application of crane trolley slip while braking is studied using the Cart with Pendulum model.

Chapter III develops two performance metrics for assessing system backdrivability, or the degree of coupling between rigid and flexible modes. These metrics are useful for illustrating which system parameters influence backdriving effects and to what degree. The first metric is based on mode shapes and system response ratios. The second is based on the system open-loop poles and zeros. The metrics are applied to the fundamental models to demonstrate and compare the metrics, and to evaluate the backdrivability of the fundamental models as a function of their key system parameters.

Chapter IV evaluates control methods for backdrivable flexible systems. The effectiveness of both input shaping and feedback control are studied separately, using the fundamental models as examples for demonstration. Also, a controller that stabilizes the Cart with Inverted Pendulum model is developed as an example of how backdriving effects can arise from feedback control. Then, a combined input-shaping and PD feedback controller is presented that uses optimization to determine the input shaping and controller parameters subject to illustrative performance constraints. The combined controller is demonstrated with the Rotary Hub with Flexible Arm model.

Chapter V develops constant-amplitude input-shaped step sequences that are useful for actuating stepper motors that drive flexible elements, for example the flexible appendages of spacecraft. The constant-amplitude input shapers address challenges of discretized amplitude to be compatible with stepper motors, and robustness to modeling error in the fundamental flexible mode. Robustness to natural frequency modeling error is analyzed using typical input shaping methods, and limitations of the constant-amplitude input shaping

technique are addressed.

Chapter VI presents the first demonstrative application of a spacecraft with flexible appendages driven by stepper motors. The Rotary Hub with Flexible model is used to demonstrate the effectiveness of the constant-amplitude input-shaped step sequences at slewing the flexible appendages with limited vibration while also limiting the resulting point error of the main spacecraft body.

Chapter VII presents the second demonstrative application of helicopters carrying suspended loads. The effectiveness of input shaping is shown on an experimental model-scale, radio-controlled helicopter. Then, a dynamic model of a Sikorsky S-61 helicopter from the literature is used to study the helicopter flight modes with and without a suspended load to illustrate the backdriving effects it has on the helicopter, in particular the helicopter attitude. Finally, a combined input-shaping and model-following controller is presented that shows improved performance and reduced backdriving effects for near-hover flight with a suspended load.

Lastly, Chapter VIII summarizes the contributions of this thesis and provides suggestions for future work.

CHAPTER II

FUNDAMENTAL MODELS OF BACKDRIVABLE FLEXIBLE SYSTEMS

Fundamental models of backdrivable flexible systems are useful for studying key dynamic response characteristics. They will also be used for identifying backdrivability criteria or performance metrics and for evaluating control methods. This chapter presents the three fundamental models that will be utilized in this thesis.

2.1 Model I: Cart with Pendulum

The first fundamental model is a Cart with Pendulum. Figure 5 shows a schematic diagram of the model. The system states are the cart position x and pendulum angle θ. The flexible pendulum element can backdrive the cart as it swings. The cart and pendulum masses are M and m, respectively, and the pendulum length is given by L. The system inputs are forces u and f applied to the cart and pendulum mass, respectively. The force f is applied perpendicular to the pendulum. This model configuration is suitable for studying cranes, and is also an effective planar approximation of some dynamics of helicopters carrying suspended loads [1]. However, it does ignore coupling effects between heave and pitch/roll.

The nonlinear equations of motion for the Cart with Pendulum are:

$$\begin{bmatrix} M + m & -mL\cos(\theta) \\ -mL\cos(\theta) & mL^2 \end{bmatrix} \begin{bmatrix} \ddot{x} \\ \ddot{\theta} \end{bmatrix} = \begin{bmatrix} mL\dot{\theta}^2\sin(\theta) + u + f\cos(\theta) \\ -mgL\sin(\theta) - fL \end{bmatrix}. \tag{1}$$

The equations of motion in (1) can be linearized by assuming small angles and ignoring terms involving $\dot{\theta}^2$. Linearizing then solving for $\ddot{x}$ and $\ddot{\theta}$ yields the following linear equations of motion for the Cart with Pendulum:

$$\ddot{x} = -\frac{mg\theta}{M} + \frac{1}{M}u \tag{2a}$$

$$\ddot{\theta} = -\frac{(M+m)g\theta}{ML} + \frac{1}{ML}u - \frac{1}{mL}f \tag{2b}$$

12
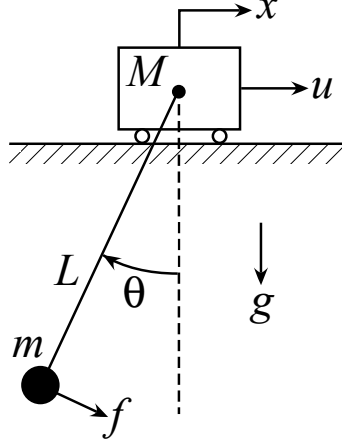
Figure 5: Cart with Pendulum model schematic.

By taking the Laplace transform of both (2a) and (2b) and solving for the input-output relationships, the model can be expressed in transfer function form as follows:

$$\frac{X(s)}{U(s)} = \frac{s^2 + \frac{g}{L}}{s^2 \left[Ms^2 + \frac{(M+m)g}{L} \right]}, \tag{3a}$$

$$\frac{X(s)}{F(s)} = \frac{\frac{g}{L}}{s^2 \left[Ms^2 + \frac{(M+m)g}{L} \right]}, \tag{3b}$$

$$\frac{\Theta(s)}{U(s)} = \frac{\frac{1}{L}}{Ms^2 + \frac{(M+m)g}{L}}, \tag{3c}$$

$$\frac{\Theta(s)}{F(s)} = \frac{-\frac{M}{mL}}{Ms^2 + \frac{(M+m)g}{L}}. \tag{3d}$$

For studying backdrivable system dynamics, the most interesting of these transfer functions is (3a), the relationship between cart position and the applied force on the cart. The presence of the pendulum introduces a pair of complex zeros to this relationship which capture the effect of the pendulum on the cart. The natural frequency of the flexible mode is:

$$\omega_n = \sqrt{\frac{g}{L} \left(\frac{M+m}{M} \right)}. \tag{4}$$

The cart and pendulum mass ratio appears in this expression, suggesting its important role in the system dynamics. On the other hand, the complex zeros of (3a) occur at $\pm i \sqrt{g/L}$, or the simple pendulum frequency. Figure 6 shows an illustrative pole-zero plot of (3a) to show the relative locations of the complex poles and zeros.
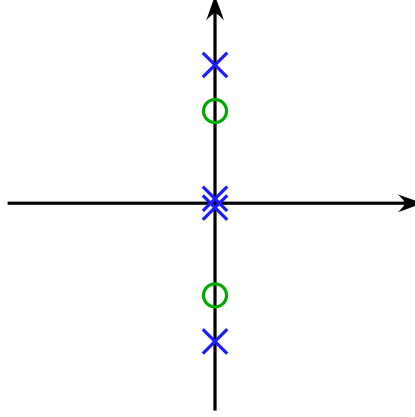
Figure 6: Pole-Zero Plot of Cart with Pendulum $X(s)/U(s)$ transfer function.

2.1.1 Sample Backdriven Response

As an illustrative example of the backdrivable flexbile dynamics, consider the response of the linear Cart with Pendulum model to a bang-bang command applied to the cart. Figure 7 shows such a response for a command designed to move the cart 1 m. The system parameters are $M = 30$ kg, $m = 15$ kg, and $L = 5$ m. Figure 7(a) shows the cart position. The cart moves 1 m and begins to oscillate around this position. This oscillation is the backdriving effect caused by the swing of the pendulum, shown in Figure 7(b).

2.2 Model II: Rotary Hub with Flexible Appendage

The second fundamental model is a Rotary Hub with Flexible Arm. Figure 8 shows a schematic diagram of the model. This model may be used to study flexible robots and spacecraft with flexible appendages. The model consists of a rigid hub with mass m_1 and inertia I_1 rotating about a fixed origin O through angle θ_1, and an uniform arm with mass m_2, and inertia I_2. The distance from the arm pivot M to the arm center of mass is L_2, and the total arm length is $2L_2$. The system states are the hub angle θ_1 and the arm angle θ_2. Vibration of the flexible arm affects the angular position of the rotary hub. The system inputs are a torque T applied to the hub, and a specified angle θ_d corresponding to the driving actuator for the arm. The specified angle θ_d acts through a torsional spring with stiffness k that models the flexibility of the appendage. Angles θ_2 and θ_d are measured relative to the hub. This allows the model to be used to study robot arms with specified
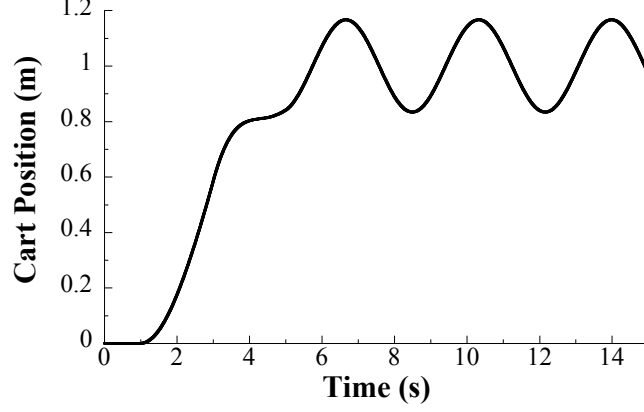
(a) Cart position.
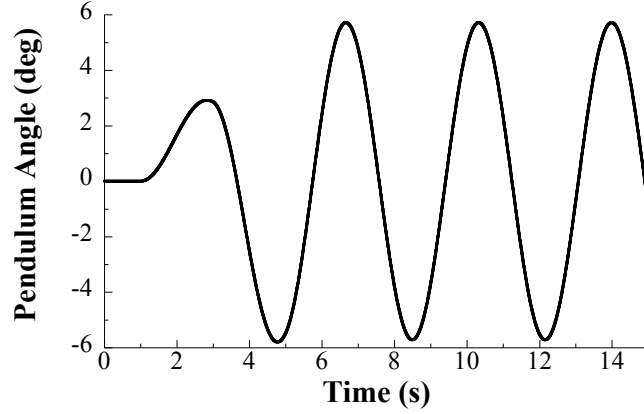
(b) Pendulum angle.

Figure 7: Response of Cart with Pendulum model to a bang-bang command designed to move the cart 1 m.

joint angles or spacecraft with flexible appendages driven by stepper motors.

In this thesis, the hub is modeled as a disk and the arm as a slender rod such that $I_1 = \frac{1}{2}m_1L_1{}^2$ and $I_2 = \frac{1}{3}m_2L_2{}^2$. For small angles and rotational speeds, the linearized equations of motion of this system are:

$$\begin{bmatrix} \frac{1}{2}m_1L_1{}^2 + m_2\left(\frac{1}{3}L_2{}^2 + (L_1 + L_2)^2\right) & m_2L_2\left(L_1 + \frac{4}{3}L_2\right) \\ m_2L_2\left(L_1 + \frac{4}{3}L_2\right) & \frac{4}{3}m_2L_2{}^2 \end{bmatrix} \begin{bmatrix} \ddot{\theta}_1 \\ \ddot{\theta}_2 \end{bmatrix}$$
$$= \begin{bmatrix} T \\ k\left(\theta_d - \theta_2\right) \end{bmatrix}. \quad (5)$$
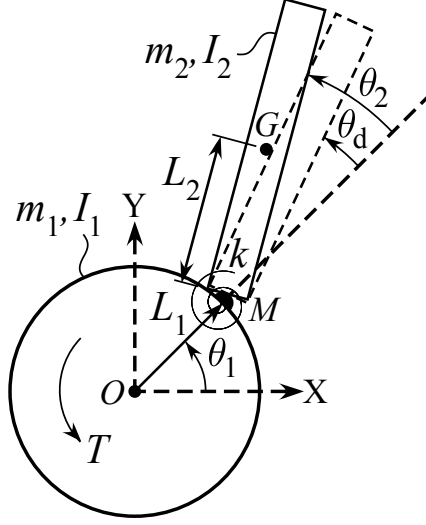
Figure 8: Rotary Hub with Flexible Arm model schematic.

Converting the model to transfer-function form results in:

$$\frac{\Theta_1(s)}{T(s)} = \frac{\frac{4}{3}m_2 L_2^2 s^2 + k}{s^2 \left[(2m_1 + m_2) \frac{m_2 L_1^2 L_2^2}{3} s^2 + k \left(\frac{1}{2}m_1 L_1^2 + m_2 \left(L_1^2 + \frac{4}{3}L_2^2 + 2L_1 L_2 \right) \right) \right]}, \quad (6a)$$

$$\frac{\Theta_1(s)}{\Theta_d(s)} = \frac{-k \left(\frac{4}{3}m_2 L_2^2 + m_2 L_1 L_2 \right)}{(2m_1 + m_2) \frac{m_2 L_1^2 L_2^2}{3} s^2 + k \left(\frac{1}{2}m_1 L_1^2 + m_2 \left(L_1^2 + \frac{4}{3}L_2^2 + 2L_1 L_2 \right) \right)}, \quad (6b)$$

$$\frac{\Theta_2(s)}{T(s)} = \frac{- \left(\frac{4}{3}m_2 L_2^2 + m_2 L_1 L_2 \right)}{(2m_1 + m_2) \frac{m_2 L_1^2 L_2^2}{3} s^2 + k \left(\frac{1}{2}m_1 L_1^2 + m_2 \left(L_1^2 + \frac{4}{3}L_2^2 + 2L_1 L_2 \right) \right)}, \quad (6c)$$

$$\frac{\Theta_2(s)}{\Theta_d(s)} = \frac{k \left(\frac{1}{2}m_1 L_1^2 + m_2 \left(L_1^2 + \frac{4}{3}L_2^2 + 2L_1 L_2 \right) \right)}{(2m_1 + m_2) \frac{m_2 L_1^2 L_2^2}{3} s^2 + k \left(\frac{1}{2}m_1 L_1^2 + m_2 \left(L_1^2 + \frac{4}{3}L_2^2 + 2L_1 L_2 \right) \right)}. \quad (6d)$$

There is clearly a more complex relationship between the system parameters and poles, zeros, and flexible mode natural frequency than for the Cart with Pendulum model, yet the number of poles and zeros is the same. The natural frequency of the flexible mode is:

$$\omega_n = \sqrt{\frac{k \left(3m_1 L_1^2 + 2m_2 \left(3L_1^2 + 4L_2^2 + 6L_1 L_2 \right) \right)}{2m_2 \left(2m_1 + m_2 \right) L_1^2 L_2^2}}. \quad (7)$$

which has a complex dependence on the hub and arm masses m_1 and m_2, the hub radius L_1, the arm length L_2, and the stiffness k. Figure 9 shows an illustrative pole-zero plot for the $\Theta_1(s)/T(s)$ transfer function given by (6a) to show the relative locations of the complex poles and zeros. There is a similar structure to the Cart with Pendulum pole-zero plot from Figure 6, but there is a slight difference in the location of the complex zeros relative to the complex poles due to the transfer function structure and dependence on the system

16
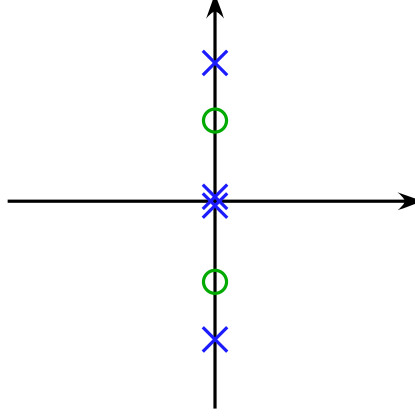
Figure 9: Pole-Zero Plot of Rotary Hub with Flexible Arm $\Theta_1(s)/T(s)$ transfer function.

parameter values. In general, stable backdrivable flexible systems without damping have pole-zero plots with similar layouts, where the double integrator is necessary for the base state to exhibit the "freely floating" backdriving effects.

2.3 Model III: Cart with Inverted Pendulum

The final fundamental model considered in this thesis is a Cart with Inverted Pendulum. Figure 10 shows a schematic diagram of the model. The system states are the cart position x and pendulum angle θ. The cart and pendulum masses are M and m, respectively, and the distance from the pendulum pivot to its center of mass is given by L. The overall pendulum length is $2L$. The pendulum is modeled as a slender uniform rod (pendulum inertia $I_G = \frac{1}{3}mL^2$). The system inputs are forces u and f applied to the cart and pendulum mass, respectively. This model serves as an example of an unstable system that exhibits backdrivable behavior when feedback control is used to stabilize the pendulum angle. Such a controller may exhibit flexible behavior due to underdamped complex closed-loop poles for certain combinations of system and controller parameters. This model may be used to study inverted-pendulum human transporters.

For small pendulum angles, the linearized equations of motion are:

$$
\begin{bmatrix} M+m & mL \\ mL & \frac{4}{3}mL^2 \end{bmatrix} \begin{bmatrix} \ddot{x} \\ \ddot{\theta} \end{bmatrix} = \begin{bmatrix} u+f \\ 2fL+mgL\theta \end{bmatrix}.
\tag{8}
$$

17
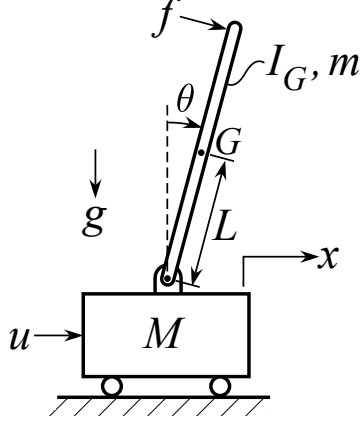
Figure 10: Cart with Inverted Pendulum model schematic.

Converting the model to transfer-function form results in:

$$\frac{X(s)}{U(s)} = \frac{\frac{4}{3}Ls^2 - g}{s^2\left[\frac{1}{3}L\left(4M+m\right)s^2 - g\left(M+m\right)\right]} \tag{9a}$$

$$\frac{X(s)}{F(s)} = \frac{-\left(\frac{2}{3}Ls^2 + g\right)}{s^2\left[\frac{1}{3}L\left(4M+m\right)s^2 - g\left(M+m\right)\right]} \tag{9b}$$

$$\frac{\Theta(s)}{U(s)} = \frac{-1}{\frac{1}{3}L\left(4M+m\right)s^2 - g\left(M+m\right)} \tag{9c}$$

$$\frac{\Theta(s)}{F(s)} = \frac{\frac{2M+m}{m}}{\frac{1}{3}L\left(4M+m\right)s^2 - g\left(M+m\right)} \tag{9d}$$

Figure 11 shows an illustrative pole-zero plot of (9a) that indicates the relative locations of the complex poles and zeros. While this system is unstable, the poles and zeros follow a layout that is rotated by 90 degrees compared to Figures 6 and 9.

2.4 Comparison Between Nonlinear and Linear Models

It is necessary to demonstrate that the linear model given by (2) is a valid approximation of the system dynamics for the response conditions explored in this thesis. Detailed exploration of backdrivable dynamics may require using the model to predict large cart and/or pendulum response amplitudes that could exceed small-angle approximations used to linearize the model. This section validates the linear model as a useful approximation of the nonlinear model for investigating backdrivable dynamics by comparing the nonlinear and linear model responses for a variety of system parameter values and initial pendulum swing angles.
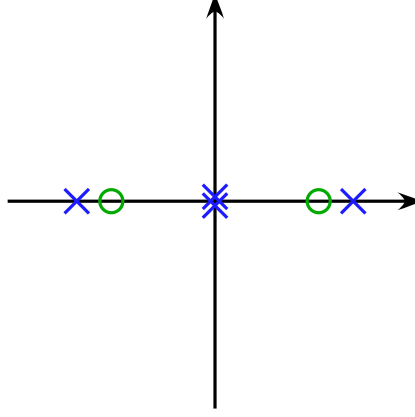
Figure 11: Pole-Zero Plot of Cart with Inverted Pendulum $X(s)/U(s)$ transfer function.

One common error metric for evaluating and comparing performance of models is Root Mean Square Error (RMSE). The nonlinear model (1) and linear model (2) are compared to each other by simulating the free response to an initial pendulum angle, then calculating the RMSE between the resulting cart position and pendulum angle responses found using the two models. The RMSE for cart position and pendulum angle are defined as

$$RMSE_{Position} = \sqrt{\frac{\sum_{i=1}^{N}(x_{NL,i} - x_{L,i})^2}{N}} \tag{10}$$

$$RMSE_{Angle} = \sqrt{\frac{\sum_{i=1}^{N}(\theta_{NL,i} - \theta_{L,i})^2}{N}} \tag{11}$$

where $x_{NL,i}$ is the ith sample of the nonlinear cart position response, $x_{L,i}$ is the ith sample of the linear cart position response, $\theta_{NL,i}$ is the ith sample of the nonlinear pendulum angle response, $\theta_{L,i}$ is the ith sample of the linear pendulum angle response, and N is the total number of data points in the simulated responses.

Figure 12 shows example free responses of the nonlinear and linear models for selected initial pendulum angles, θ_0, and mass ratios, m/M, with $L = 3$ m. The other initial conditions are zero, and $N = 30,000$ time steps are simulated for each response over ten linear periods. Figure 12(a) shows the cart position and Figure 12(b) shows the pendulum angle when $\theta_0 = 5$ deg and $m/M = 0.2$. For this case, $RMSE_{Position} = 9.58 \times 10^{-4}$ m and $RMSE_{Angle} = 0.11$ deg. As shown by these results, when the initial pendulum angle and mass ratio are small, the linear model is a good approximation of the nonlinear model.

Figure 12(c) shows the cart position and Figure 12(d) shows the pendulum angle when

$\theta_0 = 20$ deg and $m/M = 0.2$. The error between the nonlinear and linear models increases with the larger initial swing angle, and $RMSE_{Position} = 0.059$ m and $RMSE_{Angle} = 6.83$ deg. A slight error in frequency is increasingly noticeable in the second half of the response.

Figure 12(e) shows the cart position and Figure 12(f) shows the pendulum angle when $\theta_0 = 5$ deg and $m/M = 2.0$. With the increased mass ratio (heavier pendulum), the errors are $RMSE_{Position} = 0.019$ m and $RMSE_{Angle} = 0.55$ deg. This is an increase over the first case, but not as much as for the larger initial pendulum angle in the second case.

Lastly, Figure 12(g) shows the cart position and Figure 12(h) shows the pendulum angle when $\theta_0 = 20$ deg and $m/M = 2.0$. With both the large initial pendulum angle and mass ratio, there is visibly significant error in the response due to the linear model not accurately representing the frequency. Despite the overall large error, the peak-to-peak amplitudes of the cart position responses have similar amplitude: 1.40 m for linear model and 1.37 m for the nonlinear model. The errors are $RMSE_{Position} = 0.75$ m and $RMSE_{Angle} = 21.66$ deg

Table 1 summarizes the resulting RMSE for each case. The linear model is a worse approximation of the nonlinear model for larger initial pendulum angles and mass ratios, but increasing the initial pendulum angle appears to have a larger impact on the accuracy of the model than increasing the mass ratio. It is expected that the linear model will be inaccurate for larger angles due to the small-angle approximation that was utilized to obtain the linear model, but these results also suggest that increasing the mass ratio magnifies the inaccuracy. The magnifying effect occurs because the nonlinear equations of motion in (1) include a $M + m\sin^2(\theta)$ term in the denominator when solved for $\ddot{x}$ and $\ddot{\theta}$, whereas the linear equations do not include the $m\sin^2(\theta)$ term. It is worth noting that the majority of the error appears due to a frequency desynchronization; the linear and nonlinear responses have similar amplitudes even for the fourth case shown in Figures 12(g) and 12(h).

To develop a complete picture of the impact of the initial pendulum angle and the mass ratio on the accuracy of the linear model relative to the nonlinear model, free responses were simulated for initial pendulum angles between 0.1 and 30 degrees and for mass ratios from 0.05 to 5 for a pendulum length of 3 m. Figure 13 shows 3D surface plots of the cart and pendulum RMSE vs. initial pendulum angle and mass ratio. As the initial pendulum angle
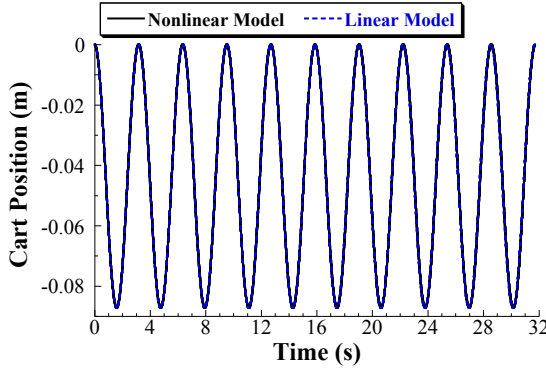
(a) Cart, $\theta_0 = 5$ deg and $m/M = 0.2$.
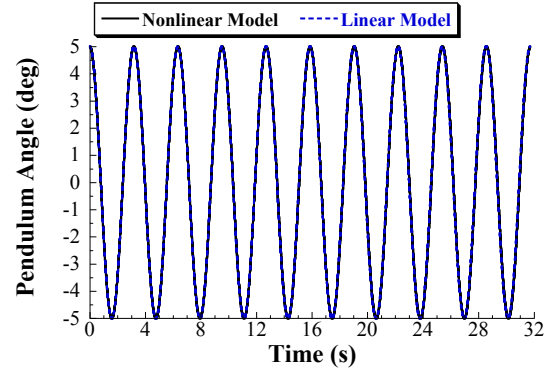
(b) Pendulum, $\theta_0 = 5$ deg and $m/M = 0.2$.
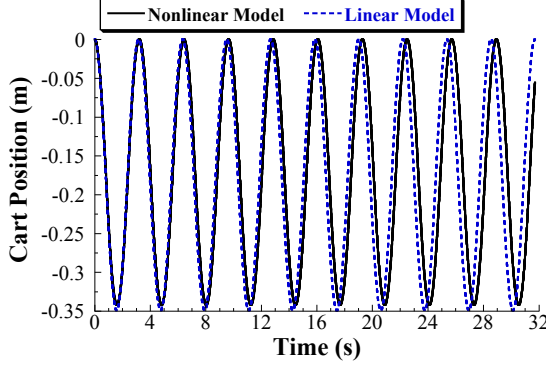
(c) Cart, $\theta_0 = 20$ deg and $m/M = 0.2$.
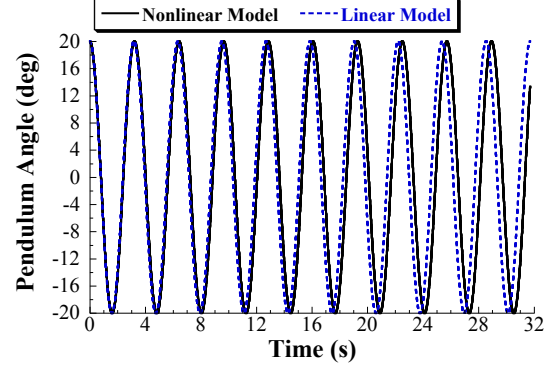
(d) Pendulum, $\theta_0 = 20$ deg and $m/M = 0.2$.
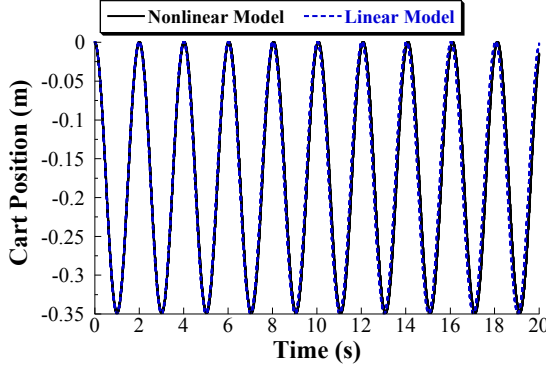
(e) Cart, $\theta_0 = 5$ deg and $m/M = 2.0$.
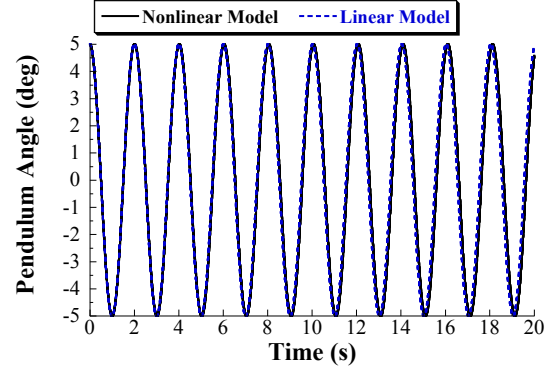
(f) Pendulum, $\theta_0 = 5$ deg and $m/M = 2.0$.
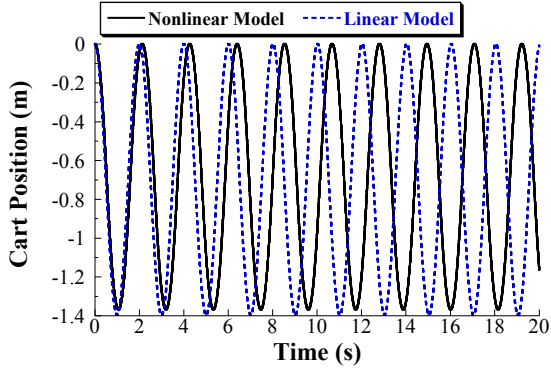
(g) Cart, $\theta_0 = 20$ deg and $m/M = 2.0$.
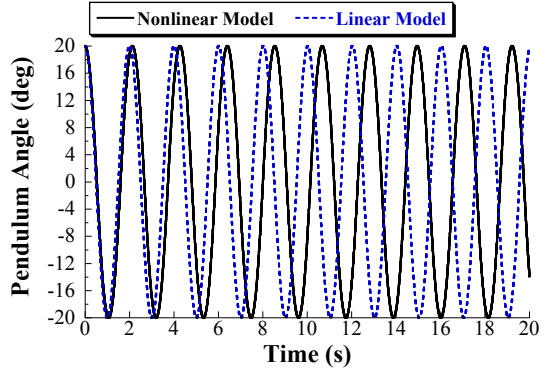
(h) Pendulum, $\theta_0 = 20$ deg and $m/M = 2.0$.

Figure 12: Comparison of sample free responses of Cart with Pendulum nonlinear and linear models for different initial swing angles and mass ratios ($L = 3$ m).

increases, the RMSE of the cart position and pendulum angle responses strictly increases. The relationship with the mass ratio is slightly more complicated, but still shows an overall trend of higher RMSE for larger mass ratios. Investigating this error behavior in detail requires examining 2D plots of selected sections of these surface plots.

Figure 14 shows the cart and pendulum RMSE vs. initial pendulum angle for selected mass ratios. The RMSE of both the cart and pendulum responses strictly increase as the initial pendulum angle increases, as expected due to the small-angle approximation used in the small-angle approximation. The cart and pendulum RMSE for the larger mass ratios increase more quickly. However, there is more complicated behavior for mass ratios above 1. For example, there is larger pendulum RMSE for a mass ratio of 2 than a mass ratio of 5 for some initial pendulum angles around 20 degrees.

To explain why this occurs, Figure 15 shows the cart and pendulum RMSE vs. mass ratio for selected initial pendulum angles. The RMSE of the cart and pendulum responses do not strictly increase as the mass ratio increases. There are local maxima for certain mass ratios, which are particularly noticeable in the pendulum RMSE at larger initial pendulum angles. This variation as a function of mass ratio explains why Figure 14(b) shows larger mass ratios have smaller RMSE than smaller mass ratios over some initial pendulum angle ranges. Figures 14 and 15 show that there is negligible RMSE for pendulum oscillation below 5 degrees regardless of mass ratio, and small RMSE for pendulum oscillation below 10 degrees when the mass ratio is below 1. These are the parameter ranges where the surface plots in Figure 13 are dark blue.

As was illustrated in Figure 12, most of the RMSE results from the linear model not

Table 1: Summary of nonlinear vs. linear model RMSE for the sample free responses shown in Figure 12.

Case	Initial Pendulum Angle, θ_0 (deg)	Mass Ratio, m/M	$RMSE_{Position}$ (m)	$RMSE_{Angle}$ (deg)
Case 1	5	0.2	9.58×10^{-4}	0.11
Case 2	20	0.2	0.059	6.83
Case 3	5	2.0	0.019	0.55
Case 4	20	2.0	0.75	21.66

accurately approximating the *frequency* that arises from larger pendulum response amplitudes and mass ratios. However, one primary system performance characteristic of interest when studying backdrivable flexible systems is the amplitude of the rigid body response because it captures the amount of backdriving that occurs. In this case, the amplitude of the cart position is the performance characteristic of interest for studying backdrivability.
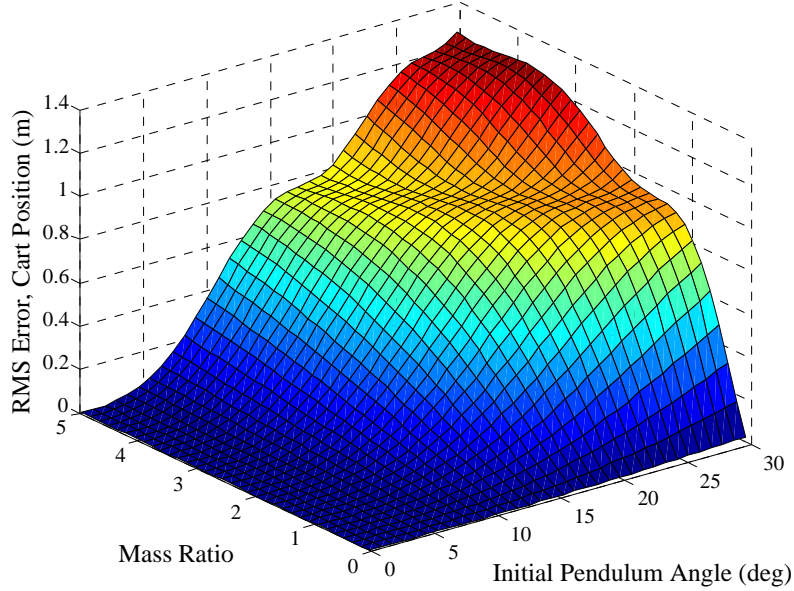
(a) RMSE for cart position response.
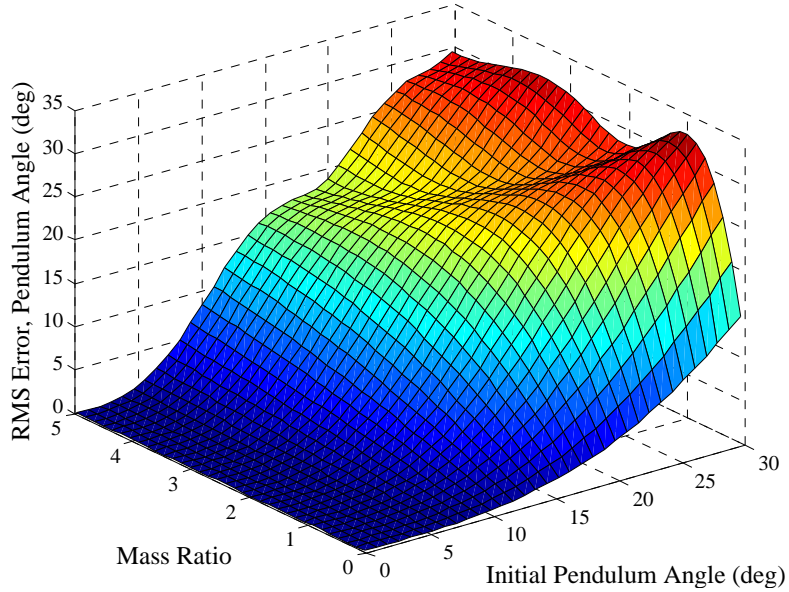
(b) RMSE for pendulum angle response.

Figure 13: RMSE between linear and nonlinear model cart and pendulum free responses vs. initial pendulum angle and mass ratio ($L = 3$ m).

The example responses in Figure 12 showed that the linear and nonlinear models predict approximately the same response amplitudes a wide range of initial pendulum angles and mass ratios.

To further investigate the error between the linear and nonlinear response amplitudes, Figure 16 shows the error between the nonlinear and linear cart response amplitudes as a
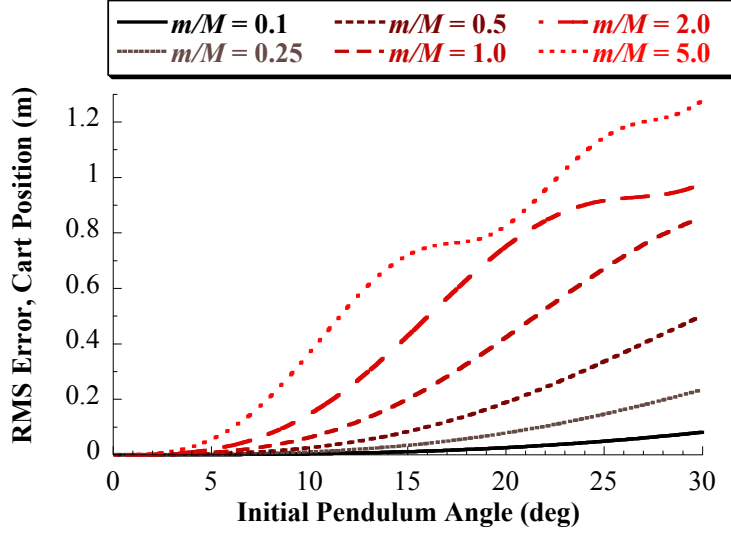
(a) RMSE for cart position response.
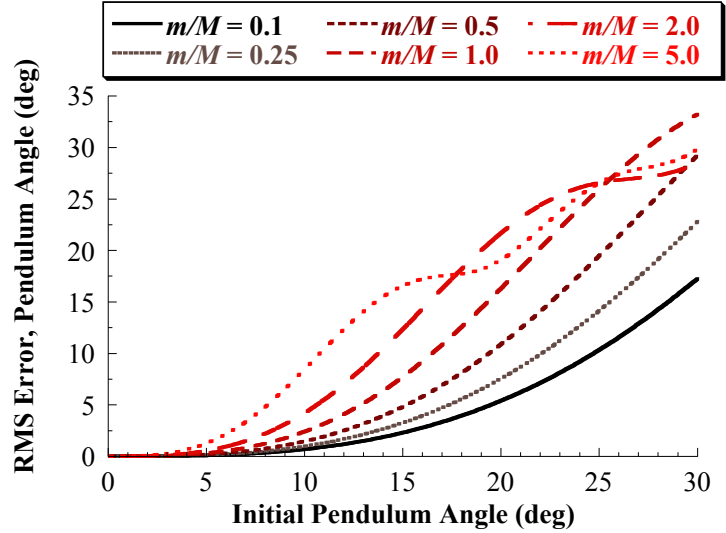
(b) RMSE for pendulum angle response.

Figure 14: RMSE between linear and nonlinear model cart and pendulum free responses vs. initial pendulum angle for selected mass ratios ($L = 3$ m).
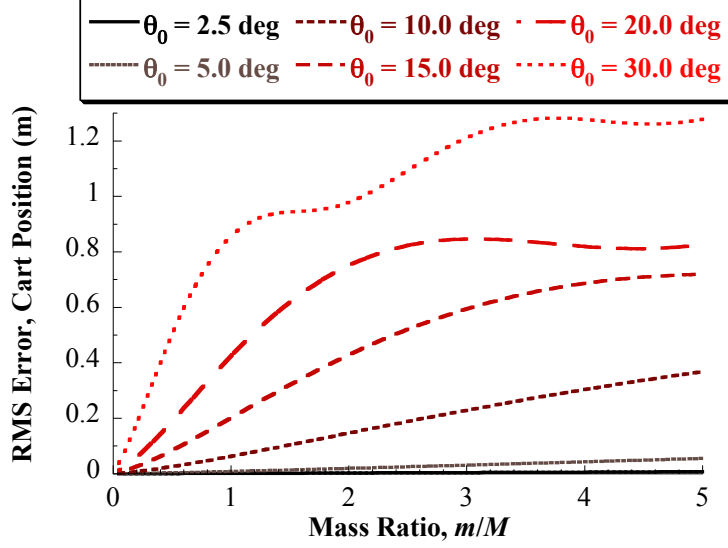
(a) RMSE for cart position response.
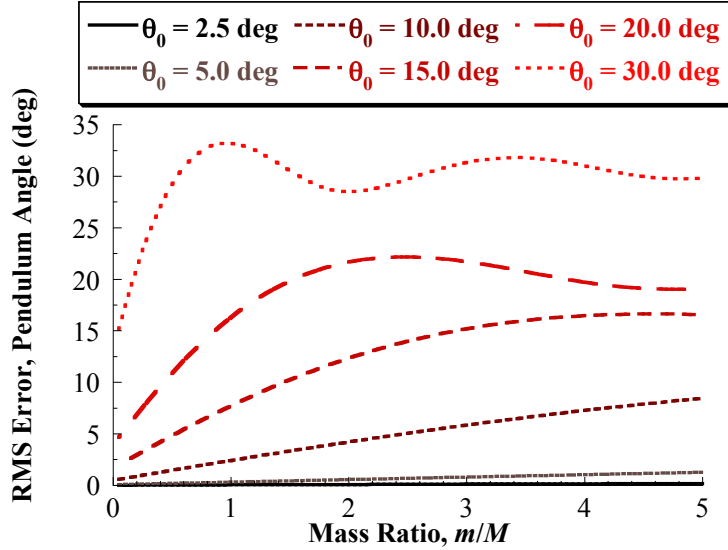
(b) RMSE for pendulum angle response.

Figure 15: RMSE between linear and nonlinear model cart and pendulum free responses vs. mass ratio for selected initial pendulum angles $(L = 3 \text{ m})$.

function of initial pendulum angle and mass ratio. The amplitude error is defined as

$$\text{Amplitude Error} = A_{x,L} - A_{x,NL} \tag{12}$$

where $A_{x,L}$ is the peak-to-peak amplitude of the linear cart position free response and $A_{x,NL}$ is the peak-to-peak amplitude of the nonlinear cart position free response. Figure 16(b) shows the amplitude error vs. the initial pendulum angle for selected mass ratios. There is negligible amplitude error below pendulum oscillation angles of 10 degrees, regardless of

mass ratio. The amplitude error can increase rapidly above 10 degrees if there is a high mass ratio. Figure 16(c) shows the amplitude error vs. mass ratio for some initial pendulum angles. For larger initial pendulum angles, the amplitude error initially increases quickly as the mass ratio increases before approaching asymptotes at higher mass ratios. The larger errors for larger initial pendulum angles should be expected based on use of the small-angle approximation when linearizing.

Figure 17 shows the percent error of the cart position response amplitude between the nonlinear and linear models. The percent error is defined by normalizing (12) by the nonlinear response amplitude:

$$\text{Amplitude Percent Error} = \frac{A_{x,L} - A_{x,NL}}{A_{x,NL}} \times 100\% \qquad (13)$$

The plots in Figure 17 show that the percent error does not depend on the mass ratio and increases as the initial pendulum angle increases. The amplitude percent error is less than 1% for initial pendulum angles below 14 degrees.

As an aside, consider the cart position amplitude for larger initial pendulum angles up to, and above, 90 degrees. Figure 18 shows the cart position amplitude for the linear and nonlinear models and the amplitude error between the nonlinear and linear models for larger initial pendulum angles. Figure 18(a) shows that the cart amplitude with the linear model continues to grow proportionally with the pendulum angle, as should be expected from a linear model. However, the cart amplitude with the nonlinear model reaches a maximum for each mass ratio for every initial pendulum angle $\geq$ 90 degrees. This is a result of the cart reaching a maximum, or minimum, position as the pendulum swings through $\pm$90 degrees, even for initial angles above 90 degrees (or below -90 degrees). Because the rotation of the pendulum is properly accounted for in the nonlinear model, the horizontal velocity of the pendulum reverses direction as the pendulum swings through $\pm$90 degrees. The horizontal position of the center of mass of the system must remain unchanged, and using this information, the value for this maximum cart peak-to-peak amplitude for initial pendulum angles $\geq$ 90 degrees can be predicted based on the position of the center of mass
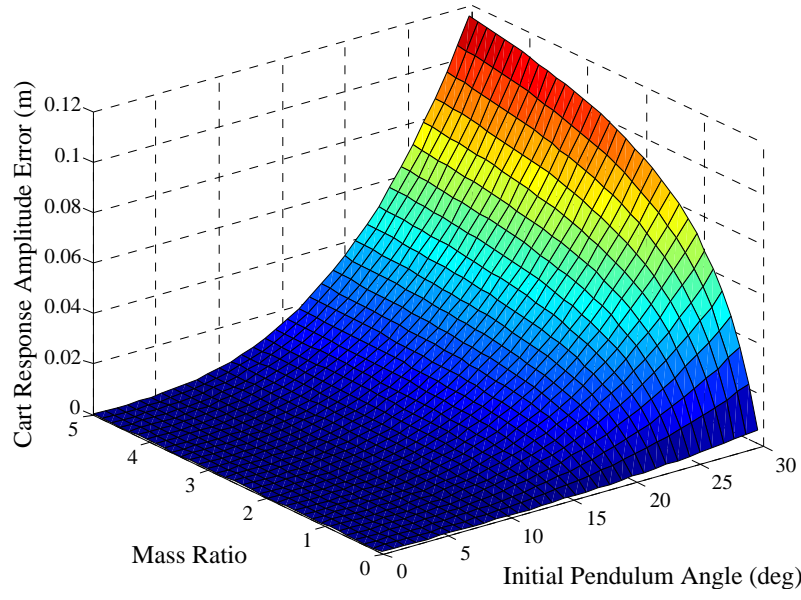
(a) Cart position response amplitude error vs. initial pendulum angle and mass ratio.
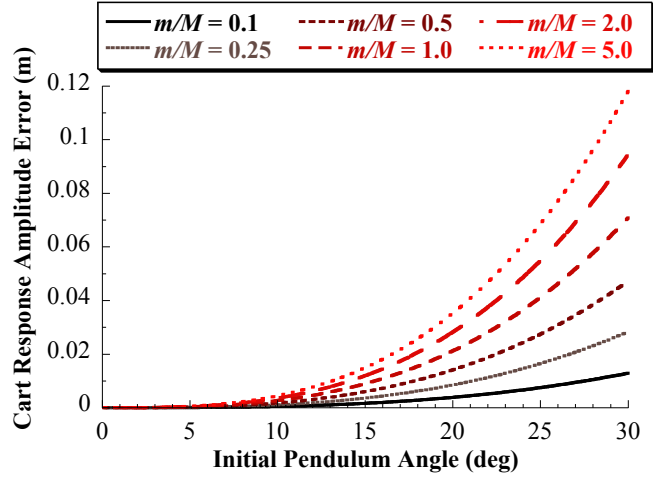
(b) Cart position response amplitude error vs. initial pendulum angle for selected mass ratios.
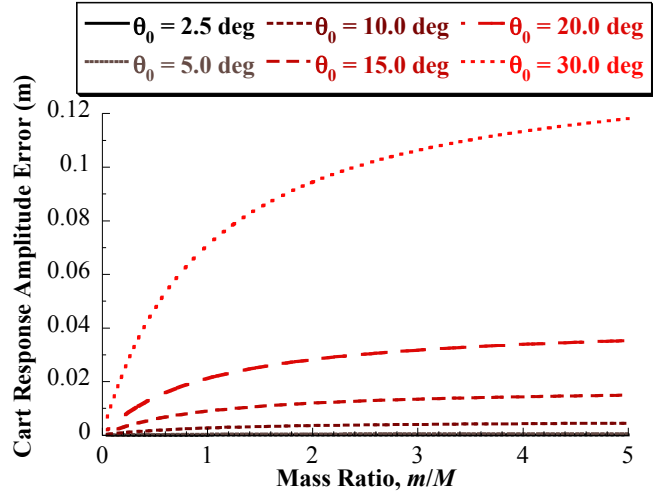
(c) Cart position response amplitude error vs. mass ratio for selected initial pendulum angles.

Figure 16: Amplitude error of cart position response as a function of initial pendulum angle and mass ratio ($L = 3$ m).

when the pendulum is at 90 degrees. This yields the maximum peak-to-peak cart amplitude:

$$\max\left(A_{x,NL}\right) = 2\frac{mL}{M+m}. \tag{14}$$

Figure 18(b) shows the cart amplitude error between the linear and nonlinear models found using (12) for initial pendulum angles up to 120 degrees. Note that this plot is an extended version of Figure 16(b) for a larger range of initial swing angles. Because the cart amplitude found using the nonlinear model reaches a maximum at 90 degrees while the amplitude found using the linear model continues increasing, the amplitude error begins
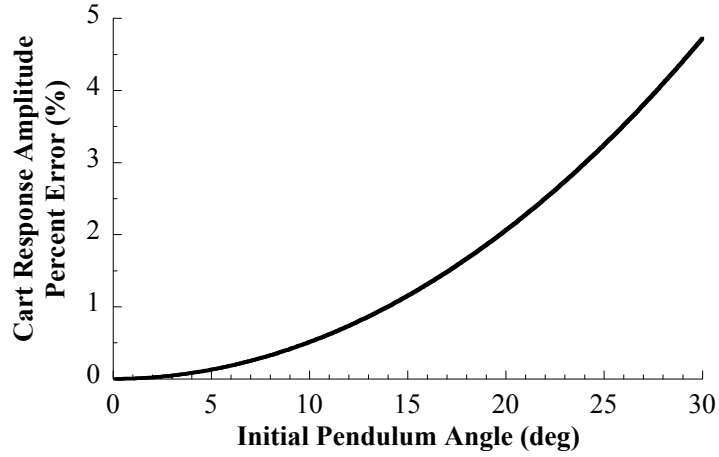
(a) Cart position response amplitude percent error vs. initial pendulum angle.
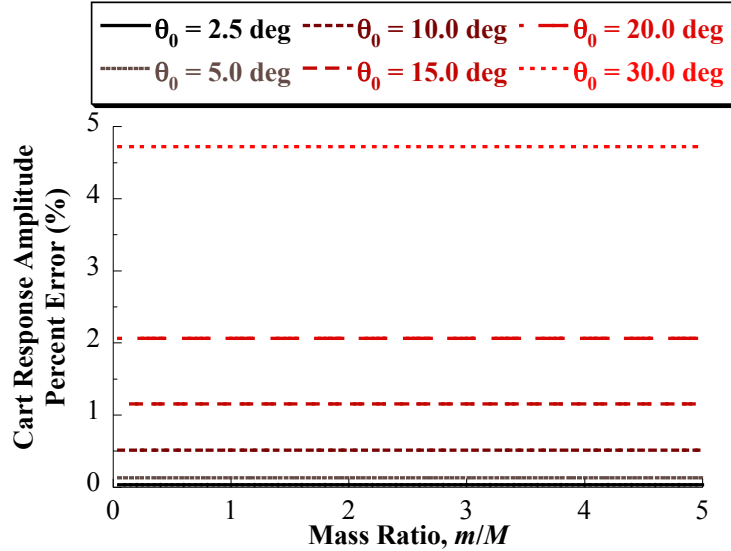
(b) Cart position response amplitude percent error vs. mass ratio.

Figure 17: Cart position response amplitude percent error as a function of initial pendulum angle and mass ratio ($L = 3$ m).

28
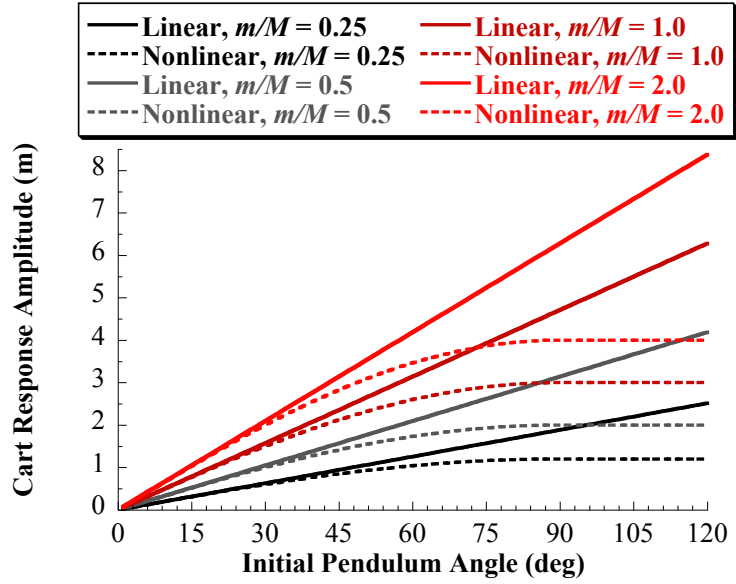
(a) Cart position response amplitude vs. initial pendulum angle for linear and nonlinear models.
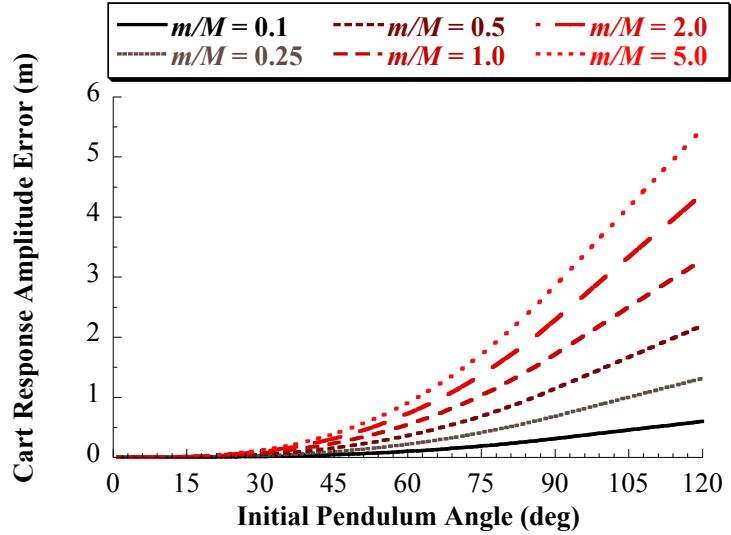
(b) Cart position response amplitude error vs. initial pendulum angle.

Figure 18: Cart position amplitude and amplitude error for larger initial pendulum angles ($L = 3$ m).

increasing at a constant rate for initial pendulum angles above 90 degrees. The amplitude percent error calculated using (13) for larger initial pendulum angles remains independent of the mass ratio and begins increasing at a constant rate for initial pendulum angles above 90 degrees.

These results show that the linear model of the Cart with Pendulum system should be suitable for studying backdrivable dynamics for smaller pendulum oscillation angles and for

reasonable mass ratios ($m/M < 2$), particularly when the performance characteristic of interest is the response amplitude. Similar results could be obtained for the other fundamental models presented in the previous sections of this chapter.

2.5   *Application Example - Studying Crane Trolley Slip While Braking*

One application of the Cart with Pendulum model is for studying swing-induced slipping or drag of crane trolleys when they are braked following motion commands. With sufficiently heavy payloads or large payload swing, the crane trolley can be dragged even under braking load. The sliding mechanism considered here is slip between the crane trolley wheel(s) and the surface they roll on (e.g., rail(s) or the ground) rather than slip at or between the braking surfaces. In other words, this analysis assumes that the braking forces are large enough to lock the wheel(s). To study this slipping effect and analyze when it can occur, the nonlinear model given by (1), which is representative of a planar crane, is augmented with a regularized stick-slip friction law to model slip of the trolley/cart while braking. This section will first show sample system responses where slip occurs for braking following bang-bang trolley commands. Then, illustrative results are shown for the combinations of payload-trolley mass ratio, friction coefficient, and payload swing amplitude that may lead to trolley slip.

2.5.1   Cart with Pendulum Model with Stick-Slip Friction

While numerous stick-slip friction models have been proposed [5], it is important to choose a model that is suitable for simulation with a continuous stick region and transition from stick to slip. Garcia et al. [32] used a continuous transition definition for velocities around zero (the stick-slip region) by defining a very steep linear relationship with a slope of μ_s/ε, where ε is a small number representing the velocity at which slip begins. To model the Stribeck effect at low velocities, a decaying exponential function of the velocity is used to transition from static μ_s to kinetic μ_k coefficients of friction. Figure 19 shows the regularized stick-slip

friction model used for this study. This friction model can be described mathematically as

$$\mu(v) = \begin{cases} \frac{\mu_s}{\varepsilon} v, & \text{if } |v| \leq \varepsilon \\ \text{sign}(v) \left[\mu_k + (\mu_s - \mu_k) e^{-\frac{|v| - \varepsilon}{v_m}} \right], & \text{otherwise} \end{cases} \tag{15}$$

where v is the relative velocity between the two surfaces and v_m is a coefficient for the decaying exponential envelope shown in Figure 19 that models the Stribeck effect.

While Garcia used this friction model as part of studying crane payload slip during off-centered lifts [32], this type of friction model is also useful for this study due to its smooth and continuous nature. This makes it suitable for simulation as part of an augmented Cart with Pendulum nonlinear model. The nonlinear Cart with Pendulum model is used over the linear model due to the expected large payload masses and swing angles required to initiate slip.

The nonlinear equations of motion given by (1) can be augmented with the friction model in (15) by applying a horizontal friction force to the cart in the negative x direction. This yields the following augmented equations of motion:

$$\begin{bmatrix} M + m & -mL\cos(\theta) \\ -mL\cos(\theta) & mL^2 \end{bmatrix} \begin{bmatrix} \ddot{x} \\ \ddot{\theta} \end{bmatrix} = \begin{bmatrix} mL\dot{\theta}^2 \sin(\theta) + u - F_f + f\cos(\theta) \\ -mgL\sin(\theta) - fL \end{bmatrix} \tag{16}$$

where F_f is the friction force. To model stick-slip friction, let:

$$F_f = \mu(\dot{x})N \tag{17}$$

Friction Coefficient
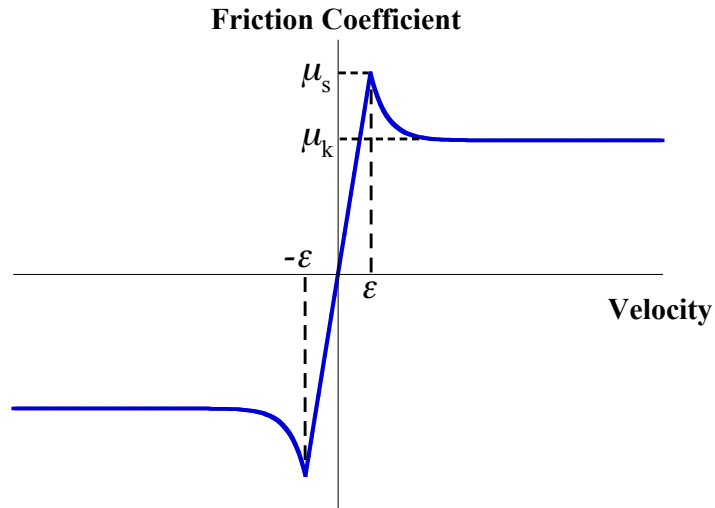
Figure 19: Continuous stick-slip friction model [32].

31

where μ is the friction coefficient given by (15) as a function of the cart velocity $\dot{x}$, and N is the normal force between the cart and the ground. The normal force is given by:

$$N = (M + m)\, g + mL\dot{\theta}^2 \cos(\theta) + mL\ddot{\theta} \sin(\theta) + f \sin(\theta). \qquad (18)$$

Substituting (18) into (17), and then substituting the resulting expression into (16) and rearranging to move the term multiplying $\ddot{\theta}$ to the left side yields the following equations of motion for the Cart with Pendulum model with stick-slip friction:

$$\begin{bmatrix} M + m & mL\left(\mu(\dot{x})\sin(\theta) - \cos(\theta)\right) \\ -mL\cos(\theta) & mL^2 \end{bmatrix} \begin{bmatrix} \ddot{x} \\ \ddot{\theta} \end{bmatrix}$$
$$= \begin{bmatrix} mL\dot{\theta}^2 \sin(\theta) + u - \mu(\dot{x})\left[(M+m)\, g + mL\dot{\theta}^2 \cos(\theta) + f\sin(\theta)\right] + f\cos(\theta) \\ -mgL\sin(\theta) - fL \end{bmatrix}. \qquad (19)$$

Due to the continuous stick-slip model used, these equations can be solved with standard numerical ordinary differential equation solvers such as MATLAB's `ode45` without significant numerical difficulties.

2.5.2 Sample Time Response with Trolley Slip

To illustrate the slip that can occur following trolley motion that excites large payload swing, a sample time response of (19) will be shown for a bang-bang command. For this example response, $m/M = 4$, $L = 3$ m, $\mu_s = \mu_k = 0.5$, and $\varepsilon = 0.01$ m/s. As a simplification, the friction is modeled with $\mu_s = \mu_k$. The braking friction is activated immediately following the completion of the bang-bang command at $t = 6$ s (in other words, $\mu = 0$ for $t <= 6$ s). If at any point in time the cart velocity exceeds $\varepsilon = 0.01$ m/s while the braking friction is activated, the friction model transitions out of the stick region and the cart is slipping.

The response of the trolley/cart is shown in Figure 20(a). During the transient motion between 0 and 6 s, the cart moves with some backdriving from the payload swing shown in Figure 20(b). The cart motion excites significant payload swing, which is large enough to disturb the trolley position following the end of the command at 6 s. The braking friction serves to remove energy from the system, so the payload response in Figure 20(b) steadily
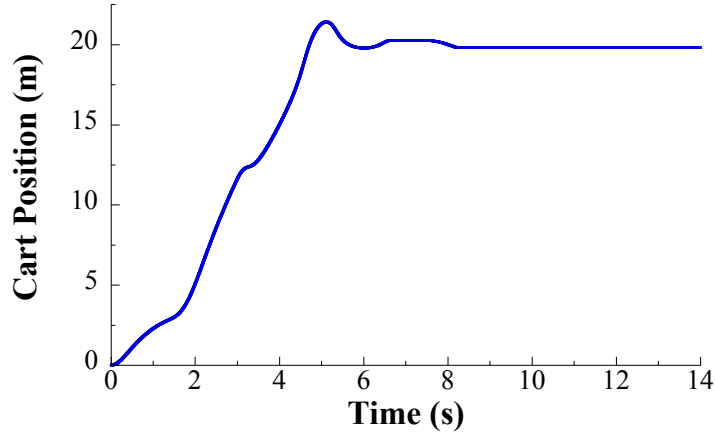
(a) Cart position response to bang-bang command.
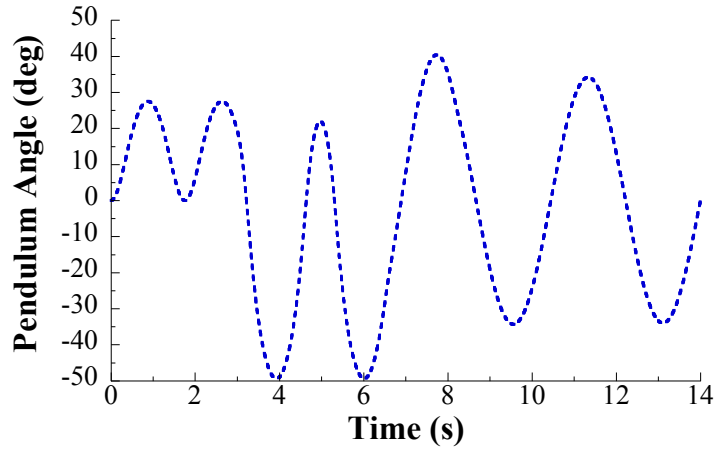
(b) Payload angle response to bang-bang command.

Figure 20: Response of cart with pendulum model with stick-slip friction to bang-bang command, with braking friction activated at $t = 6$ s ($m/M = 4$, $L = 3$ m, $\mu_s = \mu_k = 0.5$, and $\varepsilon = 0.01$ m/s).

decays and has a slower, damped frequency after 6 s even though the pendulum is modeled with no direct damping effects.

Figure 21 shows the cart position and velocity after the braking friction is activated at $t = 6$ s to better examine the slip as it occurs. Figure 21(b) shows that the cart initially slips from 6 s to 6.6 s as it is pulled by the swinging payload and simultaneously decelerated by the braking friction. The cart comes to a stop at 6.6 s due to the braking friction. However, the payload swing amplitude is still large enough to cause the cart to slip again beginning at 7.4 s. This secondary slip pulls the cart about 45 cm before the cart finally comes to
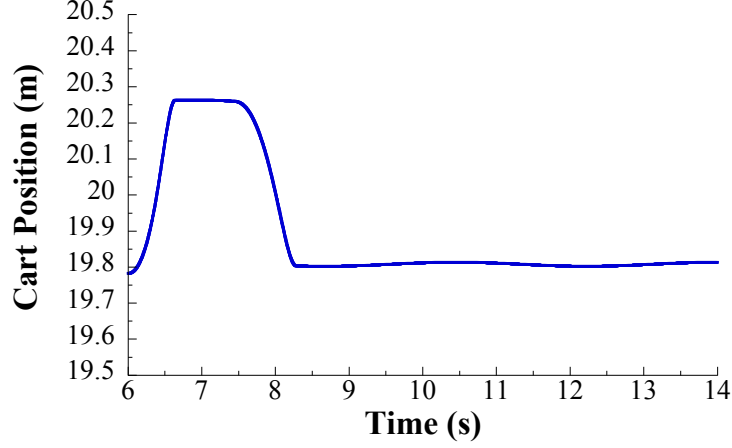
(a) Cart position during braking period following command.
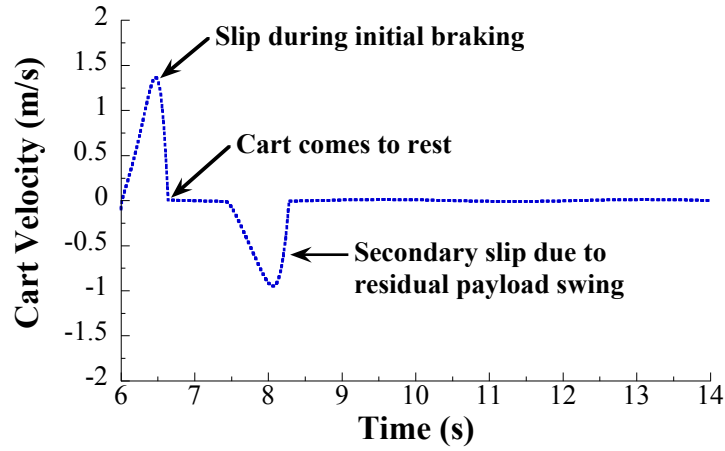
(b) Cart velocity during braking period following command.

Figure 21: Response of cart with pendulum model with stick-slip friction following completion of bang-bang command and activation of braking friction at $t = 6$ s $(m/M = 4$, $L = 3$ m, $\mu_s = \mu_k = 0.5$, and $\varepsilon = 0.01$ m/s).

a final stop around 8.3 s. The small deviations in position after 8.3 s that are visible in Figure 21(a) result from the continuous stiction transition used in the friction model.

2.5.3 Slipping Parameter Study

A parameter study is performed to more fully examine the payload swing amplitudes, system mass ratios, and friction parameters which lead to slip. To control for the varied effects on the response caused by commanded trolley motion depending on the mass ratio and command amplitude, it is more effective to simulate the system for a given parameter set

with a specified amount of payload swing. This is done by simulating the free response of the system with an initial payload angle θ_0 and braking friction activated immediately at $t = 0$ s. This is somewhat equivalent to restarting the simulation following the completion of the commanded motion using the final state values as initial conditions for simulation of the residual motion with braking friction activated. However, this approach ignores any nonzero cart velocity following the command (i.e., any initial slipping). Also, this approach assumes that the residual payload swing can be modeled simply as an initial angle rather than some combination of angle and angular velocity. In other words, the initial total energy in the residual payload swing is modeled solely as potential energy rather than some combination of potential and kinetic energy. This simplifies the parameter space in terms of how the effect of the residual payload swing is parameterized and investigated. Also, the interdependent effects of command switch times and mass ratio on the residual payload swing are ignored by studying the free response. Lastly, as was done for the sample slipping response in Section 2.5.2, the static and kinetic coefficients of friction are assumed to be equal ($\mu = \mu_s = \mu_k$). This simplification of the friction model further reduces the parameter space that must be investigated.

For a range of friction coefficients μ between 0.1 and 0.9 and mass ratios from 0.1 to 5, the minimum pendulum angle that leads to cart slip was found. Slip is defined to occur if the cart velocity exceeds $\varepsilon = 0.01$ m/s. The simulation would only search angles up to 90 degrees, and would return no solution for a given mass ratio and friction coefficient pair if 90 degrees of pendulum swing did not cause slip. Note that this would be an unrealistically extreme amount of swing anyways and would not be encountered in practice, but for the purposes of this investigation it was chosen as an artificial upper limit upon which the search would be abandoned.

Figure 22 shows the resulting minimum pendulum angles that lead to cart slip as a function of the mass ratio and friction coefficient for $L = 3$ m. Figure 22(a) shows a 3D surface of the minimum angle required for slip. Angles below the surface would not lead to any cart slip for the given friction coefficient and mass ratio pair, while angles at and above the surface would result in slip. Figure 22(b) shows a side view of Figure 22(a), with the

minimum angle required for slip plotted vs. mass ratio for selected values of the friction coefficient. Swing angles above each line would result in slipping for the given amount of friction. The results in Figure 22 show that the minimum angle required for slip increases as the friction coefficient increases but decreases as the mass ratio increases. This is expected behavior given that higher friction coefficients allow the cart to more strongly resist the backdriving effect of the swinging pendulum, while higher mass ratios result in larger forces applied by the swinging pendulum to the cart that can overcome the stiction forces and lead to slip.

2.5.4 Trolley Slip Results Analysis and Discussion

Figure 22 shows that a large portion of the friction coefficients and mass ratios require extremely large swing angles to cause slip. These angles would not be realistically encountered during crane operation. Therefore, slip would not likely occur for many combinations of mass ratio and friction coefficients, particularly as the friction coefficient gets larger (e.g., as the braking system is more effective). Also, the model assumes that the suspension cable is rigid and does not consider that the cable could go slack, which may occur for larger swing angles.

Payload swing approaching 30 degrees of amplitude can be considered a more realistic upper bound on extreme swing that could be encountered when operating a crane. Figure 23 shows a 2D plot of the friction coefficient and mass ratio parameter space considered in this study, with the solid line indicating the transition from the parameter pairs that do not lead to slip and those that do for up to 30 degrees of payload swing. Mass Ratios and friction coefficients above the solid line will not lead to cart/trolley slip as long as the payload swing is $\leq$ 30 degrees. For mass Ratios and friction coefficients below the solid line, the cart/trolley can slip if the the payload swing is $\geq$ 30 degrees. Mass ratios up to 5 require a friction coefficient less than 0.45 for slipping, and this is a relatively low friction coefficient that should only occur if some debris or a contaminant is present between the trolley wheel(s) and rail.

For some of the friction coefficients and mass ratios explored in the parameter space,
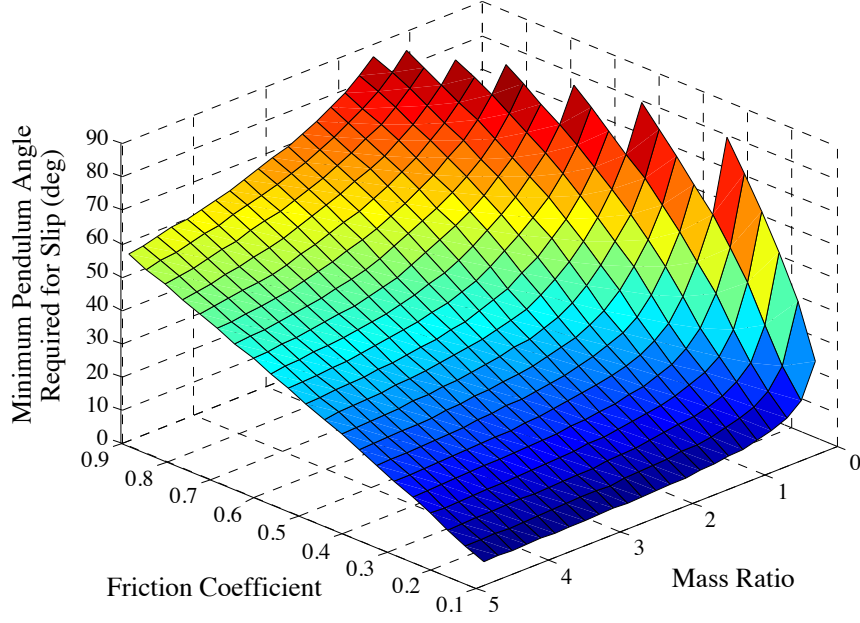
(a) Minimum pendulum angle required for cart slip vs. mass ratio and friction coefficient.
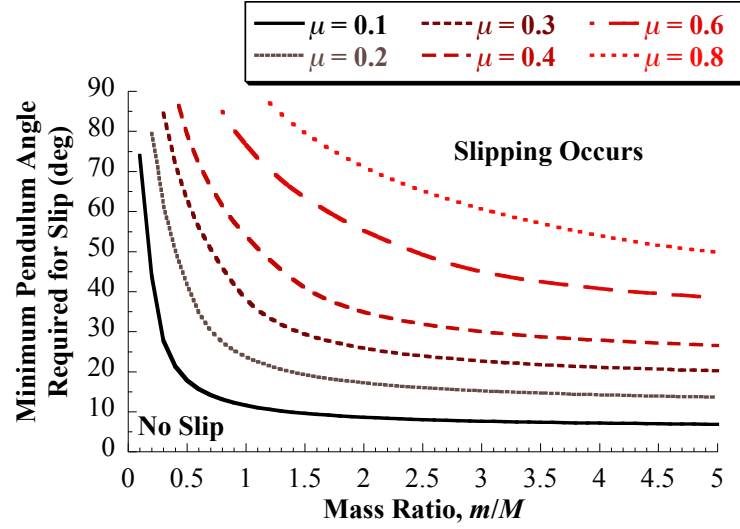
(b) Minimum pendulum angle required for slip as a function of mass ratio for selected friction coefficients.

Figure 22: Minimum pendulum angle required for cart slip as a function of mass ratio and friction coefficient ($L = 3$ m).

no solution (i.e., pendulum swing angle large enough to cause transition from no slip to slipping) below 90 degrees of pendulum swing was found. This region with no solution below 90 degrees of swing is also shown in Figure 23. It consists primarily of low mass ratios where the pendulum is not heavy enough to cause the trolley to slip, and grows wider to include heavier mass ratios as the friction coefficient increases.

37
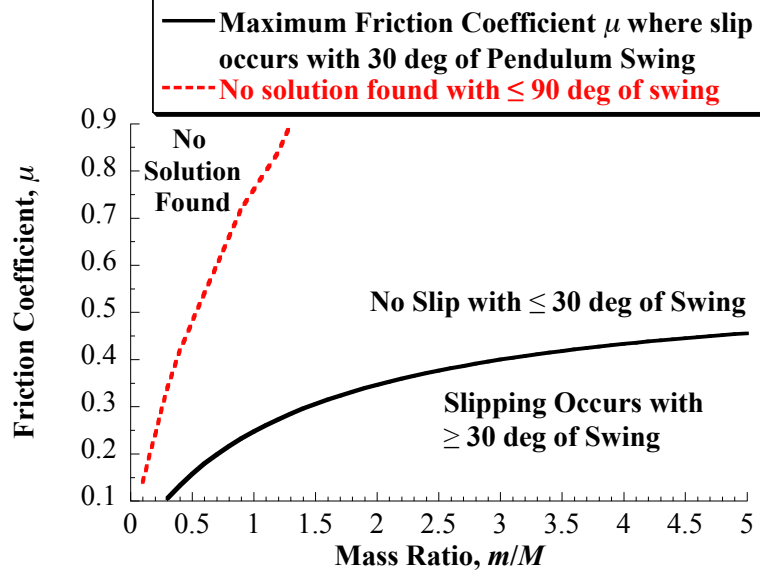
Figure 23: Transition from no slip to slipping when there is 30 degrees of pendulum swing as a function of mass ratio and friction coefficient ($L = 3$ m). The region of the friction coefficient and mass ratio parameter space where no slipping solution was found is also shown.

When slipping does occur, it is useful to examine how much the cart/trolley slips. For the purposes of this discussion, the results from the parameter study with $\mu = 0.2$ will be examined. While this could be perceived as an abnormally low friction coefficient, it serves as a useful example of a slipping failure scenario where there is debris or some other contaminant that significantly lowers the traction of the trolley wheels. Figure 24 shows the resulting cart response peak-to-peak amplitude for a range of pendulum swing angles between 5 and 30 degrees and mass ratios from 0.1 to 5. For many of the smaller swing angles and the lower mass ratios, the cart does not slip and the amplitude is negligible. The solid line indicates the transition to results that include slip, where cart amplitude values above this line include responses where the cart slipped. For large enough swing angles or high enough mass ratios, the cart slips and peak-to-peak slip amplitudes up to 1 m are predicted by the simulation model.

Figure 24(b) shows the cart amplitude as a function of the mass ratio for selected pendulum swing angle amounts. The transition point, or lowest mass ratio that results in cart slip, is indicated for each selected swing angle case. No cart slip was found for any mass ratio with 10 degrees of swing (or less). However, slipping occurs for high enough
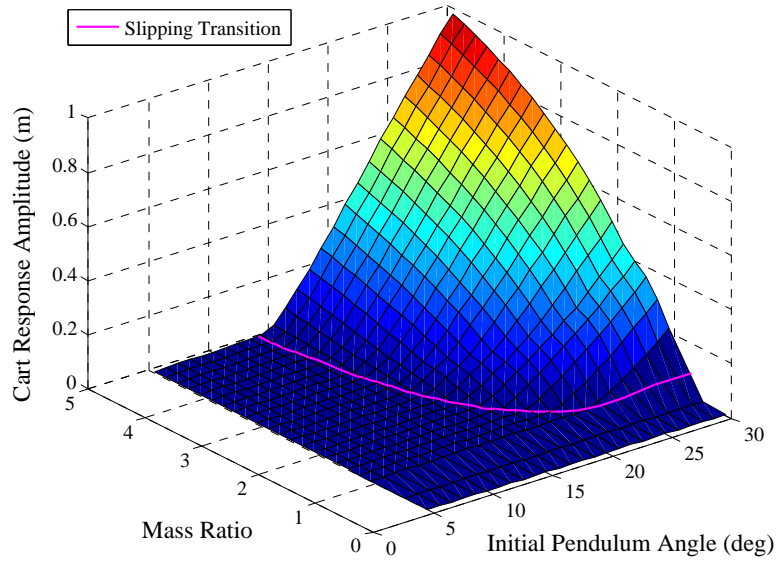
(a) Cart amplitude vs. initial pendulum angle and mass ratio.
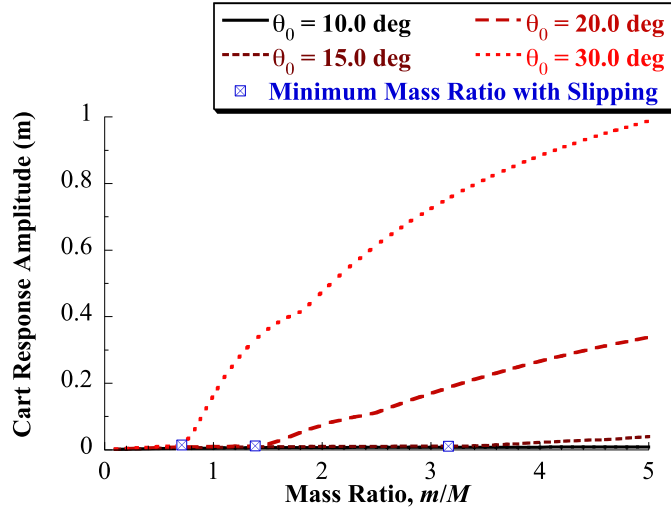
(b) Cart amplitude vs. mass ratio for selected initial pendulum angles.
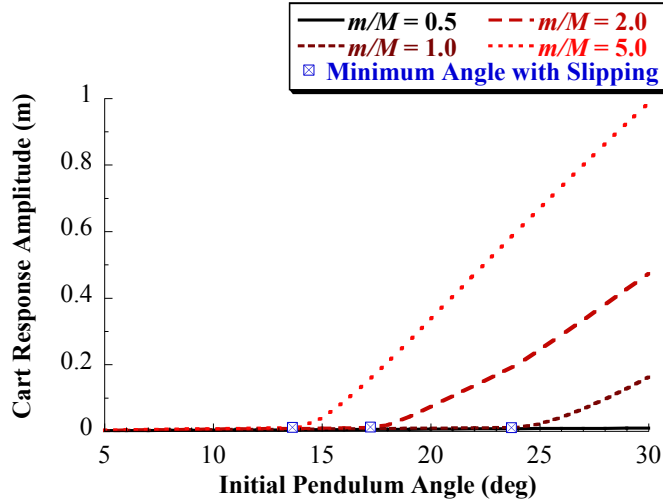
(c) Cart position response amplitude error vs. pendulum swing angle for selected mass ratios.

Figure 24: Maximum residual cart response amplitude as a function of initial pendulum angle and mass ratio ($\mu = 0.2$ and $L = 3$ m). The lowest parameter values where slipping first occurred are indicated on each plot.

39

mass ratios as the angle increases. For example, mass ratios above 3.16 lead to trolley slip with 15 degrees of swing (or more).
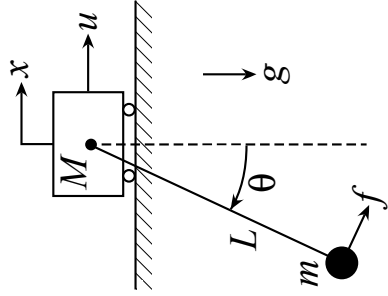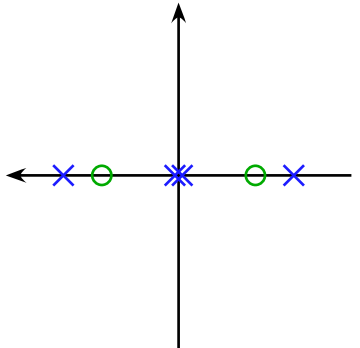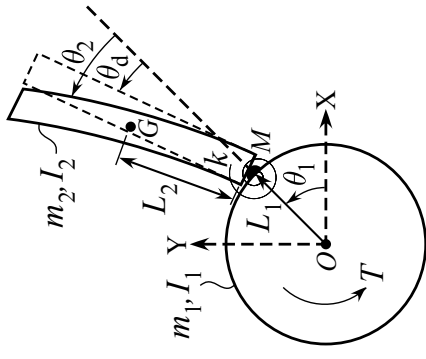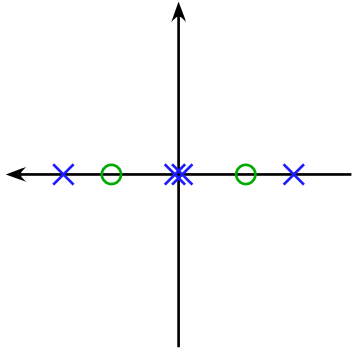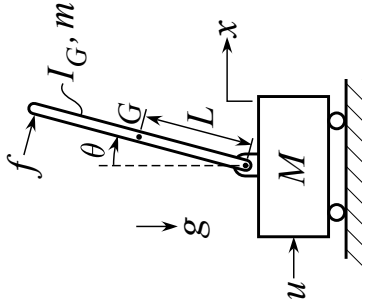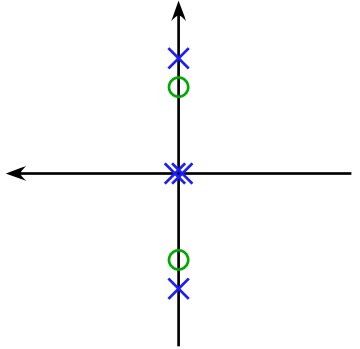
Figure 24(c) shows the cart amplitude as a function of the pendulum swing angle for selected mass ratios. The transition point, or minimum swing angle that causes cart slip, is indicated for each selected mass ratio case. No cart slip was found for a mass ratio of 0.5 for swing angles up to 30 degrees. (Figure 22(b) predicts that a minimum of 47.8 degrees of payload swing would be required for slipping at this mass ratio with $\mu = 0.2$.) However, slipping occurs for the higher mass ratios with large enough pendulum swing angle. For a mass ratio of 5, slipping occurs with a minimum of 13.6 degrees of payload swing with $\mu = 0.2$.

2.6 Comparison and Summary of Fundamental Models

Table 2 summarizes the three fundamental models presented in this chapter, showing schematics and the backdrivable transfer function with a pole-zero plot. Notice that the pole-zero plots for Models I and II have a similar layout: a double integrator, with a pair of complex of poles and zeros where the poles have larger imaginary components than the zeros. Model III has the same pattern but rotated onto the real axis, with a stable real zero and pole, unstable pole, and non-minimum phase zero. This system can be made conditionally stable with a feedback controller, with one such controller being proposed by the designers of the Segway [62]. Depending on the design of the feedback controller, some of the closed-loop poles may be complex and result in underdamped oscillations. This is an example of a case where the backdrivability may arise from a feedback controller used to stabilize the system.

These fundamental models of backdrivable flexible systems will be used throughout the remainder of this thesis. They will be used as example systems for application of proposed performance metrics for backdrivability, and to evaluate control systems designed to mitigate the negative effects and performance of backdrivable systems. The contributions of this chapter include the fundamental models and the classification of types of backdrivable systems.

Model I - Cart with Pendulum	Model II - Rotary Hub with Flexible Arm	Model III - Cart with Inverted Pendulum

Model I - Cart with Pendulum

$$\frac{X(s)}{U(s)} = \frac{s^2 + \frac{g}{L}}{s^2 \left[Ms^2 + \left(\frac{(M+m)\,g}{L} \right) \right]}$$

Model II - Rotary Hub with Flexible Arm

$$\frac{\Theta_1(s)}{T(s)} = \frac{N_2 s^2 + N_0}{s^2 \left(D_4 s^2 + D_2 \right)},$$
where
$$N_2 = I_2 + m_2 L_2^2, \quad N_0 = k,$$
$$D_4 = I_1 I_2 + I_2 m_2 L_1^2 + I_1 m_2 L_2^2,$$
$$D_2 = k \left(I_1 + I_2 + m_2 \left(L_1^2 + L_2^2 + 2L_1 L_2 \right) \right)$$

Model III - Cart with Inverted Pendulum

$$\frac{X(s)}{U(s)} = \frac{N_2 s^2 - N_0}{s^2 \left(D_4 s^2 - D_2 \right)},$$
where
$$N_2 = I_G + mL^2, \quad N_0 = mgL,$$
$$D_4 = I_G \left(M + m \right) + MmL^2,$$
$$D_2 = mgL \left(M + m \right)$$

CHAPTER III

PERFORMANCE METRICS FOR BACKDRIVABLE FLEXIBLE SYSTEMS

This chapter presents performance metrics for determining the degree of backdrivability, or coupling between rigid and flexible modes, as a function of any key system parameters. A goal is to develop metrics that identify what conditions or system parameter combinations a system can be classified as backdrivable. This allows thresholds between 'backdrivable' and 'not backdrivable', like the one seen in Figure 4, to be defined. To predict the level of backdrivablity for a given system, the performance metric should capture the impact that various system parameters have on the degree of coupling or backdrivability between the rigid and flexible modes. In the case of Figure 4, the mass ratio of the rigid and flexible elements is the key system parameter that determines the response ratio, or the degree of backdrivability.

The performance metrics are directed to stable backdrivable flexible systems. For illustrative purposes, the metrics developed in this chapter will be applied to the two stable models presented in Chapter II. Application of the performance metrics to the unstable Cart with Inverted Pendulum model will be addressed in Chapter IV after presenting a stabilizing control system for this model. Because the feedback controller is the source of flexibility in the stabilized system, whether or not it exhibits backdriving effects depend on the system and controller parameters. If there are backdriving effects, then the degree of backdrivability also depends on the system and controller parameters. Therefore, it makes sense to analyze the backdrivability of the Cart with Inverted Pendulum model in the context of the control system design and discussion.

Two performance metrics are proposed in chapter. The first is based on eigenvectors, mode shapes, and system response ratios. The second is based on the system open-loop poles and zeros. The metrics are applied to the stable fundamental models to demonstrate

and compare the metrics and to evaluate the backdrivability of the fundamental models as a function of their key system parameters.

3.1 Backdrivable Amplitude Ratio from System Time Response

The amount of backdrivability exhibited by a system can be examined by considering the time response of the rigid and flexible states. For a given amount of flexible-state oscillation, a system can be classified as more backdrivable if the corresponding rigid-state oscillation has large amplitude. In other words, the ratio between the rigid-state and flexible-state response amplitudes is a useful metric for characterizing the degree of system backdrivability.

For example, consider the time response of the Cart with Pendulum to a bang-bang command, similar to Figure 7. Figure 25 compares the bang-bang response for two different pendulum-cart mass ratios m/M with $L = 5$ m and a command designed to move the cart 1 m. The response with mass ratio $m/M = 0.5$ is the same as was shown in Figure 7. The natural frequency of the system with $m/M = 1$ is higher than the system with $m/M = 0.5$, in accordance with (4). The amplitudes of the residual cart and pendulum responses can be used to assess the system backdrivability for the two mass ratios. The system with $m/M = 0.5$ has a cart residual amplitude of 0.17 m and a pendulum residual amplitude of 5.72 deg (0.10 rad), yielding a cart-to-pendulum amplitude ratio of 1.7 m/rad. The system with $m/M = 1$ has a cart residual amplitude of 0.21 m and a pendulum residual amplitude of 4.91 deg (0.086 rad), yielding a cart-to-pendulum amplitude ratio of 2.5 m/rad. Because a linear model is used, the same amplitude ratio would be obtained regardless of if a free or forced response is analyzed and independent of the type of command.

Note that the pendulum residual vibration amplitude with $m/M = 1$ is slightly less than with $m/M = 0.5$ even though the residual amplitude ratio is larger. The pendulum residual amplitude is less because the same switching time and move distance were used for the bang-bang commands applied to both systems, yet the natural frequency is higher with the increase in mass ratio. Residual vibration amplitude changing with system natural frequency and bang-bang command parameters is a well-known behavior [99]. In fact, some researchers have used this property to generate vibration-free bang-bang commands for
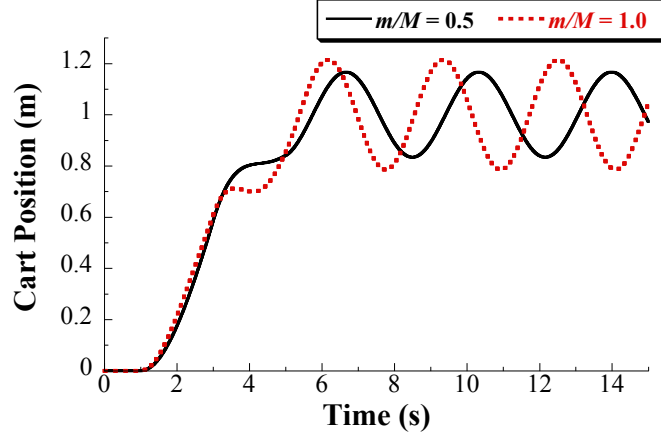
(a) Cart position.
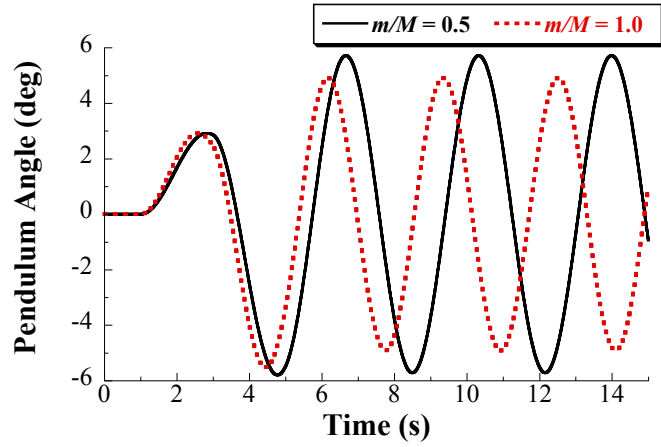
(b) Pendulum angle.

Figure 25: Response of Cart with Pendulum fundamental model to a bang-bang command designed to move the cart 1 m with two different pendulum-cart mass ratios, $m/M = 0.5$ and $m/M = 1.0$.

specified move distances and system frequencies, assuming the command magnitude and switching times can be freely chosen [79].

The downside of using this approach to determine amplitude ratio and assess backdrivability is that it requires obtaining residual amplitudes from simulated time responses or from analytic expressions for the time responses of the rigid and flexible states. Obtaining the time responses through simulation can be a slow approach when there are a variety of trade studies that may be required to identify the parameters that influence backdrivability and their relationships to the response ratio. Also, analytic expressions for time responses

can be unwieldy or difficult to obtain for some systems. Therefore, the amplitude ratio calculated directly from time responses has limited usefulness as a performance metric except as a brute-force simulation approach. Two alternative performance metrics are proposed in this chapter.

3.1.1 Amplitude Ratio Comparison Between Nonlinear and Linear Models

Section 2.4 presented the RMSE and amplitude errors between the nonlinear and linear Cart with Pendulum models to validate the use of the linear model in this thesis. However, it is also worthwhile to investigate how the cart-to-pendulum amplitude ratio predicted by the linear and nonlinear models varies to further illustrate when the linear model is a sufficient approximation for use when studying backdrivable systems.

Figure 26 shows a comparison between the Cart-to-pendulum amplitude ratio from free responses of the linear and nonlinear models as a function of initial pendulum angle (a) and mass ratio (b). Figure 26(a) shows that the amplitude ratio is higher for larger mass ratios, and the amplitude ratio predicted by the linear model does not depend on the initial pendulum angle as should be expected from a linear model. Figure 26(b) shows that the amplitude ratio increases quickly as the mass ratio increases for small mass ratios. As the initial pendulum angle increases, the amplitude ratio predicted by the nonlinear model decreases and larger error develops between the linear and nonlinear model amplitude ratios due to deviation from the small-angle approximation. The amplitude ratio predicted by the linear model serves as an upper bound, or a conservative worst-case estimate, on that from the nonlinear model response. Also, the amplitude ratio percent error does not depend on the mass ratio based on the results shown in Figure 17.

3.2 Performance Metric 1 - Eigenvector Response Ratio

3.2.1 Eigenvector Response Ratio Performance Metric Definition

A useful performance metric can be obtained from analysis of eigenvalues and eigenvectors. Because eigenvectors represent the mode shapes of a system, they capture the relative steady-state response ratios between the various system states for each mode. By examining the flexible mode shape(s) of the system, the relative response ratio between the rigid and
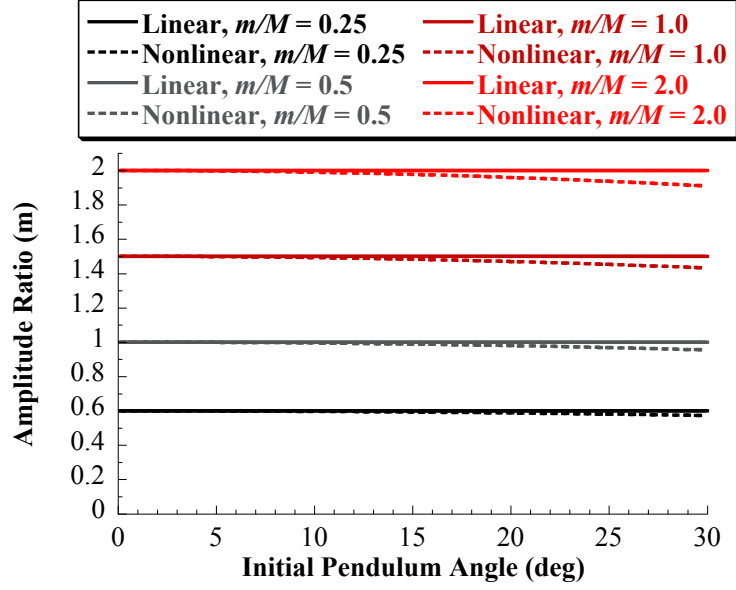
(a) Cart-to-pendulum amplitude ratio vs. initial pendulum angle.
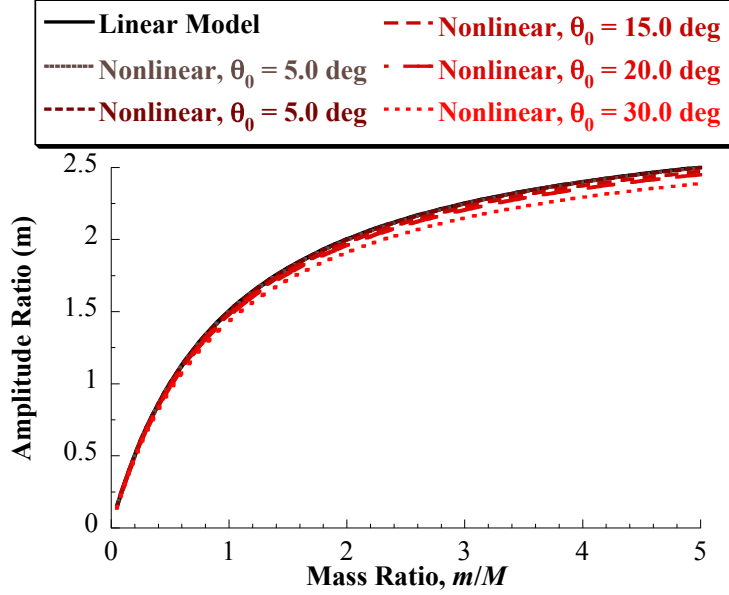
(b) Cart-to-pendulum amplitude ratio vs. mass ratio.

Figure 26: Cart-to-pendulum amplitude ratio as a function of initial pendulum angle and mass ratio for the linear and nonlinear models ($L = 3$ m).

flexible element states can be identified without needing to calculate or simulate the time response of the system.

The state matrix for a generic 4th-order system with a rigid-body mode and one undamped flexible mode with state defined relative to the rigid body can be represented in

the form:

$$\mathbf{A} = \begin{bmatrix} 0 & 1 & 0 & 0 \\ 0 & 0 & -k_1 & 0 \\ 0 & 0 & 0 & 1 \\ 0 & 0 & -k_2 & 0 \end{bmatrix} \tag{20}$$

where the state vector is defined as:

$$\vec{x} = \begin{bmatrix} x_1 & \dot{x}_1 & x_2 & \dot{x}_2 \end{bmatrix}^T \tag{21}$$

with x_1 and $\dot{x}_1$ corresponding to the rigid element position or angle and velocity, and x_2 and $\dot{x}_2$ corresponding to the position or angle and velocity of the flexible element.

The eigenvalues of the state matrix (20) are:

$$\lambda_{1,2} = 0, \quad \lambda_{3,4} = \pm\sqrt{k_2}i,$$

The corresponding generalized eigenvectors can be listed as the columns of a matrix that has the form:

$$\mathbf{Q} = \begin{bmatrix} 1 & 0 & R\sqrt{\frac{1}{k_2}}i & -R\sqrt{\frac{1}{k_2}}i \\ 0 & 1 & R & R \\ 0 & 0 & \sqrt{\frac{1}{k_2}}i & -\sqrt{\frac{1}{k_2}}i \\ 0 & 0 & 1 & 1 \end{bmatrix},$$

where $R = \frac{k_1}{k_2}$. While each column/eigenvector is the specific mode shape, the entries in each row correspond to that state's contribution to each mode. The third and fourth columns are the flexible mode shape. The magnitude of the first two rows–which correspond to the states of the rigid element–are scaled by R relative to the third and fourth rows which correspond to the states of the flexible element. Therefore, R is defined as the *Eigenvector Response Ratio*. This ratio can be calculated for each of the fundamental backdrivable models presented in Chapter II. The resulting ratio is a function of the relative values of the system parameters that contribute to the degree of coupling between the rigid and flexible modes of the system. Therefore, the ratio serves as an effective performance metric for evaluating the degree of backdrivability as a function of the system parameter values.

47

Note that this approach yields an equivalent result to calculating the amplitude ratios from the system time response, as was considered in Section 3.1. However, neither time response simulations for a variety of system parameters nor obtaining analytic expressions for the time responses are required when using the eigenvector analysis approach to obtain the response ratio performance metric.

3.2.2 Eigenvector Response Ratios of Fundamental Backdrivable Systems

This section derives Eigenvector Response Ratios for the stable fundamental models presented in Chapter II and shows illustrative results of the ratio magnitude for a range of system parameters for each model.

3.2.2.1 Cart with Pendulum

Consider a state-space representation of the Cart with Pendulum model from (2):

$$
\begin{bmatrix} \dot{x} \\ \ddot{x} \\ \dot{\theta} \\ \ddot{\theta} \end{bmatrix} = \begin{bmatrix} 0 & 1 & 0 & 0 \\ 0 & 0 & -\frac{mg}{M} & 0 \\ 0 & 0 & 0 & 1 \\ 0 & 0 & -\frac{(M+m)g}{ML} & 0 \end{bmatrix} \begin{bmatrix} x \\ \dot{x} \\ \theta \\ \dot{\theta} \end{bmatrix} + \begin{bmatrix} 0 & 0 \\ \frac{1}{M} & 0 \\ 0 & 0 \\ \frac{1}{ML} & -\frac{1}{mL} \end{bmatrix} \begin{bmatrix} u \\ f \end{bmatrix}.
\tag{22}
$$

The eigenvalues of the state matrix are:

$$
\lambda_{1,2} = 0, \quad \lambda_{3,4} = \pm \sqrt{\frac{-(M+m)\,g}{ML}},
\tag{23}
$$

with the corresponding generalized eigenvectors listed as the columns of the matrix:

$$
\mathbf{Q_I} = \begin{bmatrix} 1 & 0 & \frac{mL}{M+m}\sqrt{\frac{-ML}{(M+m)g}} & -\frac{mL}{M+m}\sqrt{\frac{-ML}{(M+m)g}} \\ 0 & 1 & \frac{mL}{M+m} & \frac{mL}{M+m} \\ 0 & 0 & \sqrt{\frac{-ML}{(M+m)g}} & -\sqrt{\frac{-ML}{(M+m)g}} \\ 0 & 0 & 1 & 1 \end{bmatrix}
\tag{24}
$$

The first two rows correspond to the cart position x and velocity $\dot{x}$ and the last two rows correspond to the pendulum angle θ and rotation rate $\dot{\theta}$. The ratio between the first and
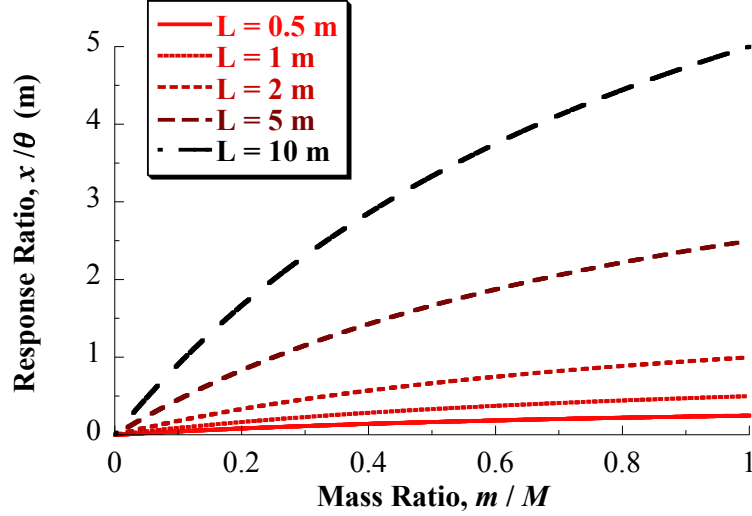
Figure 27: Eigenvector Response Ratio of the Cart with Pendulum Model vs. mass ratio m/M for different pendulum lengths L.

third (or second and fourth) rows gives the Eigenvector Response Ratio performance metric R_I for this model:

$$R_I = \frac{mL}{M + m} \tag{25}$$

Figure 27 shows the Cart with Pendulum Eigenvector Response Ratio for pendulum lengths L ranging from 0.5 m to 10 m. As the mass of the pendulum relative to the cart increases, the response ratio increases. Also, increasing the length leads to larger response ratios. The latter trend occurs because the response ratio is defined for states of cart position and pendulum angle, and increases in pendulum length for a given pendulum angle correspond to larger horizontal deflection of the pendulum relative to the cart. This is consistent with expectations based on conservation of momentum, where for larger pendulum masses and/or larger amounts of deflection, the cart will have a larger response.

3.2.2.2 Rotary Hub with Flexible Arm

The Eigenvector Response Ratio R_{II} for the Rotary Hub with Flexible Arm model is defined as the relative response ratio of the hub angle θ_1 to the arm angle θ_2 in steady state. The ratio can be calculated using the method in Section 3.2.1 after converting (6) to state-space form. With the hub modeled as a disk ($I_1 = \frac{1}{2}m_1{L_1}^2$) and the flexible arm modeled as a

slender rod ($I_2 = \frac{1}{3} m_2 L_2{}^2$),

$$R_{II} = \frac{-2m_2 L_2 \left(3L_1 + 4L_2\right)}{3m_1 L_1{}^2 + 2m_2 \left(3L_1{}^2 + 4L_2{}^2 + 6L_1 L_2\right)} \tag{26}$$

This ratio has a more complex dependence on the system parameters than the ratio for the Cart with Pendulum given by (25). The ratio depends on the hub and arm masses m_1 and m_2, the hub radius L_1, and the arm length L_2. Figure 28 shows the Rotary Hub Eigenvector Response Ratio as functions of mass ratio m_2/m_1 and length ratio L_2/L_1. The values are negative here due to the positive directions for the states θ_1 and θ_2 defined in the model. The magnitude of the response ratio increases as the mass ratio m_2/m_1 and length ratio L_2/L_1 increase. Smaller relative arm masses and lengths have a smaller impact on the hub response.

In the limit as the flexible arm gets larger (mass and length) relative to the hub:

$$\lim_{m_2/m_1 \to \infty} R_{II} = -\frac{4L_2{}^2 + 3L_1 L_2}{3L_1{}^2 + 4L_2{}^2 + 6L_1 L_2} \tag{27}$$

$$\lim_{L_2/L_1 \to \infty} R_{II} = -1 \tag{28}$$

As the arm mass gets larger relative to the hub mass, the ratio depends on the relative sizes. As the arm gets longer relative to the radius of the hub, the ratio approaches an asymptote with magnitude 1 independent of the relative masses. For a response ratio with magnitude 1, the responses of both the rigid and flexible elements have equal amplitude.

3.2.3 Eigenvector Response Ratio Discussion

The Response Ratio performance metric can also be applied and validated for more complex systems with multiple flexible modes. While closed-form expressions of the response ratio may be obtained for simple models with two degrees of freedom, more complex models will not easily produce closed-form expressions for the eigenvectors. This requires studying the eigenvectors and response ratios numerically. However, it is still possible to identify the response ratio as a function of the relevant system parameters.
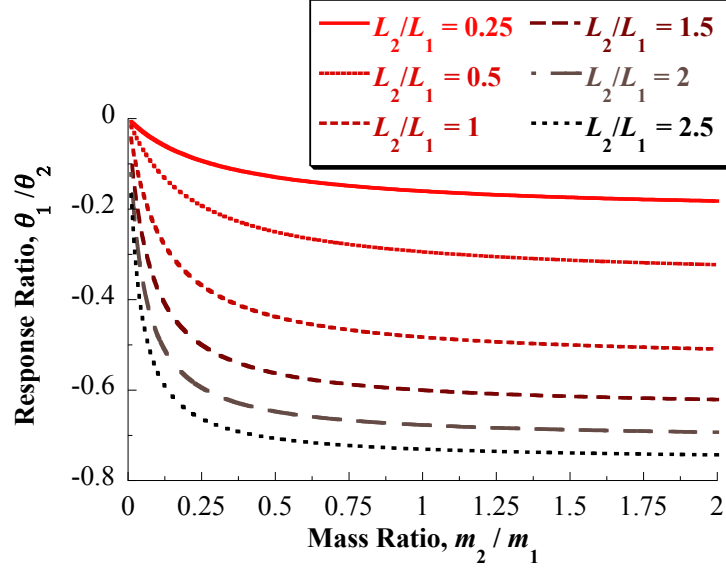
(a) Rotary Hub Response Ratio vs mass ratio for selected length ratios.
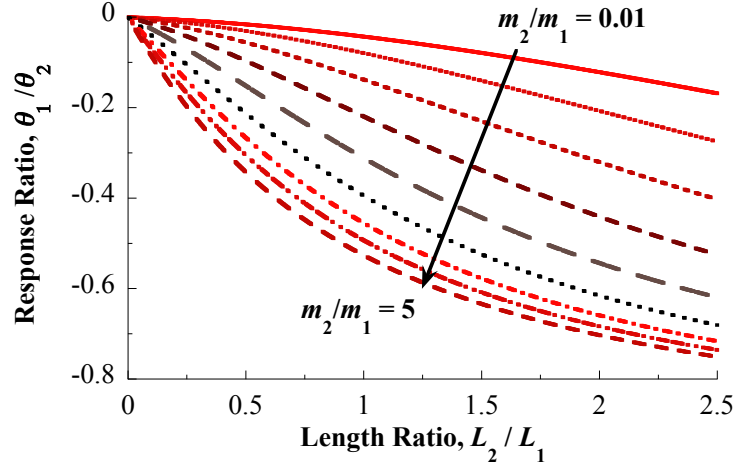
(b) Rotary Hub Response Ratio vs length ratio for selected mass ratios.

Figure 28: Eigenvector Response Ratio of the Rotary Hub with Flexible Arm model as a function of mass and length ratios.

3.3   *Performance Metric 2 - Complex Pole-Zero Ratio*

3.3.1   Complex Pole-Zero Ratio Performance Metric Definition

An additional useful performance metric is based on the relationship between the complex poles and zeros of the backdrivable system. For a given backdrivable system, the transfer function between the rigid state and an input (force or torque) applied to the rigid body can be defined as the backdrivable open-loop transfer function. A backdrivable open-loop transfer function has a pair of complex zeros in addition to the rigid and flexible mode poles

for the system. This section uses a relationship between the complex poles and zeros for a backdrivable transfer function to quantify the degree of backdrivabiltiy of the system.

For the Cart with Pendulum, the backdrivable transfer function is the $X(s)/U(s)$ transfer function given by (3a). Figure 6 showed an illustrative pole-zero plot of (3a) to show the relative locations of these complex poles and zeros. Studying the Eigenvector Response Ratio revealed that the payload-cart mass ratio is an important parameter for assessing the backdrivability of the Cart with Pendulum system. To examine the effect of the mass ratio on the poles and zeros, Figure 29 shows the imaginary part of the positive complex pole and zero of (3a) vs. the mass ratio m/M with $L = 5$ m. The complex zeros of (3a) occur at $\pm i\sqrt{g/L}$ and do not depend on the mass ratio. As the mass ratio increases, the imaginary part of the complex pole increases in value and moves further away from the complex zero along the imaginary axis of the pole-zero plot. This increasing trend for the pole is a similar pattern to that shown by the Eigenvector Response Ratio in Figure 27.

Based on this analysis and understanding of the behavior of the complex poles and zeros, a performance metric for backdrivability can be defined. First, the backdrivable transfer function for the system should be identified based on the definition for the rigid body mode and the presence of a pair of complex zeros. Then, the *Complex Pole-Zero Ratio* κ is defined
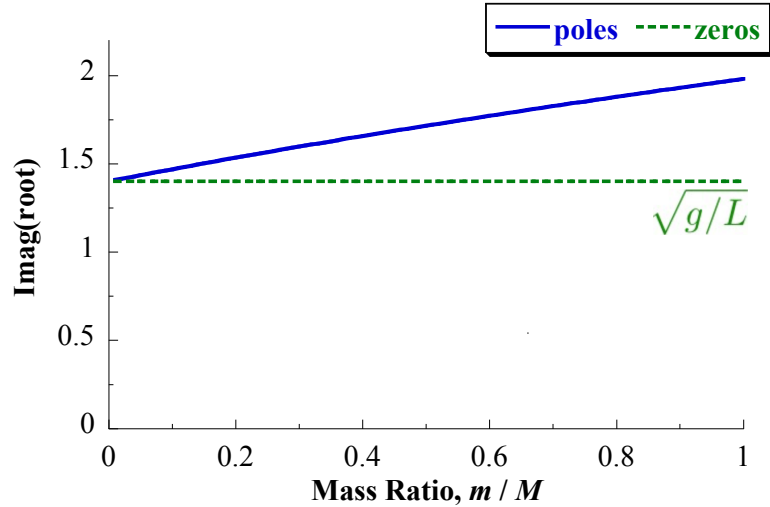
Figure 29: Positive complex poles and zeros of Cart with Pendulum $X(s)/U(s)$ transfer function vs. payload-cart mass ratio m/M ($L = 5$ m).

as:

$$\kappa = \frac{p_i - z_{11,i}}{p_i} \tag{29}$$

where p_i is the positive complex pole and $z_{11,i}$ is the positive complex zero of the backdrivable transfer function. The following subsections illustrate application of this metric to the fundamental models.

3.3.2 Complex Pole-Zero Ratios for Fundamental Backdrivable Systems

This section derives Complex Pole-Zero Ratios for the stable fundamental models presented in Chapter II and shows illustrative results of the ratio for a range of system parameters for each model.

3.3.2.1 Cart with Pendulum

For the Cart with Pendulum model, the backdrivable transfer function is $X(s)/U(s)$ given by (3a). The positive complex pole of (3a) is:

$$p_i = i\sqrt{\frac{g}{L}\left(\frac{M+m}{M}\right)} \tag{30}$$

and the positive complex zero is:

$$z_i = i\sqrt{\frac{g}{L}}. \tag{31}$$

Substituting (30) and (31) into (29) yields the Complex Pole-Zero Ratio κ_I for the Cart with Pendulum model:

$$\kappa_I = 1 - \sqrt{\frac{M}{M+m}} \tag{32}$$

This results in a performance metric that does not depend on the pendulum length because the definition for the Complex Pole-Zero Ratio uses the complex pole as a normalizing factor.

Figure 30 shows the Cart with Pendulum Complex Pole-Zero Ratio as a function of the mass ratio m/M. As the mass of the pendulum relative to the cart increases, the pole-zero ratio increases. As a performance metric, this suggests that the cart will have a larger relative response as the mass ratio increases. This is consistent with the results predicted by the Eigenvector Response Ratio and expectations based on conservation of momentum,
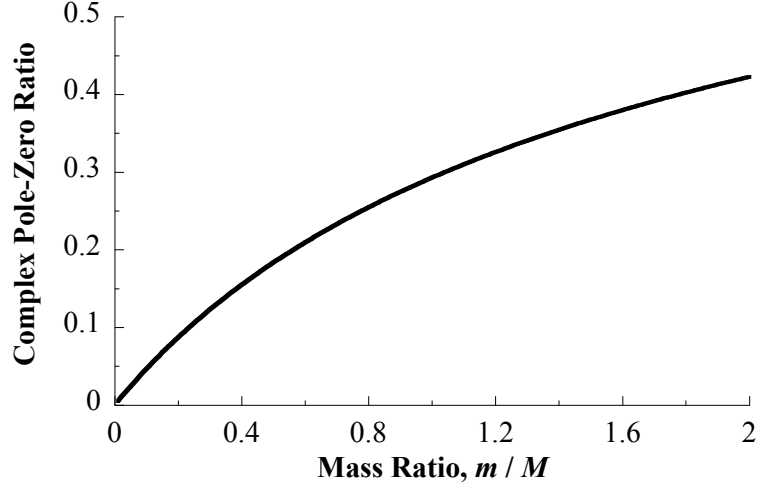
Figure 30: Complex Pole-Zero Ratio of the Cart with Pendulum Model vs. mass ratio m/M.

where for larger pendulum masses and/or larger amounts of deflection, the cart will have a larger response. Also note that the pole-zero ratio and Eigenvector Response Ratio shown in Figure 27 follow a similar overall trend in terms of their dependence on the mass ratio. However, the Complex Pole-Zero Ratio for the Cart with Pendulum model is independent of the pendulum length. Unlike the Eigenvector Response Ratio, it does not matter that the two system states are cart position and pendulum angle and have different units.

3.3.2.2 Rotary Hub with Flexible Arm

For the Rotary Hub with Flexible Arm model, the backdrivable transfer function is $\Theta_1(s)/T(s)$ given by (6a). With the hub modeled as a disk ($I_1 = \frac{1}{2}m_1L_1^2$) and the flexible arm modeled as a slender rod ($I_2 = \frac{1}{3}m_2L_2^2$), the positive complex pole of (6a) is:

$$p_i = i\sqrt{\frac{k\left(3m_1{L_1}^2 + 2m_2\left(3{L_1}^2 + 4{L_2}^2 + 6L_1L_2\right)\right)}{2m_2\left(2m_1 + m_2\right){L_1}^2{L_2}^2}} \tag{33}$$

and the positive complex zero is:

$$z_i = i\sqrt{\frac{3k}{4m_2{L_2}^2}}. \tag{34}$$

54

Substituting (33) and (34) into (29) yields the Complex Pole-Zero Ratio κ_{II} for the Rotary Hub with Flexible Arm model:

$$\kappa_{II} = 1 - \frac{\left(\sqrt{6}m_1 + \sqrt{\frac{3}{2}}m_2\right)L_1}{\sqrt{(2m_1 + m_2)\left(3m_1 L_1{}^2 + 2m_2\left(3L_1{}^2 + 4L_2{}^2 + 6L_1 L_2\right)\right)}} \tag{35}$$

This Complex Pole-Zero Ratio has a more complicated dependence on the system parameters than the ratio for the Cart with Pendulum given by (32). This resulting dependence on the hub and arm masses m_1 and m_2, the hub radius L_1, and the arm length L_2 is similar to the Eigenvector Response Ratio (26) for this model. The more complicated relationship arises due to the rotational dynamics of both the hub and arm and the presence of rigid bodies rather than the point masses in the Cart with Pendulum model.

In the limit, as the flexible arm gets larger (mass and length) relative to the hub:

$$\lim_{m_2/m_1 \to \infty} \kappa_{II} = 1 - \frac{\sqrt{3}L_1}{2\sqrt{3L_1{}^2 + 4L_2{}^2 + 6L_1 L_2}} \tag{36}$$

$$\lim_{L_2/L_1 \to \infty} \kappa_{II} = 1 \tag{37}$$

As the arm mass gets larger relative to the hub mass, the ratio depends on the lengths. As the arm gets longer relative to the radius of the hub, the ratio approaches an asymptote with magnitude 1 independent of the relative masses. This behavior is similar to the Eigenvector Response Ratio for the Rotary Hub with Flexible Arm model.

Figure 31 shows the Rotary Hub with Flexible Arm Complex Pole-Zero Ratio as a function of the mass ratio m_2/m_1 and length ratio L_2/L_1. Figure 31(a) shows that the pole-zero ratio increases as the mass of the arm relative to the hub increases, with higher ratios for longer arm lengths relative to the hub radius. Figure 31(b) shows that the pole-zero ratio also increases as the the length ratio increases. However, the increase can be more gradual for small mass ratios. As a performance metric, this suggests that the arm can have a larger impact on the hub as the arm mass increases, and longer arms can exacerbate this effect. This is consistent with the results predicted by the Eigenvector Response Ratio and expectations based on conservation of angular momentum, where for larger arm inertias, the hub will have a larger response. Also, note that the Complex Pole-Zero Ratio and Eigenvector Response Ratio shown in Figure 28 follow a similar overall trend in terms of

their dependence on the mass ratio. They differ in sign only due to the choice of positive direction for the system states, and what really matters is the magnitude of the ratios themselves.
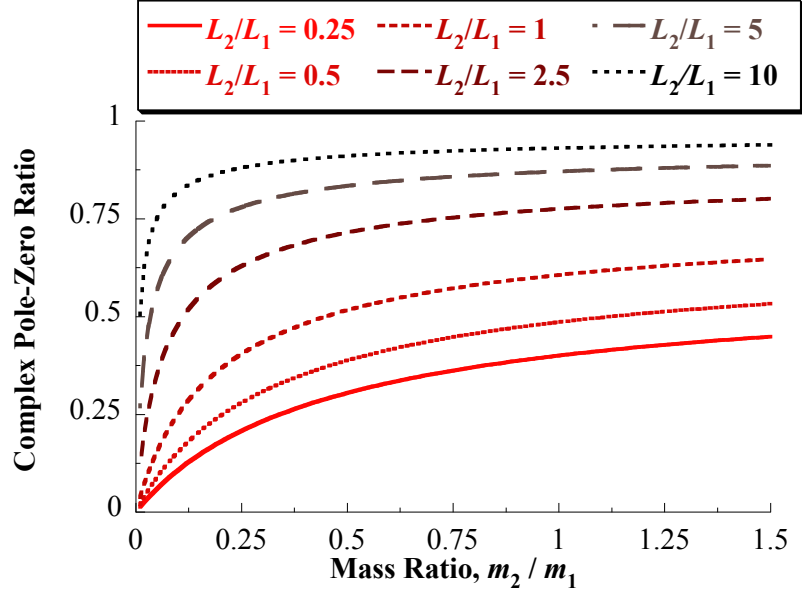
(a) Rotary Hub Complex Pole-Zero Ratio vs mass ratio for selected length ratios.
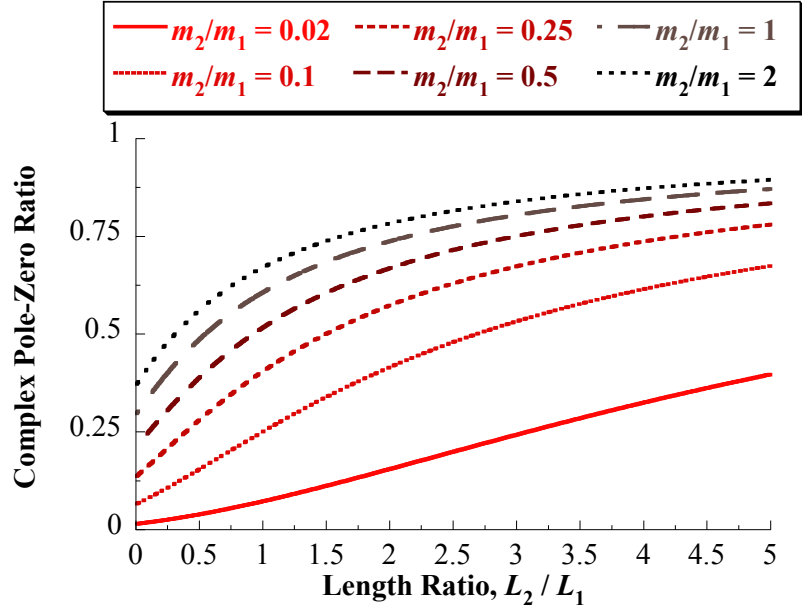
(b) Rotary Hub Complex Pole-Zero Ratio vs length ratio for selected mass ratios.

Figure 31: Complex Pole-Zero Ratio of the Rotary Hub with Flexible Arm model as a function of mass and length ratios.

3.3.3 Comparison of Eigenvector Response Ratio and Complex Pole-Zero Ratio Performance Metrics

One advantage of the Eigenvector Response Ratio as a performance metric is that it has an inherent, direct relationship with the physical behavior of the system in terms of predicting the amplitude ratio of the time response. The Complex Pole-Zero Ratio does not have this same direct connection to the time response behavior. Rather, it provides insight into the frequency response and, should a feedback controller be applied to the system, the closed-loop behavior. Another way to visualize the results for the Cart with Pendulum depicted in Figures 29 and 30 is with Bode magnitude plots for the $X(s)/U(s)$ transfer function for different mass ratios. Figure 32 shows Bode magnitude plots for four mass ratios, and illustrates how the resonant peaks arising from the complex poles shift further away from the complex zero at $\sqrt{g/L}$ as the mass ratio increases. A physical interpretation of this behavior is that the pendulum acts as a vibration absorber for the cart that becomes further out of tune as the mass ratio increases. Another explanation is that damping the oscillatory behavior of cart caused by the swinging pendulum would require more control effort as the mass ratio increases.

Due to its connection to the time response behavior, the magnitude of the Eigenvector
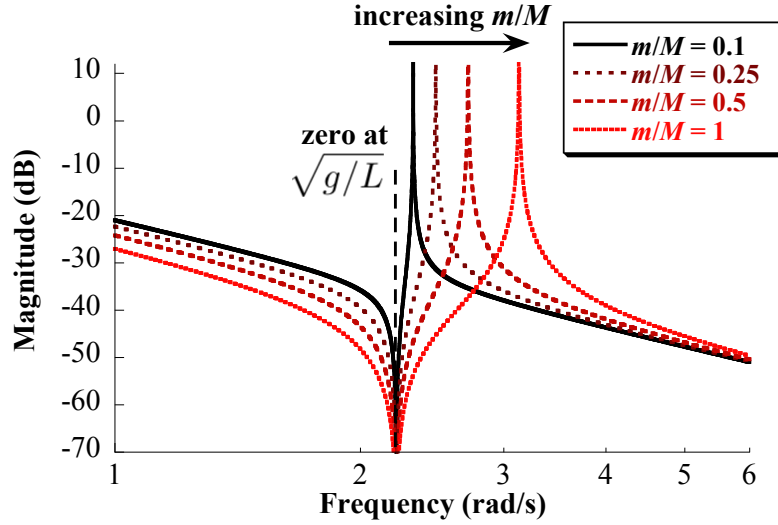
Figure 32: Bode magnitude plot of Cart with Pendulum $X(s)/U(s)$ transfer function for a variety of payload-cart mass ratios m/M ($L = 2$ m, $M = 10$ kg).

Response Ratio has physical meaning whereas the Complex Pole-Zero Ratio magnitude does not. This gives it the advantage of allowing designers to study the impact of the various configurations on the rigid body state amplitude.

3.4   Summary

This chapter presented two performance metrics for evaluating the degree of backdrivability as a function of key system parameters. The first metric is based on eigenvector analysis, and provides a means to assess the relative amplitude ratio between the responses of the system states. The second metric is defined based on the complex poles and zeros of the system. As their values become further apart, the oscillation of the flexible mode has a larger impact on the system response. Both metrics show that changing system parameters, such as increasing the mass or length of a flexible element, can result in a system that exhibits larger backdriving effects that may degrade performance.

CHAPTER IV

CONTROL OF BACKDRIVABLE SYSTEMS

This chapter investigates the control of backdrivable flexible systems. The goal is to improve response performance of the rigid element, while also reducing residual vibration of the flexible mode.

We are considering applications where the performance degradation of the rigid element is caused primarily due to coupling with the flexible mode. Therefore, we seek to develop control techniques that improve performance by reducing vibration of flexible modes. Input shaping is one such technique, and its application to backdrivable flexible systems is considered in this chapter and throughout the remainder of this thesis.

While input shaping can be used to suppress residual vibration caused by the flexible mode, it does not provide a direct means to improve transient performance, reject disturbances, or eliminate steady-state error. Therefore, input shaping should often be combined with a feedback controller to improve the performance of the rigid element of the backdrivable system.

One such feedback control architecture is illustrated in the block diagram shown in Figure 33. An input-shaped reference command is used as the feedback controller input. The controller generates a control effort to move the plant. It is assumed that only the rigid element states may be measured, and no sensor is available to measure the flexible body states. The response of the rigid body element may optionally be used as input to a state estimator to estimate the flexible states if full state feedback is required by the controller, although this configuration will not be considered in this thesis.

This chapter presents the design process for backdrivable flexible system feedback controller. Then, the controller is combined with an input shaper through use of optimization to solve for the input shaper parameters and controller gains.

This chapter also addresses control of unstable backdrivable systems, such as the Cart
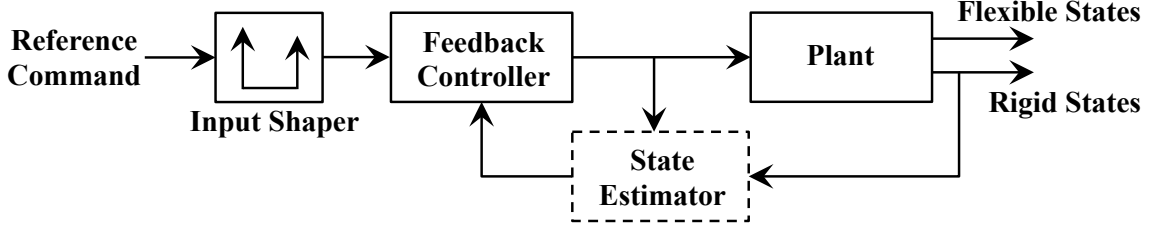
Figure 33: Block diagram of combined input-shaping and feedback control for backdrivable flexible systems.

with Inverted Pendulum model presented in Chapter II. This will illustrate how the addition of a stabilizing feedback controller can introduce backdriving dynamics to a system. The feedback controller presented for the Cart with Inverted Pendulum will be studied to gain insight into the backdriving dynamics of inverted-pendulum transporters, such as was shown in Figure 3.

4.1 Input Shaping

One technique that is effective at controlling vibration and oscillation is input shaping. Input shaping strategically modifies a command by convolving it with a series of impulses, called an *input shaper*. The resulting command induces little or no residual vibration [92, 109]. Designing input shapers only requires estimates of the natural frequency and damping ratio of the undesired vibratory mode. A major advantage of this approach is that it does not require real-time measurement or estimation of the load states.

Input shaping has proven effective on many kinds of machines, including cranes [112], robotic arms [9, 27, 67, 83], coordinate measuring machines [49, 106], and satellites [33, 93, 94, 104, 102, 120, 128]. The performance of many of these flexible systems can suffer due to backdrivability. Because input shaping eliminates residual vibration, it can also reduce the backdriving effect of the flexible mode on the rigid body or base. In addition, input shaping does not require measurements of the flexible system states. These properties make it well-suited for controlling backdrivable flexible systems. Input shaping is chosen as a primary control method to study in this research because of its proactive suppression of vibration or oscillation that can prevent the backdriving effect from occurring. Input shaping is also compatible with feedback controllers that only use partial state feedback of rigid body motion.

Input shapers can be designed to suppress multiple flexible modes [46, 95, 97, 103]. Also, many studies of crane operators have shown that input shaping can greatly improve performance [53, 54]. The primary disadvantages of input shaping are that it cannot reduce vibration caused by external disturbances, and it introduces a small response lag due to the method used to form the shaped commands.

Figure 34 illustrates the input-shaping concept. In the top of Figure 34, an impulse is applied to a flexible system, and induces a lightly-damped response. A similar response (shown by the dashed line) would result if a second impulse were applied a short time later. The bottom of Figure 34 shows the response that results from both impulses. The two responses combine linearly, and the oscillation is eliminated. Furthermore, the two specially-timed impulses can be convolved with any arbitrary function, and when used in this way, the resulting function will maintain the oscillation-canceling properties of the original impulses. The series of impulses is called an *input shaper*.

Input shapers may have more than two impulses. The transfer function of a generic input shaper with n impulses is:

$$\mathbf{G}_{is}(s) = A_1 e^{-t_1 s} + A_2 e^{-t_2 s} + \cdots + A_n e^{-t_n s}. \tag{38}$$
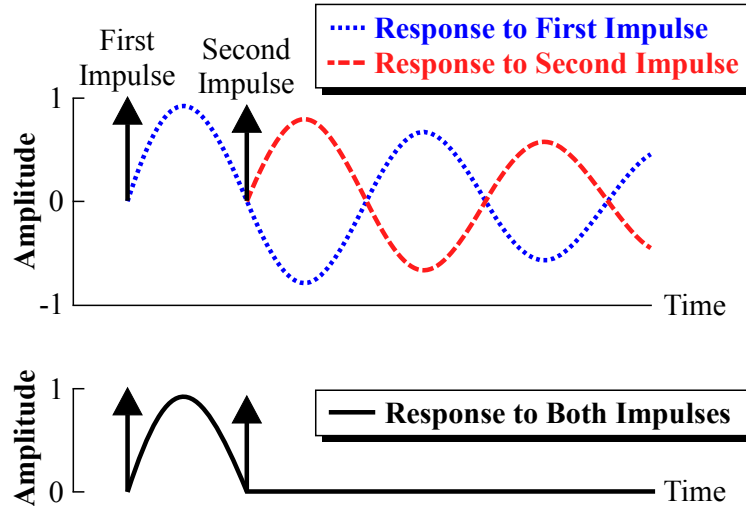
Figure 34: Demonstration of the input-shaping concept using two impulses, where the vibration caused by the first impulse is cancelled by strategic selection of the amplitude and time of the second impulse.

where A_i are the impulse amplitudes, and t_i are the time locations of each impulse. Without loss of generality, the first impulse time is chosen as $t_1 \equiv 0$. The impulse amplitudes and time locations are designed using the estimated natural frequencies and damping ratios of the undesired flexible modes. Input shapers can be made robust to errors and changes in these parameters [92, 125].

Input shapers can be designed using different combinations of performance requirements. By constraining the impulses to be all positive and the residual oscillation to be zero when parameter estimates are perfect, a *Zero Vibration* (ZV) input shaper [109] is obtained. Its transfer function is:

$$\mathbf{G}_{zv}(s) = A_1 + A_2 e^{-t_2 s}, \tag{39}$$

where A_1, A_2, and t_2 depend on the natural frequency and damping ratio of the flexible mode. The ZV shaper amplitudes and times are [109, 98]:

$$\begin{bmatrix} A_i \\ t_i \end{bmatrix} = \begin{bmatrix} \frac{1}{1+K} & \frac{K}{1+K} \\ 0 & \frac{T_d}{2} \end{bmatrix}, \tag{40}$$

where

$$K = e^{\left(\frac{-\zeta\pi}{\sqrt{1-\zeta^2}}\right)}. \tag{41}$$

For descriptions and comparisons of other kinds of input shapers such as *Extra-Insensitive* (EI) and *Specified-Insensitivity* (SI) input shapers, see [125].

To demonstrate the effect input shaping has on suppressing the flexible mode response and therefore eliminating the backdriving response, a ZV input shaper can be designed for the Cart with Pendulum fundamental model for the system parameters used previously in Figure 7 ($M = 30$ kg, $m = 15$ kg, and $L = 5$ m). A frequency of 1.72 rad/s is calculated for this parameter set using (4), and the system is undamped. With the natural frequency and damping ratio, the input shaper can be calculated using (40). Figure 35 compares the system response with and without the ZV shaper. Figure 35(a) shows that the ZV-shaped bang-bang command moves the cart 1 m, and the cart arrives with zero residual oscillation. This is due to the input shaper suppressing the oscillation of the pendulum, as shown in Figure 35(b). Because the pendulum residual oscillation is proactively eliminated by the
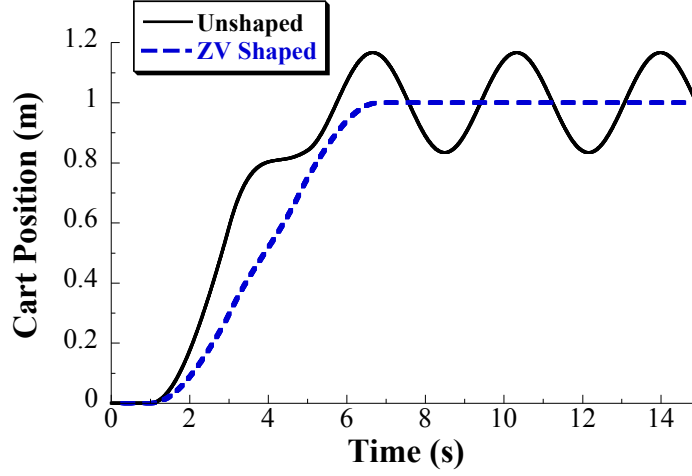
(a) Cart position.
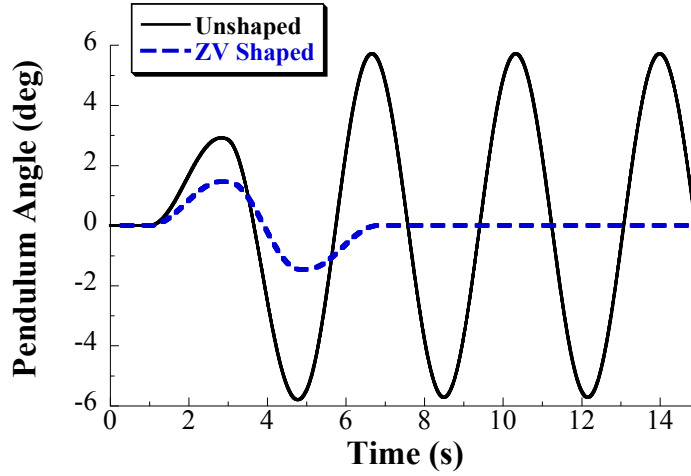
(b) Pendulum angle.

Figure 35: Comparison of the response of the Cart with Pendulum to unshaped and ZV-shaped bang-bang commands designed to move the cart 1 m.

shaped command, it is not able to backdrive the system.

4.2 Feedback Control

4.2.1 Control of Stable Backdrivable Systems

This section examines feedback control of stable backdrivable systems, and the Rotary Hub with Flexible Arm fundamental model given by (5) will be studied for demonstration purposes. A PD controller is selected for investigation given its ubiquitous nature, and because it is effective at meeting performance requirements on standard response characteristics such as rise time and maximum overshoot with this fundamental model. It is also provides

an effective form of attitude control for spacecraft, and this application will be investigated in Chapter VI.

An explicit form of the control system block diagram is shown in Figure 36. The closed-loop transfer functions between the commanded arm angle θ_d and the output angles θ_1 and θ_2 can be found using block diagram reduction. The Rotary Hub with Flexible Arm model in (5) was expressed in transfer function form in (6), where the four transfer functions $\mathbf{G}_{P11}$, $\mathbf{G}_{P12}$, $\mathbf{G}_{P21}$, and $\mathbf{G}_{P22}$ that relate the inputs T and θ_d to the outputs θ_1 and θ_2 are defined as:

$$\mathbf{G}_{P11}(s) = \frac{\Theta_1(s)}{T(s)}, \tag{42a}$$

$$\mathbf{G}_{P12}(s) = \frac{\Theta_1(s)}{\Theta_d(s)}, \tag{42b}$$

$$\mathbf{G}_{P21}(s) = \frac{\Theta_2(s)}{T(s)}, \tag{42c}$$

$$\mathbf{G}_{P22}(s) = \frac{\Theta_2(s)}{\Theta_d(s)}. \tag{42d}$$

Through block diagram reduction of Figure 36, the closed-loop transfer functions can be found:

$$\frac{\Theta_1(s)}{R_{\theta_1}(s)} = \frac{\mathbf{G}_C(s)\mathbf{G}_{P11}(s)}{1 + \mathbf{G}_C(s)\mathbf{G}_{P11}(s)}, \tag{43a}$$

$$\frac{\Theta_1(s)}{\Theta_d(s)} = \frac{\mathbf{G}_{P12}(s)}{1 + \mathbf{G}_C(s)\mathbf{G}_{P11}(s)}, \tag{43b}$$

$$\frac{\Theta_2(s)}{R_{\theta_1}(s)} = \frac{\mathbf{G}_C(s)\mathbf{G}_{P21}(s)}{1 + \mathbf{G}_C(s)\mathbf{G}_{P11}(s)}, \tag{43c}$$

$$\frac{\Theta_2(s)}{\Theta_d(s)} = \mathbf{G}_{P22}(s) - \frac{\mathbf{G}_C(s)\mathbf{G}_{P12}(s)\mathbf{G}_{P21}(s)}{1 + \mathbf{G}_C(s)\mathbf{G}_{P11}(s)}. \tag{43d}$$

The controller is a standard Proportional-Derivative (PD) controller such that $\mathbf{G}_C(s) = K_P + K_D s$. By substituting the open-loop transfer function expressions (6a), (6b), (6c), and (6d) into (43b) and (43d) with $R_{\theta_1} = 0$, the closed-loop transfer functions between the commanded arm angle θ_d and the outputs θ_1 and θ_2 are:

64
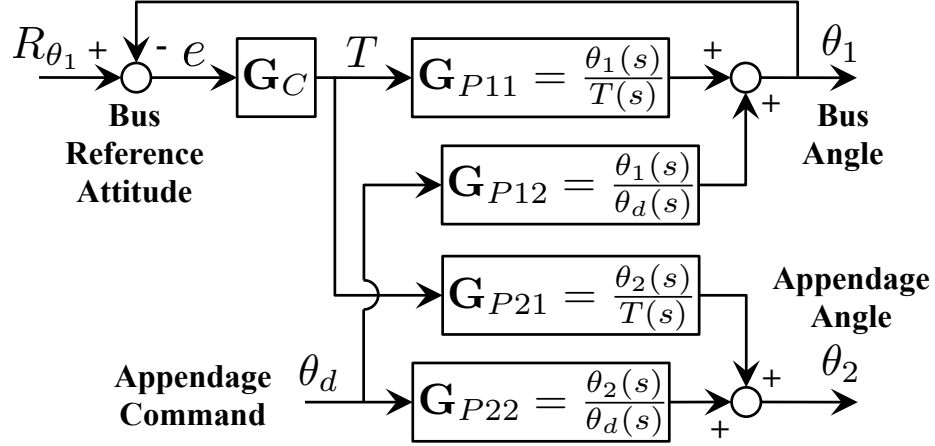
Figure 36: Block diagram of the hub angle PD controller applied to the Rotary Hub with Flexible Arm fundamental model.

$$\frac{\Theta_1(s)}{\Theta_d(s)} = \frac{m_2\left(L_1 + \frac{4}{3}L_2\right)s^2}{\frac{(2m_1+m_2)m_2 L_1^2 L_2}{3k}s^4 + \frac{4K_D m_2 L_2}{3k}s^3 + \left[\frac{4K_P m_2 L_2}{3k} + \frac{m_1 L_1^2}{2L_2} + m_2\left(\frac{L_1^2}{L_2} + 2L_1 + \frac{4}{3}L_2\right)\right]s^2 + \frac{K_D}{L_2}s + \frac{K_P}{L_2}}$$

(44)

$$\frac{\Theta_2(s)}{\Theta_d(s)} = \frac{\left(\frac{m_1 L_1^2}{2L_2} + \frac{m_2 L_1^2}{L_2} + 2m_2 L_1 + \frac{4m_2 L_2}{3}\right)s^2 + \frac{K_D}{L_2}s + \frac{K_P}{L_2}}{\frac{(2m_1+m_2)m_2 L_1^2 L_2}{3k}s^4 + \frac{4K_D m_2 L_2}{3k}s^3 + \left[\frac{4K_P m_2 L_2}{3k} + \frac{m_1 L_1^2}{2L_2} + m_2\left(\frac{L_1^2}{L_2} + 2L_1 + \frac{4}{3}L_2\right)\right]s^2 + \frac{K_D}{L_2}s + \frac{K_P}{L_2}}$$

(45)

The following parameter values will be used with this model for the rest of this section: $m_1 = 5{,}000$ kg, $L_1 = 1$ m, $m_2 = 100$ kg, $L_2 = 5$ m, and $k = 5{,}000$ N-m/rad. The denominator in (44) and (45) suggests that the closed-loop modes have a complicated dependence on the system parameters and controller gains. The behavior of the closed-loop modes must be understood before designing input shapers for the closed-loop system.

4.2.1.1 Controller Root Loci

Figure 37 shows the loci of the closed-loop poles of (44) and (45) as K_P varies and for selected K_D values. Note that these loci are merely the roots of the characteristic equation $1 + \mathbf{G}_C(s)\mathbf{G}_{P11}(s)$, and are not plotted assuming another feedback loop exists around the control system. With no derivative gain, the poles remain on the imaginary axis. As K_D increases, the pole on the real axis moves further to the left and the pair of complex conjugate poles is pulled to the left. For every K_D other than zero, there are always at least two complex conjugate poles, with the other poles either being real or complex conjugates

depending on the value of K_P. At low K_D, the complex conjugate poles at low K_P have their imaginary parts grow towards infinity along $\pm$90-degree asymptotes as K_P increases. The other set of poles remains on the real axis at low K_P, then breakaway towards the open-loop zeros of $\mathbf{G}_{P11}(s)$ becoming complex at larger K_P. Between $K_D = 5,000$ and $K_D = 10,000$, the loci change shape. After this transition occurs and for higher K_D, the complex conjugate poles at low K_P move towards the open-loop zeros as K_P increases, while the poles on the real axis breakaway and tend towards infinity along $\pm$90-degree asymptotes. The breakaway points occur at larger and larger real values as K_D increases.

To more closely examine the behavior and loci shape when the shape transition occurs between $K_D = 5,000$ and $K_D = 10,000$, Figure 38 shows the loci over a smaller range of K_D gains where the transition occurs. This shows how the shape changes as the breakaway point moves further to the left with increasing K_D.

The loci show that the poles have a complex dependance on the K_P and K_D gains. The closed-loop system either has two complex conjugate poles and two real poles, or two pairs of complex conjugate poles depending on the controller gains. For the purposes of designing a PD controller for this system and combining it with an input shaper, it is also useful to understand how the frequency and damping ratio of the closed-loop underdamped mode(s) changes with the gain values. The relationships between the gains and the frequency and damping ratio of the underdamped mode(s) are shown in the next section.

4.2.1.2   Modal Analysis of Closed-Loop Behavior

Choosing PD controller gains that will be utilized with an input shaper requires understanding of the closed-loop modes, in particular the frequency and damping ratio. This section shows the behavior of the closed-loop modes as a function of the proportional and derivative gains. The results inform selection of controller gains and give context for the illustrative results shown for the combined input-shaping and PD controller presented later. This analysis is primarily focused on the underdamped modes because they will be the primary driver of large overshoot and long settling times, and are suitable for targeted suppression using input shaping. In this analysis, Mode 1 is defined as the mode with the

66
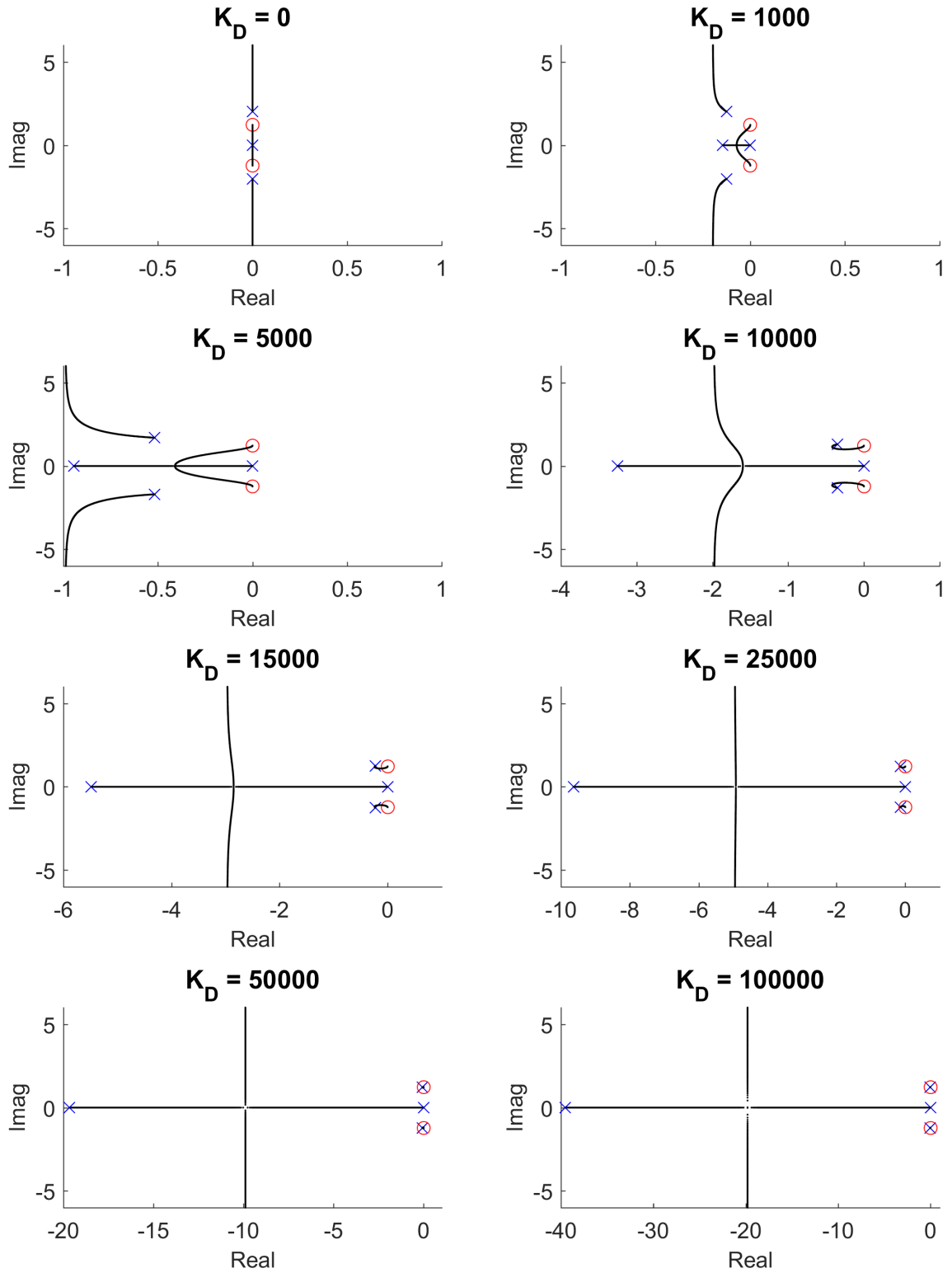
Figure 37: Root loci showing the pole locations as K_P varies for selected K_D gains.
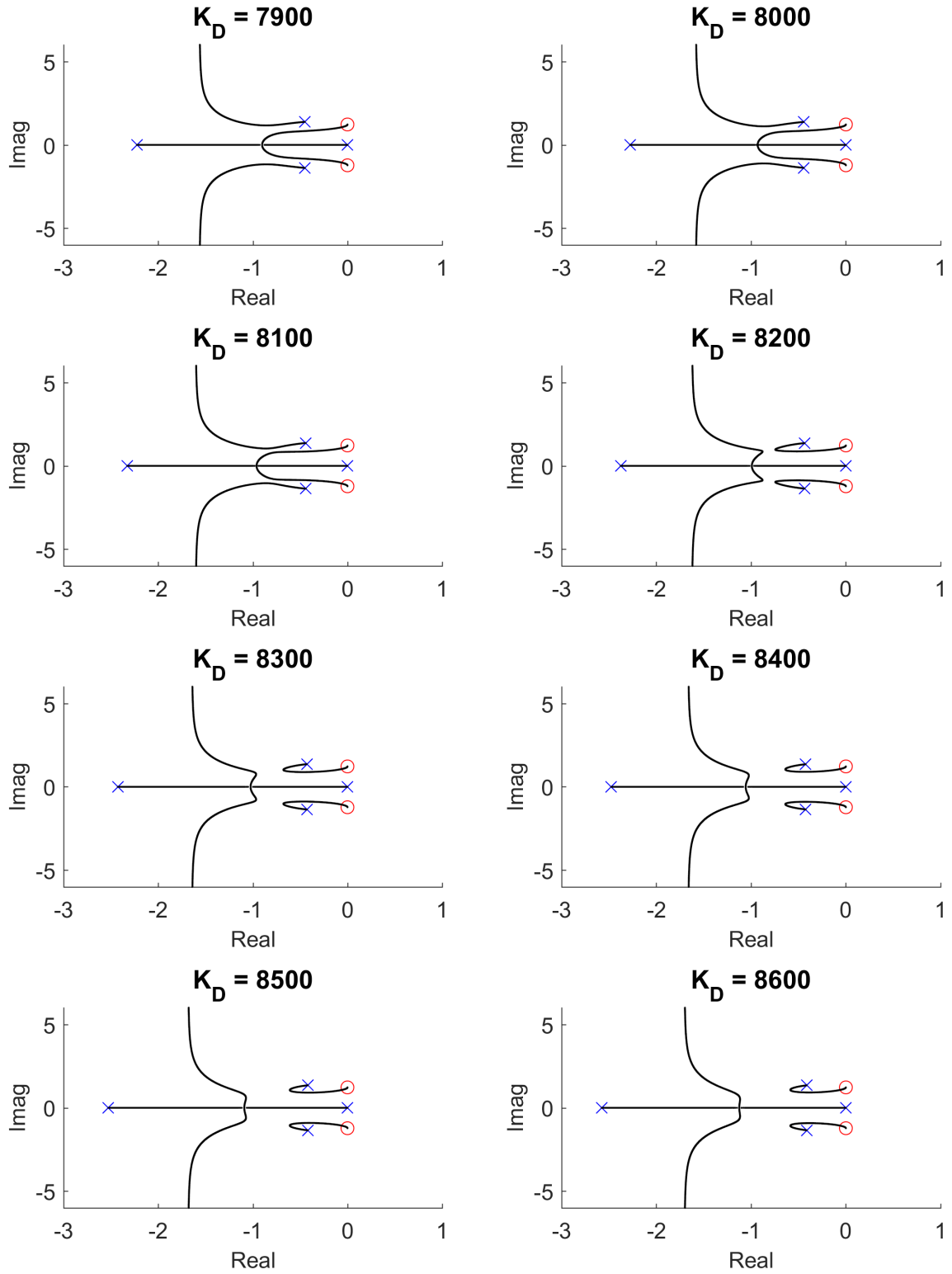
Figure 38: Root loci showing the closed-loop pole locations as K_P varies for selected K_D gains around where the transition in loci shape occurs.

68

lower natural frequency, and Mode 2 is only shown for controller gain values where it is underdamped. (This closed-loop system always has at least one underdamped mode.)

The first illustrative results are shown for a derivative gain of 8,100. Figure 39 show the modes vs K_P. For proportional gains less than approximately 3,000, there is only a single underdamped mode. The second mode has two real roots and is overdamped. For proportional gains greater than 3,000, all four poles are complex and both modes are underdamped. The natural frequencies in Figure 39(a) show that, when both modes are underdamped, the low mode remains near 1 rad/s while the frequency of the high mode increases. The damping ratios are shown in Figure 39(b), and illustrate that the overdamped mode for low proportional gain values becomes the mode with lower natural frequency as the proportional gain increases. Also, the damping ratios of both modes decrease as the proportional gain increases.

The next illustrative results are shown for a slightly higher derivative gain of 8,800. Figure 40 show the modes vs K_P for this case. Similar results to the previous case occur here, and for proportional gains less than approximately 3,700, there is only a single underdamped mode. Again, the damping ratios of both modes decrease as the proportional gain increases. However, in this case, the low frequency mode continues to have a lower damping ratio except during a brief transition range around $K_P \approx 3,700$.

To further examine this transition range, Figure 41 shows the modes vs. K_D for $K_P = 3,700$. As the derivative gain is increased, there is a transition from two underdamped modes to a single underdamped mode with an overdamped mode. For this proportional gain and derivative gains less than 8,800, there are two underdamped modes. This is consistent with the results in Figure 39, where there are two underdamped modes for $K_P > 3,000$ with $K_D = 8,100$. For derivative gains greater than 8,800 and proportional gains less than 3,700, there is a single underdamped mode with an overdamped mode. The mode with the higher frequency has the lower damping ratio. For low derivative gains, the damping ratios of both modes increase as the gain is increased. After derivative gains around 8,000, the damping ratio for one mode decreases as the derivative gain increases. The mode with the lower frequency has a damping ratio that strictly increases until it becomes the overdamped
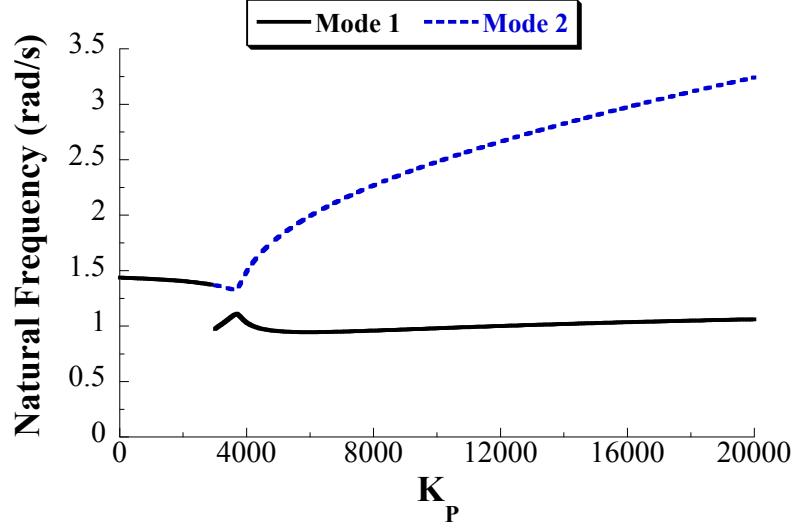
(a) Natural Frequency.
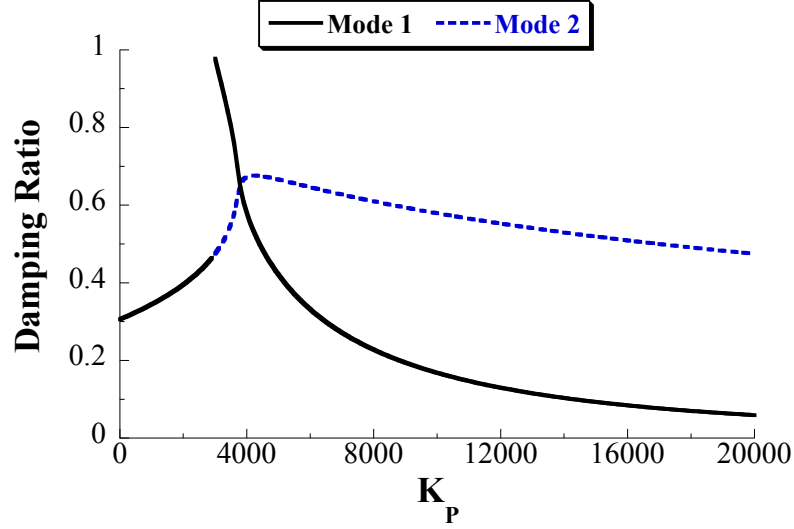
(b) Damping Ratio.

Figure 39: Natural frequency and damping ratio of the underdamped closed-loop modes vs. K_P for $K_D = 8{,}100$.

mode.

Similar patterns exist for proportional gain values greater than the transition range from Figure 40. Figure 42 shows the modes vs. K_D for $K_P = 3{,}800$. As the derivative gain increases, the modes transition from two underdamped modes to a single underdamped mode with an overdamped mode. However, in this case, the mode with higher frequency becomes the overdamped mode. As with the results shown in Figure 41, the single underdamped mode for larger derivative gains has a damping ratio that decreases as the derivative gain
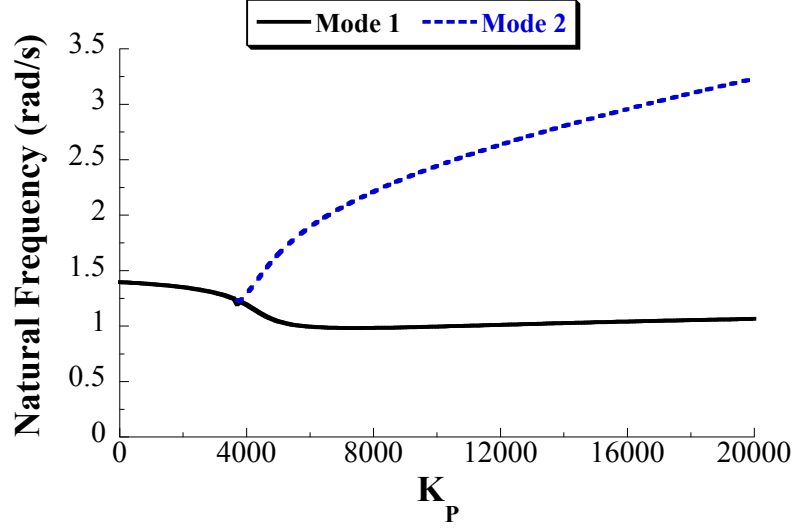
(a) Natural Frequency.
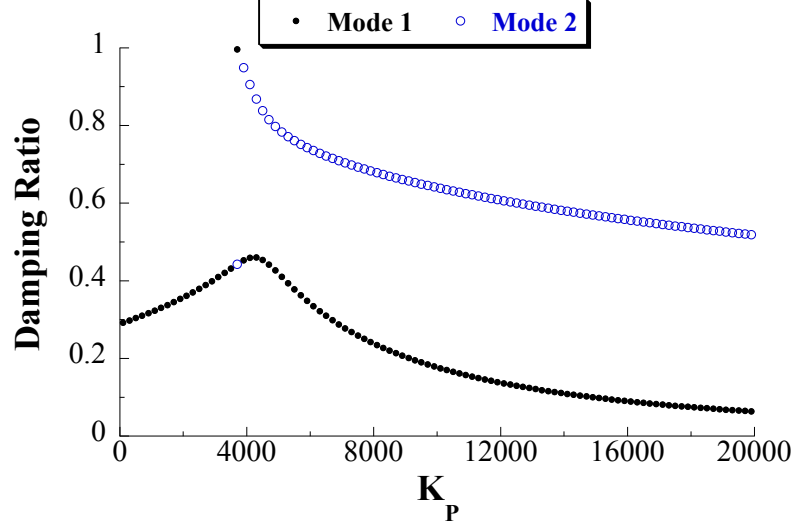
(b) Damping Ratio.

Figure 40: Natural frequency and damping ratio of the underdamped closed-loop modes vs. K_P for $K_D = 8,800$.

increases.

It is also worth examining the modal behavior at higher derivative gain values as a function of a larger range of proportional gain values. The next illustrative results are shown for a higher derivative gain of 10,000. Figure 43 show the modes vs K_P. The transition from one to two underdamped modes occurs at a higher proportional gains than for the cases shown in Figures 39 and 40. There is only a single underdamped mode for proportional gains less than approximately 5,400. At lower proportional gains when there is
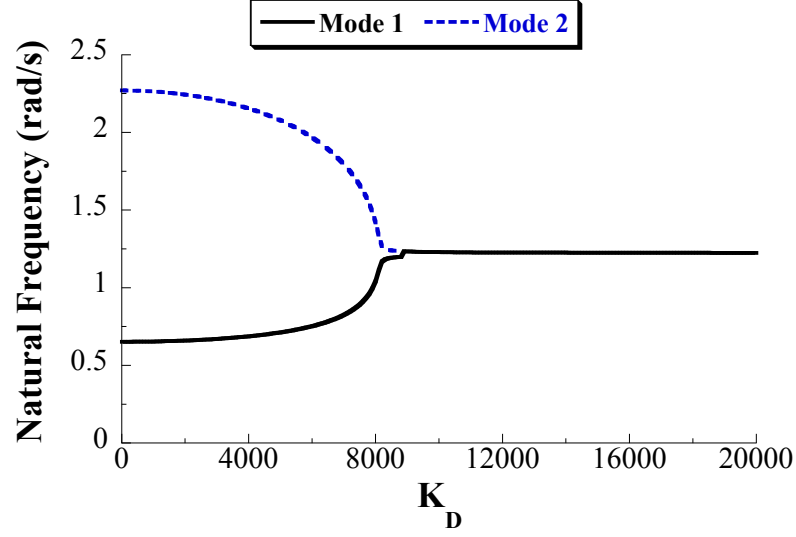
(a) Natural Frequency.
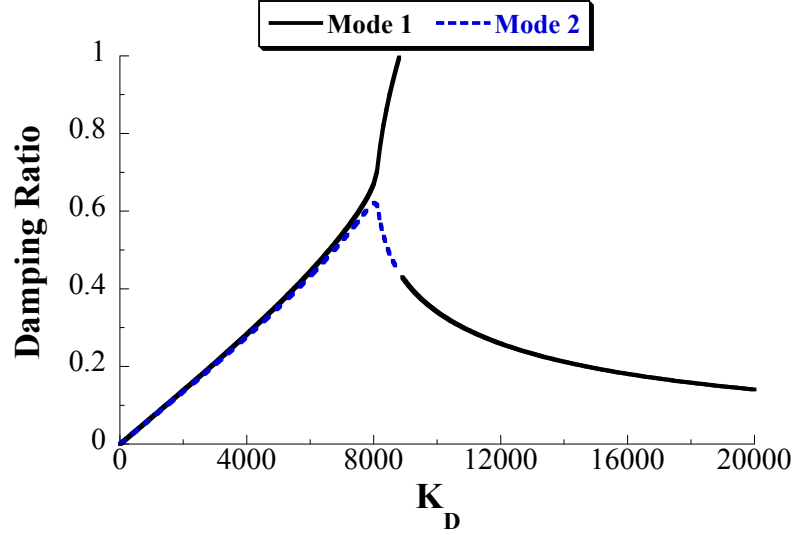
(b) Damping Ratio.

Figure 41: Natural frequency and damping ratio of the underdamped closed-loop modes vs. K_D for $K_P = 3{,}700$.

a single underdamped mode, Figure 43(b) shows that the damping ratio initially increases the proportional gain increases. After the transition from one to two underdamped modes, the damping ratios of both modes decrease as the proportional gain increases.

As the derivative gain increases, the transition to two underdamped modes occurs at larger proportional gains. Figure 43 show the modes vs K_P for $K_D = 15{,}000$. The transition from one to two underdamped modes does not occur until $K_P \approx 16{,}600$. Again, the damping ratios of both modes decrease as the proportional gain increases after the transition from
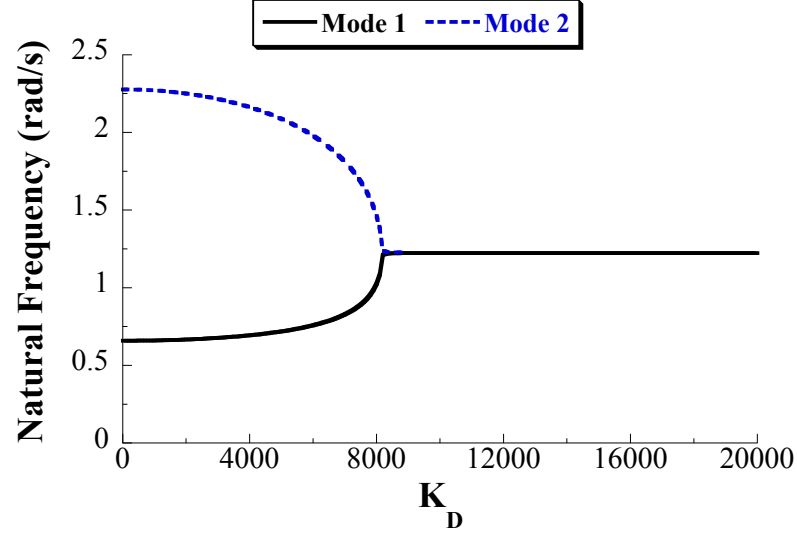
(a) Natural Frequency.
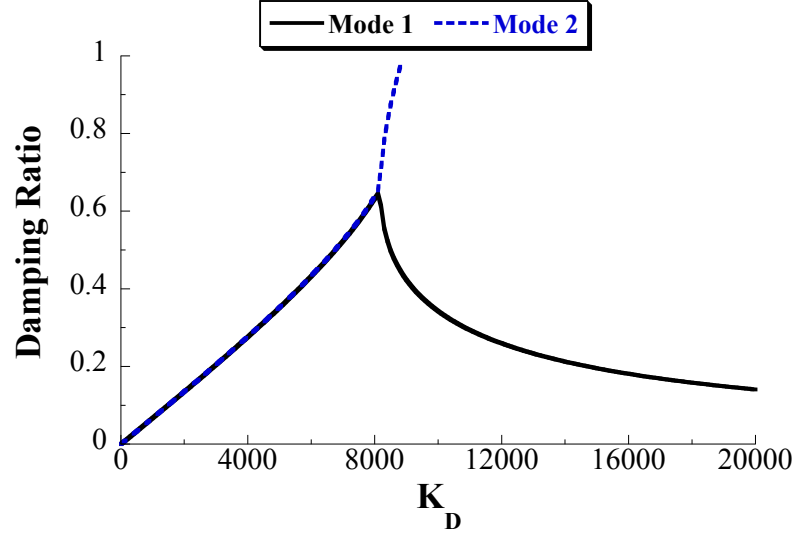
(b) Damping Ratio.

Figure 42: Natural frequency and damping ratio of the underdamped closed-loop modes vs. K_D for $K_P = 3{,}800$.

one to two underdamped modes. Moreover, the damping ratio of Mode 1 remains below 0.2 for all proportional gains.

This modal analysis and the results shown in Figures 39-44 have a number of significant implications. For certain ranges of proportional and derivative gains, there are two pairs of complex poles or one pair of complex poles and two real poles. As the proportional or derivative gains change, transitions occur between these two cases. Two underdamped modes exist for larger proportional gains and lower derivative gains. As the derivative
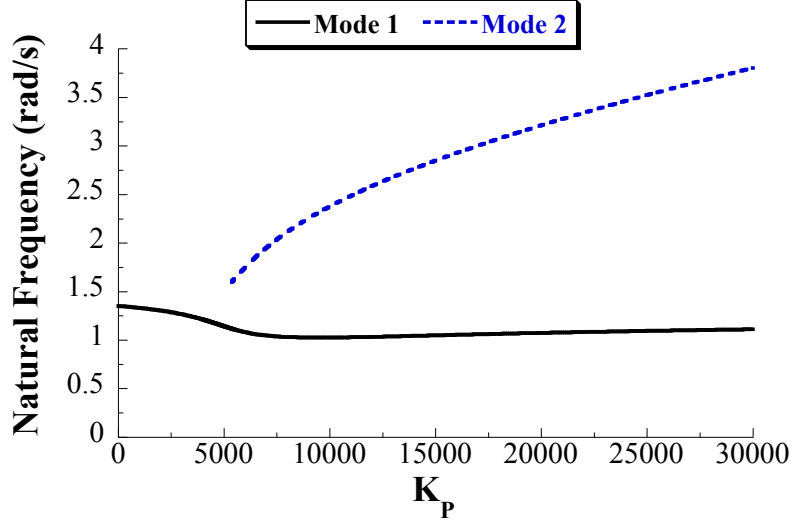
(a) Natural Frequency.
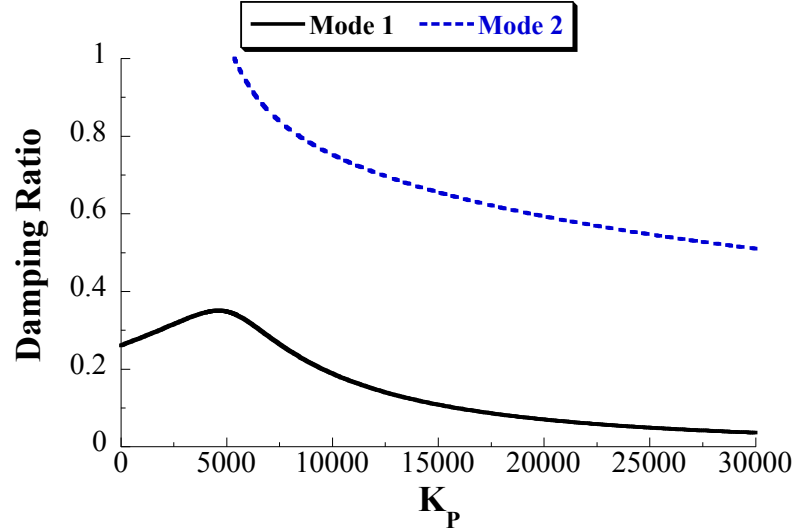
(b) Damping Ratio.

Figure 43: Natural frequency and damping ratio of the underdamped closed-loop modes vs. K_P for $K_D = 10,000$.

gain increases to larger values, two underdamped modes only occur for higher and higher proportional gains. At the lower ranges of proportional and derivative gains, the damping ratio of Mode 1 increases as the gains increase until a maximum occurs for specific gain values. However, at higher gains, the damping ratio of the single underdamped mode decreases as the gains increase. That the damping ratio decreases for increased derivative gains is surprising and perhaps nonintuitive when compared to traditional PD control design philosophies. There is a trade-off between having a high-enough damping ratio for one mode
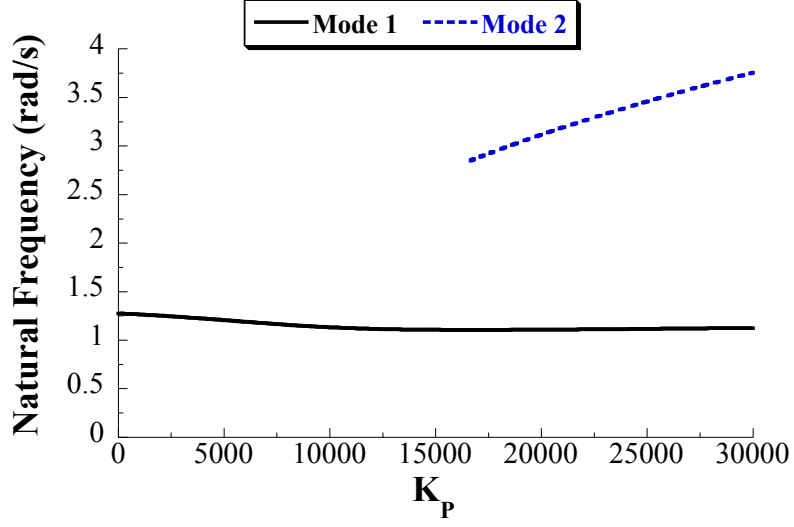
(a) Natural Frequency.
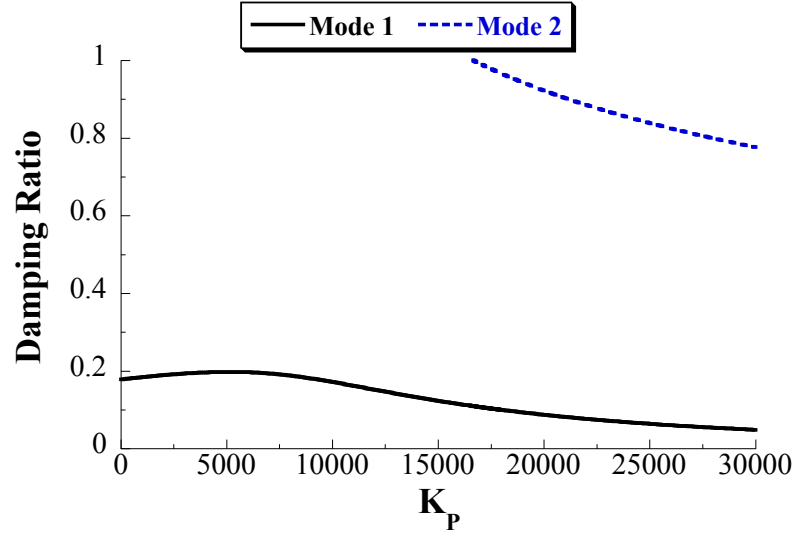
(b) Damping Ratio.

Figure 44: Natural frequency and damping ratio of the underdamped closed-loop modes vs. K_P for $K_D = 15{,}000$.

to be overdamped, while not being so high as to lead to further decrease in the damping ratio(s) of the underdamped mode(s).

4.2.1.3 Sample Step Response

To illustrate the behavior of the closed-loop system for a sample set of PD gains, Figure 45 shows the response of (44) and (45) to a 1 deg step of the commanded arm angle θ_d with $K_P = 2{,}000$ and $K_D = 10{,}000$. With these gains, the closed-loop system has one pair of
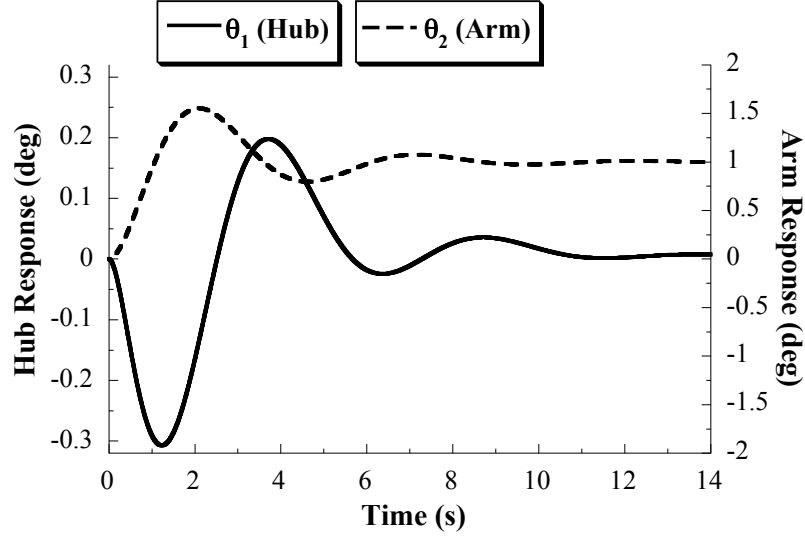
Figure 45: Sample step response of the closed-loop PD controller for the Rotary Hub with Flexible Arm model with $K_P = 2{,}000$ and $K_D = 10{,}000$.

underdamped poles. The underdamped mode has a natural frequency of 1.3 rad/s and damping ratio of 0.3. The arm angle has a 2% settling time of 10.3 seconds. The hub angle θ_1 has a peak amplitude of -0.31 deg and takes over 12 seconds to settle.

Further sample time responses of this closed-loop system model are shown in Section 4.3 in the context of the combined input-shaping and feedback control design. Also, Chapter VI utilizes more examples of the application of this controller for attitude control of a spacecraft.

4.2.2 Control of Unstable Backdrivable Systems

This section will study feedback control of unstable backdrivable systems, using the Cart with Inverted Pendulum fundamental model given by (8) for demonstration purposes. For unstable systems such as the Cart with Inverted Pendulum, the feedback controller can introduce the backdriving flexibility through the changed closed-loop dynamics. The goal of this section is to analyze the possible system parameter and controller gain combinations that can lead to backdriving flexibilty in the closed-loop dynamics.

While there are numerous control methods in the literature that stabilize and improve the performance of inverted pendulum systems, one of the simplest for a Cart with Inverted Pendulum system is a PD controller applied to the pendulum angle. A block diagram with state-feedback of the pendulum angle and angular velocity is shown in Figure 46. The input
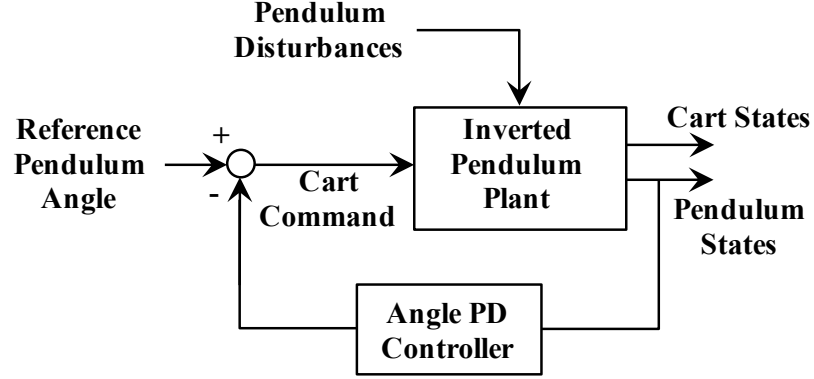
Figure 46: Block diagram of the pendulum angle state feedback PD controller applied to the Cart with Inverted Pendulum fundamental model.

is a reference pendulum angle, which can be used to model rider lean for inverted-pendulum transporters. The pendulum angle is fed back through a PD state-feedback controller, where the gains can be selected to stabilize the unstable inverted pendulum plant dynamics. The system is actuated through a force applied to the cart specified by the controller.

This structure is similar to a controller presented in a paper published by designers of the Segway [62]. The most significant difference is that the fundamental model focuses on the planar pitch dynamics and so the controller does not include components for the transporter turning/yaw dynamics. A PD pendulum angle controller results in marginally stable cart behavior, but this is acceptable for modeling inverted-pendulum transporters because the expectation is that the rider controls the overall vehicle position through their leaning commands.

An explicit form of the control system block diagram is shown in Figure 47. The closed-loop transfer functions between the reference pendulum angle θ_d and the output angles θ_1 and θ_2 can be found using block diagram reduction. The Cart with Inverted Pendulum model in (8) was expressed in transfer function form in (9), where the four transfer functions $\mathbf{G}_{P11}$, $\mathbf{G}_{P12}$, $\mathbf{G}_{P21}$, and $\mathbf{G}_{P22}$ that relate the input u and disturbance f to the outputs x
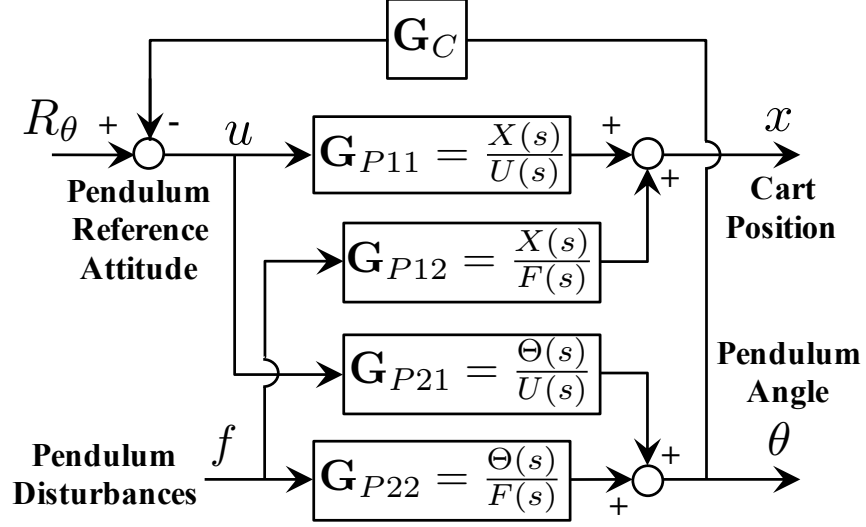
Figure 47: Explicit block diagram of the pendulum angle state feedback PD controller applied to the Cart with Inverted Pendulum fundamental model.

and θ are defined as:

$$\mathbf{G}_{P11}(s) = \frac{X(s)}{U(s)}, \tag{46a}$$

$$\mathbf{G}_{P12}(s) = \frac{X(s)}{F(s)}, \tag{46b}$$

$$\mathbf{G}_{P21}(s) = \frac{\Theta(s)}{U(s)}, \tag{46c}$$

$$\mathbf{G}_{P22}(s) = \frac{\Theta(s)}{F(s)}. \tag{46d}$$

Through block diagram reduction of the diagram in Figure 47, the closed-loop transfer functions can be found:

$$\frac{X(s)}{R_\theta(s)} = \frac{\mathbf{G}_{P11}(s)}{1 + \mathbf{G}_C(s)\mathbf{G}_{P21}(s)}, \tag{47a}$$

$$\frac{X(s)}{F(s)} = \mathbf{G}_{P12}(s) - \frac{\mathbf{G}_C(s)\mathbf{G}_{P11}(s)\mathbf{G}_{P22}(s)}{1 + \mathbf{G}_C(s)\mathbf{G}_{P21}(s)}, \tag{47b}$$

$$\frac{\Theta(s)}{R_\theta(s)} = \frac{\mathbf{G}_{P21}(s)}{1 + \mathbf{G}_C(s)\mathbf{G}_{P21}(s)}, \tag{47c}$$

$$\frac{\Theta(s)}{F(s)} = \frac{\mathbf{G}_{P22}(s)}{1 + \mathbf{G}_C(s)\mathbf{G}_{P21}(s)}. \tag{47d}$$

The controller is a standard PD controller with $\mathbf{G}_C(s) = K_P + K_D s$. As a reminder, the pendulum was modeled as a slender rigid rod such that $I_G = \frac{1}{3}mL^2$. By substituting the open-loop transfer function expressions (9a) and (9c) into (47a) and (47c), the closed-loop

transfer functions between the reference angle R_θ and the outputs x and θ are:

$$\frac{X(s)}{R_\theta(s)} = \frac{4Ls^2 - 3g}{s^2 \left[(4M+m)Ls^2 - 3K_Ds - 3\left((M+m)g + K_P\right)\right]} \tag{48}$$

$$\frac{\Theta(s)}{R_\theta(s)} = \frac{3}{(4M+m)Ls^2 - 3K_Ds - 3\left((M+m)g + K_P\right)} \tag{49}$$

Note that double pole-zero cancellation has occurred at zero in (49).

An equivalent and useful formulation for the closed-loop system can be obtained in state-space form, where the Cart with Inverted Pendulum model is given by:

$$\dot{\vec{x}} = \mathbf{A}\vec{x} + \mathbf{B}\vec{u}, \tag{50}$$

where

$$\vec{x} = \begin{bmatrix} x & \dot{x} & \theta & \dot{\theta} \end{bmatrix}^T, \tag{51}$$

$$\vec{u} = \begin{bmatrix} u & f \end{bmatrix}^T, \tag{52}$$

$$\mathbf{A} = \begin{bmatrix} 0 & 1 & 0 & 0 \\ 0 & 0 & -\frac{3mg}{4M+m} & 0 \\ 0 & 0 & 0 & 1 \\ 0 & 0 & \frac{3g(M+m)}{(4M+m)L} & 0 \end{bmatrix}, \tag{53}$$

and

$$\mathbf{B} = \begin{bmatrix} \mathbf{B}_1 & \mathbf{B}_2 \end{bmatrix} = \begin{bmatrix} 0 & 0 \\ \frac{4}{4M+m} & -\frac{2}{4M+m} \\ 0 & 0 \\ -\frac{3}{(4M+m)L} & \frac{6M+3m}{(4M+m)mL} \end{bmatrix}. \tag{54}$$

where $\mathbf{B}_1$ is the first column and $\mathbf{B}_2$ is the second column of the input matrix $\mathbf{B}$.

Considering only the cart input u, the system is completely state controllable. The controllability matrix $\mathbf{R}$ for the open-loop system can be formed as:

$$\mathbf{R} = \begin{bmatrix} \mathbf{B}_1 & \mathbf{A}\mathbf{B}_1 & \mathbf{A}^2\mathbf{B}_1 & \mathbf{A}^3\mathbf{B}_1 \end{bmatrix}. \tag{55}$$

79

Substituting the matrices $\mathbf{A}$ and $\mathbf{B}_1$, (55) can be evaluated as:

$$\mathbf{R} = \begin{bmatrix} 0 & \frac{4}{4M+m} & 0 & \frac{9mg}{(4M+m)^2 L} \\ \frac{4}{4M+m} & 0 & \frac{9mg}{(4M+m)^2 L} & 0 \\ 0 & -\frac{3}{(4M+m)L} & 0 & -\frac{9(M+m)g}{(4M+m)^2 L^2} \\ -\frac{3}{(4M+m)L} & 0 & -\frac{9(M+m)g}{(4M+m)^2 L^2} & 0 \end{bmatrix}, \tag{56}$$

This matrix has full rank ($= 4$) for all $M > 0$, $m > 0$, $L > 0$, and $g > 0$. To show this, the determinant of (57) is:

$$\det \mathbf{R} = \frac{81g^2}{(4M+m)^4 L^4} \tag{57}$$

which is > 0 for all M, m, L, and g. With $\det \mathbf{R} \neq 0$, $\mathbf{R}$ is full rank and the system is completely controllable.

A gain matrix $\mathbf{K}$ for the PD state feedback controller can be defined as:

$$\mathbf{K} = \begin{bmatrix} 0 & 0 & K_P & K_D \end{bmatrix}. \tag{58}$$

Then, the closed-loop state dynamics are described by:

$$\dot{\vec{x}} = \left(\mathbf{A} - \mathbf{B}_1 \mathbf{K} \right) \vec{x} + \mathbf{B}_1 R_\theta + \mathbf{B}_2 f. \tag{59}$$

The term involving the second column of the input matrix, $\mathbf{B}_2 f$, can be ignored when disturbances are not being considered or studied.

Through finding the eigenvalues of $\left(\mathbf{A} - \mathbf{B}_1 \mathbf{K} \right)$, the closed-loop poles of this control system are:

$$\lambda_{1,2} = 0, \ \lambda_{3,4} = \frac{3K_D \pm \sqrt{9K_D{}^2 + 48M^2 gL + 60MmgL + 48MLK_P + 12m^2 gL + 12mLK_P}}{2\left(4M + m\right)L}. \tag{60}$$

Due to the definition of the positive direction of the system states, both K_P and K_D must be negative for the cart position closed-loop transfer function (48) to be marginally stable and the pendulum angle closed-loop transfer function (49) to be stable. This can be seen through inspection of (60) with $M > 0$, $m > 0$, $L > 0$, and $g > 0$, where the requirement for stability is:

$$3K_D + \sqrt{9K_D{}^2 + 48M^2 gL + 60MmgL + 48MLK_P + 12m^2 gL + 12mLK_P} < 0. \tag{61}$$

Any right-half-plane poles are purely real if they exist, and (61) can be simplified to show that the closed-loop system is stable when:

$$K_D < 0 \text{ and } K_P < -\left(M + m\right)g. \tag{62}$$

Note that these requirements for stability do not depend on the pendulum center of mass height L. There are a pair of complex conjugate poles when:

$$3K_D{}^2 + 16M^2gL + 20MmgL + 16MLK_P + 4m^2gL + 4mLK_P < 0. \tag{63}$$

With the requirements on K_D and K_P from (62), (63) can be rearranged as:

$$K_P < -\frac{3K_D{}^2 + 16M^2gL + 20MmgL + 4m^2gL}{4\left(4M + m\right)L}. \tag{64}$$

The system is critically damped when K_P is exactly equal to the right-hand side of (64).

Using the result from (64), Figure 48 shows the type of closed-loop poles that occur for various PD controller gain pairs as a function of the mass ratio. For this and the following plots, a value of $M = 48$ kg is used for the cart mass because that is the approximate weight of a Segway i2 transporter, and riders with different masses are considered using an illustrative value of $L = 0.9$ m. Figure 48(a) shows a 3D surface plot of the right-hand side of (64) as a function of mass ratio and the controller gains. K_P and K_D gain pairs that fall on this surface result in a critically damped system. Gain pairs above the surface result in underdamped closed-loop poles, and gain pairs below the surface result in overdamped poles. In general, the nonzero poles are underdamped for larger K_P and smaller K_D, while overdamped poles occur with smaller K_P and larger K_D. The surface can be thought of as the transition between underdamped and overdamped controller gain pairs.

Figure 48(b) shows the controller gain pairs that result in critically damped dynamics for selected mass ratios. Again, controller gain pairs above the curves result in underdamped poles while gain pairs below the curves result in overdamped poles. The interesting behavior visible from this 2D view of Figure 48(a) are the intersection and crossover of the critically damped transition curves for the various selected mass ratios. Higher mass ratios are more likely to result in underdamped poles for large K_P and overdamped poles for small K_P.
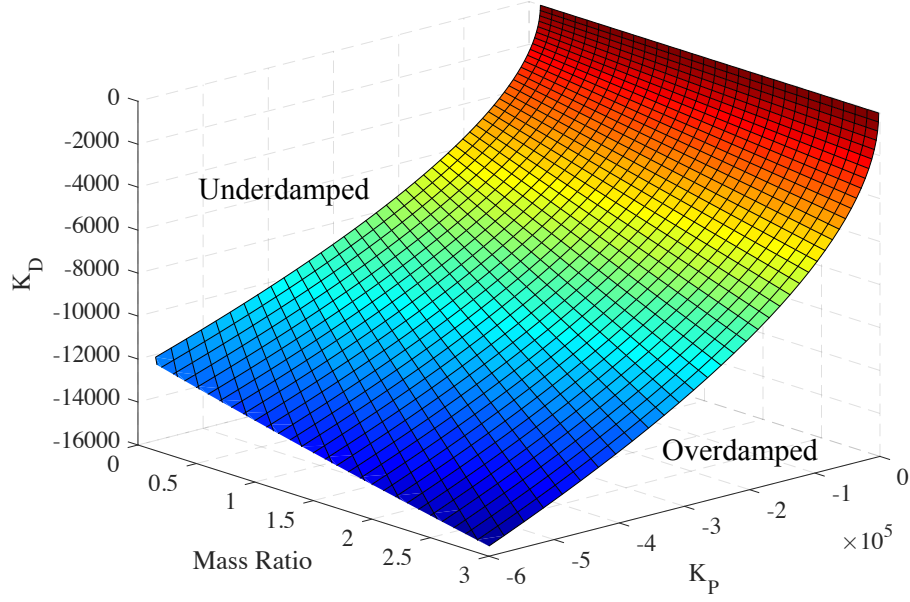
(a) Surface showing PD controller gain pairs where the closed-loop system is critically damped.
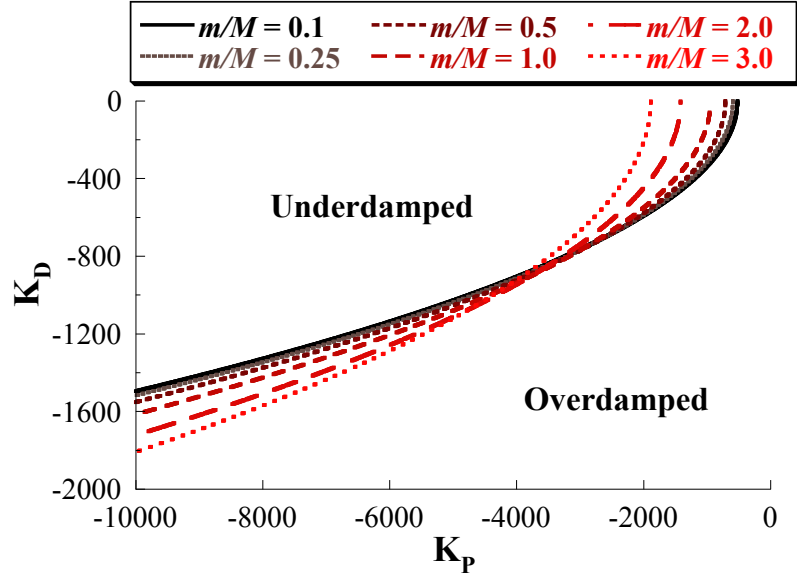
(b) PD controller gain pairs where the closed-loop system is critically damped for selected mass ratios.

Figure 48: Closed-loop pole dynamic characteristics as functions of mass ratio and PD controller gains ($L = 0.9$ m, $M = 48$ kg).

At larger K_P values, higher mass ratios require a larger K_D than smaller mass ratios for overdamped poles.

Figure 49 includes lines showing the requirement on K_P for stability for the selected mass ratios based on (62). Small K_P gains to the right of these lines result in unstable
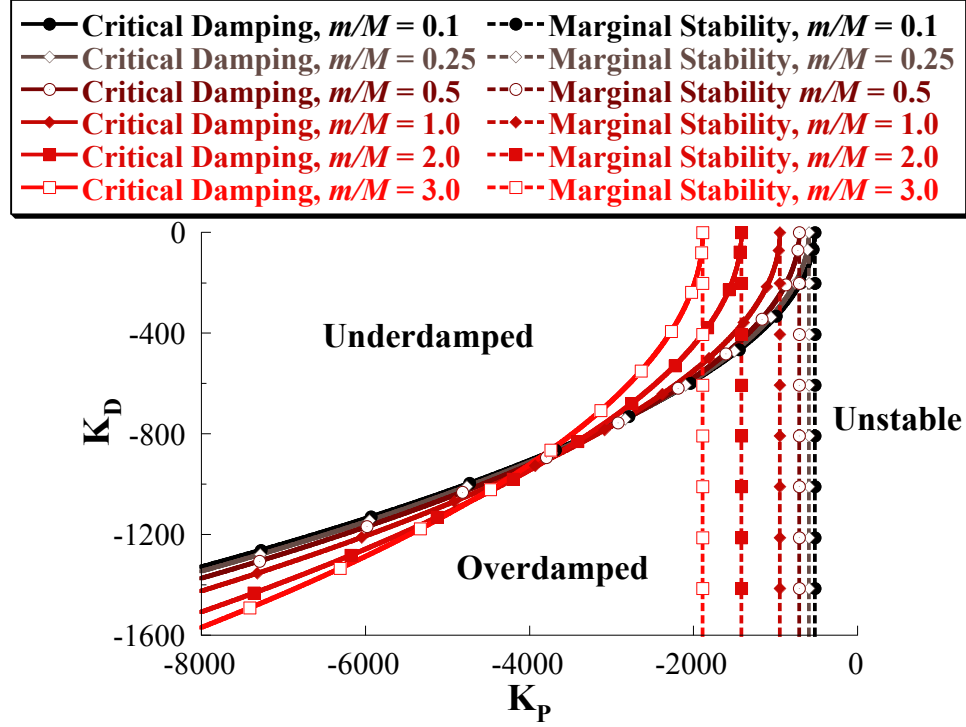
Figure 49: PD controller gain pairs where the closed-loop system is critically damped and the minimum K_P gain for stability for selected mass ratios ($L = 0.9$ m, $M = 48$ kg).

closed-loop behavior. Therefore, the controller is conditionally stable depending on the value of K_P, with the minimum value for stability dependent on the system masses (and g).

This analysis has shown that K_P and K_D must be negative for a stable closed-loop system, and there can be underdamped poles for certain system and control parameter values. With this understanding, and in light of the requirements for stability in (62), the closed-loop transfer function for the cart position (48) has a similar form to other stable open-loop backdrivable systems such as (3a). There are only two differences: the addition of a damping term, and the zeros are along the real axis, including a non-minimum phase zero. The combination of two poles at zero along with a possibility for underdamped poles for certain parameter values is significant in that it suggests the dynamic behavior can be similar to stable open-loop backdrivable systems, other than the non-minimum phase behavior. This is an example showing how feedback control systems can introduce backdriving dynamics, even in the absence of physical flexibility.

This analysis has several implications for control of inverted-pendulum transporters. First, the control system is conditionally stable, requiring large enough gains depending on the transporter and rider masses. If the drive motors are unable to generate large enough torques to replicate the commanded actuator effort for the higher gains, then the transporter may lose the ability to effectively balance itself and the rider. Also, the stability and closed-loop behavior depends on the rider mass, so inverted-pendulum transporters often state values for maximum rider weights. For example, the Segway i2 manual states a maximum rider weight of 117 kg (260 lbs) [88]. Assuming the transporter does not adapt its controller gains based on measuring the rider weight and the gains are fixed, the gain pair could be such that the controller has overdamped behavior for some riders and underdamped behavior for others. When the system is underdamped, backdriving behavior can occur. It would be more effective for an inverted-pendulum transporter to use gain scheduling based on measured rider mass to keep the closed-loop dynamics the same or similar for every rider regardless of their mass. For example, pressure sensors on the base could be used to estimate rider weight when the rider first steps on the transporter, and the controller could adjust the gains accordingly to maintain the desired closed-loop dynamics.

Due to the use of state feedback, the controller also requires a precompensation gain to have unity steady-state gain in response to a reference pendulum angle command. The value of the required precompensation gain K_{ss} can be calculated as:

$$K_{ss} = \frac{1}{\mathbf{G}_{CL2}(0)} = K_P + (M + m)\,g \tag{65}$$

where $\mathbf{G}_{CL2}(0)$ is the steady-state gain of (49). Note that for stable K_P according to (62), K_{ss} is strictly negative. The expression for K_{ss} in (65) also implies that the closed-loop steady-state gain changes with rider mass. Practically, this is not a significant problem because the nature of an inverted-pendulum transporter and this controller design require the rider to act as an outer-loop position or velocity controller, and the rider could adjust their lean commands accordingly. However, it is another example where gain scheduling based on rider mass could be used to update K_{ss} in addition to K_P and K_D, providing more consistent behavior for different riders.

As an example of the controller performance and these issues, consider the system response with $L = 0.9$ m, $M = 48$ kg, $K_P = $ -2,000, $K_D = $ -100 for two different rider masses $m = 60$ kg and 80 kg. The reference command is a bang-bang rider lean command with amplitude of 5 degrees. This is meant to model the rider leaning forward 5 degrees for a period of time to move forward, then leaning back to stop. For this example, the precompensation gain is calculated using (65) with $m = 80$ kg. The cart position and pendulum angle responses for both masses are shown in Figure 50. The reference rider lean command is also shown. For both of these rider masses and this set of controller gains, the closed-loop dynamics are underdamped, and pendulum angle oscillation and cart backdriving occur. Larger angle oscillation and cart backdriving amplitudes occur with the larger rider mass. However, the larger rider mass results in slightly more closed-loop damping (a damping ratio of 0.203 for $m = 80$ kg compared to 0.188 for $m = 60$ kg). Also, the total distance traveled is different using the same reference rider lean command due to the fact that the closed-loop steady-state gain changes with rider mass.

Numerous scenarios encountered in the real world can cause an inverted-pendulum transporter to fail to apply the forces or torques needed to balance the device and rider. These
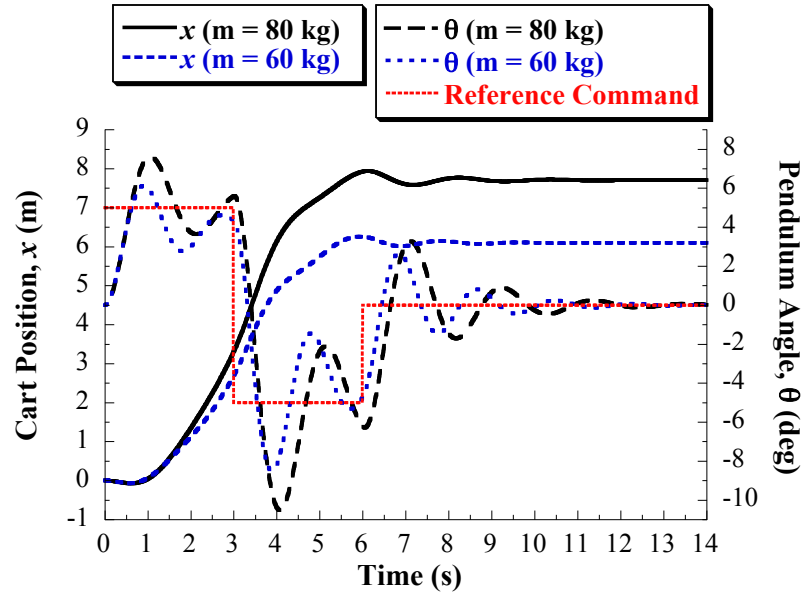
Figure 50: Response of closed-loop Cart with Inverted Pendulum controller to a bang-bang reference pendulum angle command for $m = 60$ kg and 80 kg (with $L = 0.9$ m, $M = 48$ kg, $K_P = $ -2,000, and $K_D = $ -100).

include exceeding the actuator limits due to backdriving pitch oscillation such as occurred in the example shown in Figure 3, loss of traction, one wheel leaving the ground due to roll instability, and striking obstacles/bumps/potholes. Appendix A details the many dynamic hazards of inverted-pendulum transporters. Due to the hazards that arise when attempting to transport people with these devices, attempting to use the feedback controller presented in this section for balancing a person is not recommended. The purpose of this section was merely to illustrate how backdriving dynamics can arise from a feedback control system, and the Cart with Inverted Pendulum model is fundamentally effective at illustrating this behavior. The analysis in this section is also useful for explaining some of the dynamic behavior of inverted-pendulum transporters.

4.3   Combined Input-Shaping and Feedback Control

4.3.1   Overview and Previous Research

Control architectures consisting of a combination of input shaping and feedback control have been studied previously. Many previous methods first calculate the controller gains, and then subsequently design the input shaper based on the closed-loop system flexible mode(s). Xianren and Zhengxian [131] and Mar *et al.* [58] designed combined input-shaping and PD control systems for a flexible spacecraft and a double-pendulum crane, respectively. In both cases, the design was done sequentially – the PD controller was designed based on system requirements, and then the input shaper was determined based on the closed-loop dynamics. Magee and Book [57] used input shaping inside a joint angle feedback loop to reduce the base motion of a flexible micro/macro robotic manipulater. Cannon *et al.* [14] investigated the combination of inertial damping and outside-the-loop command filtering with a joint PD controller for the same flexible micro/macro robotic manipulater. The micro/macro robot structure has some coupling similarities to backdrivable flexible systems, in the sense that the micro manipulator can excite and be used to cancel vibration in the macro robot structure. In both [57] and [14], the input shaping and feedback controllers were designed separately.

Greater performance may be achieved if the input shaper and controller are design

concurrently rather than sequentially. For example, Kenison and Singhose [52] studied the combination of input shaping and PD position control for an inertia plant. The input shaper impulse sequence and PD gains were chosen with an optimization routine that included step response constraints on percent overshoot, residual vibration, and controller effort. Huey and Singhose [44] extended this work with a different optimization approach and compared the concurrent design methods with sequentially designed-controllers. Banerjee *et al.* [7] used optimization to concurrently design a combined input-shaping and PID controller for a flexible spacecraft. However, flexible coupling or backdriving effects between the rigid body and flexible arms were not included in the model, and the method required solving the system differential equations for each parameter set considered by the optimization routine. Fujioka and Singhose [30, 31] studied the combination of input shaping and model reference control for a double-pendulum crane where the two techniques work together to yield improved state tracking, oscillation suppression, and control effort reduction. Also, Schmidt *et al.* [87] developed a combination of linear-quadratic regulator feedback control with input shaping to achieve crane payload tracking control for an autonomous surface vehicle pick-up operation. Their controller uses switching logic based on the retrieval stage and system state to combine the input shaper with the feedback loop.

Another controller architecture that has been studied has input shaping inside the feedback loop. This is sometimes known as closed-loop signal shaping [43, 45]. While this method has advantages such as rejection of sensor noise due to the shaping filter [45], stability concerns that arise due to the time delay introduced to the feedback loop by the shaping process must be addressed [43]. For this reason, closed-loop input shaping will not be the focus in this thesis.

The concurrent design of combined input-shaping and PD control studied by Kenison and Singhose [52] investigated the controller stability in the presence of unmodeled modes. While the analysis used a system model similar to the fundamental structure of backdrivable flexible systems, the flexible mode was not accounted for during the controller design and optimization process.
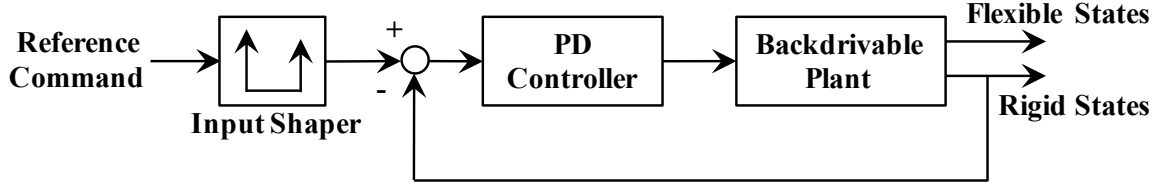
Figure 51: Block diagram of combined input-shaping and PD control for backdrivable flexible systems.

This section presents a concurrently-designed input shaping and PD controller for backdrivable flexible systems. This controller structure is represented with the block diagram shown in Figure 51. Advantages of this approach include not requiring sensors or an estimator for the flexible states. The controller only utilizes measurements of the rigid states, which are assumed to be readily available in most applications. Optimization is used to solve for the input shaper impulse sequence amplitudes and times and PD gains that minimize the time of the final impulse. The presence of an input shaper allows the PD controller to provide a more aggressive rise time or error regulation without the associated increases in overshoot and settling time. The goal is to illustrate improved response performance of the rigid element while also reducing residual vibration of the flexible mode.

The Rotary Hub with Flexible Arm model will be utilized here to demonstration the design process and performance of combined input-shaping and PD control for backdrivable flexible systems. The closed-loop feedback controller for this system was developed and some of its key characteristics were presented in Section 4.2.1. Understanding of the closed-loop behavior, in particular the modal characteristics, is critical to designing the combined controller.

4.3.2 Sequential Design Example

A sequentially designed controller and input shaper is presented in this section. The feedback controller for the Rotary Hub with Flexible Arm model is used as the demonstration system. As with Section 4.2.1, the following parameter values are used with the closed-loop system (72), and (74) for the rest of this section: $m_1 = 5{,}000$ kg, $L_1 = 1$ m, $m_2 = 100$ kg, $L_2 = 5$ m, and $k = 5{,}000$ N-m/rad.

Suppose that the sample closed-loop response shown previously in Figure 45 sufficiently

satisfies all performance requirements should the damped residual oscillation of the arm be suppressed. To achieve this, an input shaper may be included with the controller. The input shaper should be designed using the closed-loop natural frequency and damping ratio for this controller gain pair (1.3 rad/s and 0.3, respectively). A ZV shaper that suppresses this vibration can be designed using (40), yielding the following impulse sequence:

$$
\begin{bmatrix} A_i \\ t_i \end{bmatrix} = \begin{bmatrix} 0.732 & 0.268 \\ 0 & 2.53 \text{ s} \end{bmatrix}. \tag{66}
$$

Including this input shaper with the controller improves the response by removing the damped residual vibration of the arm. This can be seen in Figure 52, where the original unshaped response with the feedback controller only is compared to the response obtained by including the shaper in (66) with the control system. The 2% settling time of the arm is improved from 10.3 s to 2.96 s, and the peak amplitude of the hub response is reduced from -0.31 deg to -0.22 deg.

This sequential design process could be performed again by updating the controller gains, then redesigning an input shaper that suppresses vibration of the closed-loop underdamped
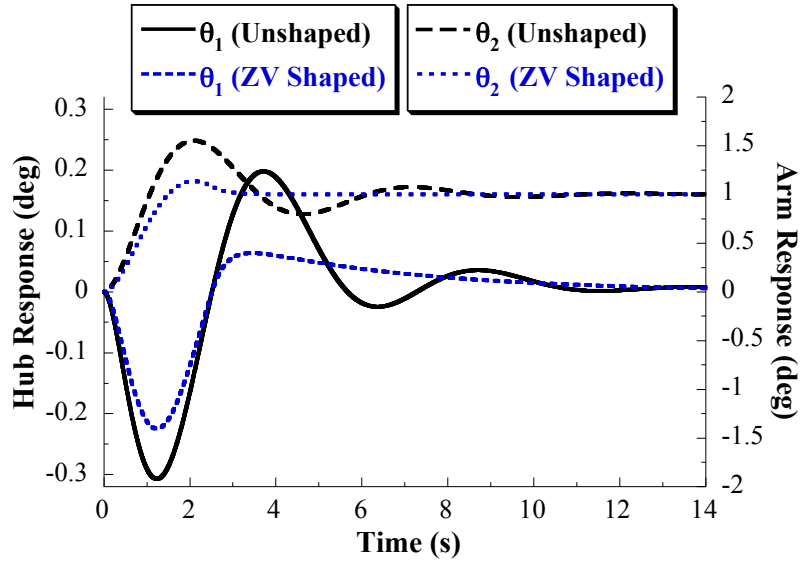
Figure 52: Comparison of unshaped and ZV shaped step response of the closed-loop PD controller for the Rotary Hub with Flexible Arm model with $K_P = 2{,}000$ and $K_D = 10{,}000$.

mode(s). It can be repeated until further performance improvements are obtained or to satisfy other requirements for the response characteristics. Suitable performance for a given application could be obtained through such trial-and-error tuning of the controller gains followed by updating of the input shaper based on the closed-loop underdamped modes. However, the closed-loop dynamics of backdrivable flexible systems are complicated, and Section 4.2.1 demonstrated that some traditional characteristics and behaviors of PD controllers do not apply to backdrivable systems. This can make traditional trial-and-error controller tuning tedious and inefficient.

4.3.3 Concurrent Design Through Optimization

As discussed in Section 4.3.1, a more sophisticated approach than sequential design is to select the input shaper and PD controller parameters concurrently through an optimization routine with constraints on overshoot, residual vibration, and control effort. However, the transition points between the two closed-loop mode cases (two pairs of complex poles vs. one pair of complex poles and two real poles) illustrated in Figures 39-44 make optimization challenging.

The optimization method presented in the section seeks to simultaneously solve for impulse amplitudes and times of the input shaper and the PD controller gains. This achieves the objective of concurrently designing both components of the controller for the backdrivable flexible system.

4.3.3.1 Optimization Objective Function and Constraints

This section describes the optimization objective function and constraints. While many of the traditional input shaping constraints are required, some additional constraints on the rigid body motion/state are included to improve the overall performance of the system. The constraints on the rigid body state are similar to those used by Kenison and Singhose [52] when designing the concurrent input shaping and PD controller for an inertia plant.

The optimization seeks to solve for the following vector of control parameters:

$$\vec{z} = \begin{bmatrix} K_P & K_D & A_1 & ... & A_i & ... & A_n & t_1 & ... & t_i & ... & t_n \end{bmatrix}^T, \qquad i = 1, \ldots, n \qquad (67)$$

subject to the objective function and constraints described in this section. A_1 through A_n and t_1 through t_n are the input shaper impulse amplitudes and times, respectively, and n is the total number of impulses in the input shaper. Therefore, the size of the vector $\vec{z}$ is $(2n+2) \times 1$.

Input shapers may be designed using different combinations of performance requirements. For example, one set of constraints consists of requiring zero residual vibration at the time of the last impulse and restricting the steps to be positive. The residual vibration resulting from a sequence of impulses divided by the vibration resulting from a single, unity-magnitude impulse is given by [92]:

$$V = e^{-\zeta\omega_n t_n}\sqrt{\left[\sum_{i=1}^{n} A_i e^{\zeta\omega_n t_i}\cos\left(\omega_n\sqrt{1-\zeta^2}t_i\right)\right]^2 + \left[\sum_{i=1}^{n} A_i e^{\zeta\omega_n t_i}\sin\left(\omega_n\sqrt{1-\zeta^2}t_i\right)\right]^2}$$
(68)

where ω_n and ζ are the natural frequency and damping ratio of the flexible mode. When V is set to zero, (68) results in a zero residual vibration constraint. For the combined input-shaping and PD controller for backdrivable flexible systems, the natural frequency and damping ratio of the closed-loop system depend on the controller gains. The constraints to require positive impulses that sum to 1 are:

$$0 < A_i < 1, \qquad i = 1, \ldots, n,$$
$$A_1 + A_2 + \cdots + A_n = 1.$$
(69)

Due to the transcendental nature of (68), there are multiple solutions that yield zero residual vibration. There is often a desire to make the solution time optimal subject to the zero residual vibration and amplitude constraints, and in this case the input shaper duration must be as short as possible. The time optimality objective function is:

$$\min(t_n).$$
(70)

Also, a constraint of $t_1 \equiv 0$ is used to assist with (70).

By seeking a solution with two steps ($n = 2$), assuming an undamped flexible mode, and solving the above optimization problem (68)-(70), the ZV shaper described by (39)-(41) is obtained. Input shapers that are robust to uncertainty or error in the modeled natural

91

frequency may also be designed. One such input shaper is the *Zero Vibration and Derivative* (ZVD) shaper, which adds a constraint requiring that the derivative of (68) equal zero at the design natural frequency [92]. However, robust input shapers will not be considered here, and a two-impulse shaper is designed for combination with the PD feedback controller for backdrivable flexible systems.

To also improve performance of the rigid body mode, additional constraints are required. Three additional constraints based on step response characteristics are included to optimize the combined controller. The first constraint limits the peak overshoot of the rigid body state to below a specified level $M_{p,\text{tol}}$:

$$M_{p,x} \leq M_{p,\text{tol}} \tag{71}$$

where $M_{p,x}$ is the overshoot of the rigid body state in response to step controller input. For Rotary Hub with Flexible Arm, this corresponds to the peak hub amplitude following an arm angle step command.

The second response characteristic constraint is the settling time of the flexible mode state, in this case the arm angle. It is desirable to have the arm angle within the 2% settling envelope at the same time as or before the time of the final impulse. This constraint can be written as:

$$t_{s,\theta} \leq t_n \tag{72}$$

where $t_{s,\theta}$ is the settling time of the flexible mode state. This constraint is important and necessary because the two-impulse shaper can only suppress the vibration from a single mode[1], and it is possible for the closed-loop system to have two underdamped modes as shown in Section 4.2.1. Because the optimization is looking for a solution that satisfies (70), this constraint also has a secondary effect of producing a fast settling time.

The third and final response characteristic constraint is a limit on the maximum control effort. From Figure 36, the control effort is the hub torque T. With $R_{\theta_1} = 0$, the hub torque

---

[1]The second mode can also be suppressed by chance if it happens to have a similar frequency and damping ratio as the first mode, or if the second mode frequency is an odd multiple of the first mode frequency.

is the output of the PD controller:

$$T(t) = -K_P \theta_1(t) - K_D \dot{\theta}_1(t). \tag{73}$$

The constraint can then be written as:

$$\max\left(|T(t)|\right) \le U_{\max} \tag{74}$$

where $U_{\max}$ is the maximum allowable control torque. A constraint of this form can be necessary to prevent actuator saturation.

The step response constraints in (71), (72), and (74) are evaluated by finding the shaped step response of the linear closed-loop system (44) and (45), where a one degree step command is shaped using the input shaper defined in the solution vector. This is repeated for each update to the solution vector during the optimization routine.

4.3.3.2 Optimization Results

The optimization problem in Section 4.3.3.1 can be solved using a nonlinear optimization routine to find the two-impulse input shaper and controller gains that satisfy the constraints. However, the transition between the two closed-loop mode cases (two pairs of complex poles vs. one pair of complex poles and two real poles) at various combinations of control gains make the optimization sensitive to the initial guess.

It is possible for the initial guess and/or potential solutions found by the optimization to fail to satisfy all of the constraints. Such infeasible solutions are much more likely to cause the optimization to fail with stricter constraint values. To address this, a multi-level optimization approach is utilized [80, 81]. A solution is first sought with relatively relaxed constraints. Once a solution is found, the constraints are reduced by a small amount and the optimization is solved again using the previous solution as the initial guess. The system parameters and initial constraint values used are listed in Table 3.

For the Rotary Hub with Flexible Arm model, the most challenging constraint is the peak hub amplitude constraint (71). Due to conservation of angular momentum, the hub always moves in response to arm motion. It is up to the controller to correct this, and any solution found must not violate the control effort constraint (74). Therefore, a relaxed

93

Table 3: System parameters and optimization constraints.

Parameter	Value
m_1	5,000 kg
L_1	1 m
m_2	100 kg
L_1	5 m
k	1 N-m/rad
$U_{\max}$	75 N-m
$M_{p,\text{tol}}$	0.1 deg

value of $M_{p,\text{tol}} = 0.1$ deg is used for the initial iteration. This value is then reduced until the optimization cannot find a solution.

With input shaping, the settling time and overshoot constraints can be satisfied even with lower closed-loop damping ratios. In fact, the combined controller can perform better in these cases, particularly when the other mode is overdamped. The modal results illustrated in Figures 43 and 44 show that one underdamped mode with a low damping ratio occurs at higher K_D and for relatively lower K_P. Therefore, an initial guess of $K_P = 7,000$ and $K_D = 18,000$ is used. The closed-loop frequency and damping ratio for these gains are used to calculate a ZV shaper using (40) to serve as the initial guesses for the shaper amplitudes and times. Table 4 summarizes the parameters used for the initial guess.

The optimization is solved, yielding a solution that satisfies the constraints. Then, the value of the hub amplitude constraint $M_{p,\text{tol}}$ is reduced a small amount, and the optimization is solved again. The results from each iteration of this process are shown in Table 5. The multi-level optimization approach allows for the hub amplitude to be steadily reduced while also satisfying the baseline optimization constraints. For each solution, the arm 2% settling

Table 4: Initial solution guess for first iteration of multi-level optimization (iteration 0).

Parameter	Value
K_P	7,000
K_D	18,000
A_1	0.62
A_2	0.38
t_1	0
t_2	2.67 s

Table 5: Summary of multi-level optimization iteration results for concurrently-designed, combined input-shaping and PD controller.

	Optimization Solution							Response Characteristics		
	Controller Gains		Input Shaper Parameters				Hub Amplitude Constraint (deg)	Hub Max. Amplitude (deg)	Arm 2% Settling Time (s)	Max. Control Effort (N-m)
Iter. #	K_P	K_D	A_1	A_2	t_1 (s)	t_2 (s)				
0	7000	18000	0.62	0.38	0	2.670	0.100	0.109	2.65	54.19
1	7970	19807	0.61	0.39	0	2.665	0.100	0.097	2.61	53.98
2	8761	21139	0.60	0.40	0	2.662	0.090	0.090	2.58	53.85
3	10873	24694	0.58	0.42	0	2.654	0.080	0.075	2.10	53.55
4	13764	24966	0.58	0.42	0	2.677	0.070	0.070	2.14	53.60
5	16147	25919	0.57	0.43	0	2.684	0.065	0.065	2.18	53.50
6	17438	27694	0.57	0.43	0	2.676	0.060	0.060	2.20	53.37
7	19053	29992	0.56	0.44	0	2.667	0.055	0.055	2.22	53.23
8	21198	32709	0.56	0.44	0	2.659	0.050	0.050	2.25	53.08
9	23591	36071	0.55	0.45	0	2.650	0.045	0.045	2.26	52.92
10	26985	39650	0.54	0.46	0	2.644	0.040	0.040	2.28	52.77
11	30869	44964	0.54	0.46	0	2.635	0.035	0.035	2.30	52.59
12	-	-	-	-	-	-	0.030	-	-	-

time is less than the shaper duration t_n, satisfying (72). The control effort is less than 75 N-m, satisfying (74). The optimization was not able to find a solution that satisfied the constraints on the 12$^{\text{th}}$ iteration. By then, the hub amplitude constraint had been reduced to 0.03 deg. The solution found on the previous iteration is accepted instead, resulting in a peak hub amplitude of 0.035 deg.

The evolution of selected parameters over each iteration are plotted in Figure 53, where (a) shows the updates to the hub amplitude constraint as it is reduced following each iteration, and (b) and (c) show the PD controller gains and input shaper impulse amplitude solutions, respectively, from each iteration. Note that the initial guess (iteration 0) does not satisfy the hub amplitude constraint, but this does not prevent the first iteration of the optimization from finding a solution. With a relaxed value of the hub amplitude constraint enforced by the multi-level approach, the first iteration has many feasible solutions to search in the solution space nearby to the initial guess.

Examining the solution from each iteration reveals other interesting results. To achieve the smaller peak hub amplitudes, the PD gains had to be increased as shown in Figure 53(b). The modal analysis results in Figures 39-44 showed that higher K_D gains result in lower damping ratios. The lower closed-loop damping ratio can then be handled by the input shaper. This is reflected in the input shapers found for the later iterations, where the shaper becomes more and more symmetric with the impulse amplitudes becoming closer in value as shown in Figure 53(c). Also, increasing K_D allowed for K_P to increase as well while keeping only a single underdamped mode for the input shaper to suppress. The higher K_P and K_D together then allowed for the controller to respond more quickly to the hub angle error, resulting in the decreasing peak hub amplitude possible with each iteration.

Note that the maximum control effort listed in the final column of Table 5 changes very little through each iteration. Even though the gains increase as the peak hub amplitude is reduced as shown in Figure 53(a) and Figure 53(b), the maximum control effort actually drops slightly. This occurs because the higher gains allow the controller to respond more quickly before the hub angle error grows larger. The smaller hub angle error balances out the larger gain values in (73). Another way to view this is that the 1 deg arm command
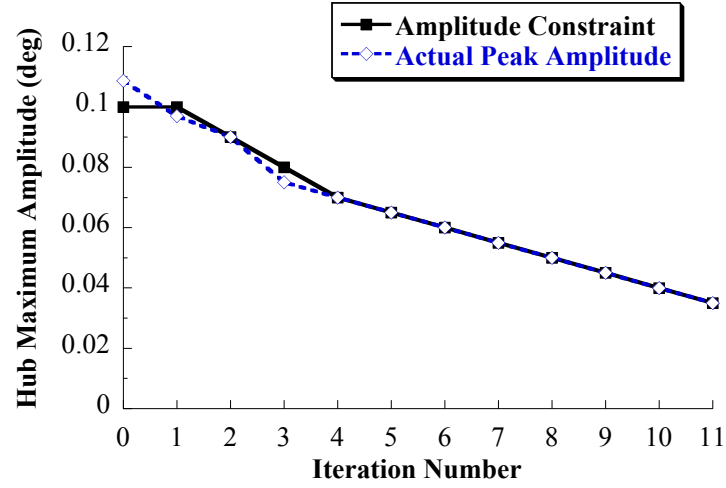
(a) Hub amplitude constraint updates with each iteration.
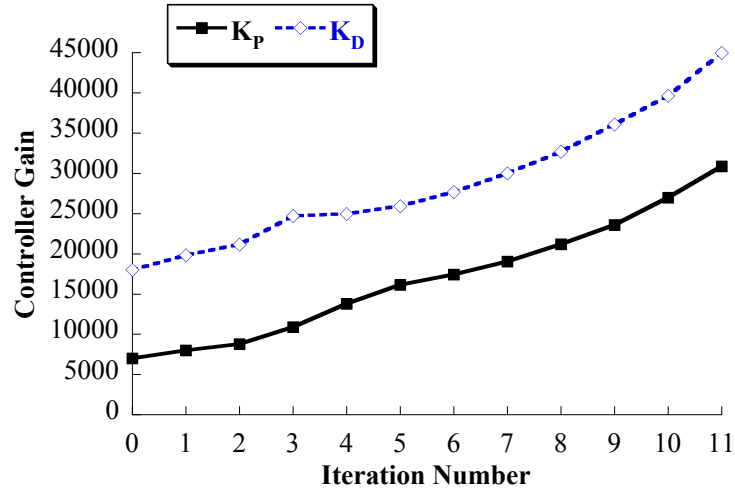
(b) PD controller gain solution values from each iteration.
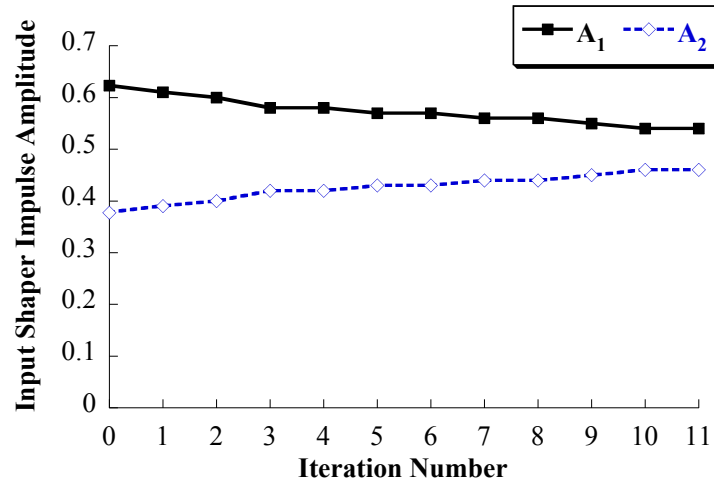
(c) Solution values for input shaper impulse sequence amplitudes solution values from each iteration.

Figure 53: Multi-level optimization iteration results for selected parameters.

causes a certain amount of momentum transfer to hub, and approximately 53 N-m of peak torque is required to correct the hub angle back to the zero reference with the system inertias used.

Figure 54 shows the time response and control effort using the input shaper and control gains found in the 1st iteration. The time response using no shaper but the same controller gains is also shown for comparison purposes. The shaped hub and arm responses shown
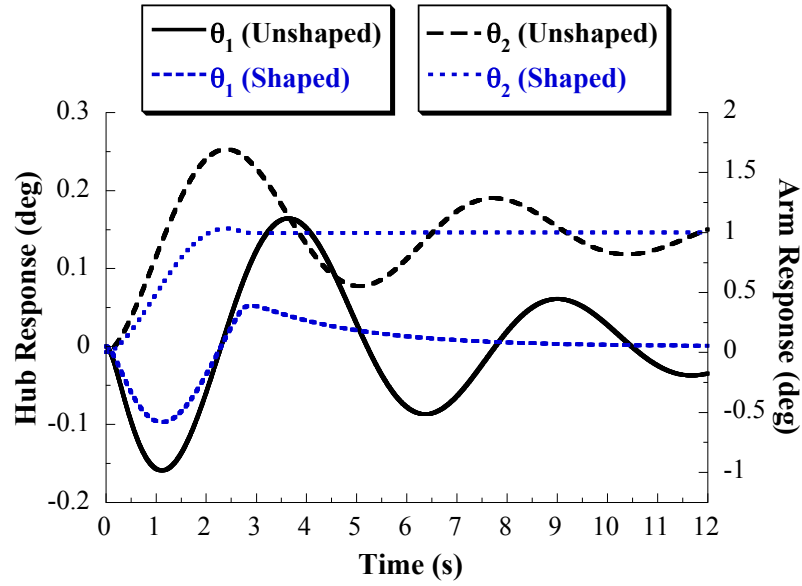
(a) Unshaped vs. shaped hub and arm responses.
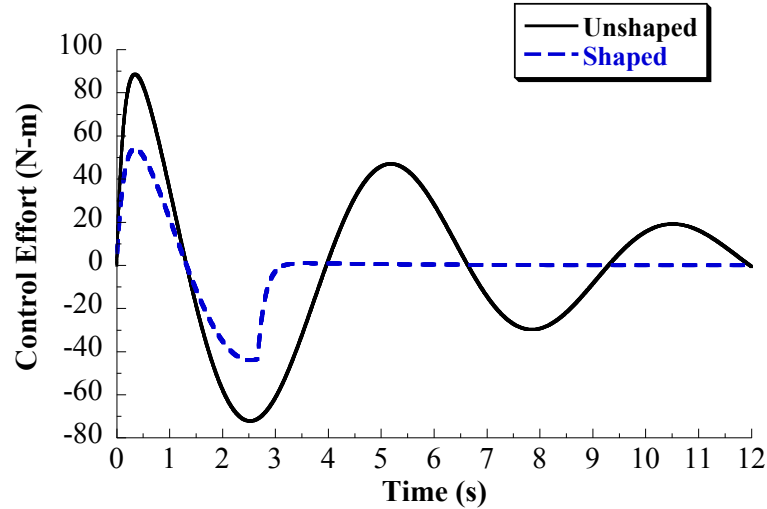
(b) Required control effort.

Figure 54: Time response and control effort using the results from the solution of the 1st iteration.

in Figure 54(a) satisfy the response constraints listed in Table 3. Also, the control effort shown in Figure 54(b) is greatly reduced from the unshaped case, and its maximum value satisfies (74).

Figure 55 shows the time response and control effort using the input shaper and control gains found in the final successful iteration. Again, the time response using no shaper but the same controller gains is also shown for comparison purposes.
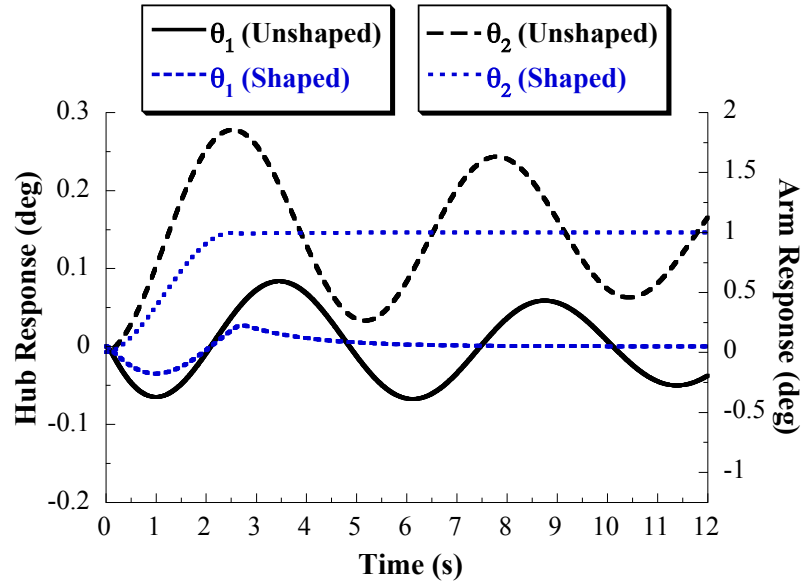
(a) Unshaped vs. shaped hub and arm responses.
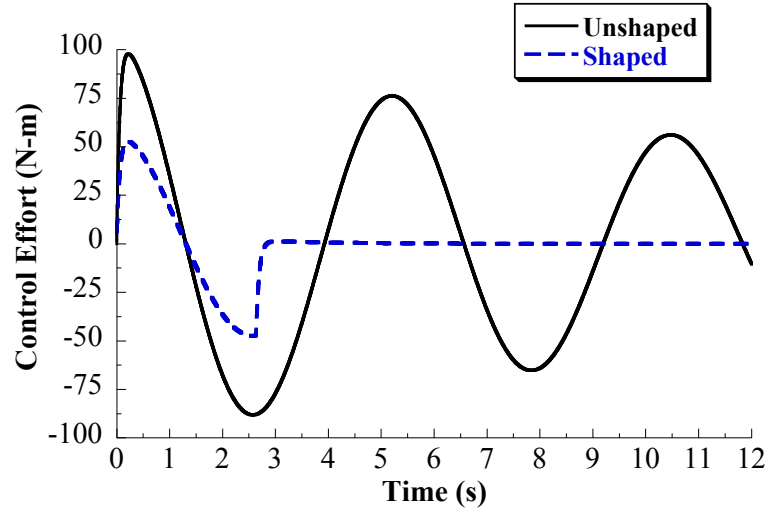
(b) Required control effort.

Figure 55: Time response and control effort using the results from the solution of the final successful iteration.

Figure 56 compares the results from the first and final iterations. Figure 56(a) shows that the iteration process has allowed the optimization to find a controller and input shaper that results in a peak hub amplitude that is 65% less than the solution from the initial iteration. Also, the arm angle settles more quickly using the solution from the final iteration. However, the arm has a slightly longer rise time because the amplitude of the first impulse is less for the final iteration solution. The peak hub amplitude is significantly reduced compared to
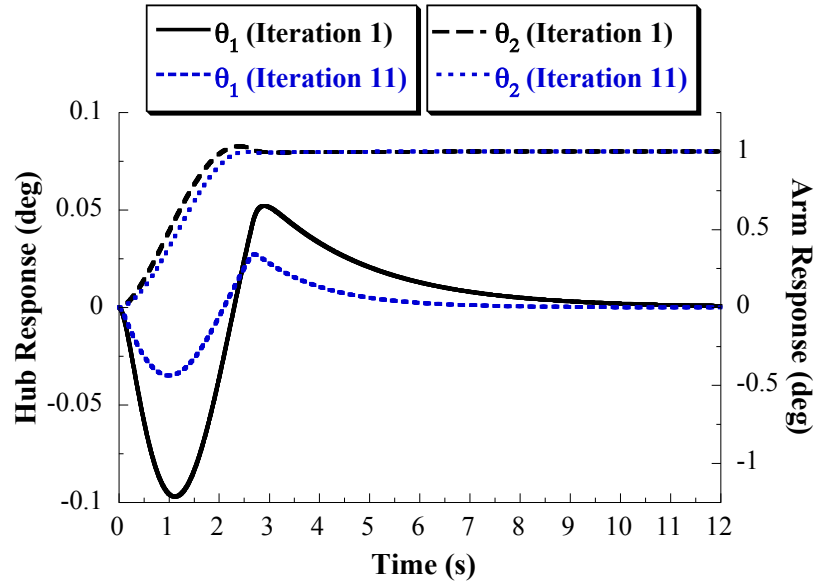
(a) Hub and arm time responses.
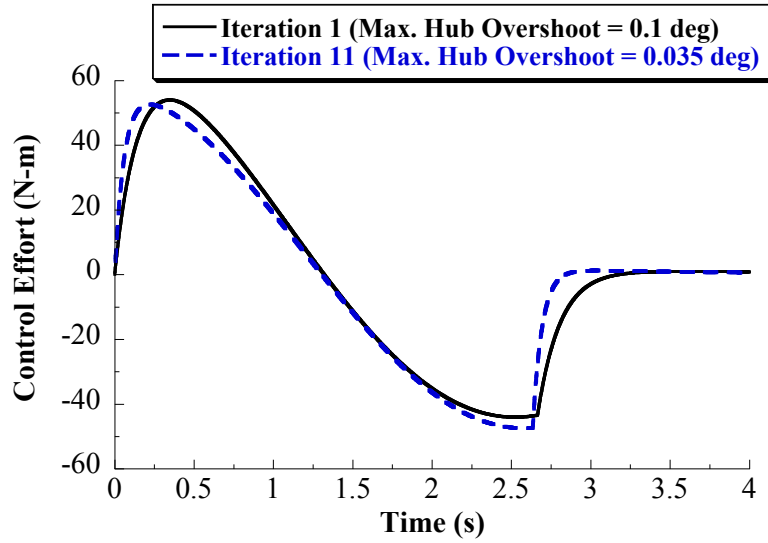
(b) Required control effort.

Figure 56: Comparison of the time responses and control effort using the solutions of the first and final successful iterations.

Table 6: Combined input-shaping and PD controller solution found from the final successful iteration of the concurrent design optimization.

Parameter	Value
K_P	30,869
K_D	44,964
A_1	0.54
A_2	0.46
t_1	0
t_2	2.635 s

the first iteration due to the significantly higher gain values. Yet, Figure 56(b) shows that there is no significant increase in the required control effort for the reasons explained above.

The PD gains and input shaper from the final successful iteration are listed in Table 6.

4.3.3.3   Comparison Between Results from Sequential and Concurrent Designs

An important outcome of the concurrent design optimization process is that it yields an input shaper and controller gains that are substantially different from those obtained through a sequential design process without requiring any tedious gain tuning. In addition, the multi-level optimization approach yields results that satisfy constraints on the hub back-driving response. Figure 57(a) compares the results from the concurrent design to those from the sequential design that were previously shown in Figure 52. The response with the concurrently designed controller has a peak hub amplitude that is 84% less than that of the sequentially designed controller. By choosing to solve for a two-impulse input shaper, the optimization approach favors a solution where the closed-loop dynamics have a single underdamped mode. Coupled with the constraint to have an arm angle settling time that is at least as fast as the time of the final input shaper impulse, the optimization yields an arm angle 2% settling time of 2.30 seconds for the concurrently designed controller compared to 2.96 seconds for the sequentially designed controller. Figure 57(b) also shows a comparison between the hub control effort required for both controllers. Both controllers require a similar maximum control effort, with the concurrent design control effort rising and returning to zero more quickly due to the higher gains.
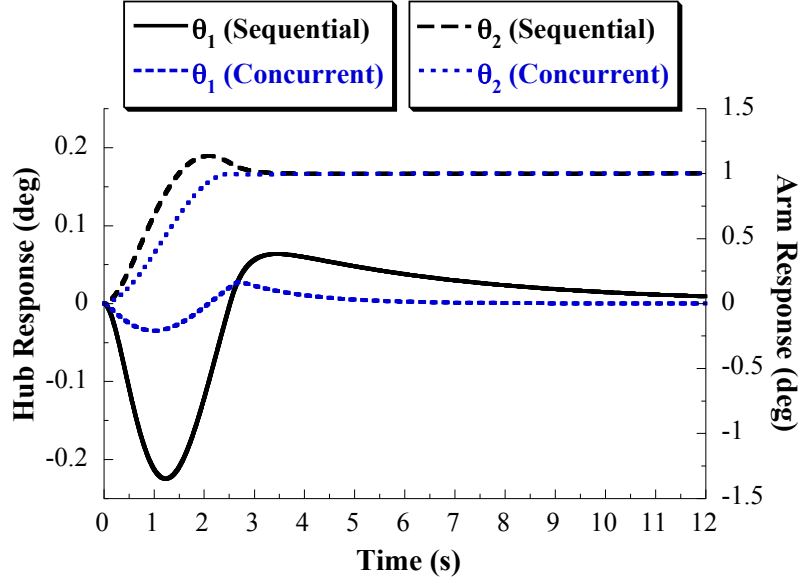
(a) Sequential vs. concurrent design hub and arm responses.
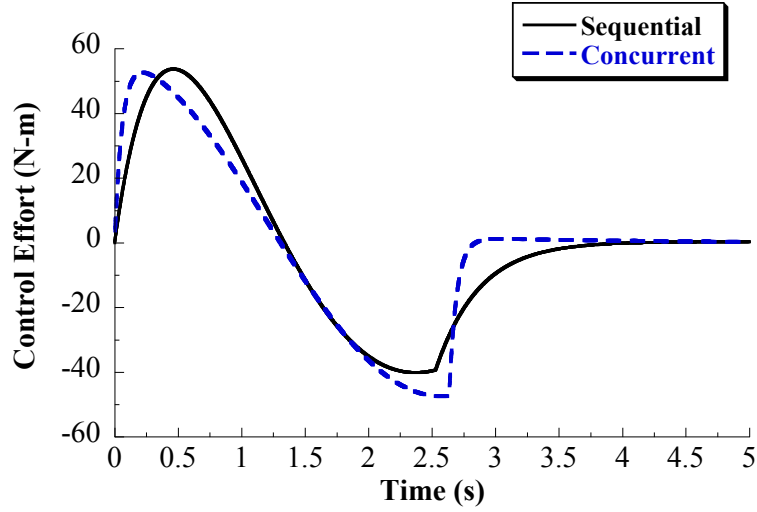
(b) Sequential vs. concurrent design required control effort.

Figure 57: Time response and control effort comparison between the results from the sequential and concurrent controller designs.

4.4 Summary

This chapter presented control techniques for backdrivable flexible systems. Input shaping was shown to be an effective technique because it cancels the vibration or oscillation caused by the flexible mode, preventing backdriving effects proactively. Also, PD controllers were designed for the Rotary Hub with Flexible Arm and Cart with Inverted Pendulum models. Analysis of the controller for the latter model showed how backdriving dynamics could

arise from feedback control. Also, the PD controller for the Rotary Hub with Flexible Arm was combined with input shaping. Using optimization and a concurrent design process, a combined input-shaping and PD controller was developed that reduces the maximum hub amplitude error caused by backdriving effects, slews the flexible arm with little residual vibration and fast settling time, and satisfies a control effort constraint. The concurrent design process yields a combined input-shaping and PD controller that is substantially different from controllers that may be obtained with a typical sequential design.

CHAPTER V

CONTROL OF BACKDRIVABLE SYSTEMS WITH DISCRETE ACTUATORS

In this chapter, input-shaped stepping sequences are developed. These input-shaped stepping sequences address challenges of discretized amplitude to be compatible with stepper motors, and robustness to modeling error in the fundamental flexible mode. While discretization and robustness are challenges that have been addressed before when designing input shapers [65, 80, 82, 111], most previous approaches have not directly considered cases where all shaper amplitudes must be positive and constant, or applied input shaping techniques to designing stepper motor stepping sequences. Also, the step sequences can be configured to reduce backdriving effects on the rigid body motion by giving a feedback controller more time to regulate the error while still eliminating residual vibration.

Some current techniques for stepper motors on spacecraft use vibration-limiting stepping profiles [10, 51, 76], however they are not very robust to modeling error or uncertainty in the natural frequencies of vibration of the appendages. Other input shaping techniques considered for stepper motors are applicable to larger slewing distances, and shape the stepping rate or break the maneuver into slewing pulses devised with duration proportional shaper impulse amplitudes [26]. The methods discussed here meant for shorter-distance slewing of stepper motors and are also compatible with other types of on-off actuators, such as relays and thrusters.

5.1 Constant-Amplitude Input Shaping for Stepper Motors

5.1.1 Input-Shaped Step Sequences

As discussed in Chapter IV, input shaping is a command-filtering method that limits unwanted vibration [92, 109, 110]. While traditional input-shaping techniques were developed using series of impulses, input-shaped commands may also be constructed from a series of steps, such as the output from stepper motors. An example of this step-shaping is shown in
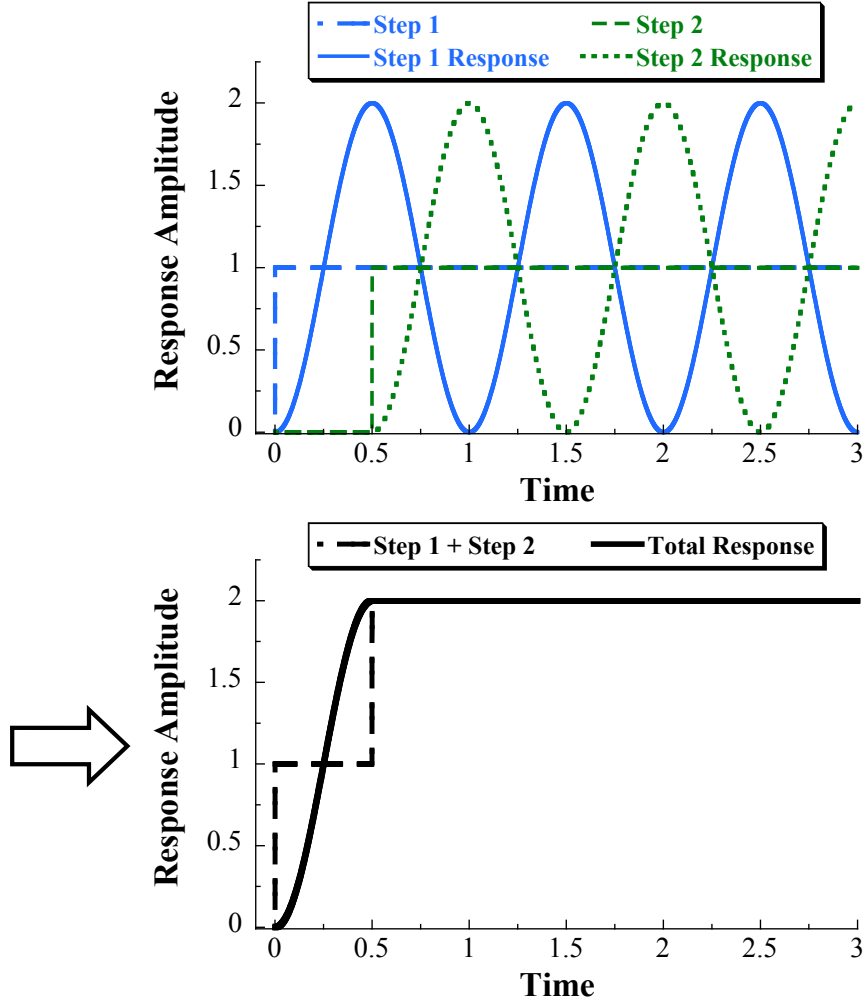
Figure 58: Creating an input-shaped step sequence by combining two step commands.

Figure 58. In the top plot, the Step 1 command is applied to a flexible linear system, and the system vibrates in response. A similar result would occur should the Step 2 command be issued a short time later. The bottom of Figure 58 shows the response that would result if the command was the sum of Steps 1 and 2. The system is assumed to be linear and time-invariant, so by superposition the responses to Steps 1 and 2 combine linearly, and the residual vibration is eliminated. The step sequence can be considered an *input-shaped step sequence* in the sense that it results in zero residual vibration.

Input-shaped step sequences may consist of more than two steps. In the time domain, a generic step sequence with i steps may be represented as:

$$\mathbb{S}(t) = A_1 h(t - t_1) + A_2 h(t - t_2) + \cdots + A_N h(t - t_N), \tag{75}$$

105

where A_i are the step amplitudes, t_i are the time locations of each step, N is the number of steps, and $h(t)$ is the Heaviside function representing a unity-magnitude step command beginning at $t = 0$. Without loss of generality, the first step time is chosen as $t_1 \equiv 0$. The amplitudes and times of the steps may be written in matrix form as follows:

$$\begin{bmatrix} A_i \\ t_i \end{bmatrix} = \begin{bmatrix} A_1 & \ldots & A_i & \ldots & A_N \\ t_1 & \ldots & t_i & \ldots & t_N \end{bmatrix}. \tag{76}$$

The step amplitudes and time locations are designed using estimated natural frequencies and damping ratios of the flexible modes to be suppressed. Input shapers can be made robust to errors and changes in these parameters [92, 97, 100, 96, 125, 105]. Even in the face of such modeling errors, input-shaped step sequences that utilize solely positive steps never excite more vibration than would be caused by not using input shaping.

5.1.2 Design Constraints and Performance Requirements

Input-shaped step sequences use many of the same design constraints as typical input shapers stated in Section 4.3.3.1. For example, the residual vibration given by (68) can be constrained to zero or less than some tolerable level.

For stepper motors, the times of each step correspond to when a single step of the motor should be taken. Each step taken by a stepper motor has the same amplitude, so each amplitude in an input-shaped step sequence must be equal. For the purposes of input shaper design, each amplitude can be set equal to 1, and (68) can be normalized by the number of steps in the sequence. When the desired amount of stepping equals N steps, the amplitude constraint can be written as

$$A_i = 1, \qquad i = 1, \ldots, N. \tag{77}$$

The amplitudes of the N steps then sum to the number of steps in the sequence. Equation (68) may still be applied by normalizing by the number of steps. After normalization, the residual vibration predicted by (68) corresponds to the amount of vibration caused by the step sequence, divided by the amount of vibration that would be caused by taking all of the steps at the same time. As a result of this design approach, the resulting input-shaped

106

step times may be used with any stepper motor regardless of its step size. Each time in the sequence corresponds to when the stepper motor should take a single step.

A ZV-shaped step sequence can be formed by converting the impulses in (39) to steps. The step sequence is:

$$\mathbb{ZV}(t) = h(t) + h(t - t_2),\tag{78}$$

For an undamped flexible mode, the ZV shaper step sequence amplitudes and times are [109]:

$$\begin{bmatrix} A_i \\ t_i \end{bmatrix} = \begin{bmatrix} 1 & 1 \\ 0 & \frac{T_n}{2} \end{bmatrix},\tag{79}$$

where T_n is the vibration or oscillation period. This is the sequence of steps used in Figure 58 to create a command that results in zero residual vibration for a flexible system with a period of $T_n = 1$. The undamped ZV shaper given by (79) is a 2-Step input-shaped stepping sequence for stepper motors, where the stepping times for this sequence are:

$$\begin{bmatrix} t_i \end{bmatrix} = \begin{bmatrix} 0 & \frac{T_n}{2} \end{bmatrix}.\tag{80}$$

In actual implementation, these stepping times are rounded to the nearest stepping period of the stepper motors. This rounding can slightly degrade the vibration-canceling properties of the input-shaped command, as the rounded stepping times are no longer the exact ZV input-shaping times.

5.1.3 Vector Diagram Design Approach

Another approach to designing input shapers uses vector diagrams [100]. Each step in the input-shaped step sequence is represented by a vector on the vector diagram. The amplitude of each vector equals the magnitude of the corresponding step. The angle of each vector is determined by the step time, $\phi_i = \omega_n t_i$. The magnitude of the vector sum of these vectors is proportional to the residual vibration that would result from applying the step sequence to a flexible system with natural frequency ω_n. Figure 59 shows the vector diagram for a generic two-step sequence. The first step has magnitude A_1 and zero angle, and the second step has magnitude A_2 and angle $\omega_n t_2$. The vector sum of the two vectors representing

the steps is shown in the figure as $\sum \vec{A}$. The magnitude of this vector equals the residual vibration caused by this two-step sequence for a flexible mode with natural frequency ω_n.

When $t_2 = \frac{\pi}{\omega_n}$, the input shaper is a 2-Step (Undamped ZV) shaper. Figure 60 shows the vector diagram for this input shaper. Note that the vector magnitudes are equal to A here because the 2-Step shaper can be applied to step sequences with any arbitrary step size, as long as the size of both steps are the same. The vector sum of these two vectors is the zero vector. Therefore, this step sequence will result in zero residual vibration for a flexible mode with natural frequency ω_n.

5.1.4 Robust Stepping Sequence Design Using Vector Diagrams

An input-shaped stepping sequence that is more robust to frequency modeling error may be designed by including additional steps in the sequence. One such sequence consists of four steps given by:

$$
\begin{bmatrix} A_i \\ t_i \end{bmatrix} = \begin{bmatrix} \frac{1}{4} & \frac{1}{4} & \frac{1}{4} & \frac{1}{4} \\ 0 & \frac{T_n}{2} & \frac{3T_n}{2} & 2T_n \end{bmatrix}.
\tag{81}
$$

This step sequence is suitable for implementing with discrete actuators because the amplitudes are equal. To implement this step sequence using stepper motors, the stepping
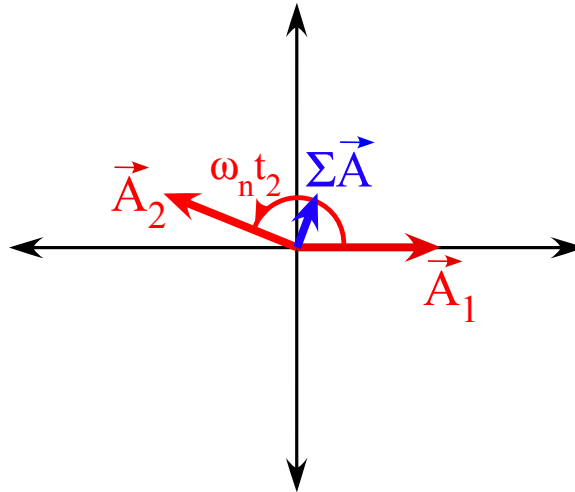
Figure 59: Example vector diagram for a two-step impulse sequence.
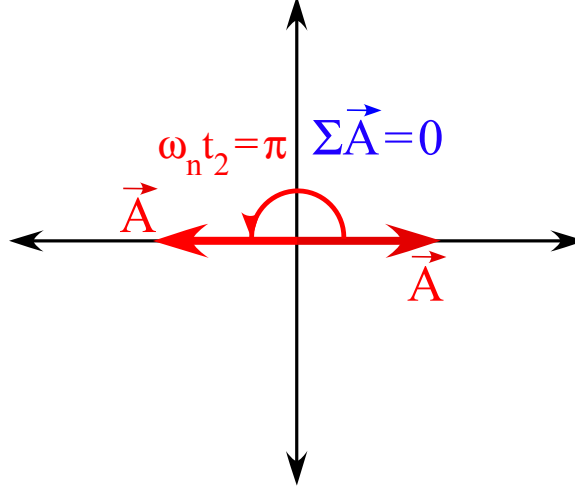
Figure 60: Vector diagram for a 2-Step (undamped ZV) input shaper.
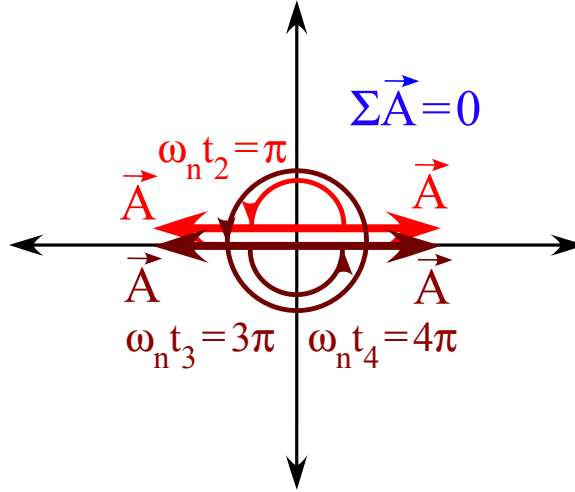
Figure 61: Vector diagram for a 4-Step impulse sequence.

times are:

$$\begin{bmatrix} t_i \end{bmatrix} = \begin{bmatrix} 0 & \frac{T_n}{2} & \frac{3T_n}{2} & 2T_n \end{bmatrix}. \tag{82}$$

Note that in actual implementation these stepping times must be rounded to the stepper motor's stepping period.

The fact that this step sequence suppresses vibration with period T_n can be seen using a vector diagram analysis (with $\omega_n = \frac{2\pi}{T_n}$), assuming unrounded stepping times. The vector diagram for the step sequence given by (82) is shown in Figure 61. Note that the vector magnitudes are equal to A here because the 4-Step shaper can be used as stepping sequences for a stepper motor with any step size.
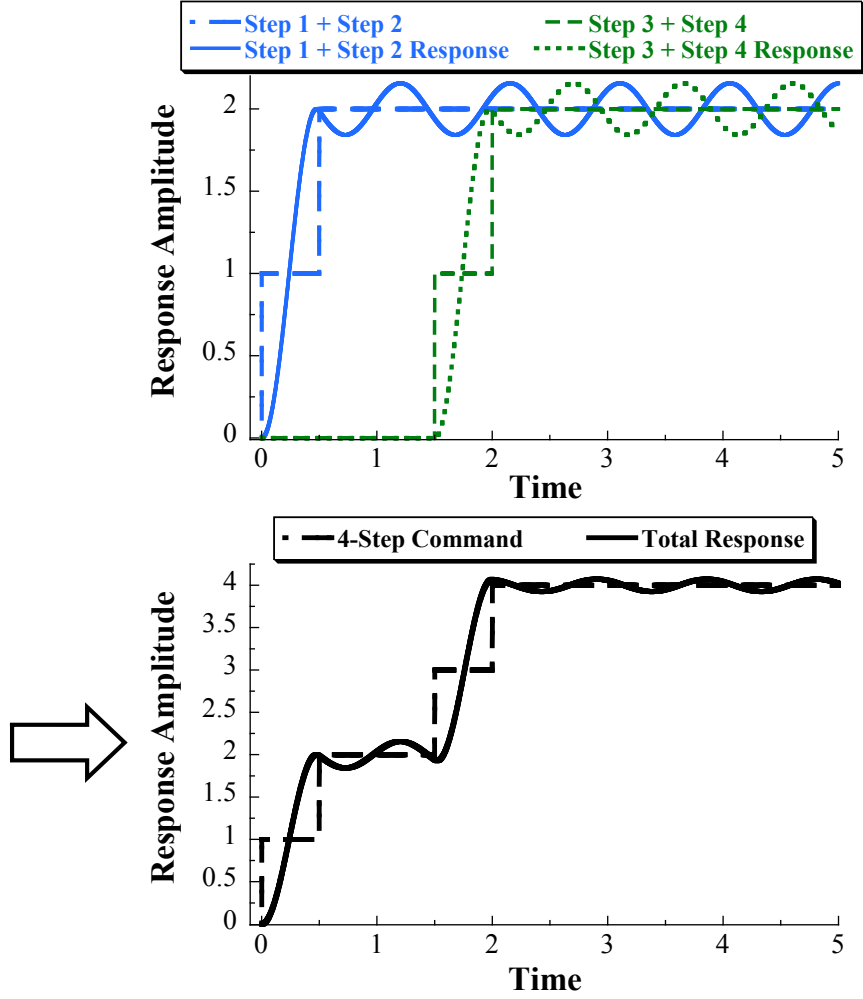
Figure 62: 4-step vibration cancellation when there is a frequency error of 5%.

The effectiveness of this stepping sequence at limiting vibration introduced by natural frequency modeling error is demonstrated in Figure 62 for a 5% frequency modeling error. In the top plot, a 2-Step command is applied to a flexible linear system. Due to the 5% frequency error, the vibration is not completely eliminated following the 2-Step command. A similar result would occur should an identical 2-Step command, representing steps 3 and 4 of the 4-Step sequence, be issued a short time later. The bottom of Figure 62 shows the response that would result if the command was the sum of both 2-Step commands. The responses to the two commands combine, and the residual vibration caused by the command is less than what would be caused by either of the individual 2-Step commands on their own.
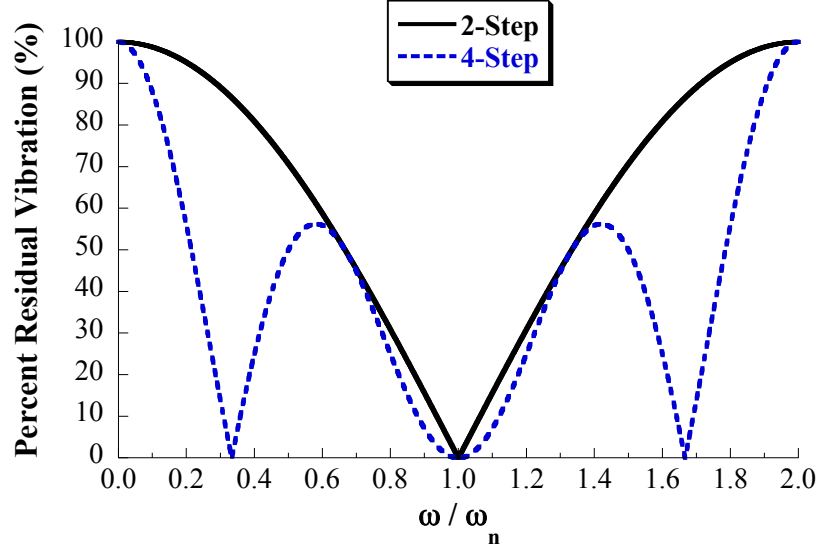
Figure 63: Comparison between sensitivity curves for 2-Step and 4-Step shaping sequences.

As is demonstrated in the time responses shown in Figure 62, the stepping sequence given by (82) provides additional robustness over the 2-Step sequence. Figure 63 shows sensitivity curves for the 2-Step and 4-Step sequences. Sensitivity curves are traditionally used to illustrate input shapers' robustness to error in the flexible mode natural frequency. The sensitivity curve plots the residual vibration (as a percentage of the vibration caused by a step command with magnitude equal to the total number of steps) given by (68) versus the actual frequency of the flexible mode. The 4-Step sensitivity curve is wider around the modeled frequency, $\frac{\omega}{\omega_n} = 1$. Note that these robustness predictions are theoretical in nature - effects such as nonlinearities and gyroscopic effects in spacecraft motions are not accounted for in (68), which is used to plot sensitivity curves.

The step sequence described by (82) is equivalent to convolving together two ZV input shapers, one with duration $T_n/2$ and the other with duration $\tau T_n/2$, where $\tau = 3$. Figure 64 shows the convolution process between two generic ZV shapers. The two shapers $\mathbf{ZV_1}$ and $\mathbf{ZV_2}$ shown have durations T_1 and T_2, respectively, and the shaper impulses have constant amplitude A. This convolution yields step sequence times of:

$$\left[\ t_i\ \right] = \left[\ 0\quad T_1\quad T_2\quad T_1 + T_2\ \right].$$

(83)

111
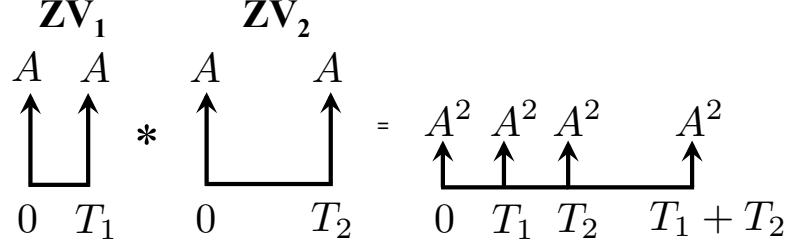
Figure 64: Convolution between two ZV shapers with constant amplitude impulses.

Letting $T_1 = T_n/2$ and $T_2 = \tau T_n/2$, the first ZV shaper targets the natural frequency through T_n while the parameter τ acts like a normalized period, or duration, for the second ZV shaper. These definitions may be used to re-parameterize the convolved ZV-ZV sequence given by (83) as:

$$\left[\begin{array}{c} t_i \end{array}\right] = \left[\begin{array}{cccc} 0 & \frac{T_n}{2} & \tau\frac{T_n}{2} & (\tau+1)\frac{T_n}{2} \end{array}\right]. \tag{84}$$

The value of τ can be varied to obtain an infinite number of 4-Step sequences with different durations and robustness characteristics. This allows the designer to select the overall duration of the shaper while still targeting a specific frequency for cancellation based on T_n. Note that letting $\tau = 3$ recovers (82).

Solutions with $\tau < 3$ have a shorter duration than the 4-Step sequence given in (82). In most cases, it is advantageous for the shaped sequence to be as short as possible, while still satisfying the robustness requirements. However, there are cases where the steps need to be further separated in time. This can be the case when slewing a flexible appendage on a spacecraft. Appendage slewing backdrives the main body of the spacecraft due to angular momentum conservation, causing a rigid body pointing error which must be corrected by the spacecraft attitude control system. By keeping the steps further separated, the attitude control system has time to correct the rigid body pointing error before the next step is taken. This is a case where the minimum time requirement of (70) is not as significant as other design requirements. The application of the input-shaped stepping sequences for slewing the flexible appendages of spacecraft is discussed further in Chapter VI. The input-shaped step sequences will be shown to reduce backdrivability by limiting vibration and allowing the attitude control system to more effectively correct the pointing error resulting from angular momentum conservation.

112

5.1.5 Robustness Study

One way of analyzing the robustness of a shaping sequence is the 5% insensitivity. This is defined as the frequency range containing the design frequency where the residual vibration is suppressed below 5% of the unshaped value. The 5% insensitivity for the 4-Step sequence in (84) for an undamped system as a function of τ is shown in Figure 65. Using $\tau = 3$ such as in (82) gives a 5% insensitivity of 0.167, while $\tau = 1$ is equivalent to a ZVD shaper.

The solutions that correspond to local maxima around these values, such as at $\tau = 0.753$, correspond to Extra-Insensitive (EI)-style shaping sequences. EI shapers have larger insensitivities to a specified amount of tolerable residual vibration V_{tol}, such as 5% [100, 104]. An example sensitivity curve for an EI input shaper is shown in Figure 66, along with the sensitivity curve for the 4-Step sequence with $\tau = 0.753$. The 5% insensitivities of the two shapers are labeled. While the 4-Step sequence has a wider insensitivity (0.47) than the standard undamped EI shaper for $V_{tol} = 5\%$ (0.40), the 4-Step sequence insensitivity range is not centered at the design frequency, as is the case for the standard EI shaper. However, this 4-Step sequence is 12.4% faster than the standard EI shaper. It also retains the advantage of being compatible with stepper motors because each impulse or step is kept equal. This trade-off comes at the cost of the off-centered insensitivity range. However, this
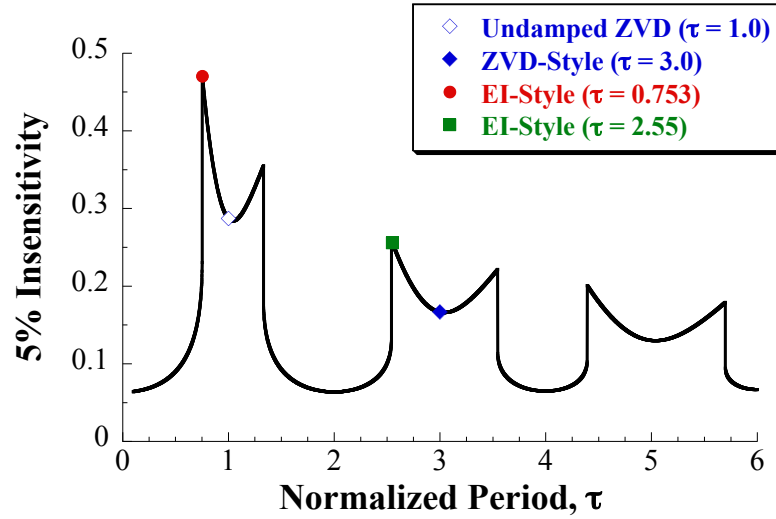
Figure 65: 4-Step sequence 5% insensitivity vs. normalized period for an undamped system.
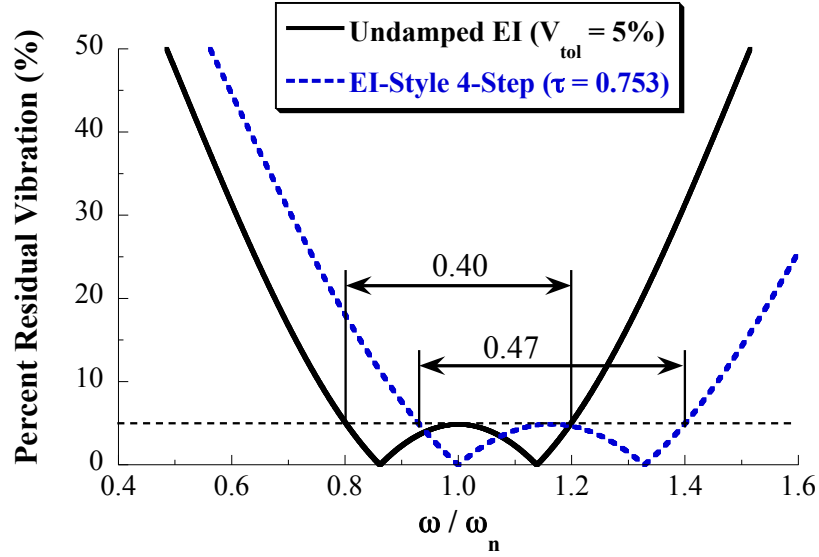
Figure 66: Sensitivity curve comparison for a standard undamped EI input shaper and an EI-style 4-Step sequence.

result can be advantageous if the designer has additional a priori information suggesting that the frequency is more likely to increase from the design value, such as from fuel burn-off or changing configurations of a robotic arm or spacecraft appendage.

Also, this result implies the shaper duration is selectable through the τ parameter. The step sequence timing can be configured to work together with a feedback controller to reduce backdrivability, assuming some loss of insensitivity is acceptable.

In cases where additional frequency modeling error bias may occur, these 4-Step sequences provide designers with options for accounting for this behavior. The example of an increase in frequency was discussed above, and there also may be design scenarios where the frequency may be more likely to decrease. The normalized frequency values where the sensitivity curve crosses the 5% residual vibration values, or the upper and lower boundaries of the 5% insensitivity range, as a function of the normalized period are shown in Figure 67. This is another useful way of representing the insensitivity values shown in Figure 65. However, this variation gives the designer insight into which choice of normalized period gives a 4-Step sequence most suitable for a predicted frequency modeling error range.

The shaped stepping sequence given by (84) can be further generalized as convolution of two ZV shapers. The convolution of two generic constant-amplitude ZV shapers was shown
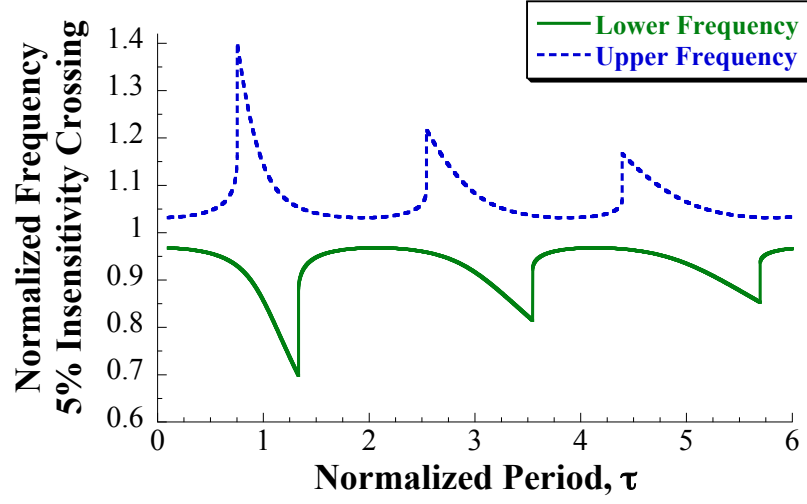
Figure 67: Upper and lower frequency values for the 5% insensitivity range for 4-Step sequences as a function of the normalized period.

in Figure 64. Introducing two normalized shaper duration parameters τ_1 and τ_2, the shaper durations can be defined as:

$$T_1 = \tau_1 \frac{T_n}{2} \tag{85a}$$

$$T_2 = \tau_2 \frac{T_n}{2} \tag{85b}$$

This defines the shaper durations as proportional to $T_n/2$ through the τ_1 and τ_2 parameters. Substituting the shaper durations (85a) and (85b) into (83) yields stepping sequence times of:

$$\begin{bmatrix} t_i \end{bmatrix} = \begin{bmatrix} 0 & \tau_1 \frac{T_n}{2} & \tau_2 \frac{T_n}{2} & (\tau_1 + \tau_2) \frac{T_n}{2} \end{bmatrix}. \tag{86}$$

When neither τ_1 and τ_2 are odd integers, the ZV shapers will not specifically target the natural frequency. However, due to the wider shape of the convolved sensitivity curves, the natural frequency may be included in the 5% insensitivity range for certain values of τ_1 and τ_2. Letting $\tau_1 = \tau$ and $\tau_2 = 1$ yields the normalized sequence in (84).

Figure 68 shows the 5% insensitivity for the generalized 4-Step sequence in (86) for an undamped system with period T_n as a function of the normalized shaper durations τ_1 and τ_2. The insensitivity is zero when the frequency range with $\leq 5\%$ residual vibration does not include the natural frequency ω_n, and these regions of zero insensitivity can be seen in

115
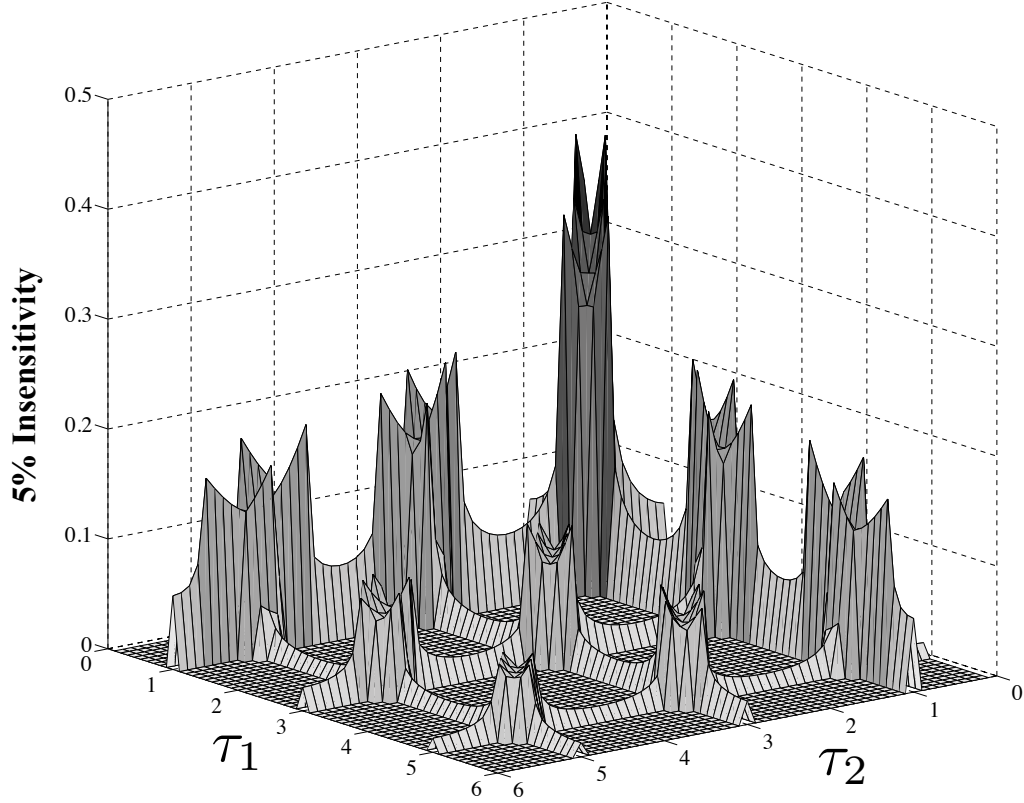
Figure 68: 4-Step sequence 5% insensitivity vs. normalized shaper durations τ_1 and τ_2 for an undamped system with period T_n.

the plot. On the other hand, certain values of τ_1 and τ_2 yield 4-Step shapers with larger insensitivity similar to Figure 65. These regions occur when τ_1 or τ_2 are approximately (but not necessarily strictly equal to) an odd integer, and the insensitivity is highest when both τ_1 or τ_2 are close to odd integers. The results shown in Figure 65 are captured here, and can be obtained by slicing the surface along $\tau_2 = 1$ and letting $\tau_1 = \tau$.

5.2 Residual Vibration of Constant-Amplitude Input Shapers Combined with Underdamped PD Controllers

Choosing control gains for a constant-amplitude input shaper combined with a PD controller requires a shift from traditional PD controller design methodology. A previous concurrent design approach for a single mass system under input-shaped PD control used optimization to pick the best combination of PD control gains and input shaper parameters subject to constraints on overshoot and actuator effort [52]. However, in that paper, the amplitude of the input shaper impulses were allowed to vary. When the additional constraint of constant

116

amplitudes is introduced along with damping through the derivative gain, the residual vibration generally cannot be completely eliminated.

To illustrate this, consider PD position control of a single mass. The closed-loop transfer function is [52]:

$$\frac{X(s)}{U(s)} = \frac{K_D s + K_P}{ms^2 + K_D s + K_P}. \tag{87}$$

Figure 69 shows the input-shaped step response of (87) for one set of system parameters, where the input shaper is a 2-Step ZV shaper with constant amplitudes. The first step begins to move the mass but results in some overshoot in the underdamped closed-loop system. The second step has the correct amplitude to cancel undamped vibration caused by the first step. However, the vibration has already begun to decay due to the damping effect from the derivative gain. The second step cancels this vibration but also causes some extra vibration that cannot be eliminated. Even the addition of more steps would have no benefit due to the constant amplitude constraint. This effect of causing extra, noncancelable vibration would continue with any additional steps.

The magnitude of this effect depends on the damping ratio, which in this case is a function of the derivative gain relative to the mass and proportional gain. Figure 70 shows
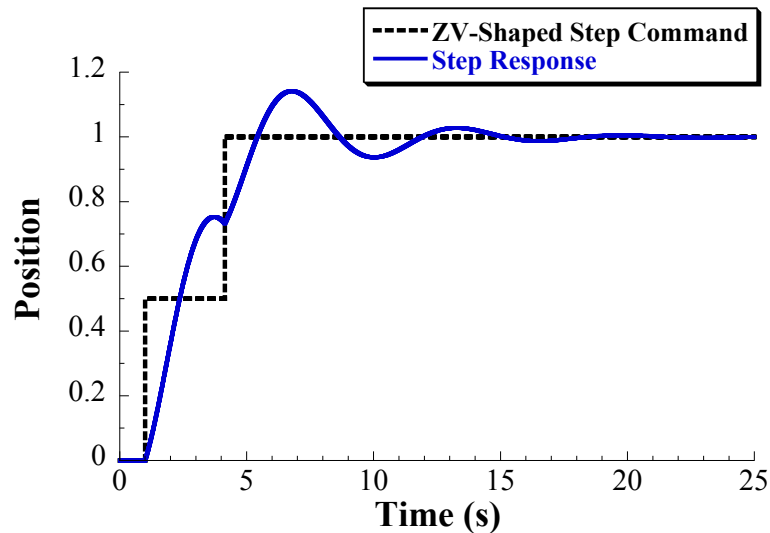
Figure 69: Step response of a mass under PD control with a constant amplitude ZV shaper ($m = 1$, $K_P = 1$, $K_D = 0.5$).
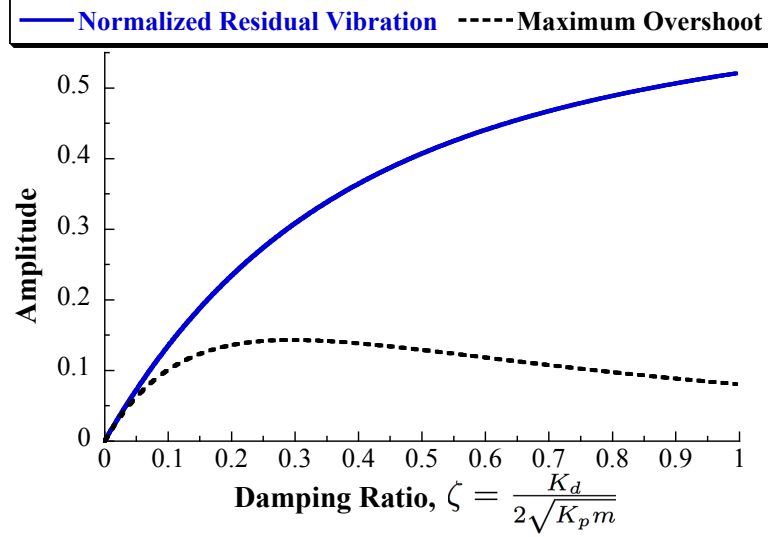
Figure 70: Effect of derivative gain damping on the residual vibration and maximum overshoot caused by a constant-amplitude 2-Step input shaper for PD control of a mass (for $m = 1$, $K_P = 1$).

the normalized residual vibration and maximum overshoot resulting from a constant amplitude 2-Step input shaper applied to the mass under PD control for a range of damping ratios. The normalized residual vibration is defined as the amount of vibration caused by the 2-Step command at the time of the second step normalized by the vibration caused by taking both steps at the same instant (*i.e.*, as an unshaped single step). The maximum overshoot amplitude is calculated for a 2-Step command with total amplitude of 1. For an undamped system, there is zero residual vibration because the 2-Step sequence is identical to an undamped ZV shaper and satisfies the zero residual vibration constraints for the system.

The residual vibration amplitude increases as the damping ratio increases. This occurs because the vibration caused by the first step decays more rapidly, and the second step introduces a relatively large amount of excess, noncancelable vibration as the damping ratio increases. The maximum overshoot illustrates that increased residual vibration is balanced by increased exponential decay as the damping increases. Also, the overshoot is small for low damping ratios where the constant amplitude input shaper is working most effectively. For damping ratios approaching 1, the system still exhibits some overshoot due to the transient numerator dynamics in (87).

This effect suggests that the proposed constant-amplitude input shaper may be most effective when combined with a PD controller with relatively low derivative gains. Any increase in overshoot that would otherwise be caused by lowering the derivative gain would be prevented by residual vibration suppression from the input shaper. However, the behavior of the closed-loop poles of backdrivable systems such as (44) and (45) as a function of the proportional and derivative gains is more complicated than for a single mass under PD control. Understanding the behavior of closed-loop modes, such as was presented in Section 4.2.1.2, can inform the controller gain selection and constant-amplitude input shaper design for the closed-loop system.

5.3 Summary

This chapter presented a method for designing constant-amplitude input shapers using vector diagrams. The constant-amplitude input shapers also have selectable duration, specified based on the τ parameter in (84). The resulting shaper's robustness to frequency error varies depending on this parameter. These constant-amplitude input shapers can be applied to design constant-amplitude stepping sequences, which can be useful for stepper motors that drive flexible elements such as the appendages of spacecraft. Chapter VI illustrates this through a demonstrative application involving a flexible spacecraft. The 4-Step shaper is used to design stepping sequences to slew the stepper motor-driven flexible appendages of a spacecraft while also limiting backdriving effects on the main spacecraft body.

CHAPTER VI

DEMONSTRATIVE APPLICATION: SPACECRAFT FLEXIBLE APPENDAGE STEPPER MOTOR CONTROL

Many spacecraft use stepper motors to slew flexible appendages, such as observation or transmitting equipment and solar arrays. An example of a flexible spacecraft is shown in Figure 71. The vibration of the flexible appendages such as solar arrays and reflectors can cause backdriving disturbance torques on the main spacecraft body (or bus) that result in spacecraft pointing error. Pointing error arises from the rigid-body response of the spacecraft due to conservation of angular momentum as the appendages are slewed and any vibration of the flexible appendages that acts to backdrive the bus. Limiting pointing error is critical when the spacecraft must keep observation or transmitting equipment pointed in the correct direction. For example, for a spacecraft in a circular geosynchronous orbit observing or transmitting to a location on the Earth, 0.1 degrees of bus pointing error corresponds to approximately 62 km of error on Earth's surface. Because the appendages are driven by stepper motors, angular position commands are discretized in amplitude and time (based on maximum stepping rate), which can increase the control complexity.

In the case of solar arrays, the arrays are often moved slowly to track the Sun during orbit. For example, on a spacecraft in a geosynchronous orbit the solar arrays need only be slewed at an average rate of 15 degrees per hour, and very few steps may be taken at any one time depending on the design of the appendage actuator. This makes design of short-distance stepping sequences important. This differs from the focus on a stepping rate that exists in other stepper motor command generation problems.

An additional concern is that the vibration control techniques used on spacecraft should be robust to modeling error or uncertainty in the natural frequencies of vibration of the appendages. Input shaping techniques designed for flexible spacecraft applications include designing fuel-efficient thruster commands [102, 129] and deflection-limiting commands that
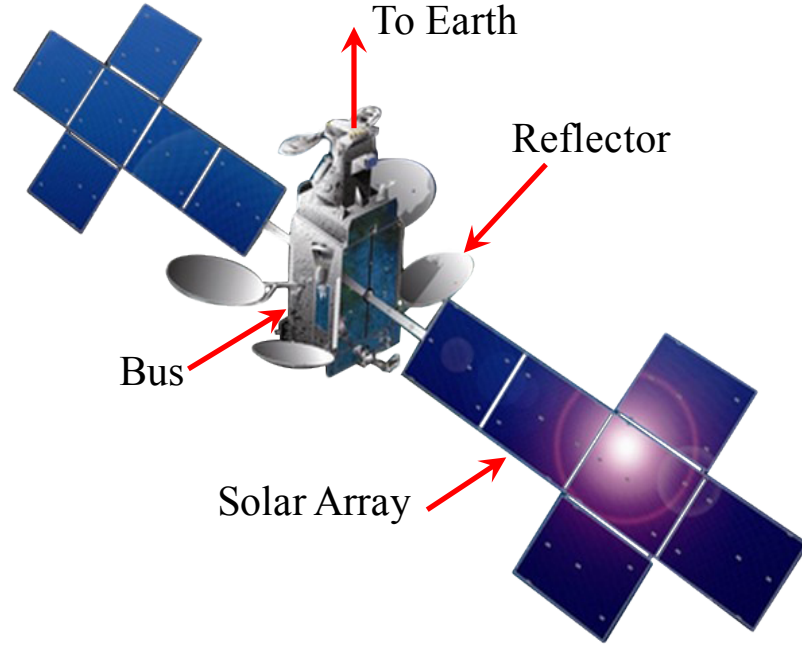
Figure 71: Spacecraft with flexible appendages[1].

limit transient deflection in addition to eliminating residual vibration [8, 82, 107]. Input smoothing methods have been used to develop shaped angular acceleration profiles for flexible spacecraft attitude maneuvers [42]. Adaptive input shaping for spacecraft flexible appendages has also been studied to address cases where significant appendage configuration changes are expected [18, 19]. These two papers assume strain gauges or other sensors are available to measure the vibratory response so that the controller may update the ZV shaper impulses.

Some current techniques for stepper motors use vibration-limiting stepping profiles with characteristics similar to ZV input shaping [10, 51, 76] , however they are not very robust to modeling error or uncertainty in the natural frequencies of vibration of the appendages. Doherty and Tolson [26] used input shaping techniques to develop robust, multi-mode stepping profiles. Their technique splits each impulse into a stepping rate command, with the duration proportional to the amplitude of the impulse. This is an effective approach for cases where hundreds of steps need to be taken. Use of the robust 4-Step constant-amplitude input

---

[1]Image Source: SSL. (2014). "DIRECTV 14", Date Accessed: March 5, 2014, Available: `http://sslmda.com/html/satexp/directv14.html`.

shapers developed in Chapter V can provide increased robustness to appendage frequency modeling errors for short-distance slewing maneuvers, while also reducing backdriving effects on the bus.

This chapter investigates attitude control and appendage stepping for a spacecraft with one flexible appendage driven by a stepper motor. Station-keeping and planar motion are considered, and the Rotary Hub with Flexible Appendage fundamental model serves as a dynamic model of the spacecraft and appendage. The constant-amplitude input shapers developed in Chapter V are used to generate appendage stepping commands, and their performance at reducing backdrivability is demonstrated and evaluated.

6.1 Attitude PD Controller Combined with Constant-Amplitude Input Shaping

Most spacecraft utilize an attitude control system to regulate the bus angle and reduce pointing error. For this chapter, the simple PD controller presented in Section 4.2.1 is applied to study and control the planar backdriving dynamics of a spacecraft with a flexible appendage. The model parameters are $m_1 = 5,000$ kg, $L_1 = 1$ m, $m_2 = 100$ kg, $L_2 = 5$ m, and $k = 5,000$ N-m/rad, which were the same used previously in Chapter IV.

A block diagram of the controller is shown in Figure 72. The Attitude PD Controller acts on the error between the reference attitude and the current attitude, producing a command that acts on the spacecraft via the torque T. An Appendage Command Generator produces the stepping command θ_d for the flexible appendage stepper motor. This model assumes perfect measurement of the bus angular states (θ_1 and $\dot{\theta}_1$), and the feedback controller does
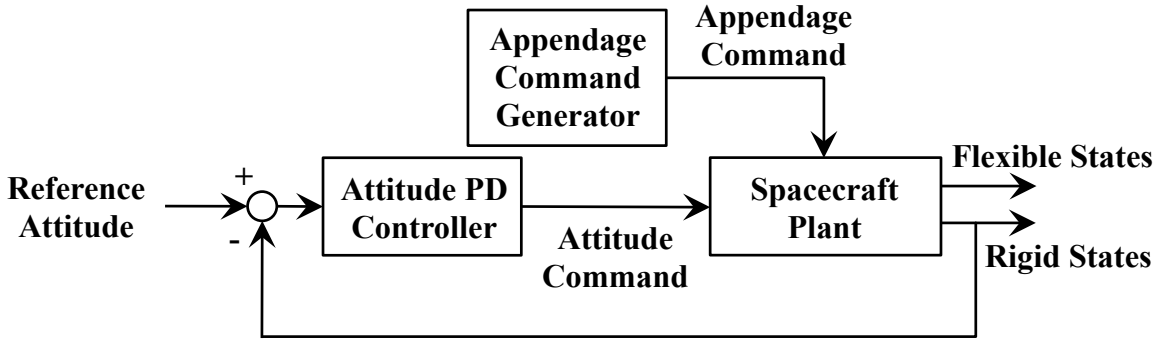
Figure 72: Block diagram of the flexible spacecraft attitude control system.

not utilize measurement of the flexible appendage states (θ_2 and $\dot{\theta}_2$). For the purposes of this chapter, the spacecraft is in a station-keeping mode and the reference attitude is zero.

The modal behavior of the closed-loop Rotary Hub with Flexible Appendage model with PD controller was studied in Section 4.2.1.2. Understanding the modal behavior is critical for the purposes of combined the constant-amplitude input shapers presented in Chapter V with a PD feedback controller used to control the spacecraft attitude. The bifurcation or transition behavior between ranges with two underdamped modes and one underdamped mode with an overdamped mode should be accounted for during input shaper design. The trends in the damping behavior of the two modes is also significant and can pose challenges for constant-amplitude input shapers. The 4-Step input shaper is designed to target a single underdamped mode.

Also, as was shown in Section 5.2, constant-amplitude shapers cannot completely eliminate the residual vibration of systems with damping ratios greater than zero, and this effect worsens as the damping ratio increases. Therefore, when combined with the attitude PD controller, the constant-amplitude input shapers presented in Chapter V work most effectively with controller gains where the damping ratios of any underdamped modes are smallest. It also may be advantageous to select controller gains that give only a single underdamped mode; however, this should be balanced with controller gains that give modes with low damping ratios. The effectiveness of the 4-Step constant-amplitude input shaper combined with the attitude PD controller for a variety of controller gains is evaluated in the next section.

6.2   Results

6.2.1   Performance Evaluation of Combined PD Controller and Constant Amplitude 4-Step Input Shaper

In this section, the 4-Step constant-amplitude input shaper developed in Chapter V is combined with the attitude PD controller and spacecraft model discussed in Sections 4.2.1 and 6.1. Simulations are used to compare the combined input shaping and PD controller to unshaped PD control alone, and to evaluate the behavior and performance of the combined controller for a variety of control parameters. Results are shown for illustrative controller

gains selected based on the analysis in Section 4.2.1.2. For each case, the command is a 1 degree step in the appendage angle, such as may be implemented using stepper motors. Unshaped and 4-Step shaper results are shown for each case, with the 4 steps for the unshaped command taken all at once. The 4-Step input shaper is designed for the closed-loop mode with the slowest frequency with $\tau = 0.753$, assuming that the controller and system parameters are known precisely to facilitate fair comparison of different controller gain pairs. The normalized shaper duration of $\tau = 0.753$ is chosen for evaluation here because it gives the largest/widest 5% insensitivity as was shown in Figure 65.

The first illustrative results use $K_P = 3700$ and $K_D = 4000$. The flexible spacecraft response to the unshaped and 4-Step shaped appendage commands is shown in Figure 73. The unshaped command moves the appendage to the 1 deg. setpoint more quickly, but the peak amplitude of bus response is four times as large. The bus also has a longer settling time. There is clear two-underdamped-mode behavior, with the higher mode being most noticeable in the unshaped bus response. While both modes have a similar damping ratio, as was shown in Figure 41, the higher mode decays more quickly. The peak bus response amplitude with the 4-Step shaper is 0.12 degrees at 2.20 s.
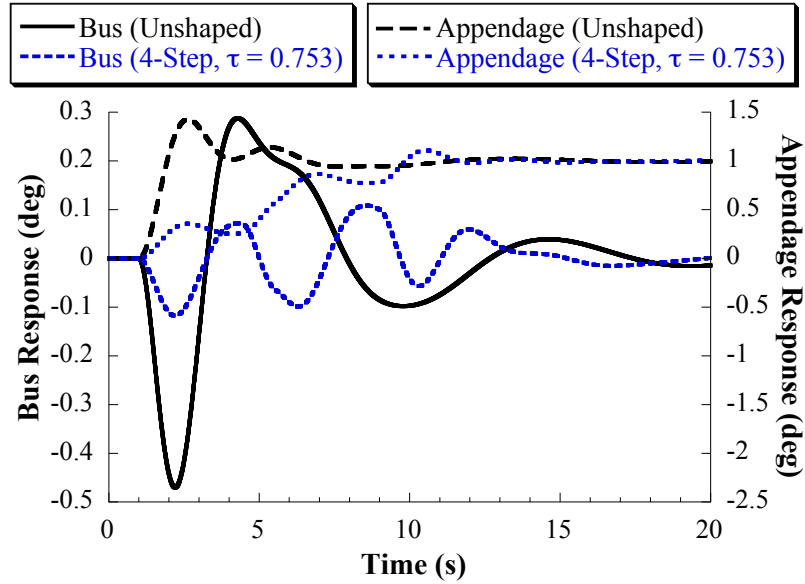
Figure 73: Flexible spacecraft response with attitude PD controller and constant amplitude shaping for $K_P = 3,700$ and $K_D = 4,000$.

The second illustrative results also use $K_P = 3{,}700$ with K_D increased to 8,800. The flexible unshaped and shaped spacecraft responses with these gains are shown in Figure 74. Both unshaped and shaped responses have low bus and appendage settling times. Again, the unshaped command moves the appendage more quickly but causes a larger peak amplitude in the bus response. This is just beyond one of the transition points identified in Figure 41, so a single underdamped mode dominates the response. This derivative gain is high enough for one mode to be overdamped yet still low enough for the underdamped mode to have a higher damping ratio and thus a small settling time. The peak bus response amplitude with the 4-Step shaper is 0.08 degrees at 4.47 s.

The third illustrative results continue to use $K_P = 3{,}700$ with K_D increased further to 20,000. Based on the modal analysis, for these gains the underdamped mode should have significantly lower damping. The flexible unshaped and shaped spacecraft responses with these gains are shown in Figure 75. The unshaped response illustrates the low damping and long settling time of the underdamped mode. However, the shaped response has significantly lower overshoot and appears to settle more quickly. This behavior occurs because the constant-amplitude input shaper is effective at targeting the low-damping underdamped
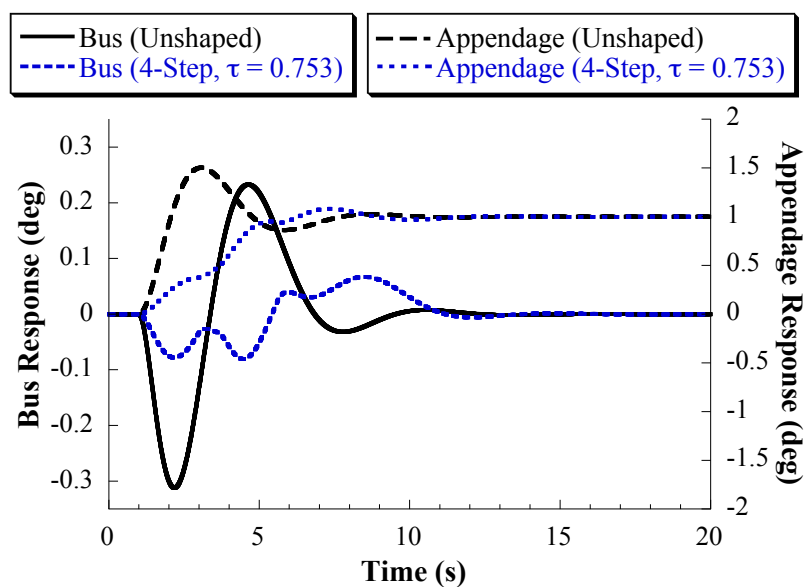
Figure 74: Flexible spacecraft response with attitude PD controller and constant amplitude shaping for $K_P = 3{,}700$ and $K_D = 8{,}800$.

125
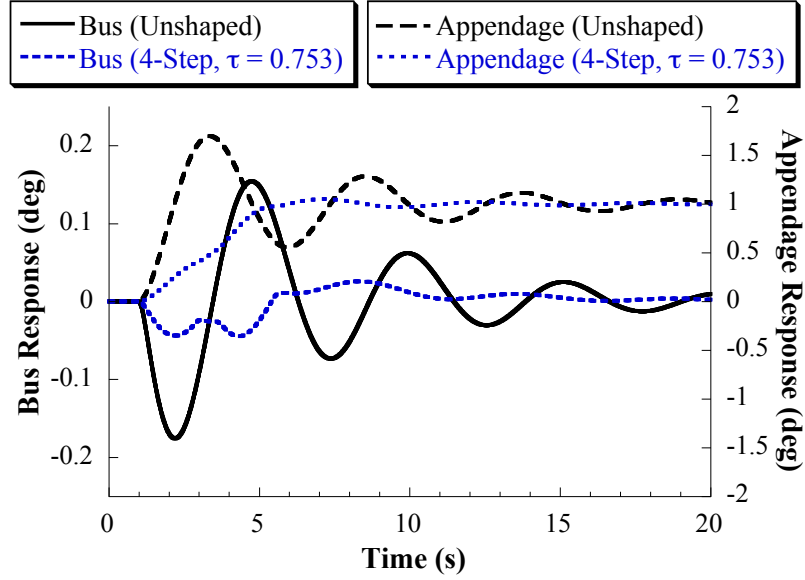
Figure 75: Flexible spacecraft response with attitude PD controller and constant amplitude shaping for $K_P = 3{,}700$ and $K_D = 20{,}000$.

mode. For this set of gains, the constant amplitude input shaping gives favorable results relative to the unshaped case. The peak bus response amplitude with the 4-Step shaper is 0.045 degrees at 4.32 s.

The fourth illustrative results now use a lower proportional gain of $K_P = 2{,}000$ for the same derivative gain from the second case, $K_D = 8{,}800$. Based on the modal analysis in Figure 40, there should be a single underdamped mode with slightly less damping than in the second case. The unshaped and shaped responses are shown in Figure 76. The peak bus response amplitude with the 4-Step shaper is 0.11 degrees at 4.17 s. The responses are not significantly different from the second case, however the bus response has a larger amplitude. This is most apparent in the shaped bus response around 4 s, where the amplitude is approximately 36% larger.

The final illustrative results examine a larger proportional gain of $K_P = 20{,}000$ for the same derivative gain from the second and fourth cases, $K_D = 8{,}800$. Based on the modal analysis in Figure 40, there should be two underdamped modes, with the lower frequency mode having a much lower damping ratio. The unshaped and shaped responses are shown in Figure 77. The unshaped response illustrates the low damping and long settling time of
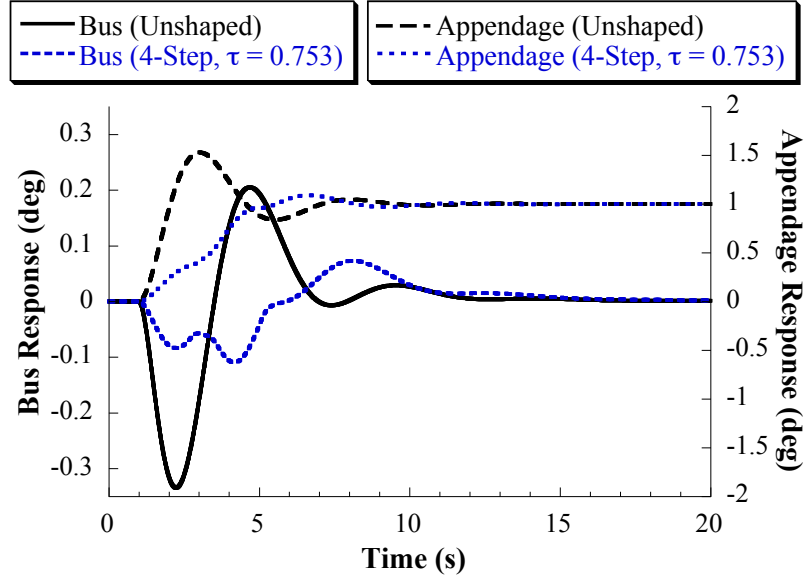
Figure 76: Flexible spacecraft response with attitude PD controller and constant amplitude shaping for $K_P = 2{,}000$ and $K_D = 8{,}800$.
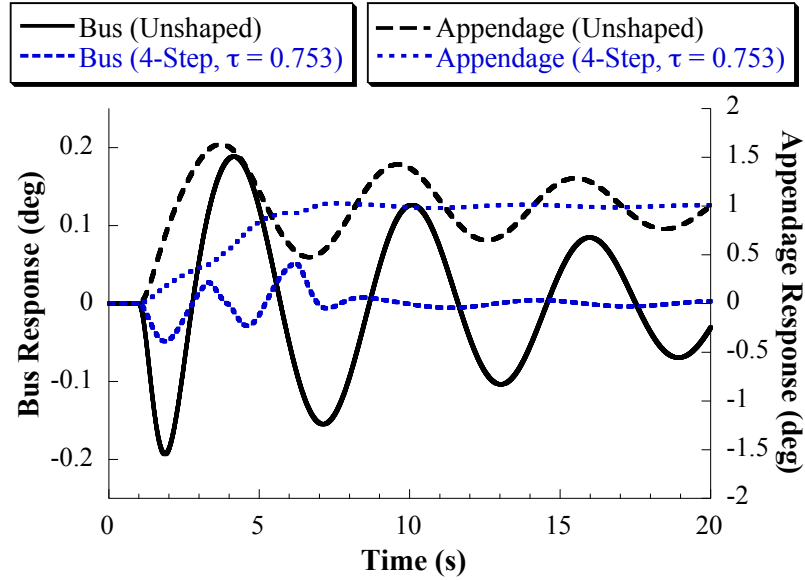
Figure 77: Flexible spacecraft response with attitude PD controller and constant amplitude shaping for $K_P = 20{,}000$ and $K_D = 8{,}800$.

the lower underdamped mode. The second mode is not apparent in the unshaped response due to its higher damping ratio. The shaped response has significantly lower overshoot and both the bus and appendage settle more quickly. As with the third illustrative case, this behavior occurs because the constant-amplitude input shaper is effective at targeting the

low-damping underdamped mode. The only residual behavior that remains is that of the second mode, which has relatively little impact because it is much more damped and has a higher frequency. The peak bus response amplitude with the 4-Step shaper is 0.052 degrees at 6.20 s. This is another example of gain pairs where the constant amplitude input shaping gives favorable results relative to the unshaped case.

An obvious advantage of the 4-Step sequence is that it can be easily calculated for any vibration period using (82). The designer does not need to solve an optimization problem to find the appropriate stepping sequence. However, it does not specifically target any other vibratory modes, and may not provide as much robustness as could be obtained from using a solution found using optimization. Also, it is designed sequentially, rather than concurrently, with the attitude PD controller. This requires the designer to have a detailed understanding of the modal behavior of the closed-loop system, as was illustrated in Section 4.2.1.2. With the objective of reducing pointing error, the case shown in Figure 75 for $K_P = 3,700$ and $K_D = 20,000$ yields the best response.

6.2.2 Effect of Constant-Amplitude Input Shaper Duration on Bus Response Amplitude

The results in the previous section all used $\tau = 0.753$ for the 4-Step constant-amplitude shaper. This section examines the effect of varying the 4-Step shaper duration on the peak amplitude of the bus response. In essence, with the goal of reducing the backdriving effect on the bus angle to limit point error, the shaper duration can be varied through the τ parameter to give the controller more time to correct any error before taking subsequent steps.

An example where this occurs is the case that was shown in Figure 76 with $K_P = 2,000$ and $K_D = 8,800$. The bus response reaches two local minima between 2 and 5 seconds, with the second having a larger amplitude. This happens because the stepping sequence is not giving the attitude controller enough time to correct the initial bus pointing error. This effect can be reduced by increasing the length of the shaper to give the attitude controller more time to respond.

To demonstrate this, Figure 78 compares the response with those same controller gains
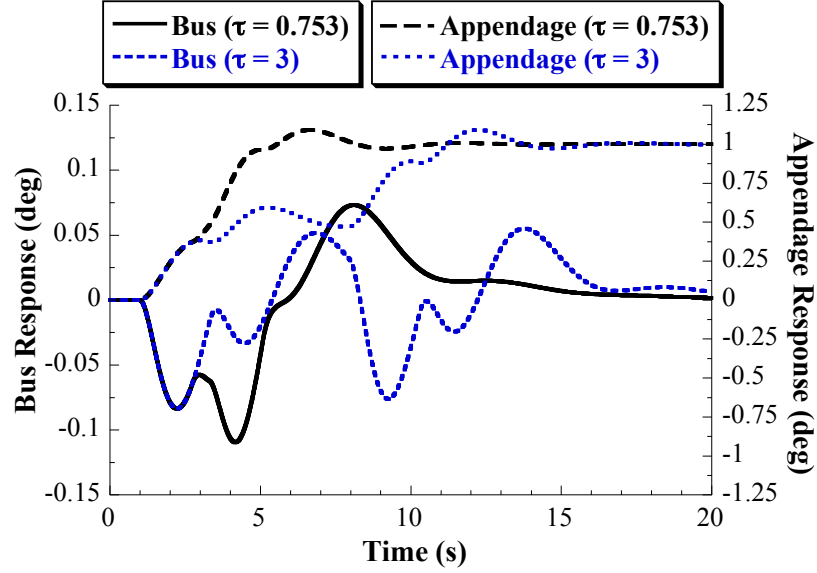
Figure 78: Flexible spacecraft response with attitude PD controller and constant amplitude shaping for $K_P = 2,000$ and $K_D = 8,800$ with $\tau = 0.753$ and $\tau = 3$.

between using $\tau = 0.753$ and $\tau = 3$ to design the 4-Step shaper. For $\tau = 3$, the peak bus response amplitude is 0.084 degrees at 2.24 s, or a 31% reduction from using $\tau = 0.753$. This comes at the cost of slowing down the appendage stepping duration, but does not require changing the controller gains.

To fully explore the effect of the 4-Step shaper duration on peak bus response amplitude, Figure 79 shows the peak bus response amplitude as a function of the normalized duration τ of the 4-Step shaper for $K_P = 2,000$ and $K_D = 8,800$. At low τ, the amplitude is largest because the steps are taken quickly with the attitude controller having little time to correct the pointing error. At larger τ, the attitude controller has enough time between pairs of steps to correct the pointing error, and the amplitude reaches a minimum where further increases in stepping duration do not provide any benefit. Between approximately $\tau = 0.5$ and 1.5, the behavior is more interesting. There is a local minimum at $\tau = 0.6$, then the amplitude increases before dropping to the minimum at $\tau = 1.43$.

To illustrate the behavior with these different durations, Figure 80 compares the time response using the 4-Step shaper with $\tau = 0.753$ and $\tau = 0.6$. The peak bus response amplitude is 0.096 degrees at 3.91 s. This is only a 14% reduction from using $\tau = 0.753$,
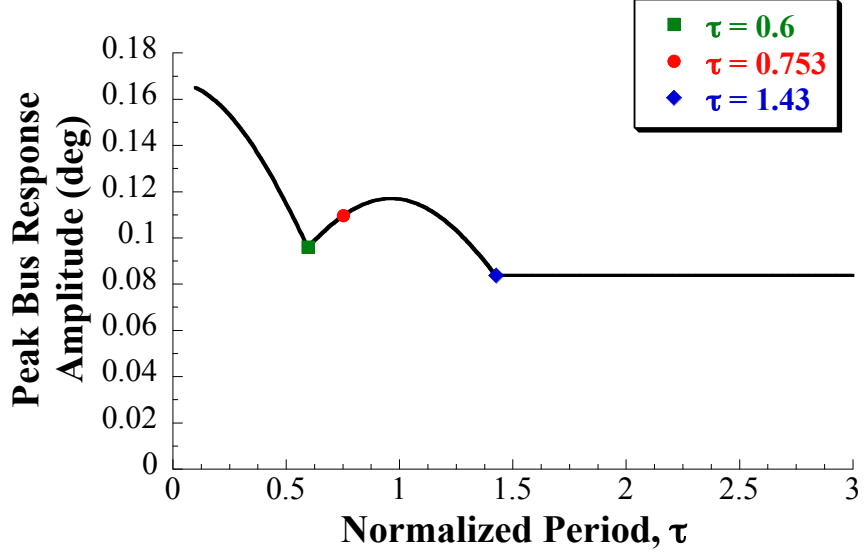
Figure 79: Peak bus response amplitude as a function of the 4-Step shaper normalized duration.
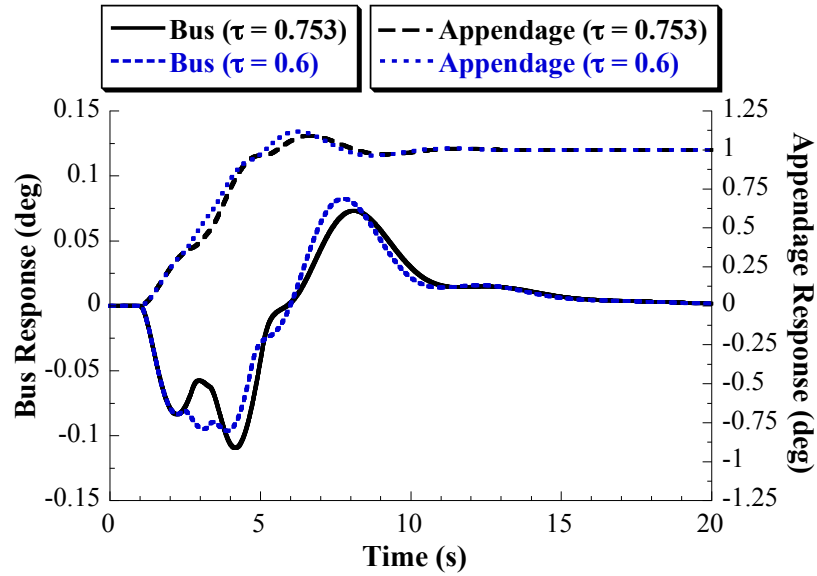
Figure 80: Flexible spacecraft response with attitude PD controller and constant amplitude shaping for $K_P = 2,000$ and $K_D = 8,800$ with $\tau = 0.753$ and $\tau = 0.6$.

but it also comes with the benefit of a faster appendage stepping time.

Figure 81 compares the time response using the 4-Step shaper with $\tau = 0.753$ and $\tau = 1.43$. The peak bus response amplitude is 0.084 degrees at 2.24 s for a 31% reduction from $\tau = 0.753$, or the same as with $\tau = 3$. However, this stepping sequence is 63% faster than the sequence using $\tau = 3$.
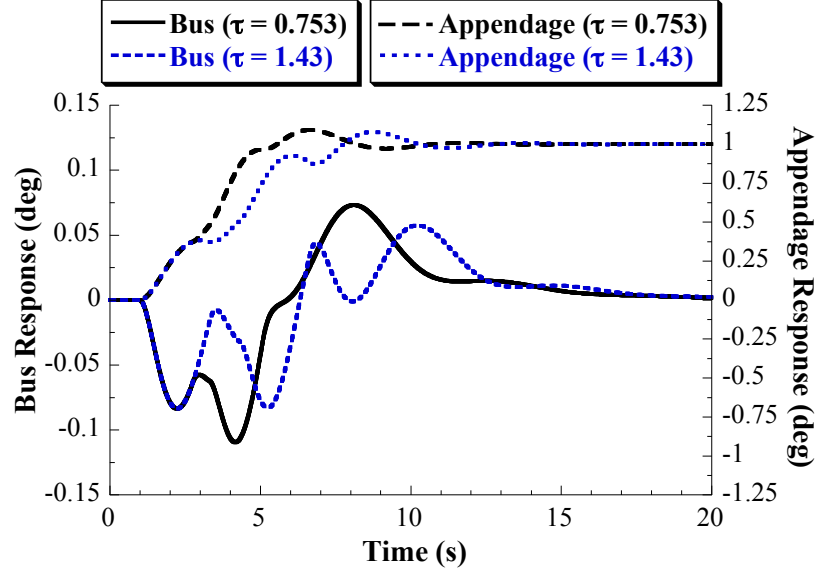
Figure 81: Flexible spacecraft response with attitude PD controller and constant amplitude shaping for $K_P = 2{,}000$ and $K_D = 8{,}800$ with $\tau = 0.753$ and $\tau = 1.43$.

The designer can choose $\tau = 0.6$ if they are willing to sacrifice some peak amplitude for a faster shaper duration, or choose to minimize the peak amplitude at the minimum duration of $\tau = 1.43$. However, Figure 65 shows that choosing either of these durations comes at the cost of robustness to frequency error in the form of the 5% insensitivity. At these τ, the 4-Step shaper loses most of its robustness gains over a standard ZV or 2-Step shaper. Similar behavior and results can be obtained for other combinations of controller gains.

6.2.3 Discussion

The results that were shown in Section 6.2.1 for various gains and the concurrent design optimization in Section 4.3 show that the bus response is reduced as the derivative gain is increased. A large derivative gain should be selected because this yields a lower damping ratio according to the modal analysis in Section 4.2.1.2. The constant-amplitude shapers limit oscillation most effectively when there is a single underdamped mode with a closed-loop damping ratio as low as possible. However, in the presence of actuator limits or other concerns that may limit gain selection, the constant-amplitude shaper duration can be increased to achieve the minimum bus response possible with the selected controller gains.

6.3 Summary

This chapter considered a flexible spacecraft as a demonstrative application that shows the importance of understanding backdrivable flexible systems, and to illustrate how the methods presented in this thesis can be applied to improve performance of a base experiencing backdriving effects. The Rotary Hub with Flexible Arm fundamental model was used as a model of a planar spacecraft with one flexible appendage. The performance of the 4-Step constant-amplitude input-shaping technique for stepper motors developed in Chapter V was investigated using the flexible spacecraft model. Also, the modal behavior of the PD hub angle controller studied in Section 4.2.1 was analyzed to inform the design of constant-amplitude input shapers and assist with gain selection for attitude control of the flexible spacecraft. It was shown that the 4-Step technique limits vibration most effectively for PD controller gain values that would otherwise lead to poor settling times and large overshoot. Also, the selectable duration of the 4-Step constant-amplitude shapers can be leveraged to design stepping sequences that reduce the peak bus pointing error.

DEMONSTRATIVE APPLICATION: INPUT-SHAPING AND MODEL-FOLLOWING CONTROL OF HELICOPTERS WITH SUSPENDED LOADS[1,2]

When a heavy load is suspended from a helicopter, excessive load swing degrades helicopter control due to backdriving effects. This chapter examines the benefits of combining input shaping and Model-Following Control (MFC) to improve performance when carrying a suspended load.

MFC architectures are used in modern helicopter flight control systems to make the helicopter respond like a prescribed model. For example, the Boeing Company used a control law architecture consisting of model-following control on several programs in the 1980's and 1990's, including the V-22 and RAH-66 [55]. On its own, MFC can be ineffective when carrying a suspended load because excessive load swing degrades tracking of the prescribed model dynamics and thus control of the helicopter. Therefore, reducing load swing improves tracking of the prescribed model and increases safety and productivity. By combining input shaping with MFC, helicopter payload swing is reduced and tracking of the prescribed model is improved.

The effectiveness of input shaping at suppressing suspended load oscillation is demonstrated using experimental results from model radio-controlled helicopter testbed. Then, the design of an attitude-command flight control system that combines input shaping and MFC is illustrated using dynamic models of a Sikorsky S-61 helicopter. Simulation results

---

(a) Helicopter delivering cargo to a remote base camp location[3].

(b) Helicopter delivering supplies to a stranded cruise ship[4].

Figure 82: Helicopters shown carrying suspended loads and delivering supplies and cargo to remote areas.

are shown for lateral and longitudinal repositioning movements. These results show that applying input shaping to simulated pilot commands greatly improves helicopter performance when carrying a suspended load.

7.1 Background

A helicopter can be used as a "flying crane" by hanging a load (often called a *suspended load* or *sling load*) from cables attached to the helicopter. A flying crane is extremely versatile, and photographs of some example applications are shown in Figure 82. It can be used to transport timber during remote logging operations, deliver power transmission towers to their installation locations, deliver equipement to remote camps such as shown in Figure 82(a), rescue people stranded in otherwise inaccessible areas, and even deliver food and supplies to disabled cruise ships, as shown in Figure 82(b). These are just a few examples of tasks that are too expensive, too slow, or physically impossible to perform with

---

[3]Photo Credit: Captain Budd Christman, NOAA Corps, "Bell UH-1H N56RF at Cape Douglas sling-loading camp equipment for shore camp.," National Oceanic and Atmospheric Administration. Flying with NOAA Collection, Image ID: fly00518. Available: https://www.photolib.noaa.gov/htmls/fly00518.htm.

[4]Photo Source: Gregory Bull. "Navy helicopter drops supplies onto the Carnival Splendor off Mexico's Baja Peninsula," Associated Press, 11 November 2010. Appears in: Gene Sloan, "On disabled cruise ship, a 'nightmare'," USA Today, page FA.
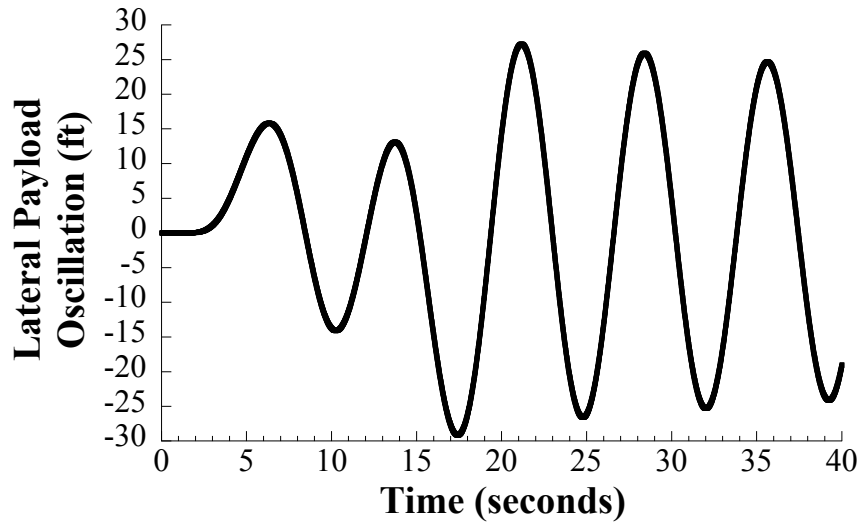
Figure 83: Lateral load oscillation caused by a lateral helicopter move.

other types of vehicles.

Unfortunately, the suspended load is a swinging pendulum that adversely affects control of the helicopter due to backdriving effects. This makes efficient and accurate transfer of the load difficult. In fact, accidents can be caused by violent suspended load swing [122]. The helicopter becomes particularly difficult to control when carrying heavy loads [39].

Figure 83 shows the lateral load oscillation during and following a simulated near-hover lateral move performed by a helicopter carrying a heavy suspended load. The load oscillates with a large amplitude and slow period. The load suspension point is below the helicopter's center of gravity, so the tension in the suspension cable produces an oscillating torque about the helicopter's center of gravity as the load swings. This is a backdriving effect known as load-attitude coupling.

A plot of the pilot's attitude command and the resulting helicopter roll attitude during and following the lateral move is shown in Figure 84. Due to load-attitude coupling, the load swing causes residual roll attitude oscillations that have an amplitude of nearly 2 degrees. Residual attitude oscillations larger than 0.5 degrees are considered excessive for any type of maneuver [124]. This attitude backdriving makes the helicopter difficult to control, and the load swing slows down load transfer operations.

Guidelines for suspended load operations suggest that the best way for a pilot to regain
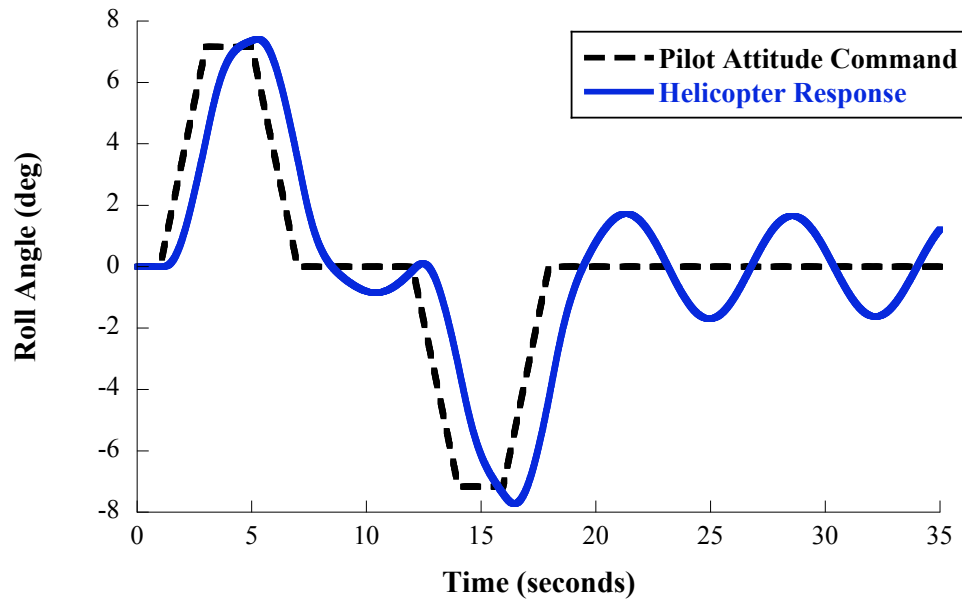
Figure 84: Helicopter roll attitude response to a pilot's attitude command when carrying a heavy suspended load.

control when load swing becomes too large is to slow down the helicopter [122, 13]. By trying to actively cancel this swing, the helicopter pilot may actually amplify the problem if his or her control inputs are not in the correct phase relative to the swing [13]. In cases where the swing amplitude becomes extreme and the pilot has difficulty stabilizing the load, the pilot may elect to jettison the load to regain control of the helicopter [122]. Additionally, the suspension cable can get tangled with objects on the ground. This can cause dangerous situations that result in damage to the cargo and helicopter, or injury to the pilot and crew. The safety of sling-load operations would be improved significantly by reducing load swing and its effects on the helicopter body.

Reducing load swing would also increase productivity during load transfer operations. Once a load is positioned above its desired location, it cannot be safely deposited until the swing amplitude settles below an acceptable level or workers on the ground wrestle it to a stop. Keeping the swing at a low amplitude would allow the pilot to transfer and deposit loads more quickly and safely.

Several strategies have been proposed for reducing suspended load swing. Some control

strategies include an actuated suspension point or some other form of active load stabilization [108]. Dukes states that an actively-controlled, moving suspension point could be an effective way of damping the load swing [28, 29]. However, retrofitting existing heavy-lift helicopters with moving suspension points would be costly compared to small modifications to the digital fight control system. Other proposed control strategies rely on feedback of the suspended load states [11, 47, 69]. Such control algorithms have shown promise because they also allow for control of external disturbances, but they require real-time measurement of the suspension cable angle, which is rarely available in current practice.

7.2 *Backdrivability of Helicopters Carrying Suspended Loads*

This section evaluates the pitch and roll backdrivability of a sample helicopter with suspended load dynamic model as a function of the load-helicopter mass ratio. A planar, nonlinear model of a helicopter with a suspended load was developed and experimentally verified on a radio-controlled helicopter in [75]. To study the effects of load-attitude backdriving, this model is linearized about hover. Then, the backdrivability of the linearized model is quantified using the Eigenvector Response Ratio performance metric presented in Section 3.2. This section focuses on the effect of suspended load mass on load-attitude backdrivability, although the effects of other parameters could also be studied using the model presented.

Figure 85 shows a schematic diagram of the planar helicopter with suspended load from [75]. The system states are the helicopter horizontal position x, helicopter attitude θ, and suspended load swing angle β. The helicopter has mass M and inertia I_G. The suspended load has mass m and suspension length L, and is suspended from a point located a distance d_S directly below the helicopter center of mass G. The model uses a quasistatic rotor assumption, which assumes that control inputs cause instantaneous changes in the rotor disk angle α, so α can be used as an input to the model. The thrust T produced by the rotor is also an input, but when linearizing about hover the thrust is set to a constant equilibrium thrust value equal the combined weight of the helicopter and load, $T_{eq} = (M + m)g$. The rotor hub is located a distance d_H directly above the helicopter center of mass G. The k_α

Figure 85: Schematic diagram of the planar helicopter with suspended load dynamic model [75].

parameter was included in [75] to model rotor stiffness effects. The model also includes linear damping on the helicopter position and angle, represented by c_x and c_θ, respectively.

A state-space version of this model linearized about hover is given by:

$$
\begin{bmatrix} \dot{x} \\ \ddot{x} \\ \dot{\theta} \\ \ddot{\theta} \\ \dot{\beta} \\ \ddot{\beta} \end{bmatrix} = \mathbf{A}_0 \begin{bmatrix} x \\ \dot{x} \\ \theta \\ \dot{\theta} \\ \beta \\ \dot{\beta} \end{bmatrix} + \mathbf{B}_0 \alpha,
\tag{88}
$$

where

$$
\mathbf{A}_0 = \begin{bmatrix}
0 & 1 & 0 & 0 & 0 & 0 \\
0 & -\frac{c_x}{M} & -\frac{T_{eq}}{M} & 0 & \frac{mg}{M} & 0 \\
0 & 0 & 0 & 1 & 0 & 0 \\
0 & 0 & -\frac{mgd_S}{I_G} & -\frac{c_\theta}{I_G} & \frac{mgd_S}{I_G} & 0 \\
0 & 0 & 0 & 0 & 0 & 1 \\
0 & \frac{c_x}{ML} & \frac{Mmgd_S{}^2 + I_G T_{eq}}{MLI_G} & \frac{c_\theta d_S}{LI_G} & \frac{m^2 gd_S{}^2 - (M+m)g\left(I_G + md_S{}^2\right)}{MLI_G} & 0
\end{bmatrix}
\tag{89}
$$

and

$$
\mathbf{B}_0 = \begin{bmatrix}
0 \\
-\frac{T_{eq}}{M} \\
0 \\
\frac{k_\alpha + T_{eq}d_H}{I_G} \\
0 \\
\frac{I_G T_{eq} - Md_S\left(k_\alpha + T_{eq}d_H\right)}{MLI_G}
\end{bmatrix}.
\tag{90}
$$

Analysis in [75] showed that this dynamic model has a pole at the origin corresponding to the rigid-body motion, a negative real pole corresponding to the short-term pitch mode, a pair of complex underdamped poles corresponding to the long-term longitudinal oscillation mode, and a second pair of complex underdamped poles corresponding to the load oscillation mode.

By numerically solving for the eigenvectors of (89), the response ratio magnitude between the helicopter attitude and load swing angle for the load oscillation mode shape can be found to quantify the degree of load-attitude backdrivability. The magnitude is considered here because the mode shapes have complex amplitudes due to the presence of damping. While the model was applied to the helicopter longitudinal direction in [75], it can also be used to model motion in the lateral direction by replacing I_G with an inertia value corresponding to the helicopter roll axis. Studying load-attitude backdrivability about both the pitch and roll axes is important because the inertia values about those axes are different. Most helicopters have significantly lower roll inertia than pitch inertia, and are therefore more susceptible to attitude backdriving about the roll axis.

Table 7 summarizes the sample parameters used for this backdrivability study. The parameters were selected to be representative of a full-scale helicopter. This study focuses on the effects of the load-to-helicopter mass ratio m/M, so the suspended load mass is varied while the other parameters are held constant. Also, two representative values of 200,000 kg-m and 50,000 kg-m are considered for the helicopter inertia I_G to evaluate and compare backdrivability about pitch and roll axes, respectively.

Figure 86 shows the response ratio magnitudes of the load oscillation mode eigenvector as a function of the load-helicopter mass ratio using the representative pitch and roll inertias. Both response ratios increase as the mass ratio increases. However, the roll response ratio is between 3.6 and 4 times as large as the pitch response ratio, depending on the mass ratio.

Practically, these response ratios allow thresholds of tolerable attitude response amplitudes to be defined. For example, if 10 degrees of load swing can be expected during operation and attitude oscillations above 2 degrees are considered intolerable (or a response ratio of 0.2), then the minimum mass ratio that requires addressing backdriving effects can be identified. Figure 87 shows the pitch and roll amplitude that would result if there is 10 degrees of load swing. A threshold of 2 degrees of attitude amplitude is shown, and the mass ratios that result in attitude oscillations above 2 degrees in the pitch and roll directions are indicated. For this sample system configuration, mass ratios above 0.22 result in at least 2 degrees of pitch backdriving. However, mass ratios above only 0.047 are required to result

Table 7: Summary of planar helicopter with suspended load model parameters for load-attitude backdrivability study.

Parameter	Value
M	15,000 kg
I_G (pitch)	200,000 kg-m^2
I_G (roll)	50,000 kg-m^2
c_x	1,000 N-s/m
c_θ	3,000 N-m-s/rad
k_α	300 N-m/rad
d_H	2.5 m
d_S	1 m
m	Varied
L	15 m
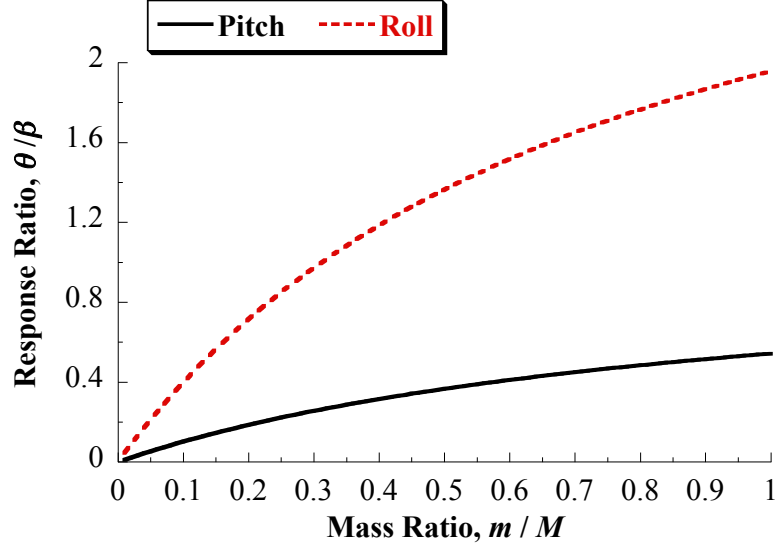
Figure 86: Pitch and roll load-attitude backdrivability.
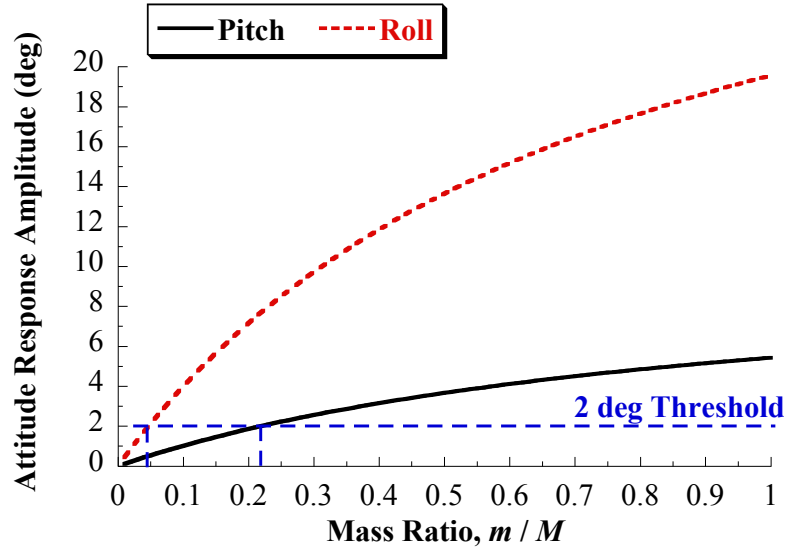
Figure 87: Load oscillation mode pitch and roll backdriving amplitude resulting from 10 degrees of load swing amplitude.

in at least 2 degrees of roll backdriving when 10 degrees of load swing results from helicopter motion. If such conditions could occur during externally-loaded operation, the backdriving load swing dynamics should be controlled or otherwise mitigated. The remainder of this chapter presents control techniques that mitigate the load swing and resulting backdriving effects.

7.3 Input Shaping for Helicopters Carrying Suspended Loads

The application of input shaping to helicopters carrying suspended loads has been considered in previous research [1, 11, 69, 74]. Bisgaard *et al.* [11] used a state estimator to measure the natural frequency of the suspended load oscillation. They then used this measurement to adaptively update an input shaper to prevent oscillation at the measured natural frequency. Ottander and Johnson [69] combined input shaping with delayed feedback control of the payload swing angle. This controller allowed the payload to more accurately track a desired trajectory. Load swing caused by helicopter motion was reduced through input shaping, and external disturbances were canceled using feedback of the load swing angle. Both studies proposed and implemented a vision system to measure the load swing, which would increase complexity and cost.

Potter *et al.* [74] experimentally verified a simple model of the suspended load oscillation, and used the model to test via simulation the effectiveness and robustness of various types of input shapers. Adams *et al.* [1] also demonstrated the effectiveness of input shaping control on an experimental radio-controlled helicopter flying in a motion-capture room.

7.3.1 Input Shaping on the Planar Experimental Radio-Controlled Helicopter

An experimental radio-controller helicopter has been used to demonstrate the effectiveness of input shaping at suppressing suspended load oscillations and reducing the load backdriving effects on the helicopter. The experimental setup that is discussed in this section is the Planar Experimental Radio-Controlled Helicopter (PERCH) [75].

A photograph of PERCH is shown in Figure 88. The experimental setup consists of an E-flite Blade 400 RC helicopter attached to a frame. The frame pivots about two carts that roll on the two guide rails. The helicopter is only able to pitch and translate forwards and backwards. The guide rails restrict motion in the lateral, yaw, and heave directions. A hard stop is positioned at the ends of each guide rail to stop the helicopter. A suspended load is attached to the helicopter. The colored circles are used to extract the helicopter attitude from videos of experimental trials using a MATLAB image processing program.
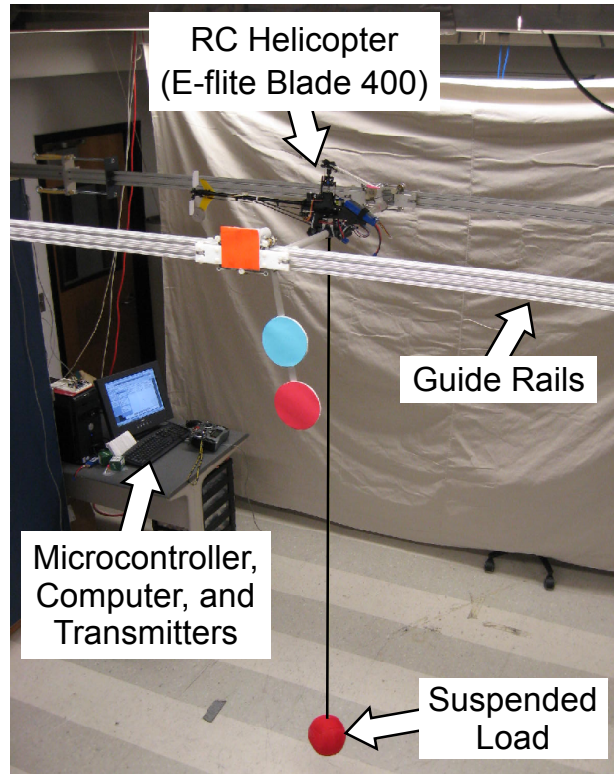
Figure 88: Photograph of the Planar Experimental Radio-Controlled Helicopter experimental setup.

A schematic diagram of PERCH is shown in Figure 89. Rather than directly transmitting operator commands to the helicopter using the transmitter, the commands are sent to an Arduino UNO microcontroller that can modifiy the operator's commands. The commands are sent from the microcontroller to the helicopter via a secondary signal-sending transmitter. This setup allows an operator to fly the RC helicopter using the primary transmitter, and input shaping may be applied to the operator's commands using the microcontroller.

The mass of the helicopter and its frame is 1.28 kg. The mass of the cart on each guide rail is 0.41 kg. The mass of the suspended load is 0.54 kg and the suspension cable length is 1.83 m. Due to the hard stops and the length of the guide rails, the usable workspace is 2.03 m long.

By constraining the angular motion of the helicopter to the pitch direction only, this experimental setup slightly changes the dynamics of the helicopter. In an unconstrained helicopter, pitching forward is accompanied by downward motion. This occurs because
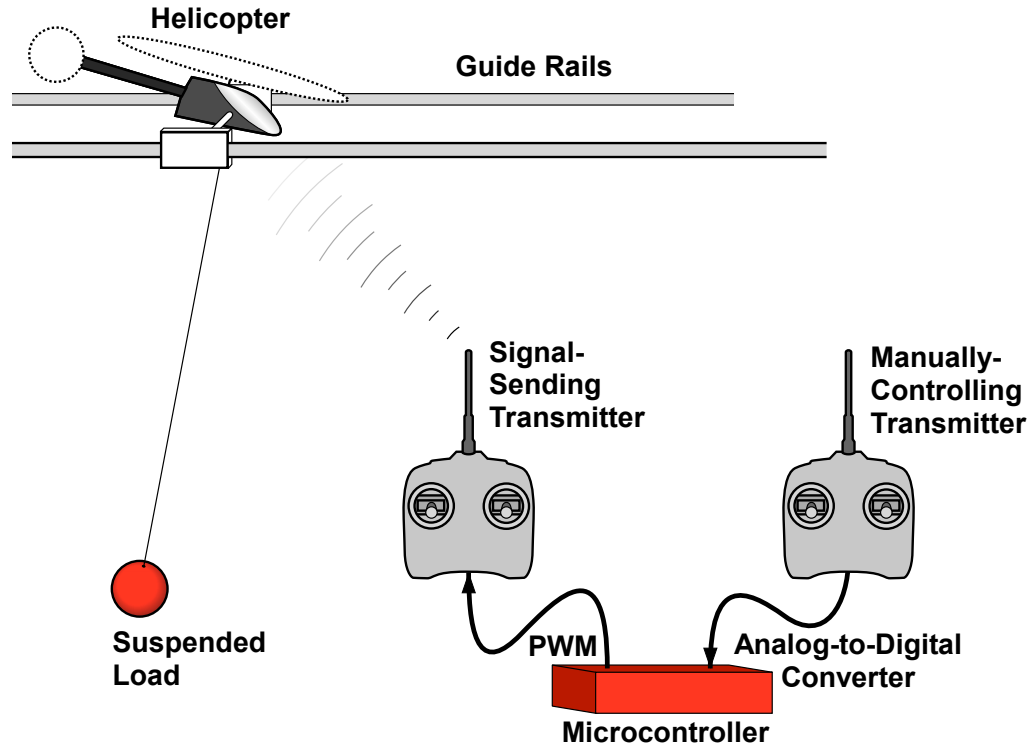
Figure 89: Schematic diagram of the Planar Experimental Radio-Controlled Helicopter.

the increase in pitch angle leads to a decrease in the vertical component of the thrust vector. The smaller vertical force does not fully support the weight of the helicopter, so pitching forward leads to a small downwards acceleration. When carrying a suspended load, this downward acceleration of the helicopter causes effects similar to a pendulum with a vertically accelerating suspension point. The accelerating suspension point affects the natural frequency load swing. This coupling between the pitch and vertical motions is small compared to the helicopter pitch and suspended load swing dynamics for small to moderate pitch angles. By allowing the helicopter to pitch and translate in the longitudinal direction, the experimental setup captures many of the important backdriving dynamics, such as attitude coupling between the load and helicopter, and allows these effects to be rigorously studied.

A ZV input shaper for the PERCH setup was designed using natural frequency and damping ratio estimates. To perform unshaped and input-shaped trials, a human operator flew the helicopter from one position to another on the guide rails. The helicopter's collective pitch input was set at the same level for all trials such that the rotor thrust balanced the

weight of the helicopter and the load.

Figure 90 shows the payload and helicopter responses for unshaped and ZV input-shaped commands. The helicopter responses are shown in Figure 90(a). In the unshaped response, the load oscillation significantly backdrives the helicopter following the move. This backdriving is not seen in the ZV-shaped response because the oscillation of the load was suppressed by input shaping. The ZV-shaped helicopter response is slightly slower. This is due to the scaling of the command by the impulses resulting in less acceleration. Figure 90(b) shows a plot of the suspended load oscillation relative to the helicopter. The use of the ZV input shaper significantly reduces the amount of payload swing caused by the helicopter motion. The peak-to-peak residual oscillation amplitude is reduced from approximately 50 cm to 2.5 cm.

7.4   *Input Shaping Combined with a Helicopter Flight Control System*

Input shaping alone is not sufficient for effective control of a helicopter carrying a suspended load. Rather, it should be combined with a feedback controller. Effective design of a helicopter's flight control system is critical to the overall performance of the aircraft. Design requirements such as ADS-33E-PRF [124] provide specifications on aircraft response characteristics that affect handling qualities ratings. While ADS-33E-PRF is a military specification, such design requirements give flight control designers guidance on response types favored by pilots. Stability augmentation systems and high authority control augmentation systems assist pilots in maneuvering their aircraft by stabilizing aircraft response, adding damping to oscillatory aircraft modes, and/or introducing different flight characteristics such as altitude or heading holds [48, 55, 78]. When carrying a heavy suspended load, the pilot's control task can be challenging despite the assistance of these control systems [122, 39, 13].

While a helicopter's control system would most likely be designed for unloaded flight, mission scenarios where the helicopter needs to carry a suspended load would require a different control system to achieve effective performance. Being able to activate an input-shaping algorithm that is compatible with the baseline flight controller for the unloaded
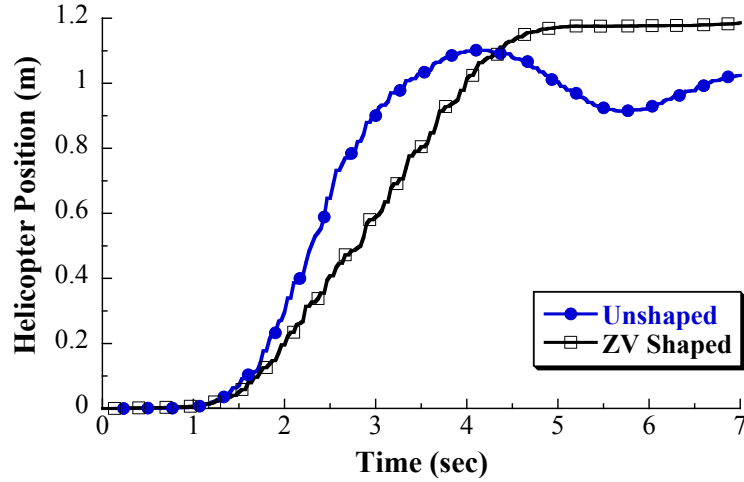
(a) Helicopter response.
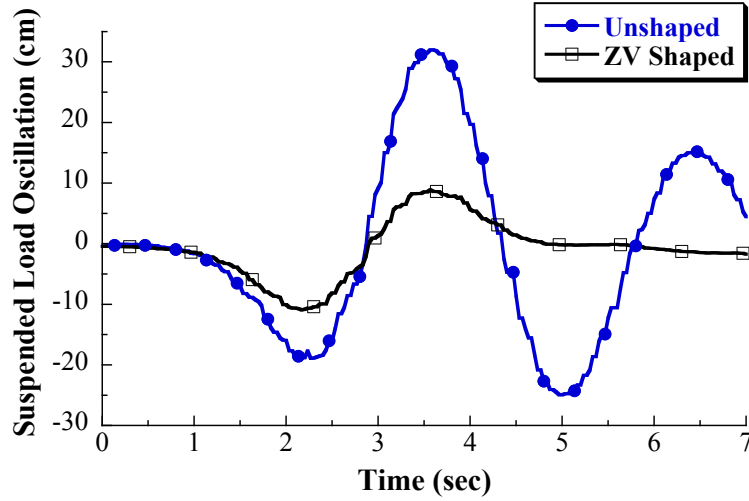
(b) Payload response.

Figure 90: Comparison of unshaped and ZV input-shaped experimental (a) helicopter and (b) payload responses for the Planar Experimental Radio-Controlled Helicopter.

helicopter would be simpler than having an entirely different flight control system designed specifically for loaded flight.

To be effective at preventing suspended load oscillations, the input-shaping technique must be well-integrated with the rest of the helicopter's flight control system. Done properly, this would combine the features of helicopter flight control systems listed above with the suspended load oscillation prevention characteristics of input shaping. The most straight-forward location for the input shaper in the controller is immediately after the pilot inputs have been received by the digital flight control system. Such a combination of input shaping

with a common flight control architecture will be investigated in this chapter.

Because input shapers are designed to suppress motion-induced residual oscillation, they will not decrease oscillation induced by external disturbance forces, such as wind gusts. Suppressing disturbance-induced swing requires feedback of the load states or an estimation technique that can accurately predict the load swing caused by a measured wind gust. Although it can be effective to combine input shaping with cable-angle feedback control [69, 47], this chapter focuses on eliminating load swing solely caused by helicopter motion by combining input shaping and model-following control.

The MFC architecture combines feedforward and feedback control. The feedback controller is used to stabilize the helicopter system and determines the error dynamics of the model tracking. The feedforward controller uses model-inversion techniques to cancel the undesired helicopter dynamics. However, tracking of the prescribed model may be significantly degraded when the helicopter is carrying a suspended load, particularly when the load is heavy relative to the weight of the helicopter. One way to improve helicopter performance would be to replace the original feedforward model with one that accounts for the sling-load dynamics. A drawback of this method is that the feedback portion of such a controller would require real-time measurement of the load position or angle. The load swing is assumed to be unmeasured in this chapter.

In the rest of this chapter, a near-hover attitude-command model-following controller is designed for a Sikorsky S-61 helicopter with and without a suspended load using linearized dynamic models of this helicopter obtained from previous studies [37, 35]. Simulation results are used to demonstrate the controller's effectiveness on the unloaded helicopter. Next, this controller is applied to the loaded helicopter, and large load oscillations are shown to occur. These oscillations can be dangerous depending on the mission scenario and degrade model tracking performance due to coupling between the load and helicopter fuselage. Additional results show that adding input-shaping to the controller i) reduces swing of the suspended load and ii) improves helicopter tracking of the prescribed model, particularly once the pilot's commands are completed, by reducing the backdriving effect on the helicopter.

An additional novelty in the proposed approach is that input shaping integrates well with

the concept of specifying a desired model. MFC is used as the underlying control because it provides good performance for the baseline helicopter dynamics. While certain performance is desired for the helicopter motion, designers (and pilots) also want the load motion to be critically damped, so input shaping is added to reduce suspended load oscillation. In a way, the input shaping control element is a form of implicit model-following control to achieve damped load motion. The input shaper is essentially part of the prescribed model, which can be referred to as an input-shaped prescribed model. Combining these two relatively simple and commonly used control methods provides a unique solution to this challenging control problem.

Section 7.4.1 describes dynamic models of the helicopter. The MFC architecture is described in Section 7.4.2. Section 7.4.3 details the MFC implementation and presents simulation results using the controller on unloaded and loaded Sikorsky S-61 helicopter models. Section 7.4.4 shows how the input-shaping technique may be combined with a MFC to improve helicopter performance when carrying a suspended load. Section 7.5 discusses why the approach presented in this chapter is effective, and why input shaping and model-following control complement one another when applied to helicopters carrying suspended loads.

7.4.1 Helicopter Dynamic Models

Designers of helicopter flight control systems often use helicopter models linearized about a given flight condition. These models can be obtained or improved using flight-test data [38, 40, 118]. One such model of a Sikorsky S-61 helicopter in near-hover operation was investigated by Hall and Bryson [37]. Gupta and Bryson [35] combined Hall and Bryson's helicopter model with a linear model of a suspended load to yield a linearized, near-hover model of a Sikorsky S-61 carrying a suspended load. The mass of the helicopter is $13,228$ lb, the suspended load is $4,409$ lb, and the suspension cable length is 65.6 ft mounted 4.9 ft below the helicopter center of mass [35].

The unloaded and loaded Sikorsky S-61 models are state-space models of the form:

$$\dot{\vec{x}} = \mathbf{A}\vec{x} + \mathbf{B}\vec{u}, \tag{91}$$

Both models use a quasistatic representation of the rotor dynamics [37, 35].

Both the unloaded and loaded models only incorporate the longitudinal and lateral motion of the helicopter. Therefore, it is assumed that the helicopter has well-performing heading-hold and altitude-hold controllers that maintain a constant direction and vertical position. Because the models are linearized, effects such as air drag on the helicopter and load are weakened by the linearization. The models also neglect the effects of wind and changes in atmospheric properties. While wind acts as a disturbance on helicopters and suspended loads, this chapter focuses only on the effects of helicopter motion on the suspended load.

7.4.1.1 Unloaded Sikorsky S-61 Model

Figure 91 shows a sketch of the unloaded helicopter. The state and input vectors are defined as:

$$\vec{x} = \begin{bmatrix} \theta_H & \dot{\theta}_H & \dot{x}_H & \phi_H & \dot{\phi}_H & \dot{y}_H \end{bmatrix}^T, \tag{92}$$

$$\vec{u} = \begin{bmatrix} \theta_s & \theta_c \end{bmatrix}^T. \tag{93}$$

By appropriately scaling the input matrix $\mathbf{B}$, the input vector given by (93) becomes identical to the rotor tilt angles [37] and is given by:

$$\vec{u} = \begin{bmatrix} \theta_R & \phi_R \end{bmatrix}^T, \tag{94}$$
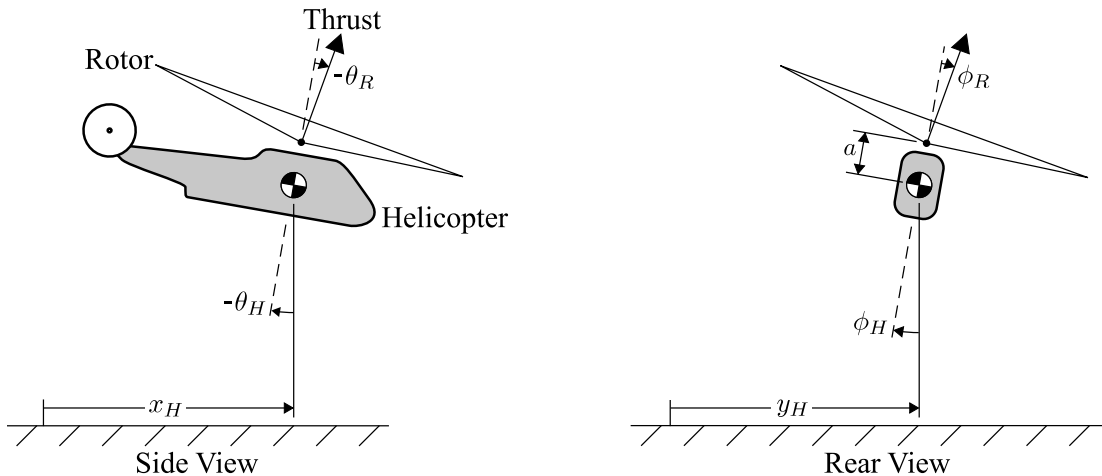
Figure 91: Helicopter without sling load.

With all units in ft, sec, and rad, the state equation for the unloaded S-61 model is [37]:

$$
\dot{\vec{x}} = \begin{bmatrix}
0 & 1 & 0 & 0 & 0 & 0 \\
0 & -0.415 & 0.00338 & 0 & 0.318 & 0.00116 \\
-32.2 & 4.70 & -0.0198 & 0 & -1.02 & -0.0059 \\
0 & 0 & 0 & 0 & 1 & 0 \\
0 & -1.23 & 0.00415 & 0 & -1.58 & -0.0124 \\
0 & -1.02 & 0.0059 & 32.2 & -4.70 & -0.0198
\end{bmatrix} \vec{x} + \begin{bmatrix}
0 & 0 \\
6.27 & 0.295 \\
-32.2 & -0.977 \\
0 & 0 \\
-1.08 & 23.1 \\
-0.977 & 32.2
\end{bmatrix} \vec{u}. \quad (95)
$$

7.4.1.2 Loaded Sikorsky S-61 Model

Gupta and Bryson [35] modified the unloaded Sikorsky S-61 model in (95) to include suspended load dynamics. Figure 92 shows a sketch of the loaded helicopter. The helicopter state and input vectors for the loaded model are defined as:

$$
\vec{x} = \begin{bmatrix} \theta_H & \dot{\theta}_H & x_H & \dot{x}_H & x_L & \dot{x}_L & \phi_H & \dot{\phi}_H & y_H & \dot{y}_H & y_L & \dot{y}_L \end{bmatrix}^T, \quad (96)
$$

$$
\vec{u} = \begin{bmatrix} \theta_R & \phi_R \end{bmatrix}^T. \quad (97)
$$
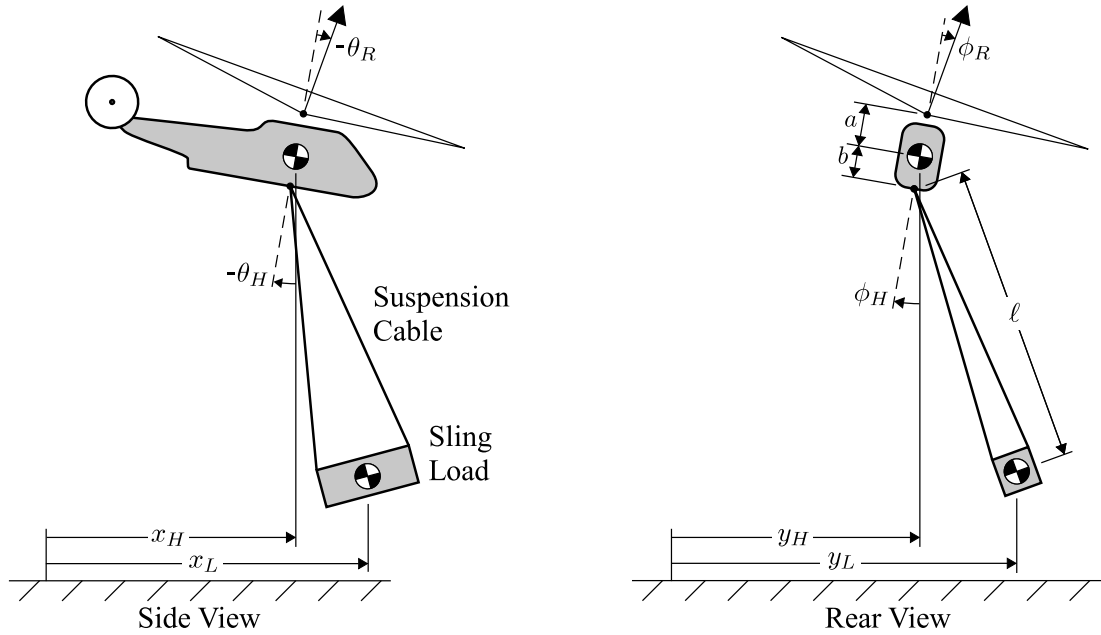
Figure 92: Helicopter with suspended load.

With all units in ft, sec, and rad, the state matrix $\mathbf{A}$ for the loaded S-61 is [35]:

$$
\mathbf{A} = \left[\begin{array}{cccccc:cccccc}
0 & 1 & 0 & 0 & 0 & 0 & 0 & 0 & 0 & 0 & 0 & 0 \\
-2.25 & -0.415 & -0.032 & 0.003 & 0.032 & 0 & 0 & 0.318 & 0 & 0.001 & 0 & 0 \\
0 & 0 & 0 & 1 & 0 & 0 & 0 & 0 & 0 & 0 & 0 & 0 \\
-43.6 & 4.69 & -0.164 & -0.020 & 0.164 & 0 & 0 & -1.02 & 0 & -0.006 & 0 & 0 \\
0 & 0 & 0 & 0 & 0 & 1 & 0 & 0 & 0 & 0 & 0 & 0 \\
2.41 & 0 & 0.491 & 0 & -0.491 & -0.003 & 0 & 0 & 0 & 0 & 0 & 0 \\
\hdashline
0 & 0 & 0 & 0 & 0 & 0 & 0 & 1 & 0 & 0 & 0 & 0 \\
0 & -1.23 & 0 & 0.004 & 0 & 0 & -8.28 & -1.58 & 0.117 & -0.012 & -0.117 & 0 \\
0 & 0 & 0 & 0 & 0 & 0 & 0 & 0 & 0 & 1 & 0 & 0 \\
0 & -1.02 & 0 & 0.006 & 0 & 0 & 43.6 & -4.69 & -0.164 & -0.020 & 0.164 & 0 \\
0 & 0 & 0 & 0 & 0 & 0 & 0 & 0 & 0 & 0 & 0 & 1 \\
0 & 0 & 0 & 0 & 0 & 0 & -2.41 & 0 & 0.491 & 0 & -0.491 & -0.003
\end{array}\right],
$$

(98)

and the input matrix $\mathbf{B}$ is [35]:

$$
\mathbf{B} = \left[\begin{array}{cccccc:cccccc}
0 & 8.38 & 0 & -42.98 & 0 & 0 & 0 & -1.43 & 0 & -1.30 & 0 & 0 \\
\hdashline
0 & 0.393 & 0 & -1.30 & 0 & 0 & 0 & 30.70 & 0 & 42.98 & 0 & 0
\end{array}\right]^{T}
$$

(99)

Figure 93 shows the magnitude plot for the lateral rotor tilt angle to the roll attitude, $\phi_H(s)/\phi_R(s)$. A significant notch is seen in the magnitude at the load swing frequency of approximately 0.9 rad/s. This notch is a result of the backdriving load swing dynamics and is indicative of degraded control when the pilot's command has components around the load swing frequency.

7.4.1.3 Eigenvalue and Eigenvector Analysis of Sikorsky S-61 Models

The unloaded and loaded Sikorsky S-61 models are open-loop unstable. This makes it difficult to simulate their time responses to evaluate the open-loop performance of the aircraft in unloaded and loaded configurations. Instead, it can be useful to plot the pole locations for each model. This is typically done to enable identification of various aircraft flight modes since each flight mode is associated with an eigenvalue or pole [70]. This
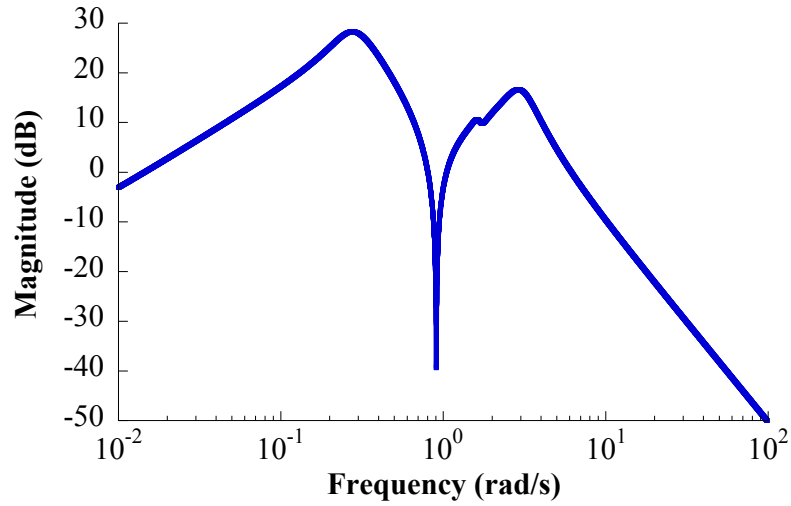
Figure 93: Bode magnitude plot for the loaded Sikorsky S-61 model.

analysis can be performed with uncoupled longitudinal and lateral helicopter models, and it is often simpler to analyze the uncoupled models [70]. However, in this thesis the coupled models will be studied. This analysis method is similar to the Eigenvector Response Ratio performance metric presented in Chapter III.

The poles can be found by calculating the eigenvalues of the models' **A** matrices. Each real eigenvalue or pair of complex conjugate eigenvalues corresponds to a flight mode of the helicopter [70]. As was discussed in Chapter III, the eigenvectors corresponding to each mode can be used to determine what model states are most affected by the mode. Each row of an eigenvector corresponds to one state from the model. States related to each flight mode have a larger magnitude in their row of the eigenvector. By determining the states that have the largest contribution in a given eigenvector, the helicopter's flight modes can be identified.

Table 8 shows the eigenvalues and eigenvectors of the unloaded Sikorsky S-61 **A** matrix given in (95). The flight mode that corresponds to each real eigenvalue or complex conjugate pair is labeled at the top of the table. As an example of how the flight modes were determined, note that the value of the third row of the Long Term Longitudinal Oscillation Mode eigenvectors is 0.8717. This value is larger than the other elements of those eigenvectors. It is also larger than any of the elements in the third row of the other eigenvectors.

Table 8: Unloaded Sikorsky S-61 model [37] eigenvectors, with the associated eigenvalues and flight modes labeled.

Modes	Roll Mode	Short Term Pitch Mode	Lateral Oscillation Mode		Long Term Longitudinal Oscillation Mode	
Eigenvalues	-1.2700	-1.0680	$0.0426 + 0.4962i$	$0.0426 - 0.4962i$	$0.1092 + 0.3635i$	$0.1092 - 0.3635i$
θ_H	0.0435	0.0507	$0.0186 - 0.0019i$	$0.0186 + 0.0019i$	$-0.0097 - 0.0335i$	$-0.0097 + 0.0335i$
$\dot{\theta}_H$	-0.0552	-0.0541	$0.0017 + 0.00092i$	$0.0017 - 0.00092i$	$0.0111 - 0.0072i$	$0.0111 + 0.0072i$
$\dot{x}_H$	0.4390	0.5772	$0.0167 + 0.3618i$	$0.0167 - 0.3618i$	0.8717	0.8717
ϕ_H	-0.0965	-0.0762	$0.0025 + 0.0476i$	$0.0025 - 0.0476i$	$-0.0163 + 0.0107i$	$-0.0163 - 0.0107i$
$\dot{\phi}_H$	0.1225	0.0814	$-0.0235 + 0.0033i$	$-0.0235 - 0.0033i$	$-0.0057 - 0.0047i$	$-0.0057 + 0.0047i$
$\dot{y}_H$	0.8820	0.8055	0.9303	0.9303	$0.1493 + 0.4649i$	$0.1493 - 0.4649i$

States

The third row corresponds to the longitudinal velocity state, $\dot{x}_H$. This suggests that the mode represented by these two eigenvectors is related to the longitudinal motion of the helicopter. Because the corresponding eigenvalues are $0.1092 \pm 0.3635i$, this mode is oscillatory. Its oscillatory nature and its relation to the longitudinal motion of the helicopter give the Long Term Longitudinal Oscillation Mode its name. This mode is also referred to as the long phugoid or long-period phugoid mode [70]. Note that this mode is also unstable.

A plot of the real and imaginary parts of the eigenvalues of the unloaded model is shown in Figure 94. The mode names are labeled for each real eigenvalue or complex conjugate pair. The source of the real, negative-valued Short Term Pitch Mode is the rotor pitch damping [48]. The Long Term Longitudinal Oscillation Mode corresponds to the unstable oscillation caused by the coupling of the helicopter pitch and longitudinal velocity [48]. The instability results from coupling between the pitch moments caused by longitudinal velocity, or speed stability, and the component of the helicopter weight force acting on the helicopter in the longitudinal direction due to the pitch angle [48].

The Roll Mode is a result of rotor roll damping [48]. The Roll Mode is faster than the Short Term Pitch Mode because the helicopter, like most traditional single-rotor helicopters,
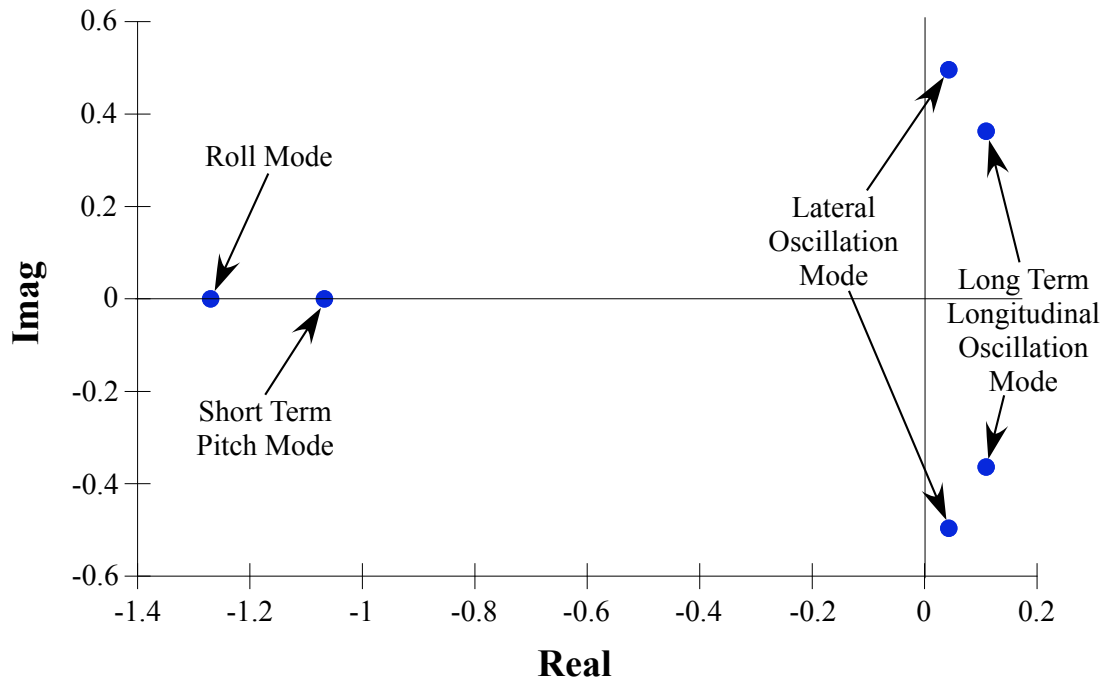
Figure 94: Eigenvalues of the unloaded Sikorsky S-61 model from [37].

has a smaller moment of inertia about the roll axis than the pitch axis. The Lateral Oscillation Mode is unstable as a result of the rotor dihedral effect [48]. The instability of the Lateral Oscillation Mode is more objectionable to pilots than the instability of the Long Term Longitudinal Mode because it has a higher frequency [48]. This means that it is important for the flight controller to stabilize this mode.

While resources such as Johnson [48] and Padfield [70] present detailed discussions of flight modes for unloaded helicopters with a variety of rotor configurations, not much work has been done on identifying or labeling flight modes of a helicopter with a suspended load. The following analysis identifies flight modes of the loaded Sikorsky S-61. This analysis will show that poles, and therefore the behavior of the flight modes, change significantly when the helicopter is carrying a suspended load.

Table 9 shows the eigenvalues and eigenvectors of the loaded Sikorsky S-61 **A** matrix given in (98). The flight mode that corresponds to each real eigenvalue or complex conjugate pair is labeled above each eigenvalue and eigenvector. Also, a plot of the real and imaginary parts of the eigenvalues is shown in Figure 95.

The first two modes listed in Table 9 result from the relationships between the helicopter
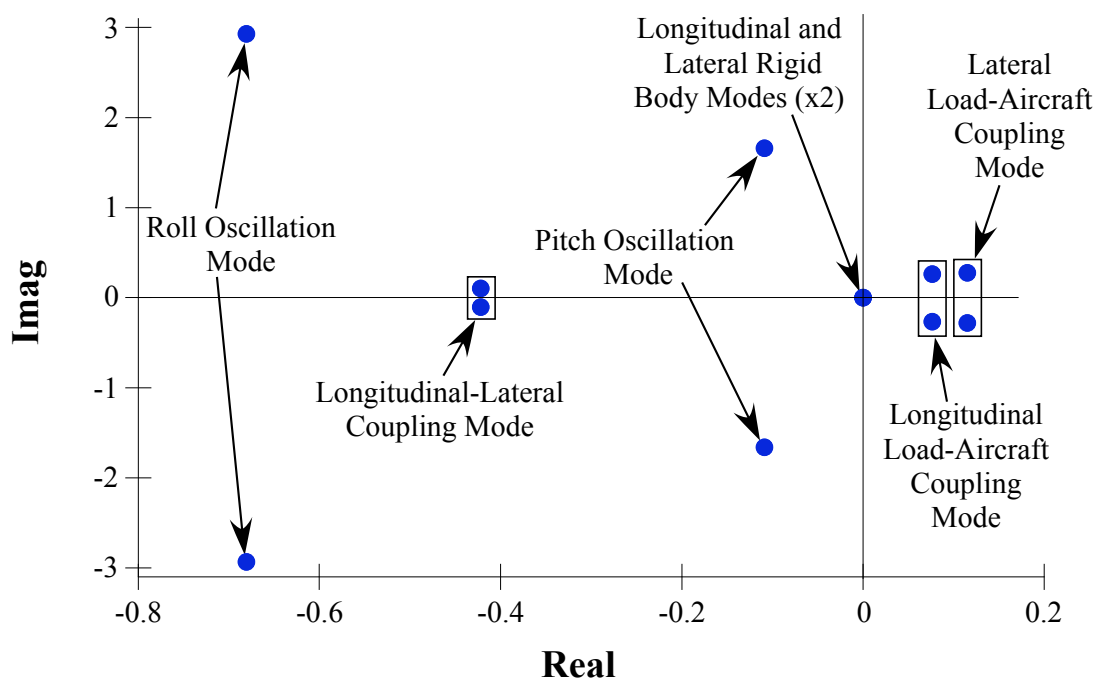
Figure 95: Eigenvalues of the loaded Sikorsky S-61 model from [35].

Table 9: Loaded Sikorsky S-61 model [35] eigenvectors, with the associated eigenvalues and flight modes labeled.

Modes	Roll Oscillation Mode		Pitch Oscillation Mode		Longitudinal-Lateral Coupling Mode	
Eigenvalues	$-0.6804 + 2.9306i$	$-0.6804 - 2.9306i$	$-0.1087 + 1.6593i$	$-0.1087 - 1.6593i$	$-0.4219 + 0.1048i$	$-0.4219 - 0.1048i$
θ_H	$0.0212 + 0.0069i$	$0.0212 - 0.0069i$	$0.0207 - 0.0854i$	$0.0207 + 0.0854i$	$-0.0052 - 0.0063i$	$-0.0052 + 0.0063i$
$\dot{\theta}_H$	$-0.0348 + 0.0575i$	$-0.0348 - 0.0575i$	$0.1394 + 0.0436i$	$0.1394 - 0.0436i$	$0.0028 + 0.0021i$	$0.0028 - 0.0021i$
x_H	$0.0183 - 0.0206i$	$0.0183 + 0.0206i$	$-0.0309 + 0.4720i$	$-0.0309 - 0.4720i$	$0.1245 + 0.4794i$	$0.1245 - 0.4794i$
$\dot{x}_H$	$0.0480 + 0.0676i$	$0.0480 - 0.0676i$	0.7866	0.7866	$-0.1028 - 0.1892i$	$-0.1028 + 0.1892i$
x_L	$-0.0023 + 0.0018i$	$-0.0023 - 0.0018i$	$0.0202 + 0.1277i$	$0.0202 - 0.1277i$	$0.0394 + 0.3566i$	$0.0394 - 0.3566i$
$\dot{x}_L$	$-0.0038 - 0.0079i$	$-0.0038 + 0.0079i$	$-0.2141 + 0.0197i$	$-0.2141 - 0.0197i$	$-0.0540 - 0.1463i$	$-0.0540 + 0.1463i$
ϕ_H	$-0.0799 + 0.1398i$	$-0.0799 - 0.1398i$	$-0.0203 - 0.0041i$	$-0.0203 + 0.0041i$	$0.0083 + 0.0039i$	$0.0083 - 0.0039i$
$\dot{\phi}_H$	$-0.3552 - 0.3292i$	$-0.3552 + 0.3292i$	$0.0089 - 0.0332i$	$0.0089 + 0.0332i$	$-0.0031 + 0.0025i$	$-0.0031 - 0.0025i$
y_H	$-0.0605 - 0.2606i$	$-0.0605 + 0.2606i$	$0.1256 - 0.0086i$	$0.1256 + 0.0086i$	0.5534	0.5534
$\dot{y}_H$	0.8049	0.8049	$0.0006 + 0.2093i$	$0.0006 - 0.2093i$	$-0.2335 + 0.0580i$	$-0.2335 - 0.0580i$
y_L	$0.0094 + 0.0253i$	$0.0094 - 0.0253i$	$-0.0331 + 0.0058i$	$-0.0331 - 0.0058i$	$0.3966 + 0.0576i$	$0.3966 - 0.0576i$
$\dot{y}_L$	$-0.0806 + 0.0103i$	$-0.0806 - 0.0103i$	$-0.0060 - 0.0556i$	$-0.0060 + 0.0556i$	$-0.1734 + 0.0173i$	$-0.1734 - 0.0173i$

Modes	Lateral Load-Aircraft Coupling Mode		Longitudinal Load-Aircraft Coupling Mode		Longitudinal Rigid Body Mode	Lateral Rigid Body Mode
Eigenvalues	$0.1149 + 0.2796i$	$0.1149 - 0.2796i$	$0.0763 + 0.2625i$	$0.0763 - 0.2625i$	0	0
θ_H	$0.0032 + 0.0025i$	$0.0032 - 0.0025i$	$-0.0033 + 0.0018i$	$-0.0033 - 0.0018i$	0	0
$\dot{\theta}_H$	$-0.0003 + 0.0012i$	$-0.0003 - 0.0012i$	$-0.0007 - 0.0007i$	$-0.0007 + 0.0007i$	0	0
x_H	$0.0244 + 0.4090i$	$0.0244 - 0.4090i$	$-0.4529 - 0.0463i$	$-0.4529 + 0.0463i$	-0.7004	-0.2774
$\dot{x}_H$	$-0.1116 + 0.0538i$	$-0.1116 - 0.0538i$	$-0.0224 - 0.1224i$	$-0.0224 + 0.1224i$	0	0
x_L	$0.1037 + 0.4596i$	$0.1037 - 0.4596i$	-0.5250	-0.5250	-0.7004	-0.2774
$\dot{x}_L$	$-0.1166 + 0.0818i$	$-0.1166 - 0.0818i$	$-0.0401 - 0.1378i$	$-0.0401 + 0.1378i$	0	0
ϕ_H	$-0.0037 + 0.0030i$	$-0.0037 - 0.0030i$	$0.0023 + 0.0028i$	$0.0023 - 0.0028i$	0	0
$\dot{\phi}_H$	$-0.0013 - 0.0007i$	$-0.0013 + 0.0007i$	$-0.0006 + 0.0008i$	$-0.0006 - 0.0008i$	0	0
y_H	$0.4698 + 0.0769i$	$0.4698 - 0.0769i$	$-0.0322 - 0.4371i$	$-0.0322 + 0.4371i$	-0.0970	0.6504
$\dot{y}_H$	$0.0325 + 0.1402i$	$0.0325 - 0.1402i$	$0.1123 - 0.0418i$	$0.1123 + 0.0418i$	0	0
y_L	0.5475	0.5475	$-0.0882 - 0.4977i$	$-0.0882 + 0.4977i$	-0.0970	0.6504
$\dot{y}_L$	$0.0629 + 0.1531i$	$0.0629 - 0.1531i$	$0.1239 - 0.0611i$	$0.1239 + 0.0611i$	0	0

attitudes, attitude rates, and translational velocities. The eigenvectors of the first mode have strong contributions from the roll rate and lateral velocity, and the mode is oscillatory. Similarly, the eigenvectors of the longitudinal mode have strong contributions from the pitch rate and longitudinal velocity, and the mode is also oscillatory. As a result, the first two modes are labeled the Roll and Pitch Oscillation Modes, respectively.

The eigenvectors of the third mode have the largest contributions from the helicopter longitudinal and lateral translational motion. The entries in the eigenvectors in the rows related to the helicopter longitudinal and lateral positions are approximately 90 degrees out of phase. This suggests an exchange of energy between the longitudinal and lateral degrees of freedom indicative of coupling between the two directions. For this reason, this mode is labeled the Longitudinal-Lateral Coupling Mode.

The eigenvectors of the fourth mode suggest backdriving coupling effects occur between the lateral helicopter and load translational motion. This mode has a complex conjugate pair of eigenvalues that have a positive real part, suggesting that the mode is unstable. Similarly, the eigenvectors of the fifth mode suggest backdriving between the longitudinal helicopter and load translational motion. This mode is also unstable because it has a complex conjugate pair of eigenvalues that have a positive real part. These modes were labeled Lateral and Longitudinal Load-Aircraft Coupling Modes. Note that the lateral mode is further from the origin, indicating that the lateral motion occurs at a higher frequency and will diverge more quickly than the longitudinal mode. The presence of these modes agree with the observation of Hoh et al. [39] that there is strong coupling between the load oscillation and the helicopter translational degrees of freedom. Hoh et al. also showed that the strength of this coupling effect has a strong influence on the pilot's controllability of the helicopter, and therefore, on the handling qualities of the helicopter.

The final two modes correspond to the helicopter and load moving together in the longitudinal and lateral directions as if they are one rigid body. They appear in the loaded model due to the integration of the helicopter and load longitudinal and lateral velocities to calculate the helicopter and load positions.

7.4.2 Model-Following Control

Model-Following Control has become an attractive control technique for helicopter flight controllers. MFC is an effective and viable control architecture because the aircraft response can be specified via a prescribed model to achieve favorable aircraft performance and the architecture is well-suited for full authority fly-by-wire control systems [55].

MFC for aircraft first appeared in the literature in the 1960's and 1970's. Murphy and Narendra [66] adjoined a model that approximates the pilot's inputs to the helicopter equations of motion, and then used optimal control to design a regulator that would track the model response. Winsor and Roy [130] used a combination of partial state feedback and feedforward compensation to achieve good tracking of the prescribed model. More recently, Trentini and Pieper [119] designed a model-following controller for a helicopter in hover to meet handling qualities requirements using an optimal control design approach. MFC has also been synthesized with other types of controllers to achieve better performance in difficult flight conditions or for specific missions, such as gust rejection during shipboard operations [41].

There are two main types of MFC. Implicit MFC uses optimal control to design a feedback controller that yields a closed-loop control system whose dynamics match the dynamics of the prescribed model [130]. The prescribed model itself does not appear in the control law directly; its output is only used in an optimal control performance index used to calculate feedback controller gains [119, 121]. Explicit (or real) MFC uses the prescribed model directly in the control system, typically as a feedforward compensator [116, 68, 119, 63]. The control law in explicit MFC is typically constructed using feedforward of the prescribed model states and a feedback controller that uses plant-state feedback [130, 121].

Explicit model-following controllers incorporate real-time measurement of the model tracking error, allowing the controller to reject disturbances and to correct the aircraft trajectory in the presence of modeling errors [68, 130]. In addition, explicit MFC can be implemented with partial state feedback and effective model tracking can still be achieved [130]. Most importantly, the feedback stabilization can be designed independently from the

feedforward compensator and prescribed model [55]. For these reasons, explicit MFC was selected for the baseline helicopter flight controller implemented in this chapter.

The implemented controller combines feedforward and feedback control. A state feedback controller is used to stabilize the helicopter system. Also, the state feedback control enables the error dynamics of the model tracking to be specified. Based on the recommendation of Tyler [121], the feedback controller is designed as a regulator independent from the rest of the controller using only the helicopter plant model. The regulator is designed using the pole placement state feedback technique. The feedforward controller uses model-inversion techniques to cancel the undesired helicopter dynamics.

However, tracking of the prescribed model is significantly degraded when the helicopter is carrying a suspended load. One way to improve helicopter performance when carrying a suspended load would be to replace the original feedforward model with one that accounts for the sling-load dynamics. A drawback of this method is that the feedback portion of such a controller would require real-time measurement of the sling load position or angle, which is almost never available in practice. This section investigates an alternative way to improve system performance without measurements of the load states by adding input shaping to the controller.

7.4.2.1   Controller Description

Figure 96 shows the block diagram of an explicit model-following controller. The structure of this controller is similar to that presented by Osder and Caldwell [68] and Landis et al. [55]. The pilot command is used as the input to a prescribed model $\mathbb{G}_M$. The rest of the controller is designed to force the output $\vec{x}$ of the helicopter plant $\mathbb{G}_P$ to track the prescribed model output $\vec{x}_M$. Generally, helicopters have one or more unstable modes, so a feedback controller is used to stabilize $\mathbb{G}_P$. The feedback element also enables the controller to reject disturbances that would otherwise degrade the model tracking [68]. Also, the feedback $\mathbb{G}_{FB}$ determines the error dynamics of the model tracking. The feedforward control $\mathbb{G}_{FF}$ is then selected to cancel undesired helicopter dynamics using model inversion techniques.
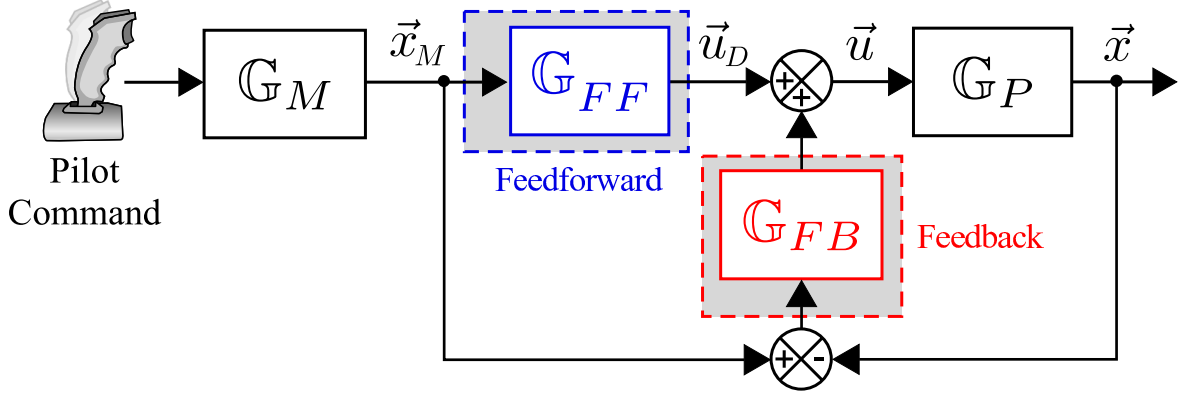
Figure 96: Block diagram of an explicit model-following control structure.

7.4.2.2   Theoretical Model-Following Controller Performance

Steady-State Performance

If the feedforward control $\mathbb{G}_{FF}$ equals the inverse of the helicopter plant, $\mathbb{G}_P^{-1}$, then the helicopter output $\vec{x}$ asymptotically tracks the model output $\vec{x}_M$. The asymptotic model tracking can easily be shown from the block diagram in Figure 96 using block diagram reduction [68]. The control law which provides asymptotic tracking is given by:

$$\vec{u} = \mathbb{G}_{FF}\vec{x}_M + \mathbb{G}_{FB}(\vec{x}_M - \vec{x}), \tag{100}$$

where $\mathbb{G}_{FF} = \mathbb{G}_P^{-1}$.

Model Tracking Error Dynamics

It can be shown that the design of the feedback controller determines the dynamic characteristics of the model tracking error. First, the helicopter plant is defined as:

$$\dot{\vec{x}} = \mathbf{A}\vec{x} + \mathbf{B}\vec{u}, \tag{101}$$

and the prescribed model is defined as:

$$\dot{\vec{x}}_M = \mathbf{A}_M\vec{x}_M + \mathbf{B}_M\vec{r}. \tag{102}$$

The model tracking error is given by:

$$\vec{e} = \vec{x}_M - \vec{x}. \tag{103}$$

Assuming that all of the helicopter states are measurable, full state feedback may be selected for the feedback controller. Full state feedback calls for feedback control of the form $\vec{u} = -\mathbf{K}\vec{x}$, where $\mathbf{K}$ is a constant state-feedback gain matrix. Therefore, $\mathbb{G}_{FB}$ from Figure 96 equals the gain matrix $\mathbf{K}$. The control law in (100) can be rewritten as:

$$\vec{u} = \vec{u}_D + \mathbf{K}\left(\vec{x}_M - \vec{x}\right). \tag{104}$$

Recall that the feedforward block is chosen to be an inverted model of the helicopter plant. A state space representation of the helicopter plant model to be inverted is given by:

$$\dot{\vec{x}}_D = \mathbf{A}_D\vec{x}_D + \mathbf{B}_D\vec{u}_D. \tag{105}$$

In practice, this model will not perfectly represent the helicopter. An expression for $\vec{u}_D$ is obtained by solving (105) for $\vec{u}_D$, or:

$$\vec{u}_D = \mathbf{B}_D^\dagger \left(\dot{\vec{x}}_D - \mathbf{A}_D\vec{x}_D\right), \tag{106}$$

where $\mathbf{B}_D^\dagger$ is the pseudoinverse of $\mathbf{B}_D$ and $\vec{x}_D$ is the input to the model inverse, which equals the prescribed model output $\vec{x}_M$ shown in Figure 96. The pseudoinverse is required because $\mathbf{B}$ is usually not a square matrix.

Substituting the plant inverse given in (106) into (104), and setting $\dot{\vec{x}}_D = \dot{\vec{x}}_M$ and $\vec{x}_D = \vec{x}_M$, the control law can be written as:

$$\vec{u} = \mathbf{B}_D^\dagger \left(\dot{\vec{x}}_M - \mathbf{A}_D\vec{x}_M\right) + \mathbf{K}\left(\vec{x}_M - \vec{x}\right). \tag{107}$$

To analyze the dynamics of the model tracking error, an expression for the derivative of $\vec{e}$ must be found. Taking the derivative of (103) and substituting (102) and (101) for $\dot{\vec{x}}_M$ and $\dot{\vec{x}}$ gives:

$$\dot{\vec{e}} = \mathbf{A}_M\vec{x}_M + \mathbf{B}_M\vec{r} - \mathbf{A}\vec{x} - \mathbf{B}\vec{u}. \tag{108}$$

Substituting (107) into (108) yields:

$$\dot{\vec{e}} = \mathbf{A}_M\vec{x}_M + \mathbf{B}_M\vec{r} - \mathbf{A}\vec{x} - \mathbf{B}\left[\mathbf{B}_D^\dagger \left(\dot{\vec{x}}_M - \mathbf{A}_D\vec{x}_M\right) + \mathbf{K}\left(\vec{x}_M - \vec{x}\right)\right]. \tag{109}$$

If the model inversion is exact, or equivalently $\mathbf{A}_D = \mathbf{A}$ and $\mathbf{B}_D = \mathbf{B}$, then (109) simplifies to:

$$\dot{\vec{e}} = \mathbf{A}_M\vec{x}_M + \mathbf{B}_M\vec{r} - \dot{\vec{x}}_M + \left(\mathbf{A} - \mathbf{B}\mathbf{K}\right)\left(\vec{x}_M - \vec{x}\right). \tag{110}$$

Recognizing that $\vec{x}_M - \vec{x} = \vec{e}$ and $\mathbf{A}_M \vec{x}_M + \mathbf{B}_M \vec{r} = \dot{\vec{x}}_M$, (110) reduces to:

$$\dot{\vec{e}} = (\mathbf{A} - \mathbf{BK})\vec{e}. \tag{111}$$

This result shows that the eigenvalues of $(\mathbf{A} - \mathbf{BK})$ determine the dynamics of the model tracking error, $\vec{e} = \vec{x}_M - \vec{x}$, and designing a controller for the model tracking error reduces to the regulator design problem, as discussed by Tyler [121]. Therefore, using techniques such as pole placement to calculate a state feedback gain $\mathbf{K}$ allows the designer to specify the model tracking error dynamics.

7.4.3 Near-Hover Attitude-Command Model-Following Controller

This section presents the design of a near-hover attitude-command model-following controller for the unloaded Sikorsky S-61 helicopter model discussed in Section 7.4.1. The unloaded S-61 model is used for designing the feedback controller gains, and only the attitude states and translational helicopter velocities are used for feedback. The model inversion is constructed using the unloaded model, which only requires the specified attitudes and velocities as inputs to the inverted model. The inversion of the unloaded model leads to full cancellation of the dynamics of the unloaded helicopter plant.

However, when the helicopter carries a suspended load, the model inversion cancels the baseline helicopter dynamics but not the additional dynamics introduced by the presence of the suspended load. The controller no longer completely cancels the dynamics of the plant, so error between the actual output and the prescribed model develops. Note that the loaded helicopter is simulated using the model of the load-carrying Sikorsky S-61 from Gupta and Bryson [35] and discussed in Section 7.4.1.

7.4.3.1 Feedback Controller Design Using Unloaded S-61 Model

The model tracking performance can be specified by selecting eigenvalues of $\mathbf{A} - \mathbf{BK}$ that give suitable model tracking error dynamics, and the pole placement technique may be used to calculate $\mathbf{K}$. The selected eigenvalues are $0.8 \pm 0.4i$, $-4.0 \pm 4.6i$, -4.0, and -28.0. Using

the unloaded Sikorsky S-61 $\mathbf{A}$ and $\mathbf{B}$ matrices results in the following gain matrix:

$$\mathbf{K} = \begin{bmatrix} 22.60 & 2.735 & -0.4642 & 1.464 & -0.1871 & 0.2352 \\ 1.339 & 0.1425 & -0.0163 & 2.083 & 0.2455 & 0.0551 \end{bmatrix} \tag{112}$$

The feedback controller could be designed using other techniques, but the pole placement technique proves simple and effective.

7.4.3.2 Prescribed Models

The prescribed model $\mathbb{G}_M$ determines how the designer intends the helicopter to respond to pilot commands. A model that yields the desired helicopter performance should be selected. However, the model should not be too aggressive. An overly-aggressive model will lead to commands that the helicopter actuators cannot produce. When the actuators cannot faithfully produce the commanded inputs, the helicopter will not follow the trajectory specified by the prescribed model.

A third-order model was selected that prescribes the desired helicopter attitude and attitude rate. This third-order model is a series combination of an underdamped second-order model and a first-order lag. The first-order lag is included to account for actuator dynamics, and effectively smooths the plant command, ensuring that the command can be produced by the helicopter rotor. The majority of the dynamics at the time scale of gross helicopter translation and attitude response is prescribed by the second-order underdamped model.

The prescribed third-order pitch and roll model is given by:

$$\dot{\vec{x}}_M = \begin{bmatrix} 0 & 1 & 0 \\ 0 & 0 & 1 \\ -\omega_n^2 \tau & -\left(\omega_n^2 + 2\zeta\omega_n\tau\right) & -(2\zeta\omega_n + \tau) \end{bmatrix} \vec{x}_M + \begin{bmatrix} 0 \\ 0 \\ 1 \end{bmatrix} \vec{r} \tag{113}$$

$$\vec{y}_M = \begin{bmatrix} \omega_n^2 \tau & 0 & 0 \\ 0 & \omega_n^2 \tau & 0 \end{bmatrix} \vec{x}_M$$

The pilot's attitude command is the input $\vec{r}$ to this model. Note that this model was designed to have a steady-state gain of unity, although this can be changed depending on the application and the source of the pilot's attitude command.

There are two of these third-order models in the control system, one each for the longitudinal and lateral channels. Each model is applied independently to the pilot's attitude command in that channel. The same first-order time constant, natural frequency, and damping ratio are used in the two models to give similar characteristics to the pitch and roll attitude responses.

The model parameters were selected to yield a damping ratio of 0.707 because this provides a good balance between fast rise time and low overshoot. A settling time t_s of 2.5 seconds was selected. Using this damping ratio and settling time, the natural frequency was found using the approximation:

$$t_s \approx \frac{4}{\omega_n \zeta} \tag{114}$$

Solving (114) with the selected damping ratio and settling time resulted in a corresponding natural frequency of 2.26 rad/s.

A first-order time constant of 0.125 seconds was selected. This time constant was slow enough to ensure that the helicopter rotor could respond to the commanded rotor tilt angles, while not significantly altering the performance characteristics prescribed by the second-order model.

The pitch and roll prescribed models are solved in real time by the controller, and both models output desired attitude and attitude-rate trajectories, $\vec{y}_M$. The result is pitch attitude, pitch rate, roll attitude, and roll rate trajectories prescribed by the models. Because the helicopter velocities are also needed to form the full state vector for inverting the unloaded model, the measured velocities of the plant are used. The attitude trajectories are combined with the measured longitudinal and lateral velocities to form the complete helicopter state vector. This state vector can be interpreted as the desired state trajectory.

7.4.3.3 Simulation Results and Controller Performance

Unloaded S-61 Performance

To evaluate the performance of this controller for the unloaded Sikorsky S-61 helicopter, a simultaneous pitch and roll maneuver was simulated. The pilot attitude command was designed to move the helicopter in both the longitudinal and lateral directions to a target

location, starting and stopping in hover. The attitude command has a maximum amplitude of 7.16 degrees, and this can be considered a small-to-moderate amplitude command.

Figure 97(a) shows the pilot command, the resulting response of the prescribed model, and the helicopter attitude response for the pitch channel. The pitch attitude tracks the prescribed model almost perfectly. Figure 97(b) shows the pilot command, the resulting response of the prescribed model, and the helicopter attitude response for the roll channel. As in the pitch channel, the roll attitude tracks the prescribed model almost perfectly. The controller also minimizes the coupling between the longitudinal and lateral motion of the
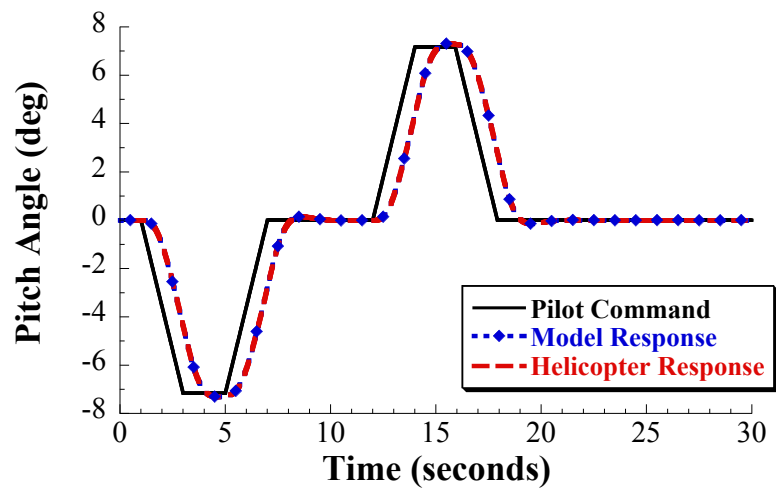
(a) Pitch Channel.
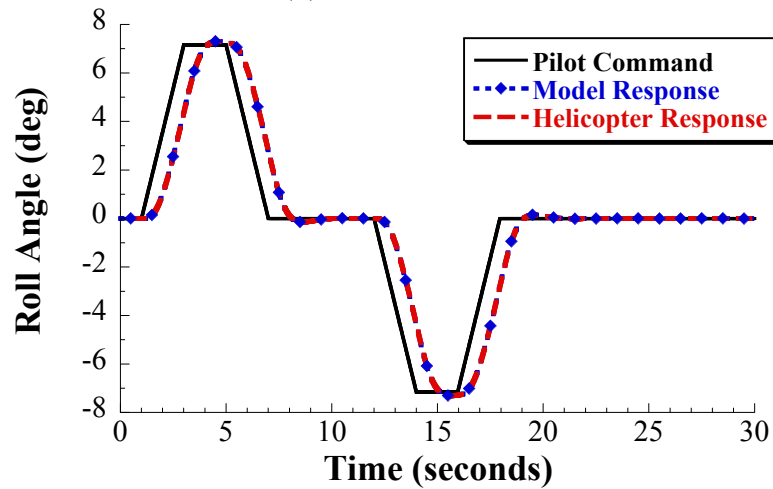
(b) Roll Channel.

Figure 97: Pilot Command, Prescribed Model Response, and Helicopter Attitude Response in (a) the Pitch Channel and (b) Roll Channel and for the Unloaded Sikorsky S-61

165

helicopter.

If the control effort required to execute this maneuver is too fast or has too large of an amplitude, then the quasistatic rotor assumption used in the modeling process may be inadequate for approximating the rotor dynamics. In other words, the commanded rotor disk angle may require the helicopter rotor to tilt faster than it can. Because the Sikorsky S-61 dynamic models do not fully model the rotor behavior or account for actuator limitations, the commanded rotor disk tilt angles need to be analyzed to verify that they are feasible. Due to the larger inertia of the helicopter about the pitch axis, it is expected that the command in the longitudinal channel will need to have a higher magnitude to produce the required forces and moments for prescribed model tracking and, therefore, the limits of the rotor are most likely to be exceeded in the longitudinal channel.

To investigate these actuator dynamics, the commands sent to the helicopter plant in the longitudinal and lateral directions are shown in Figure 98. As expected, the longitudinal command is more aggressive than the lateral command because the pitch inertia of the helicopter is larger than the roll inertia. Therefore, a larger-magnitude command is needed to accelerate the pitch states at the same rate as the roll states, as required by the prescribed models.

To verify that the control system requests feasible main rotor tilt angles, the commanded rotor disk angles must be further examined. The response of the rotor to control inputs
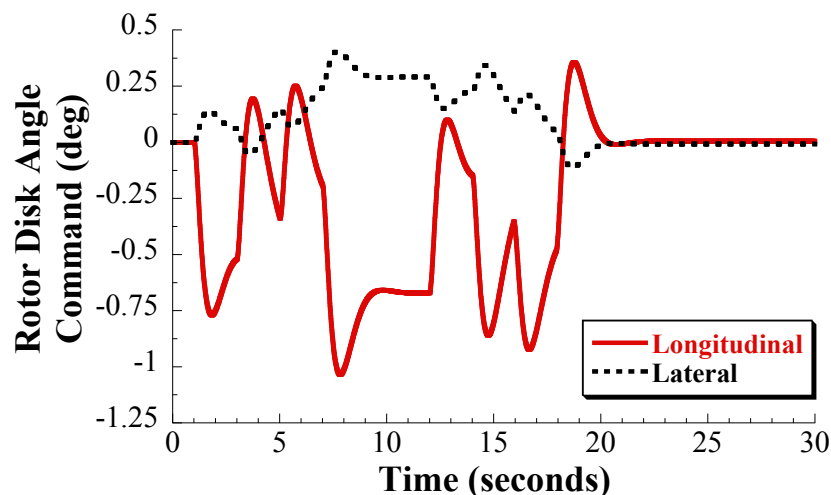
Figure 98: Longitudinal and lateral rotor disk angles for the unloaded Sikorsky S-61.

166

occurs on the same time scale as the rotor rotation rate. The time to half amplitude of the rotor tilt is on the order of 0.05 seconds [48], and the time constant of the rotor response is typically one quarter to one half of the rotor rotation period [78]. Half of the rotor rotation period for the Sikorsky S-61 main rotor is approximately 0.15 seconds [37]. The longitudinal command generated by the controller requires a rotor response with a time to half amplitude of approximately 0.4 seconds, which is almost three times slower than the rotor capability. Also, the maximum amplitude of the command is only 1 degree, which is a small rotor tilt angle. These results suggests that the controller is requesting feasible rotor tilt angles.

Loaded S-61 Performance

The performance of the load-carrying Sikorsky S-61 helicopter was investigated using the same controller and pilot commands as for the unloaded helicopter in the previous section. For feedback, the controller still uses only the unloaded helicopter states (pitch and roll attitudes and attitude rates, and longitudinal and lateral translational velocities). Measurements of the load states are not used by the controller.

Figure 99 shows the pilot command, the resulting response of the prescribed model, and the helicopter attitude response for the pitch and roll channels. The response in the pitch channel is shown in Figure 99(a). The pitch attitude tracking of the prescribed model is not significantly affected by the addition of a suspended load. This is due to the large pitch inertia of the helicopter resisting the moment applied by the swinging suspended load.

The response in the roll channel is shown in Figure 99(b). The roll attitude does not track the model response very well, particularly following the completion of the command. Following the command, there are residual roll attitude oscillations that have an amplitude of nearly 2 degrees. These oscillations are caused by the tension in the suspension cable supporting the load applying an oscillatory torque about the helicopter center of gravity as the load swings. In this sense, the load is acting like a disturbance applied to the helicopter.

According to ADS-33E-PRF design requirements [124], residual attitude oscillations larger than 0.5 degrees are considered excessive for any type of maneuver. As seen in Figure 99(a), the pitch attitude residual oscillation amplitude is less than 0.5 degrees, and
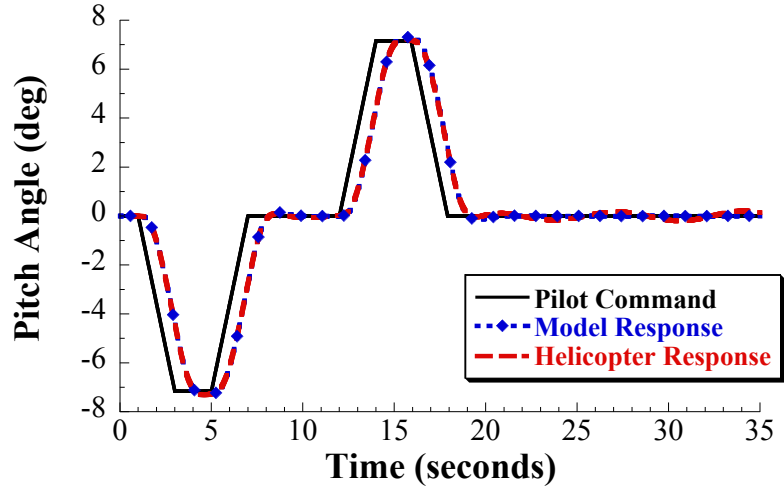
(a) Pitch channel.
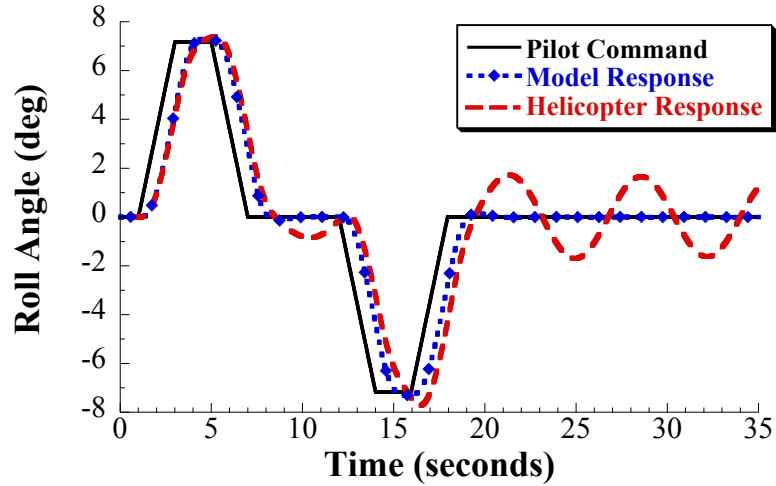
(b) Roll channel.

Figure 99: Pilot command and attitude response for the loaded Sikorsky S-61.

remains within ADS-33E-PRF requirements. However, the residual roll attitude oscillation amplitude is nearly 2 degrees, so it does not satisfy ADS-33E-PRF requirements.

Figure 100 shows the longitudinal and lateral load oscillation caused by the helicopter motion. The 65.6 ft suspension cable leads to a large-amplitude, low-frequency response of the load. The peak-to-peak amplitude of the load oscillation in both the pitch and roll directions is nearly 55 ft. This amount of load swing could be dangerous and hard for the pilot to control following the maneuver. It would also increase the time it takes for the pilot to set down the load, as he or she would have to wait for the load oscillation to damp out
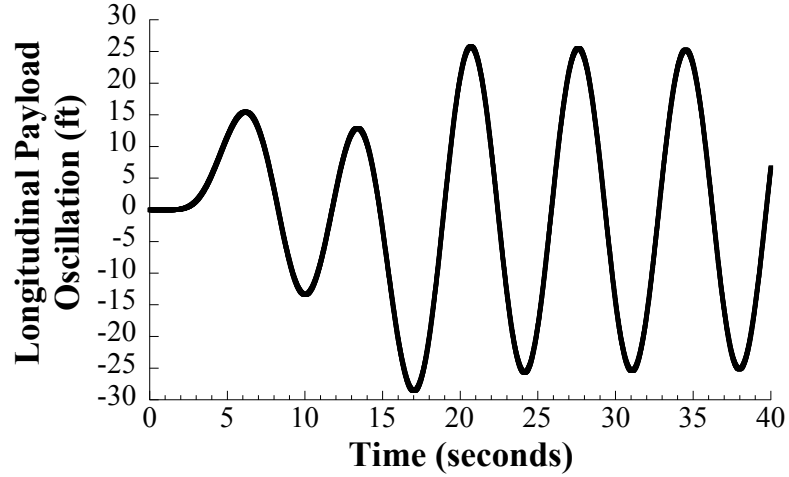
(a) Longitudinal load swing.
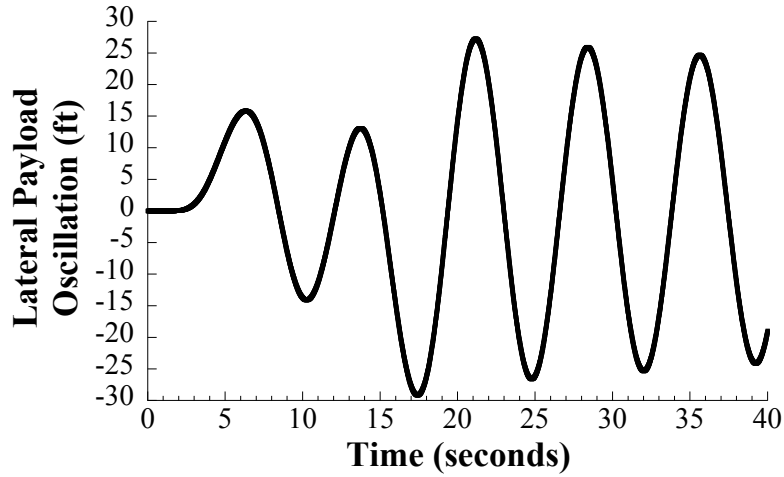
(b) Lateral load swing.

Figure 100: Suspended load swing in the (a) longitudinal and (b) lateral directions.

or actively move the helicopter to cancel out the swing before setting the load down.

The amount of residual attitude and load oscillation is dependent on properties of the pilot's commands, such as move distance and velocity. This means the amount of residual oscillation will vary depending on the pilot's commands, making the oscillations hard for the pilot to predict and thus difficult to control.

7.4.4 Combining Input-Shaping and Model-Following Control

The model-following controller does not address the load oscillation nor its disturbance-like effects on the model tracking error. To reduce the load oscillation, input shaping is added to the model-following controller. The model-following controller block diagram with input

shaping is shown in Figure 101. Input shaping is added to the controller between the pilot command and the prescribed model.

Effectively, this implementation builds input shaping into the prescribed model, and the model output is an input-shaped command that does not excite suspended load swing. The order of the input shaper and the prescribed model in the controller does not matter because input shapers and the chosen prescribed model are linear.

7.4.4.1 Input Shaper Design

To design an input shaper, the natural frequencies and damping ratios of the oscillation in the longitudinal and lateral directions are required. The log decrement method was applied to the data shown in Figure 100 to determine the natural frequency and damping ratio. The longitudinal load oscillation has a frequency of 0.907 rad/s and a damping ratio of 0.001. The lateral load oscillation has a frequency of 0.869 rad/s and a damping ratio of 0.007. The frequency is slightly different in the two directions because it mildly depends on the helicopter inertia, which is significantly different about the pitch and roll axes. Also, the lower inertia in the roll direction means that the backdrivability is higher.

It is worth noting here that the natural frequency and damping ratio are also partially influenced by the feedback control. The feedback controller tries to drive the model tracking error to zero. However, the load acts like a disturbance on the helicopter motion, as can be seen in Figure 99, because the load is coupled with the helicopter attitude and translation. This disturbance introduces an error between the trajectory specified by the prescribed
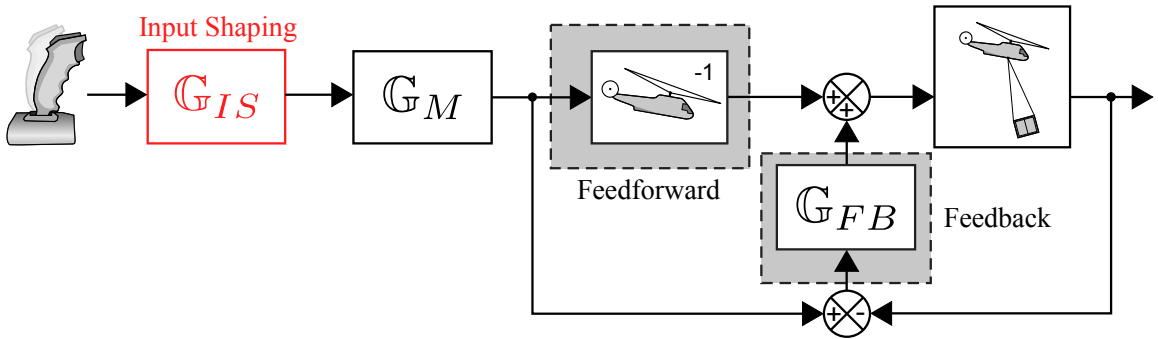
Figure 101: Combined input-shaping and model-following control for the load-carrying Sikorsky S-61 helicopter.

model and the actual helicopter states that the feedback controller attempts to eliminate. The feedback controller affects the load oscillation as the controller attempts to eliminate the model tracking error. It does so by adjusting the commands sent to the helicopter plant and therefore affects the motion of the helicopter and the load. This means the poles used to design the feedback controller and calculate the gain matrix $\mathbf{K}$ end up having a small effect on the motion of the load and its swing frequencies and damping ratio.

A ZV input shaper is selected for use in this model-following controller. The input shaper amplitudes and times are calculated from the load swing natural frequencies and damping ratios. A separate input shaper is used for the longitudinal and lateral load oscillations because their frequencies are somewhat different.

7.4.4.2 Simulation Results and Controller Performance with Input Shaping

Figure 102 shows the input-shaped pilot command, the resulting response of the prescribed model, and the helicopter attitude response for the pitch and roll channels with input shaping added to the model-following controller. The pitch response is shown in Figure 102(a). The pitch attitude tracking of the prescribed model is not as significantly affected as the roll channel by the addition of a suspended load, as was shown in Figure 99. Adding input shaping to the controller improves the tracking by reducing the small residual pitch attitude oscillations.

The real benefit, in terms of the attitude response, of adding input shaping to the controller is in the roll dynamics. The roll response is shown in Figure 102(b). The roll attitude tracking of the model response is greatly improved with input shaping added to the controller. As a result, the ADS-33E-PRF requirements for residual attitude oscillation amplitude are satisfied. With the residual attitude oscillations reduced, the addition of input shaping to the controller should make the response of the helicopter more predictable to the pilot.

Figure 103 compares the longitudinal and lateral load oscillation caused by the helicopter motion with and without input shaping. Input shaping significantly reduces the residual load oscillation in both the longitudinal and lateral directions. Note that there is a still
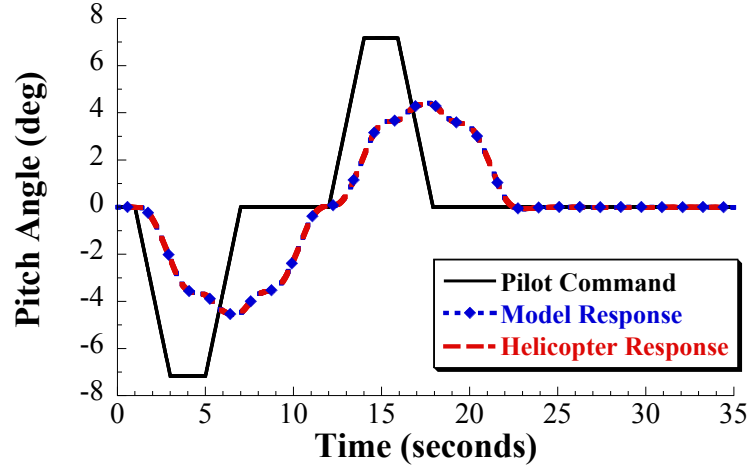
(a) Pitch channel.
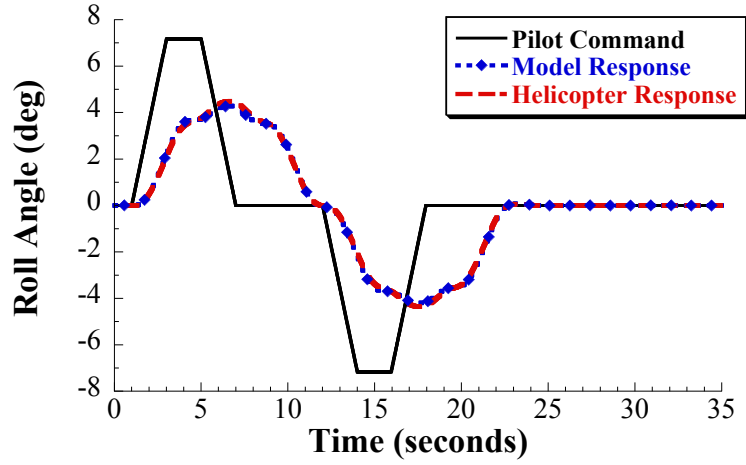
(b) Roll channel.

Figure 102: Pilot command and attitude response for the loaded Sikorsky S-61 with input shaping added to the model-following controller.

some transient swing that occurs during the command.

The effectiveness of input shaping is even more clear when looking at the load oscillation in two dimensions. Figure 104 shows the two-dimensional load oscillation. The oscillation is measured relative to the position of the helicopter, so it is what the pilot would see when looking down on the load. The small amount of swing that occurs in the ZV-shaped case is the transient oscillation.

When using input shaping, the helicopter comes to rest over the desired position at the end of the maneuver because the residual load swing is eliminated. Figure 105 shows the helicopter's position in the horizontal plane as the maneuver is executed with and

172
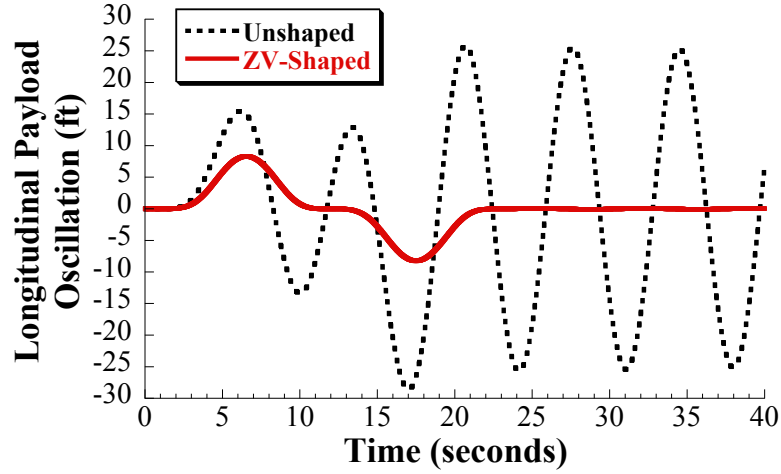
(a) Unshaped and ZV-shaped longitudinal load swing.
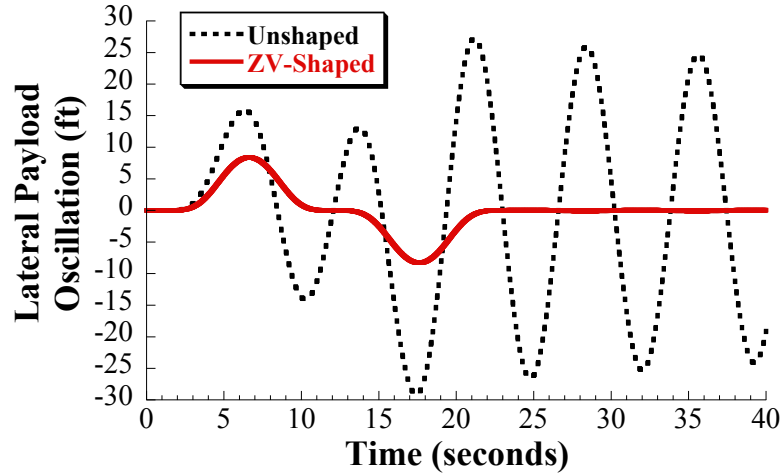
(b) Unshaped and ZV-shaped lateral load swing.

Figure 103: Unshaped and ZV-shaped suspended load swing in the (a) longitudinal and (b) lateral directions.

without input shaping. Figure 105(a) shows the helicopter traveling in the longitudinal and lateral directions during the maneuver. Figure 105(b) shows the helicopter's position at the end of the maneuver. In the unshaped case, the residual load swing back drives the helicopter, backdriving the helicopter around the desired position. In the input-shaped case, the helicopter comes to rest over the desired position. This occurs because the residual load swing has been eliminated, so the load does not backdrive the helicopter at the end of the maneuver. Because input shaping significantly reduces the residual load oscillation and results in the helicopter coming to rest over the desired position, it should decrease the
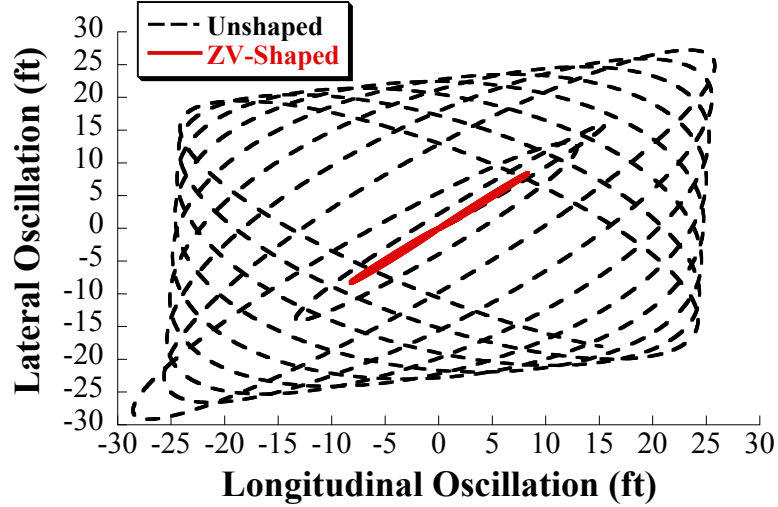
Figure 104: Unshaped and ZV-shaped two-dimensional load oscillation.

time it takes for the pilot to transfer a load from one location to another.

As with the controller for the unloaded helicopter, the control effort required to execute the maneuver should be examined. The command sent to the helicopter plant in the longitudinal and lateral channels is shown in Figure 106 with and without input shaping. Figure 106(a) shows the longitudinal command, and Figure 106(b) shows the lateral command. When there is no input shaping, the command is oscillatory and has a larger amplitude compared to the case with input shaping.

Backdriving effects on the helicopter cause error in the model tracking that the feedback controller tries to correct. This corrective action causes the command to have a larger amplitude and to be oscillatory. On the other hand, input shaping proactively eliminates the load swing before it significantly backdrives the helicopter, causing no need for extra corrective action from the feedback controller.

7.5 Discussion

While model-following control has been used in helicopter flight controllers since the 1960's, the implementation presented here for suspended-load control is unique. A model-following controller designed for an unloaded helicopter was combined with an input shaper designed to prevent suspended load oscillation in the longitudinal and lateral directions. The results
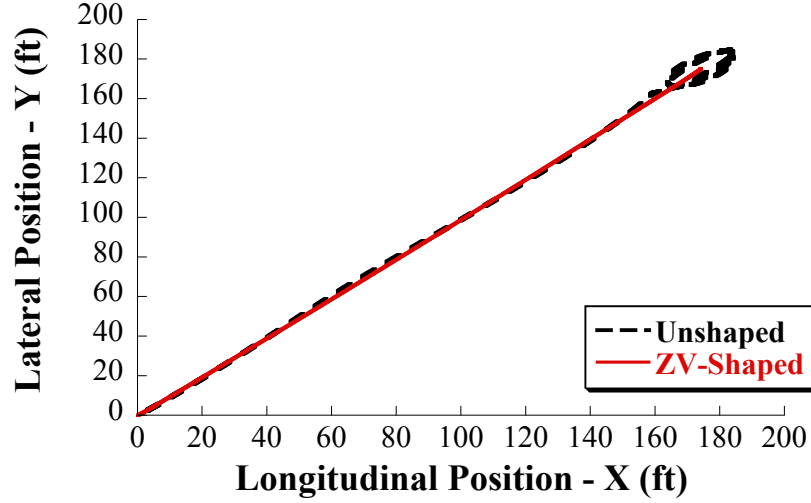
(a) Helicopter position during the maneuver.
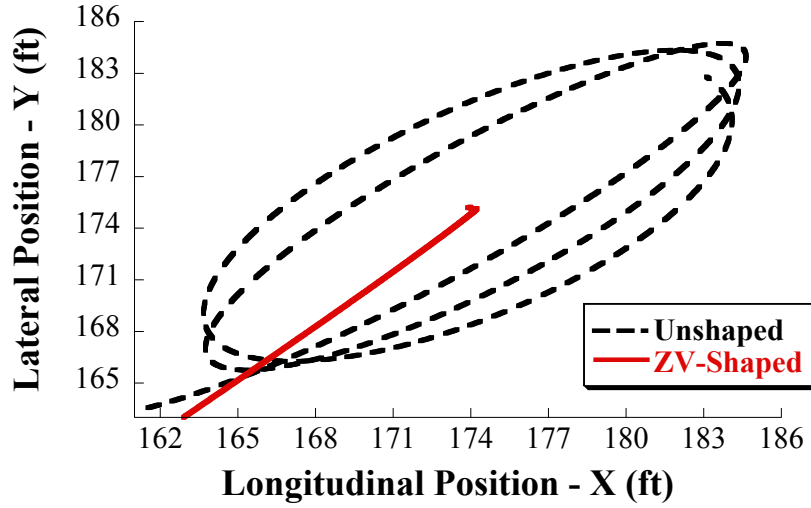
(b) Helicopter position at the end of the maneuver.

Figure 105: Helicopter position during and at the end of the maneuver.

show that the combined controller eliminates oscillations of a suspended load and improves tracking of the prescribed model by reducing backdriving effects.

This approach is effective because the model-following controller enables the motion of the aircraft to behave like the desired model, while the input shaper eliminates the undesirable oscillatory dynamics of the suspended load. In effect, an input-shaped prescribed model is used to achieve the desired helicopter response and critically damped load motion. By using input shaping to prevent load oscillation, the model-following control design can be accomplished using a model of the unloaded helicopter, which is much simpler than a
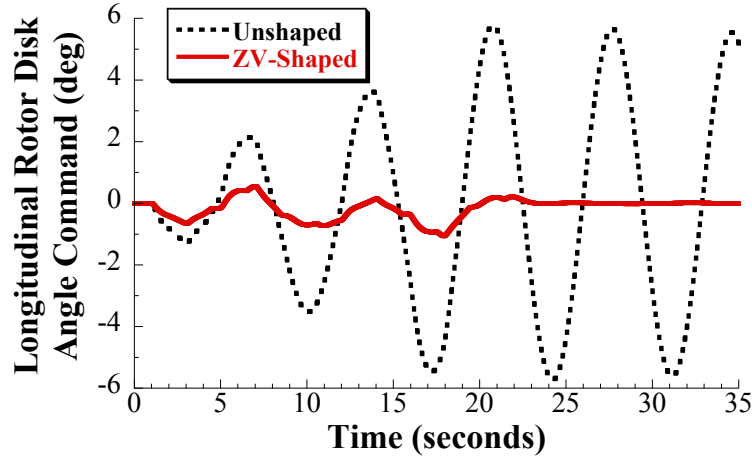
(a) Longitudinal command.
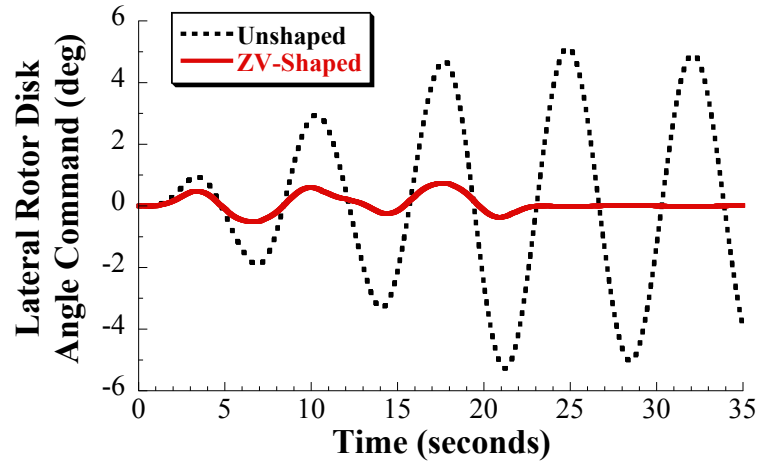
(b) Lateral command.

Figure 106: Control effort required by the model-following controller in the (a) longitudinal and (b) lateral channels for the loaded Sikorsky S-61.

model of a loaded helicopter.

Figure 107 compares the unshaped and input-shaped helicopter roll responses shown in Figures 99(b) and 102(b). While the unshaped response appears to more closely track the pilot's command during the transient motion, it results in residual oscillation of the load and backdriving of the attitude. The problematic characteristics of the pilot's command that result in the residual load oscillation are removed by applying ZV input shaping to the command. The addition of input shaping results in the ZV-shaped roll response shown in Figure 107. While the response with input shaping does not follow the pilot's transient command as closely, the helicopter completes the maneuver with almost no residual load
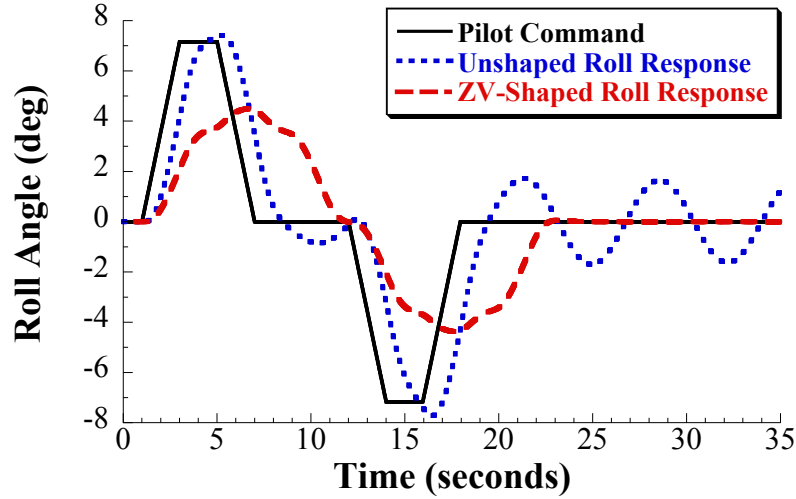
Figure 107: Comparison of unshaped and ZV-shaped helicopter roll responses.

oscillation, as is shown in Figure 103. Preventing suspended load oscillation also improves the residual helicopter attitude response because the effects of the load on the helicopter are reduced when the load swing is reduced. As a result, the maneuver is completed with almost no residual attitude oscillation.

The helicopter's response to pilot commands should be more predictable because the pilot does not need to account for the slow-period and large-amplitude load oscillations and their effects on the helicopter. The transient load oscillations are reduced, and the load hangs directly below the helicopter when it stops, as shown in Figures 103 and 104. This should make transferring a suspended load from one location to another safer, faster, and easier for the pilot. However, the response lag introduced by input shaping could make control more difficult for pilots. Past research on input shaping and operator learning suggests that operators are able to modify their control strategy, become accustomed to the response lag, and improve their overall performance [53, 54]. To fully analyze the effectiveness of the proposed control scheme, piloted evaluations and feedback must be obtained using piloted flight simulations to determine the handling qualities. Or, full evaluation of ADS-33E-PRF handling qualities requirements and flight characteristics should be determined to give an indication of the expected piloted performance. However, piloted evaluations would more effectively capture the expected learning effects.

Another significant benefit of this controller is that real-time measurement or estimation

of the suspended load states is not required. Input shaping proactively eliminates the residual swing of the suspended load, whereas a load-swing feedback controller would have to respond retroactively to measurements in the suspended load states in order to damp the load oscillation. The approach presented here simply requires an estimate of the load oscillation frequency and damping ratio in addition to the unloaded helicopter model.

One limitation of this study was the use of a helicopter model that was linearized about hover. Therefore, effects such as air drag, which should be incorporated for forward flight modeling, were weakened by the linearization. The results presented here could be further verified by using a full nonlinear model to simulate the helicopter plant. In addition, suspension cable length, load size and shape, helicopter/load mass ratio, and the location of the suspension point relative to the helicopter center of gravity will affect the natural frequency and damping ratio of load oscillation. Further studies are required to investigate the robustness of the input shaping and model-following approach to uncertainty in the load oscillation frequency and damping ratio. In addition, the effects of disturbances such as wind on the controller performance should be investigated.

7.6   Summary

Applying input shaping to simulated pilot commands greatly reduced oscillation of a helicopter's suspended load. By proactively eliminating load swing using input shaping, the helicopter response itself also improved because a swinging load can backdrive the helicopter attitude and position. The results showed that input shaping can be combined with a typical helicopter flight control system to proactively prevent suspended load oscillation and improve helicopter flight performance by reducing backdriving effects. The unique approach presented here combines the commonly-used control methods of model-following control and input shaping in a simple way to address the challenging control problems of suspended load oscillation and backdriving effects of the load on the helicopter. The combined controller eliminates the slow-period and large-amplitude load oscillations and their backdriving effects on the helicopter. The transient load oscillations are reduced, and the

load hangs directly below the helicopter when it stops. This should make transferring a suspended load from one location to another safer, faster, and easier for the pilot, but piloted simulations should be performed to fully verify this.

CHAPTER VIII

CONCLUSIONS AND FUTURE WORK

This chapter concludes the thesis by summarizing the methods and contributions, and proposes topics for future study.

8.1 Conclusions and Contributions

This thesis has clarified the backdriving dynamics that occur in systems with coupling between a rigid and flexible mode. A method for quantifying the degree of backdrivability was presented. Then, a method for controlling backdrivable flexible systems was demonstrated based on decreasing backdriving effects by reducing vibration using input-shaping techniques. Also, it was shown that input shaping can be combined with feedback controllers to improve the response of the rigid body or base of backdrivable flexible systems, while also limiting vibration.

Three fundamental models were developed that demonstrate backdriving effects. The models are i) Cart with Pendulum, ii) Rotary Hub with Flexible Arm, and iii) Cart with Inverted Pendulum. These models were used to develop two backdrivability performance metrics based on determining response ratios from mode shapes and complex poles and zeros. The metrics were applied to these models to evaluate their backdrivability, as a function of system parameter values. It was shown that increases in mass (or inertia) ratio of the flexible element relative to the rigid element lead to higher amounts of backdriving.

The Cart with Pendulum model was used to study crane trolley slip while braking. It was shown that slip should only occur for low braking coefficients of friction (< 0.4), high payload-to-trolley mass ratios, and large amounts of swing. The Rotary Hub with Flexible Arm model was used to develop and demonstrate a combination of input shaping and PD feedback control that reduces vibration of the flexible mode while also improving performance of the rigid body response through reduced overshoot and control effort. The closed-loop modal behavior of the PD feedback controller for the Rotary Hub with Flexible

Arm was studied to inform the design of the combined controller. Also, the Cart with Inverted Pendulum model was combined with a feedback controller to stabilize the system, and it was shown that feedback controllers can be a source of backdriving dynamics, in addition to physical flexibility.

A constant-amplitude input shaping method was developed for backdrivable flexible systems equipped with stepper motors (or other on-off actuators). The method provides increased robustness to frequency error, while also allowing the input shaper duration to be varied to reduce backdriving effects on the rigid body motion. The limitations that arise due to the constant-amplitude impulses were also shown, with the technique reducing vibration less effectively as the system damping ratio increases.

Finally, two demonstrative applications were presented. The first was a spacecraft with flexible appendages driven by stepper motors. Rigid body pointing error caused by backdriving effects when slewing flexible appendages is an important consideration for attitude control of flexible spacecraft. It was shown that a combination of PD attitude control and constant-amplitude shaping is effective at reducing vibration of the appendages and limiting the peak pointing error of the spacecraft main body response. The results showed that a large derivative gain should be selected because this yields a lower damping ratio according to the modal analysis of the PD feedback controller, and the constant-amplitude shapers limit oscillation most effectively when there is a single underdamped mode with a small closed-loop damping ratio. Additionally, the constant-amplitude shaper duration can be increased to achieve the minimum bus response possible in cases where the controller gains cannot be increased further. Increasing the shaper duration can allow the attitude controller more time to correct pointing error before additional steps are taken, while still preserving the vibration-reducing effects.

The second demonstrative application focused on helicopters carrying suspended loads. Backdriving effects due to load-attitude coupling can be a significant concern. Input shaping applied to an experimental model radio-controlled helicopter carrying a suspended load was shown to be effective at reducing suspended load swing and backdriving effects on the helicopter. Then, a combined input-shaping and model-following controller was developed

and evaluated in simulation using models of a Sikorsky S-61 helicopter. Analysis of the model eigenvectors showed that the backdriving effects of load-attitude coupling in the roll direction are more problematic than the pitch direction due to the lower helicopter inertia in that direction. The simulation results showed that the combined input-shaping and model-following controller improves performance by proactively eliminating the load swing, reducing backdriving effects and allowing the helicopter to better track the prescribed model.

In summary, the following contributions were made:

- Three illustrative and fundamental backdrivable system models that capture key response characteristics (Chapter II).

- An explanation of the dynamics of backdrivable flexible systems, using the three fundamental models to illustrate backdriving effects (Chapters II and III).

- Performance metrics for backdrivability based on determining system response ratios using mode shapes and based on complex poles and zeros (Chapter III).

- An optimized combination of a two-impulse input shaper and PD control for backdrivable flexible systems (Chapter IV).

- A constant-amplitude input shaping method for developing stepping sequences for stepper motors that can also be used to reduce backdriving effects, such as pointing error in flexible spacecraft attitude control systems (Chapters V and VI).

- Two demonstrative applications that illustrate the combination of input shaping and feedback control for spacecraft with flexible appendages driven by stepper motors and helicopters carrying suspended loads (Chapters VI and VII).

8.2 Future Work

The research in this thesis can be expanded in several ways. Other sources of backdrivability can be studied, such as due to fuel sloshing in spacecraft or in fuel trucks. By developing

fundamental models of these applications, the backdrivability performance metrics can be used to study and identify the key system parameters that contribute to backdriving effects.

The crane trolley slipping while braking analysis could be expanded and applied to inverted-pendulum transporter wheel slip. This would allow for studying the scenarios that lead to wheel slip. While reduced traction obviously results from lower coefficients of friction between the wheels and the ground, rider mass and inertia and pitch angle also contribute.

The combined two-impulse input shaping and PD feedback controller optimization could be expanded to also address robustness concerns. Input shapers are often designed to be robust to modeling errors in the natural frequency or other system parameters, and constraints could be included to enforce vibration reduction over a range of possible frequency or other parameter error. This requires using additional impulses in the input shaper, and may require adjustments to the multi-level optimization approach utilized to find solutions.

The combined input-shaping and model following controller for helicopters carrying suspended loads could also be studied with real pilots in flight simulators and, once it is shown to be safe in the simulators, on actual helicopters carrying suspended loads. This would allow pilots to evaluate the effectiveness of input shaping combined with the feedback controller in terms of the controllability of the helicopter and assessing the handling qualities. There is also potential for input shaping to cause pilot-induced oscillations as pilots adjust to its effects on their commands. However, it has been shown that the oscillations of the uncontrolled suspended load result in backdriving of the aircraft position and attitude, and backdriving can also result in pilot-induced oscillations [117]. If there is cause for concern about input shaping causing pilot-induced oscillations, then pilot simulation studies should be done to investigate whether the potential for pilot-induced oscillations caused by input shaping is worse than the potential for those caused by an uncontrolled suspended load backdriving the helicopter.

APPENDIX A

HAZARDS OF INVERTED-PENDULUM HUMAN TRANSPORTERS

When a product is a complex dynamic system that interacts directly with a human, engineers must consider the wide range of possible motions and forces that the device could exert on the human. Such an analysis goes beyond a simple thought exercise and requires detailed knowledge about the system dynamics and the operating environment. This appendix presents a list of hazards resulting from such an analysis of inverted-pendulum human transporters. The list of hazards is constructed by using knowledge of the dynamics and the mechanical design obtained through simulation and experimentation. However, the dynamics are so complex that the list is augmented with hazards that are revealed by studying accident videos posted on the Internet. A full hazard analysis of these failure modes and scenarios was performed in [101].

A.1 *Overview of Inverted-Pendulum Transporters*

Inverted-pendulum human transporters are devices that transport one person in a standing configuration. Figure 108 shows three such transporters: the Segway i167 in Figure 108(a), the Segway i2 in Figure 108(b), and the Ninebot Personal Transporter in Figure 108(c). The relatively low-speed (limited to approximately 5.59 m/s = 12.5 mph for the Segway) operation combined with an electric propulsion system makes two-wheeled inverted-pendulum transporters potential options for short-distance transportation on city streets, sidewalks, and inside buildings. The system is composed of mechanical components, sensors, a computerized controller, and a human operator. The device is driven by two wheels that are placed side-by-side, rather than the standard in-line configuration of bicycles, scooters, or motorcycles.

Figure 109 shows a schematic diagram of an inverted-pendulum transporter with the major components and directions labeled. When the operator leans forward, the device

(a) Segway i167.   **(b)** Segway i2.   **(c)** Ninebot Personal Transporter.

Figure 108: Two-Wheeled Inverted-Pendulum Human Transporters.

pitches forward. The machine senses the non-zero pitch angle condition and rotates the wheels forward in an attempt to get back under the center of gravity and stop the forward fall. In order to slow the rider down, the machine must first speed up in order to induce a backward pitch angle. The machine can then apply deceleration torques T_L and T_R to slow the wheels down without causing the operator to fall forward, or backward, off of the device. In order to turn, the wheels rotate at unequal speeds causing the system to yaw, and travel in an arc. If the system is not translating forward or backward, then the wheels can rotate in opposite directions to turn the machine in place.

With the side-by-side wheel configuration, the mechanical design of the transporter is inherently unstable at all speeds. Furthermore, it is not possible for the human operator to manually balance the machine. The sensors in the device must constantly measure the state of the machine and feed this information to the computer controller. The controller then uses this feedback signal to adjust the wheel speeds and maintain the forward/backward (pitch) falling motion within an acceptable envelope so that the device and rider do not fall over. Under a range of operating conditions, the system is mechanically stable in the side-to-side (roll) direction. Therefore, the computer does not attempt to control the rolling
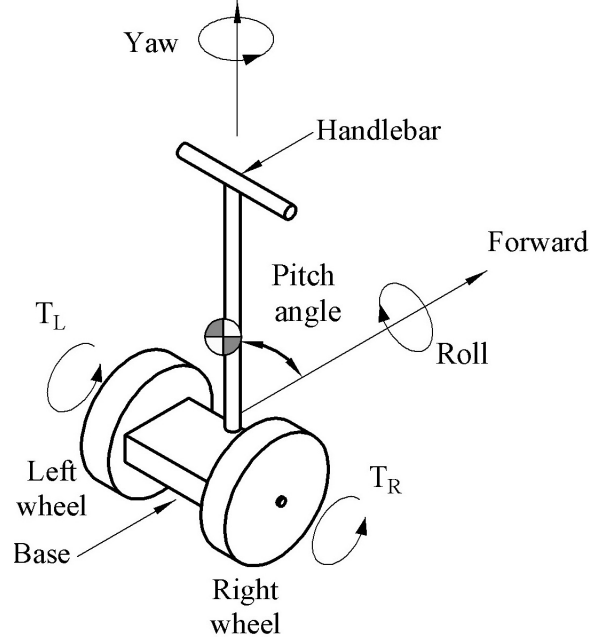
Figure 109: Schematic Diagram of an Inverted-Pendulum Human Transporter.

motion. In fact, the machine has no physical means to actively control the roll motion.

Given the unstable mechanical design and the complicated sensor and control system, the machine makes complex and unexpected motions in response to both movements of the rider and disturbances from the operating environment. Moreover, there are key differences between inverted-pendulum transporters and other transporters such as bicycles. The bicycle rider is the balancing control system, whereas the inverted-pendulum transporter utilizes an automated balancing controller. Also, a bicycle rider is able to put his or her feet down on either side of the bicycle, whereas the large wheels of inverted-pendulum transporters block the rider from stepping sideways.

A.2   Experimental and Simulation Studies

A.2.1   Experimental Results

It is difficult to accurately simulate the complex dynamic behavior of inverted-pendulum transporters. Some of the more challenging modeling aspects include: human operator motions, wheel slip, and external disturbances. Furthermore, it is challenging to experimentally investigate the behavior of inverted-pendulum transporters in most hazard scenarios due to the inherent danger. However, by testing such machines with an expert rider and using a

motion capture system to record its motions, illustrative examples of some hazard events have been recorded and analyzed [15, 16]. This section describes experimental results that illustrate the Segway's response during three example hazard events: roll instability, obstacle collision, and unexpected turns. The experiments led to the discovery of additional information about these hazard scenarios, such as how they occur and how a rider may react during the event.

During these experimental tests, a Vicon MX motion capture system was used to measure the position and orientation of a Segway i167 or i2 in real-time. The motion capture system consists of twelve MX-3+ cameras connected via two Vicon MX Ultranet HD units that stream camera data to a computer at 120 frames per second. The cameras tracked the position of reflective markers attached to the Segway. Vicon iQ version 2.5 software processed the camera data. The Segway's orientation, measured with respect to the global reference frame, was converted to Euler angles defined using the ZYX Tait-Bryan convention. The resulting position and orientation measurements were recorded. Each MX-3+ camera can record 659x493 grayscale pixels, and position measurements made using this system have a resolution of approximately 1 mm [127, 126].

A.2.1.1 Roll Instability

An inverted-pendulum transporter can experience roll instabilities when executing a turn. Figure 110 shows the Segway during a roll instability. One wheel has left the ground, and the rider is not able to balance the machine laterally.

To investigate the transporter response during turns, a Segway i2 was driven forward at a constant speed and then a 180-degree left turn was attempted. One might expect any roll instability to occur with the Segway and rider falling to the outside of the turn and the inside wheel leaving the ground. This form of roll instability typically happens when the rider does not lean into the turn. However, in these experiments roll instability occurred due to the rider *overleaning into the turn*. Leaning into the turn was necessary during the experiments to avoid a serious crash. However, in some cases the rider overcompensated and leaned too far. This resulted in the Segway rolling to the left (into the turn), and the

Figure 110: Segway roll instability.

right (outer) wheel leaving the ground.

Figure 111 shows the Segway forward speed, yaw rate, and base roll angle during a roll-unstable turning trial. Figure 111(a) shows the Segway traveling 2 m/s when the turn was initiated at 0.3 seconds. Figure 111(b) shows the yaw rate increasing as the turn was executed. When the yaw rate reached approximately 3.25 rad/s at 0.7 seconds, the Segway base suddenly rolled to the left. This can be seen in Figure 111(c), which shows the roll angle of the Segway base during the trial. The sudden change in roll angle at 0.7 seconds corresponds to the right (outer) wheel leaving the ground. The loss of contact between the wheel and the ground indicates a sudden loss of roll stability as a result of the rider overleaning into the turn.

The yaw rate began to oscillate as the rider attempted to recover from the instability while turning on one wheel. In this case, the expert rider was able to recover from the instability and continue the turn. The pair of smaller increases in roll angle around 1 second correspond to the right wheel bouncing once the right side of the Segway base fell back to the ground.

These results indicate that rider lean has a significant impact on roll instability. The roll instability may occur into or away from the turn depending on transporter speed, turning rate, and the amount of rider lean. Riders do not know the vehicle's current forward speed
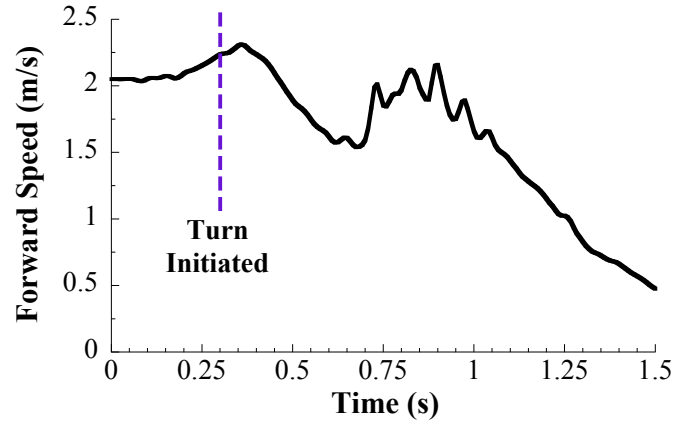
(a) Forward Speed.
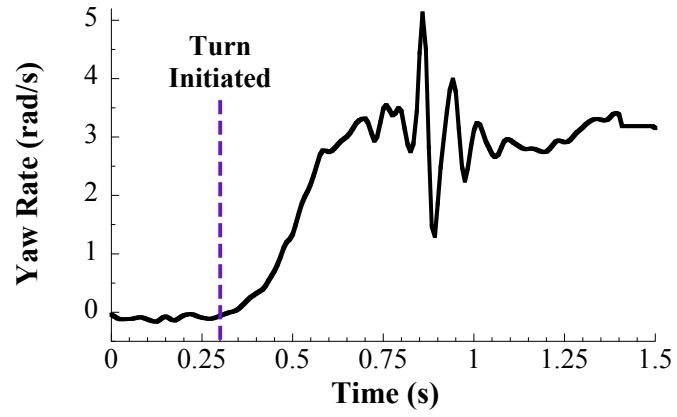
(b) Yaw Rate.
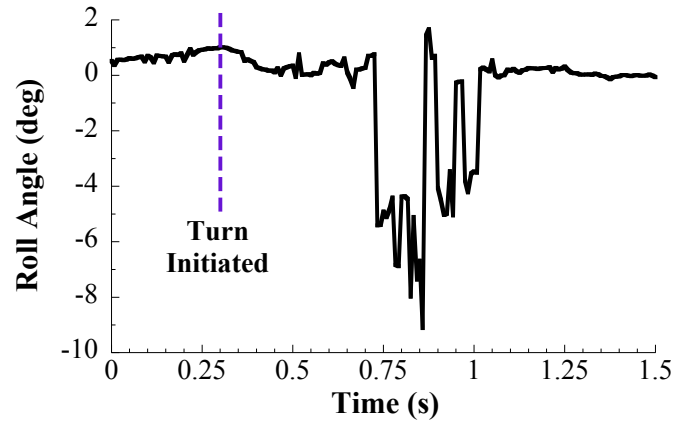
(c) Base Roll Angle.

Figure 111: Segway Forward Speed (a), Yaw Rate (b), and Base Roll Angle (c) during a roll-unstable turn [15].

or turning rate as the device does not display this information. While it is clear that there is an envelope of roll-stable rider lean and an appropriate amount of lean could be determined from the vehicle's forward speed and desired turning rate, it is up to the rider to estimate, and execute, an appropriate amount of lean in real time with no information about the vehicle speed or turning rate. It is difficult for inexperienced riders to know how much to lean into a turn without triggering a roll instability to either side, so experience with the transporter is required for riders to appropriately lean into turns. However, when turns occur unexpectedly, it is not possible for riders to compensate by intentionally leaning into them. Unexpected turns may be initiated by the machine (when riders accidentally pull or twist the handlebars) or the environment (when striking an obstacle). Such events are presented in Sections A.2.1.2 and A.2.1.3.

A.2.1.2   Obstacle Collision

Figure 112 shows an example response when the right wheel of the Segway hit a brick (laid flat in its lowest configuration). As shown in Figure 112(a), when the right wheel hit the bump at 1 second, the Segway's X-direction (forward) speed was reduced by the impact. In addition, its Y-direction (side-to-side) and Z-direction (vertical) speeds began to oscillate in response to the disturbance caused by the bump. Figure 112(b) shows the corresponding angular responses. The bump caused the Segway to pitch forward due to the horizontal force applied to the wheels by the bump while the momentum of the rider continued forward. In addition, the Segway turned toward the obstacle and experienced an oscillation in the roll direction. This example experimental response shows that the Segway turns unexpectedly even when it hits a relatively small obstacle.

A.2.1.3   Unexpected Turn when Pulling/Pushing Handlebars

On the Segway i167, the rider uses a twist steering grip to command turning (yawing) motions. A photo of the twist steer is shown in Figure 113. The rider can accidentally twist this steering grip when leaning forwards or backwards.

The response of the Segway i167 under these conditions was investigated experimentally. The expert rider leaned forward and simultaneously twisted the steering grip in the same
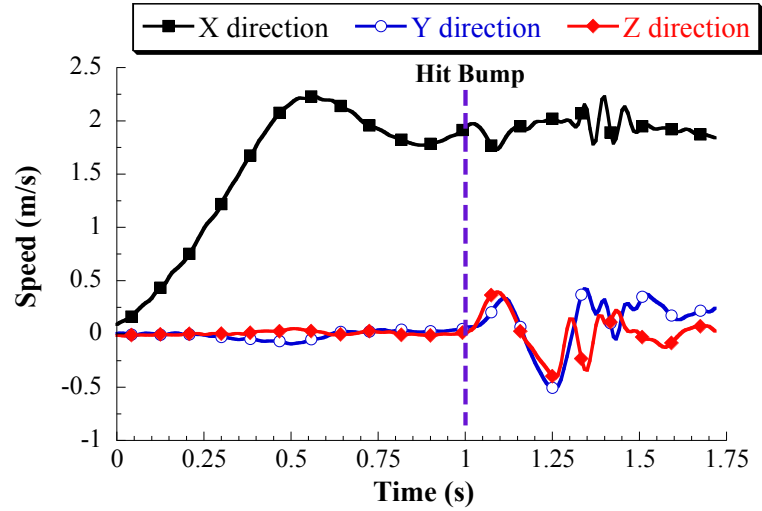
(a) Segway Speeds.
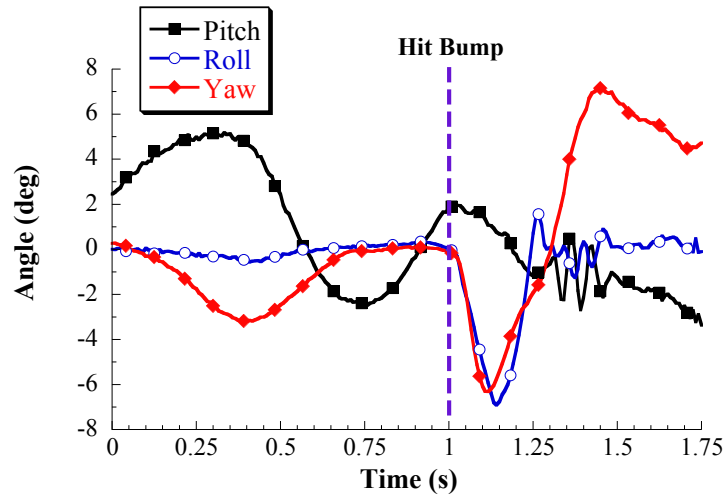
(b) Segway Orientation.

Figure 112: Segway speed and orientation during a single-wheel obstacle collision [15].

direction, which normally commands a left turn. Figure 114 shows the resulting Segway angular response. The Segway gently pitched forward due to the rider's forward lean, but sharply yawed to the left nearly 45 degrees in less than 1/2 seconds due to the sudden steering grip twist. This sharp turn caused a roll instability, which resulted in the left wheel of the Segway lifting off the ground and the Segway roll angle increasing to over 13 degrees. The expert rider (who was expecting the sharp turn) was able to wrestle the Segway back under control. These dangerous conditions could obviously dislodge an unsuspecting rider and cause an accident.
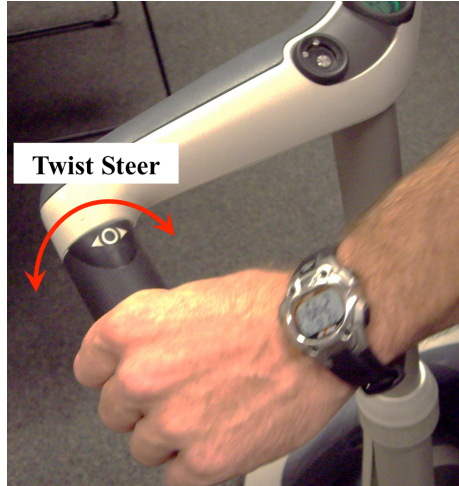
Figure 113: Segway i167 Twist Steering Grip.
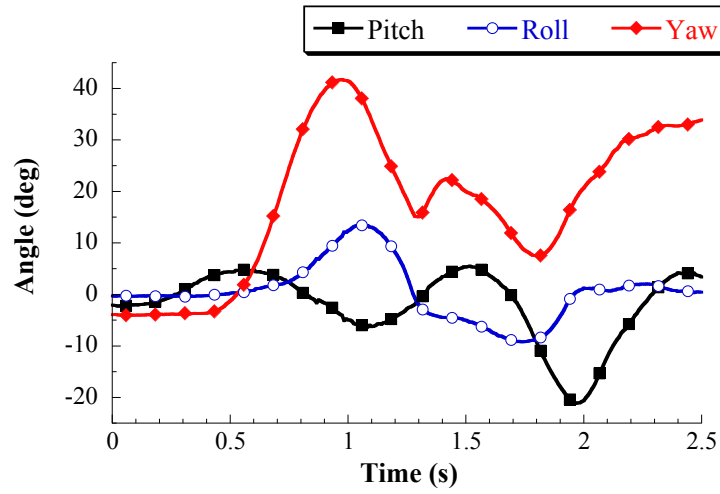
Figure 114: Segway angular response due to unexpected steering grip twist when leaning forwards [15].

A.2.2 Simulation Results

Some of the known hazards of inverted-pendulum transporters are difficult to safely test experimentally. Wheel slip is one such hazard. Therefore, numerical wheel slip simulations were used to study its effects.

A.2.2.1 Wheel Slip

Like any wheeled vehicle, the wheels of inverted-pendulum transporters can lose traction. When this occurs, the device can make unexpected motions. Slipping at a single wheel is particularly dangerous because it results in a yaw response that is difficult for the machine

and rider to control, as was shown in the previous section.

Figure 115 shows simulated yaw rate responses during wheel-slip events. These cases are based on the right wheel traveling over a medium friction surface with the machine moving at forward speeds of 1, 1.5 and 2 m/s. Yaw corresponds to turning left or right, with positive yaw and yaw rate defined as turning to the left. When traveling in a straight line and one wheel slips, the translational speeds of the wheels become unequal, so the device turns. When slip occurs at the right wheel, the device turns to the right as can be seen from the negative yaw rate response in Figure 115. For the case with a forward speed of 2 m/s, the resulting combination of forward speed and yaw rate caused the device to experience a roll instability with the right wheel coming off the ground in less than 0.2 s. At this point, the simulation was terminated because the dynamic model used to perform the simulations did not model the case of having one wheel off the ground. These simulations and the dynamic model used to perform them are described in more detail in [15, 16].

A.3 Hazards of the Segway Personal Transporter

Given the numerous complex actions that must be continually performed for inverted-pendulum human transporters to maintain balance, they have numerous failure modes. Many failures result in the rider falling off the device. However, other outcomes include: the device running into the rider after the rider has fallen from or stepped off the device,
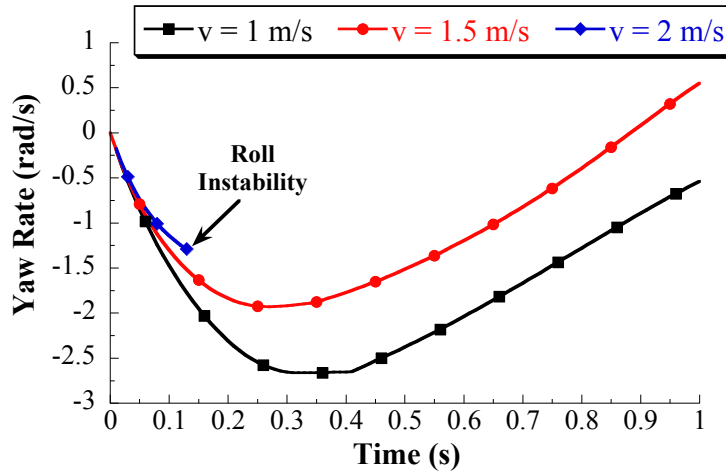
Figure 115: Segway yaw rate response with right wheel slip on a medium friction surface [15].

the device running into a nearby pedestrian, or the device damaging property.

A list of hazards was generated by examining the prior art of inverted pendulums, simulating inverted-pendulum transporter dynamic responses, conducting experiments on Segways, and examining the history of inverted-pendulum human transporter accidents available on the Internet (one significant source is YouTube videos). The list of failure modes is quite extensive, so this list focuses only on the dynamics-related hazards. (Hazards such as electronic chip failures and loose wires are not directly considered, although they could cause some of the hazards below.)

1. **The device will fall over if the user attempts to mount the device when it is not turned on.** The user will fall off because the transporter has no power to balance itself. This failure mode was made famous by President Bush in June 2003.

2. **The device turns off unexpectedly.** If the motors of the machine lose power for whatever reason, the machine will fall over in a short period of time and there is nothing the rider can do to balance the machine. The reasons for such a power failure are numerous. For example, when the battery power runs low, a Segway should sense this condition and initiate a "safety shutdown" procedure during which the device makes loud beeping noises, vibrations, and attempts to slow the transporter to a very low velocity. Under some conditions, the low-battery state is not properly sensed and the machine turns off quickly–without going through the safety shutdown procedure. The Segway was recalled in 2003 to fix an issue where the low-battery condition was not detected properly [22].

3. **The performance limits of the motors are exceeded.** When a person attempts to drive a traditional electric scooter (with a front-back inline wheel configuration) faster than the motor is capable of going, the scooter simply does not respond and keeps going at its top speed. Unfortunately, inverted-pendulum transporters react very differently when their motor limits are exceeded. For example, when an operator leans forward quickly, the center of mass of the person-vehicle system quickly moves in front of the base. In order to regain balance, the machine must accelerate forward,

Figure 116: Segway right wheel blocking rider's foot.

faster than the person, and attempt to position itself out in front of the center of mass so that the system starts to tip backwards. If the forward pitching angle is too large, then the motors cannot accelerate the wheels fast enough to regain balance. In such cases, a Segway shuts off without warning the rider. The control system is programmed to detect this condition and other conditions that are outside of the machine's ability to regain balance.

4. **The machine and/or rider experiences a roll instability when making turns.**
   At certain combinations of speed and turning radii, the device can roll to the side very suddenly, carrying with it a consequent loss of traction with one of the wheels. Even if the machine does not roll, the *rider* can experience a roll instability. Because of the large wheel hubs, riders cannot move their foot to the side to regain balance as they lean sideways. Figure 116 shows the right wheel blocking the rider's right foot as he tries to quickly step off the device to regain balance.

5. **The device makes an unexpected motion because one wheel loses traction.**
   If a wheel loses traction, then it cannot apply the correct forces to balance the system. If the wheel spins excessively, then the machine will turn off. Common ways to lose traction include: one wheel dropping off of a curb or into a pothole, and passing over

slick surfaces such as ice, sand, wet grass, and mud.

6. **The speed limiter**[1] **causes an unexpected motion.** Given the unstable mechanical design, the machine must speed up in order to slow down. When the machine decides that it needs to slow down to maintain the speed limit, the wheels must accelerate so as to move the base out in front of the person. This causes the handlebars to rotate backwards and push on the rider in an effort to tilt them backward. The machine can then start to slow the wheels down without pitching the rider off the front of the machine. This speed-limiting motion is not controlled by the rider. Therefore, this is an unexpected motion that could destabilize the person. Furthermore, the command to accelerate the wheels when the speed limiter is first engaged could lead to wheel slip. The Segway was recalled in 2006 for a stability problem originating from unexpected motion induced by the speed limiter [23].

7. **The machine makes an unexpected motion that causes one wheel to hit an obstacle.** In order to actively balance, the machine makes motions that the user does not control. These unexpected motions may drive the machine toward an obstacle. (The machine has no way of knowing that it is heading toward an obstacle.) If a wheel contacts an obstacle that stops the wheel from moving at its desired speed, then the machine cannot balance properly. The machine usually turns in the direction of the obstacle and pitches forward. In order to regain balance, the machine quickly accelerates off in the new direction. All of this occurs without control input from the rider. If the forward pitch is significant enough, then the machine will turn off and fall over without notifying the rider or going through the safety shutdown procedure (Hazard 3).

8. **The machine makes an unexpected turn when the operator pushes or pulls on the handlebars to accelerate the machine, or balance themselves.** These unexpected turns occur for three main reasons. First, the rider may accidentally twist the Segway i167 steering grip when pushing or pulling on the handlebars. Second,

---

[1]The Segway attempts to regulate its maximum speed by pushing back on the rider with the handle bars.

pulling on the handlebars in the sideways direction can generate a torque on the machine that lifts one of the wheels off the ground, or at least causes it to lose traction. When one wheel loses traction, the machine turns unexpectedly to the side. This situation is also represented by the roll instability shown in Figure 110. Third, the Segway i2 uses a tilting handlebar to induce turns, rather than a twist grip on the handlebar. Any unintended tilting of the handlebar, especially when the operator tries to stabilize themselves with the handlebars, will induce an unexpected turn by the machine.

9. **The machine runs into the rider.** This can happen if the rider steps off the device while unintentionally pulling back on the handlebars. This makes the device go backwards and run into the rider. This can also occur if a surface irregularity causes the rider to jump or fall off to the front of the device.

10. **The machine traps the rider's legs or feet when stepping off voluntarily, or when falling off during a low-speed accident.** An example of this is shown in Figure 117. The rider's right foot is trapped between the wheel and center divider on the platform while the Segway rotates and the rider has stepped off with the left foot.

11. **The device moves without a rider when in balance mode.** If the rider steps off the device and does not hold it while it is in balance mode, then the device can

Figure 117: Rider's feet trapped by wheel.

Figure 118: Segway moving without a rider in balance mode.

start moving. If this happens, then the device might run into, or over, nearby objects or people. Figure 118 shows a runaway Segway, with the rider chasing after it.

12. **The machine cannot balance properly if the rider stands too far away from the center of the platform.** If the rider inadvertently stands near the front of the platform, then the rider's center of mass is ahead of the transporter and causes it to pitch forwards. The rider is not able to pull back enough to counteract the forward lean, and the transporter races forwards. If the rider stands towards the rear of the platform, then a similar effects occurs and the transporter races backwards. Because the rider does not realize they are standing in the incorrect place, they have trouble regaining control. Many pull back on the handlebars to attempt to stop, which works on level ground. However, if the transporter is on a slope, then even strongly pulling back on the handlebars may not be enough to stop the forward motion.

There are several compounding factors that can occur during the above hazards. For example:

- The machine blocks the rider's arms during a fall from the device. This can be seen in Figure 119, where the rider's arm is blocked from extending out to catch herself.

- The wheels and the handlebars block the rider's feet and legs when trying to step off in a hazardous situation.

Figure 119: Segway handlebar blocking rider's arm.

Figure 120: Rider in a seated position on the Segway base.

- The rider may trip on or be knocked over by the transporter during or after a hazard event.

- The hazard may also result in the transporter and/or rider falling from an additional height, such as off a curb, down a flight of stairs, or over a cliff [20, 64, 113], depending on the surrounding environment.

- The rider may fall down onto the transporter base in a seated or prone position, as shown in Figure 120. The device expects to be balancing a standing person, and is not able to appropriately balance the low center of mass of the seated or prone person. This often results in the transporter racing forwards or backwards, depending on the position of the fallen rider on the device.

- The rider's foot may get trapped or run over by one of the wheels, as shown in

Figure 117. This may happen as the rider attempts to step off the device when a hazard occurs.

These compounding factors are likely to increase the severity of an outcome if one occurs during a hazard event.

A.4 Analysis of Accident Videos on the Internet

In the process of generating the list of inverted-pendulum transporter hazards, a collection of 43 videos posted to the Internet was analyzed. The videos were used to help identify hazards and complicating factors. Table 10 shows the number of occurrences of each hazard in the collection of videos. Note that each video could show instances where more than one hazard occurred (so the total number of occurrences sums to larger than 43). The frequency shows how often each hazard appeared in the video collection, and was calculated from the number of occurrences divided by the number of videos. In many accident videos, the occurrence of one hazard would trigger others. The videos demonstrated instances where up to four hazards occurred within a few seconds of each other, or simultaneously. Roll instability, obstacle collision, loss of traction, and unexpected turns due to pulling/pushing on the handlebars were the most commonly seen hazards in the videos.

Table 10: Hazard occurrence in 43 accident videos.

Hazard	Hazard Description	Number of Occurrences	Frequency
1	Stepping On with No Power	1	2%
2	Unexpected Shut-Off	4	9%
3	Motor Performance Limits Exceeded	9	21%
4	Roll Instability During Turns	17	40%
5	Loss of Traction	11	26%
6	Unexpected Motion due to Speed Limiter	1	2%
7	Obstacle Collision due to Unexpected Motion	16	37%
8	Unexpected Turn when Pulling/Pushing Handlebars	11	26%
9	Device Runs into Rider when Stepping Off	3	7%
10	Feet/Leg Trapping	8	19%
11	Moving without a Rider in Balance Mode	5	12%
12	Standing Off-Center on the Platform	3	7%

Analysis of the videos was most useful for discovering unexpected hazards and complicating factors associated with inverted-pendulum transporters. Due to the complicated and unstable motion of the device and the unpredictable response and motion of the rider, some of the hazards and complicating factors would be difficult to anticipate. For example, the rider falling into a seated or prone position on the transporter base was a complicating factor discovered in these videos. Also, many of the videos show significant backdriving of the transporter base can occur before and during accidents.

It is worth noting that videos posted to the Internet do not give a complete picture of the hazard probability. If footage is not considered entertaining, then it is less likely to attract views and thus might not be posted on the Internet. For example, the four most common hazards shown in the collection of videos–roll instability, obstacle collision, loss of traction, and unexpected turns due to pulling/pushing on the handlebars–represent cases of interesting, complex, and/or "entertaining" motion that will attract views on the Internet. On the other hand, only five videos featured Hazard 11: the transporter moving without a rider in balance mode. Using the device for a short period of time (or watching others use it) in everyday environments reveals that Hazard 11 actually occurs more frequently than this analysis of the videos suggests. In addition, Hazards 6 and 12 can be difficult to detect in videos. In most cases it is unclear if the speed limiter was engaged, and most videos do not clearly show the position of the rider's feet on the platform.

REFERENCES

[1] ADAMS, C., POTTER, J., and SINGHOSE, W., "Modeling and input shaping control of a micro coaxial radio-controlled helicopter carrying a suspended load," in *12th International Conference on Control, Automation, and Systems*, (Jeju, South Korea), pp. 645–650, 2012.

[2] ADAMS, C., POTTER, J., and SINGHOSE, W., "Input-shaping and model-following control of a helicopter carrying a suspended load," *AIAA Journal of Guidance, Control, and Dynamics*, vol. 38, no. 1, pp. 94–105, 2015.

[3] ANDERSON, C. W., "Learning to control an inverted pendulum with connectionist networks," in *American Control Conference*, (Atlanta, GA), pp. 2294–2298, June 1988.

[4] ARMSTRONG, D., "The Segway: A Bright Idea, But Business Model Wobbles," The Wall Street Journal, February 12, 2004.

[5] ARMSTRONG-HELOUVRY, B., *Control of machines with friction.* The Kluwer international series in engineering and computer science ; SECS 128. Robotics, Boston: Kluwer Academic Publishers, 1991.

[6] BAGDANOFF, J. L. and CITRON, S. J., "Experiments with an inverted pendulum subject to random parametric excitation," *Journal of the Acoustical Society of America*, vol. 38, pp. 447–452, 1965.

[7] BANERJEE, A., PEDREIRO, N., and GONZALEZ, M., "Simultaneous optimization of input shaping and feedback control for slewing flexible spacecraft," in *American Control Conference*, vol. 6, (Denver, CO), pp. 4796–4801 vol.6, 2003.

[8] BANERJEE, A. K., "Dynamics and control of the WISP shuttle-antennae system," *J. Astronaut. Sci.*, vol. 41, no. 1, pp. 73–90, 1993.

[9] BANERJEE, A. and SINGHOSE, W., "Command shaping in tracking control of a two-link flexible robot," *AIAA Journal of Guidance, Control, and Dynamics*, vol. 21, no. 6, pp. 1012–1015, 1998.

[10] BHAT, M. K. P., LIU, T. Y., and PLESCIA, C. T., "Solar array stepping to minimize array excitation," June 27 1989. U.S. Patent 4843294.

[11] BISGAARD, M., LA COUR-HARBO, A., and DIMON BENDTSEN, J., "Adaptive control system for autonomous helicopter slung load operations," *Control Engineering Practice*, vol. 18, no. 7, pp. 800–811, 2010.

[12] BONIFACE, K., MCKAY, M. P., LUCAS, R., SHAFFER, A., and SIKKA, N., "Serious injuries related to the Segway personal transporter: A case series," *Annals of Emergency Medicine*, vol. 57, no. 4, pp. 370–374, 2011.

[13] BROWN, E., "The Flying Crane," in *The Helicopter in Civil Operations*, ch. 6, pp. 56–70, New York: Van Nostrand Reinhold Co., 1981.

[14] CANNON, D. W., MAGEE, D. P., BOOK, W. J., and LEW, J. Y., "Experimental study on micro/macro manipulator vibration control," in *Proceedings of IEEE International Conference on Robotics and Automation*, vol. 3, (Minneapolis, MN), pp. 2549–2554, 1996.

[15] CASTRO, A., "Modeling and dynamic analysis of a two-wheeled inverted-pendulum," Master's Thesis, Georgia Institute of Technology, Atlanta, GA, 2012.

[16] CASTRO, A., SINGHOSE, W., POTTER, J., and ADAMS, C., "Modeling and experimental testing of a two-wheeled inverted-pendulum transporter," in *ASME Dynamic Systems and Control Conference*, (Fort Lauderdale, FL), 2012.

[17] CHANG, D., RHEE, T., NAM, K., CHANG, K., LEE, D., and JEONG, S., "A study on availability and safety of new propulsion systems for LNG carriers," *Reliability Engineering & System Safety*, vol. 93, no. 12, pp. 1877–1885, 2008.

[18] CHU, Z., CUI, J., REN, S., and GE, S. S., "Semi-physical experimental study of adaptive disturbance rejection filter approach for vibration control of a flexible spacecraft," *Proceedings of the Institution of Mechanical Engineers, Part G: Journal of Aerospace Engineering*, vol. 229, no. 11, pp. 2085–2094, 2015.

[19] CHU, Z. and HU, J., "An improved recursive least square?based adaptive input shaping for zero residual vibration control of flexible system," *Advances in Mechanical Engineering*, vol. 8, no. 4, p. 1687814016646504, 2016.

[20] CNN, "Segway company owner dies in apparent segway accident," 2010.

[21] COLLINS, J. D., "Risk analysis methodologies developed for the U.S. Department of Defense," *Reliability Engineering & System Safety*, vol. 20, no. 2, pp. 87–115, 1988.

[22] COMMISSION, C. P. S., "CPSC, Segway LLC announce voluntary recall to upgrade software on Segway$^{\text{TM}}$ human transporters," 2003.

[23] COMMISSION, C. P. S., "Segway Inc. announces recall to repair Segway® personal transporters," 2006.

[24] DEPARTMENT OF DEFENSE, "MIL-STD-882D: Standard Practice for System Safety," tech. rep., 2000.

[25] DIETER, G. E. and SCHMIDT, L. C., *Engineering Design*. New York, NY: McGraw-Hill, 4th ed., 2009.

[26] DOHERTY, M. J. and TOLSON, R. H., "Input shaping to reduce solar array structural vibrations," Tech. Rep. CR-1998-208698, NASA Langley Research Center, August 1998.

[27] DRAPEAU, V. and WANG, D., "Verification of a closed-loop shaped-input controller for a five-bar-linkage manipulator," in *IEEE International Conference on Robotics and Automation*, (Atlanta, GA), pp. 216–221, May 1993.

[28] DUKES, T. A., "Maneuvering heavy sling loads near hover part I: Damping the pendulous motion," *Journal of the American Helicopter Society*, vol. 18, no. 2, pp. 2–11, 1973.

[29] DUKES, T. A., "Maneuvering heavy sling loads near hover part II: Some elementary maneuvers," *Journal of the American Helicopter Society*, vol. 18, no. 3, pp. 17–22, 1973.

[30] FUJIOKA, D. and SINGHOSE, W., "Input-shaped model reference control of a nonlinear time-varying double-pendulum crane," in *10th Asian Control Conference (ASCC)*, (Kota Kinabalu, Malaysia), May 31-June 3 2015.

[31] FUJIOKA, D. and SINGHOSE, W., "Performance comparison of input-shaped model reference control on an uncertain flexible system," in *12th IFAC Workshop on Time Delay Systems*, vol. 48, (Ann Arbor, MI), pp. 129–134, June 28-30 2015.

[32] GARCIA, A., SINGHOSE, W., and FERRI, A., "Three-dimensional dynamic modeling and control of off-centered bridge crane lifts," *Journal of Dynamic Systems, Measurement, and Control*, vol. 139, no. 4, pp. 041005–041005–9, 2017.

[33] GORINEVSKY, D. and VUKOVICH, G., "Nonlinear input shaping control of flexible spacecraft reorientation maneuver," *AIAA Journal of Guidance, Control, and Dynamics*, vol. 21, no. 2, pp. 264–270, 1998.

[34] GRASSER, F., D'ARRIGO, A., COLOMBI, S., and RUFER, A. C., "JOE: A mobile, inverted pendulum," *IEEE Transactions on Industrial Electronics*, vol. 49, pp. 107–114, February 2002.

[35] GUPTA, N. K. and BRYSON JR., A. E., "Near-hover control of a helicopter with a hanging load," *Journal of Aircraft*, vol. 13, pp. 217–222, March 1976.

[36] HA, Y.-S. and YUTA, S., "Trajectory tracking control for navigation of the inverse pendulum type self-contained mobile robot," *Robotics and Autonomous Systems*, vol. 17, no. 1-2, pp. 65–80, 1996.

[37] HALL JR., W. E. and BRYSON JR., A. E., "Inclusion of rotor dynamics in controller design for helicopters," *Journal of Aircraft*, vol. 10, pp. 200–206, April 1973.

[38] HAMEL, P. G. and KALETKA, J., "Advances in rotorcraft system identification," *Progress in Aerospace Sciences*, vol. 33, pp. 259–284, March-April 1997.

[39] HOH, R. H., HEFFLEY, R. K., and MITCHELL, D. G., "Development of handling qualities criteria for rotorcraft with externally slung loads," U.S. Army RDECOM No. AFDD/TR-06-003, NASA Ames Research Center, 2006.

[40] HONG, S. W. and CURTISS JR, H. C., "An analytic modeling and system identification study of rotor/fuselage dynamics at hover," *Mathematical and Computer Modelling*, vol. 19, pp. 47–67, February 1994.

[41] HORN, J. F. and BRIDGES, D. O., "A model following controller optimized for gust rejection during shipboard operations," in *American Helicopter Society 63rd Annual Forum*, (Virginia Beach, VA), American Helicopter Society, May 2007.

[42] HOU, Z., GENG, Y., and HUANG, S., "Minimum residual vibrations for flexible satellites with frequency uncertainty," *IEEE Transactions on Aerospace and Electronic Systems*, vol. 54, pp. 1029–1038, April 2018.

[43] HUEY, J. R. and SINGHOSE, W., "Trends in the stability properties of CLSS controllers: A root-locus analysis," *IEEE Transactions on Control Systems Technology*, vol. 18, no. 5, pp. 1044–1056, 2010.

[44] HUEY, J. R. and SINGHOSE, W., "Design of proportional-derivative feedback and input shaping for control of inertia plants," *IET Control Theory & Applications*, vol. 6, no. 3, pp. 357–364, 2012.

[45] HUEY, J. R., SORENSEN, K. L., and SINGHOSE, W. E., "Useful applications of closed-loop signal shaping controllers," *Control Engineering Practice*, vol. 16, no. 7, pp. 836–846, 2008.

[46] HYDE, J. and SEERING, W., "Using input command pre-shaping to suppress multiple mode vibration," in *IEEE International Conference on Robotics and Automation*, vol. 3, (Sacramento, CA), pp. 2604–2609, Apr. 1991.

[47] IVLER, C. M., *Design and Flight Test of a Cable Angle Feedback Control System for Improving Helicopter Slung Load Operations at Low Speed*. PhD thesis, Stanford University, Aeronautics and Astronautics, Stanford, CA, Oct. 2012.

[48] JOHNSON, W. in *Helicopter Theory*, pp. 622–623, New York: Dover, 1994.

[49] JONES, S. and ULSOY, A. G., "An approach to control input shaping with application to coordinate measuring machines," *ASME Journal of Dynamic Systems, Measurement, and Control*, vol. 121, pp. 242–247, Jun. 1999.

[50] KALMUS, H., "The inverted pendulum," *American Journal of Physics*, vol. 38, no. 7, p. 874, 1970.

[51] KAZIMI, F., RECKDAHL, K., LIU, T., LEUNG, Y. F., and HIGHAM, J., "Spacecraft and appendage stepping methods that improve spacecraft attitude pointing and cancel solar array slew disturbances," November 6 2001. U.S. Patent 6311929.

[52] KENISON, M. and SINGHOSE, W., "Concurrent design of input shaping and proportional plus derivative feedback control," *Journal of Dynamic Systems, Measurement, and Control*, vol. 124, no. 3, pp. 398–405, 2002.

[53] KHALID, A., HUEY, J., SINGHOSE, W., LAWRENCE, J., and FRAKES, D., "Human operator performance testing using an input-shaped bridge crane," *ASME Journal of Dynamic Systems, Measurement, and Control*, vol. 128, pp. 835–841, Dec. 2006.

[54] KIM, D. and SINGHOSE, W., "Performance studies of human operators driving double-pendulum bridge cranes," *Control Engineering Practice*, vol. 18, pp. 567–576, Jun. 2010.

[55] LANDIS, K. H., DAVIS, J. M., DABUNDO, C., and KELLER, J. F., "Advanced flight control research and development at Boeing Helicopters," in *Advances in Aircraft Flight Control* (TISCHLER, M. B., ed.), ch. 4, pp. 103–141, Bristol, PA: Taylor & Francis, 1996.

[56] LOWENSTERN, E. R., "Stabilising effect of imposed oscillations on a dynamical system," *Philosophical Magazine*, vol. 13, pp. 458–486, 1932.

[57] MAGEE, D. P. and BOOK, W. J., "Filtering micro-manipulator wrist commands to prevent flexible base motion," in *Proceedings of the 1995 American Control Conference*, vol. 1, (Seattle, WA), pp. 924–928, June 21-23 1995.

[58] MAR, R., GOYAL, A., NGUYEN, V., YANG, T., and SINGHOSE, W., "Combined input shaping and feedback control for double-pendulum systems," *Mechanical Systems and Signal Processing*, vol. 85, pp. 267–277, 2017.

[59] MCCAHAN, S., ANDERSON, P., KORTSCHOT, M., WEISS, P. E., and WOODHOUSE, K. A., *Designing Engineers: An Introductory Text*. Hoboken, NJ: John Wiley & Sons, Inc., 2015.

[60] MELLENGER, A., "Segway crash." https://www.youtube.com/watch?v=BD-y8F1Fa7g, Dec. 2, 2006. Accessed: 2018-09-17.

[61] MILES, J., "Directly forced oscillations of an inverted pendulum," *Physics Letters A*, vol. 133, no. 6, pp. 295 – 297, 1988.

[62] MORRELL, J. B. and FIELD, D., "Design of a closed loop controller for a two wheeled balancing transporter," in *Proceedings of the 2007 IEEE/RSJ International Conference on Intelligent Robots and Systems*, (San Diego, CA, USA), Oct 29 - Nov 2 2007.

[63] MORROW, L. D. and BALASUBRAMANIAN, R., "Real model following control," *Journal of Aircraft*, vol. 12, no. 12, pp. 996–998, 1975.

[64] MSNBC.COM, "Segway company owner rides scooter off cliff, dies," 2010.

[65] MURPHY, B. R. and WATANABE, I., "Digital shaping filters for reducing machine vibration," *IEEE Transactions on Robotics and Automation*, vol. 8, no. 2, pp. 285–289, 1992.

[66] MURPHY, R. D. and NARENDRA, K. S., "Design of helicopter stabilization systems using optimal control theory.," *Journal of Aircraft*, vol. 6, no. 2, pp. 129–136, 1969.

[67] ORSZULIK, R. and SHAN, J., "Vibration control using input shaping and adaptive positive position feedback," *AIAA Journal of Guidance, Control, and Dynamics*, vol. 34, no. 4, pp. 1031–1044, 2011.

[68] OSDER, S. and CALDWELL, D., "Design and robustness issues for highly augmented helicopter controls," *AIAA Journal of Guidance, Control, and Dynamics*, vol. 15, no. 6, pp. 1375–1380, 1992.

[69] OTTANDER, J. A. and JOHNSON, E. N., "Precision slung cargo delivery onto a moving platform," in *AIAA Modeling and Simulation Technologies Conference*, (Toronto, Canada), 2-5 August 2010. AIAA Paper 2010-8090, doi: 10.2514/6.2010-8090.

[70] PADFIELD, G. D., *Helicopter Flight Dynamics: The Theory and Application of Flying Qualities and Simulation Modeling*. AIAA Educational Series, Washington, DC: American Institute of Aeronautics and Astronautics, Inc., 1996.

[71] Park, I.-W., Kim, J.-O., Oh, M.-H., and Yang, W., "Realization of stabilization using feed-forward and feedback controller composition method for a mobile robot," *International Journal of Control, Automation and Systems*, vol. 13, no. 5, pp. 1201–1211, 2015.

[72] Pat-Cornell, E. and Fischbeck, P. S., "Probabilistic risk analysis and risk-based priority scale for the tiles of the space shuttle," *Reliability Engineering & System Safety*, vol. 40, no. 3, pp. 221–238, 1993.

[73] Phelps, F. and Jr., J. H., "An analytical solution of the inverted pendulum," 1964.

[74] Potter, J., Singhose, W., and Costello, M., "Reducing swing of model helicopter sling load using input shaping," in *9th IEEE International Conference on Control and Automation*, (Santiago, Chile), pp. 348–353, 19-21 Dec. 2011.

[75] Potter, J. J., Adams, C. J., and Singhose, W., "A planar experimental remote-controlled helicopter with a suspended load," *Mechatronics, IEEE/ASME Transactions on*, vol. 20, no. 5, pp. 2496–2503, 2015.

[76] Prakash, A. and Wang, H. G., "Transient cancellation technique for spacecraft solar wing stepping," March 11 2008. U.S. Patent 7343228.

[77] Prakash, R., Burkhart, P. D., Chen, A., Comeaux, K. A., Guernsey, C. S., Kipp, D. M., Lorenzoni, L. V., Mendeck, G. F., Powell, R. W., Rivellini, T. P., San Martin, A. M., Sell, S. W., Steltzner, A. D., and Way, D. W., "Mars science laboratory entry, descent, and landing system overview," in *2008 IEEE Aerospace Conference*, pp. 1–18, 1-8 March 2008.

[78] Prouty, R. W., *Helicopter Performance, Stability, and Control*. Malabar, FL: Krieger Publishing Company, Inc., 1990.

[79] Richard T. O'Brien, J. and Robertson, M. J., "Bang-bang control of a floating oscillator," in *ASME Dynamic Systems and Control Conference*, (Hollywood, CA), 2009.

[80] Robertson, M., Kozak, K., and Singhose, W., "Computational framework for digital input shapers using linear optimisation," *IEE Proceedings - Control Theory and Applications*, vol. 153, no. 3, pp. 314–322, 2006.

[81] Robertson, M. J. and Singhose, W. E., "Multi-level optimization techniques for designing digital input shapers," in *Proceedings of the 2001 American Control Conference*, vol. 1, (Arlington, VA), pp. 269–274, June 2001.

[82] Robertson, M. J. and Singhose, W. E., "Robust discrete-time deflection-limiting commands for flexible systems," *IET Control Theory & Applications*, vol. 3, no. 4, pp. 473–480, 2009.

[83] Romano, M., Agrawal, B., and Bernelli-Zazzera, F., "Experiments on command shaping control of a manipulator with flexible links," *AIAA Journal of Guidance, Control, and Dynamics*, vol. 25, no. 2, pp. 232–239, 2002.

[84] Rozenblat, G. H., "Optimal parametric stabilization of an inverted pendulum," *Journal of Applied Mathematics and Mechanics*, vol. 45, no. 1, pp. 45 – 50, 1981.

[85] SAHBA, M., "Computer-aided design of feedback controllers for nonlinear systems with applications to control of a double-inverted pendulum," *IEE proceedings. D, Control theory and applications*, vol. 130, no. 6, pp. 350–358, 1983.

[86] SANTSCHI, W. R., DUBOIS, J., and OMOTO, C., "Moments of inertia and centers of gravity of the living human body," Tech. Rep. AMRL-TDR-63-36, Aerospace Medical Research Laboratory, 1963.

[87] SCHMIDT, R., BARRY, N., and VAUGHAN, J., "Tracking of a target payload via a combination of input shaping and feedback control," in *12th IFAC Workshop on Time Delay Systems*, vol. 48, (Ann Arbor, MI), pp. 141–146, June 28-30 2015.

[88] SEGWAY INC., *Reference Manual - Segway®Personal Transporter (PT) i2, x2*, 2006. Available: http://www.segway.com/media/1688/referencemanual.pdf.

[89] SEGWAY LLC, *Segway^{TM}HT Reference Manual*, 2003.

[90] SEGWAY LLC, *Basic Rider Optimization Training for the Segway^{TM}Human Transporter (HT) i Series, e Series and p Series models - Instructor Guide and Participant Workbook*, January 2004. Rev 3.5i.

[91] SEWARD, D., PACE, C., MORREY, R., and SOMMERVILLE, I., "Safety analysis of autonomous excavator functionality," *Reliability Engineering & System Safety*, vol. 70, no. 1, pp. 29–39, 2000.

[92] SINGER, N. C. and SEERING, W. P., "Preshaping command inputs to reduce system vibration," *Journal of Dynamic Systems, Measurement, and Control*, vol. 112, no. 1, pp. 76–82, 1990.

[93] SINGH, T. and VADALI, S., "Input-shaped control of three-dimensional maneuvers of flexible spacecraft," *AIAA Journal of Guidance, Control, and Dynamics*, vol. 16, no. 6, pp. 1061–1068, 1993.

[94] SINGH, T. and VADALI, S., "Robust time-optimal control: A frequency domain approach," *AIAA Journal of Guidance, Control, and Dynamics*, vol. 17, no. 2, pp. 346–353, 1994.

[95] SINGH, T. and HEPPLER, G. R., "Shaped input control of a system with multiple modes," *ASME Journal of Dynamic Systems, Measurement, and Control*, vol. 115, pp. 341–347, Sep. 1993.

[96] SINGH, T. and VADALI, S. R., "Robust time-delay control," *ASME Journal of Dynamic Systems, Measurement, and Control*, vol. 115, pp. 303–306, Jun. 1993.

[97] SINGHOSE, W., KIM, D., and KENISON, M., "Input shaping control of double-pendulum bridge crane oscillations," *ASME Journal of Dynamic Systems, Measurement, and Control*, vol. 130, p. 034504, May 2008.

[98] SINGHOSE, W. and SEERING., W., *Command Generation for Dynamic Systems*. Lulu, 2009.

[99] SINGHOSE, W. and SEERING., W., "Using elementrary commands on flexible systems," in *Command Generation for Dynamic Systems*, ch. 3, pp. 19–24, Lulu, 2009.

[100] SINGHOSE, W., SEERING, W., and SINGER, N., "Residual vibration reduction using vector diagrams to generate shaped inputs," *Journal of Mechanical Design*, vol. 116, pp. 654–659, Jun. 1994.

[101] SINGHOSE, W., ADAMS, C., and KIM, D., "A dynamics-based hazard analysis of inverted-pendulum human transporters using data-mined information," *ASCE-ASME Journal of Risk and Uncertainty in Engineering Systems, Part B: Mechanical Engineering*, vol. 2, no. 3, pp. 031007–031007–12, 2016.

[102] SINGHOSE, W., BOHLKE, K., and SEERING, W., "Fuel-efficient pulse command profiles for flexible spacecraft," *AIAA Journal of Guidance, Control, and Dynamics*, vol. 19, no. 4, pp. 954–960, 1996.

[103] SINGHOSE, W., CRAIN, E., and SEERING, W., "Convolved and simultaneous two-mode input shapers," *IEE Control Theory Appl.*, vol. 144, pp. 515–520, Nov. 1997.

[104] SINGHOSE, W., DEREZINSKI, S., and SINGER, N., "Extra-insensitive input shapers for controlling flexible spacecraft," *AIAA Journal of Guidance, Control, and Dynamics*, vol. 19, no. 2, pp. 385–391, 1996.

[105] SINGHOSE, W., SEERING, W., and SINGER, N., "Input shaping for vibration reduction with specified insensitivity to modeling errors," in *Japan-USA Symposium on Flexible Automation*, vol. 1, (Boston, MA), pp. 307–313, 1996.

[106] SINGHOSE, W., SINGER, N., and SEERING, W., "Improving repeatability of coordinate measuring machines with shaped command signals," *Precision Engineering*, vol. 18, pp. 138–146, Apr. 1996.

[107] SINGHOSE, W. E., BANERJEE, A. K., and SEERING, W. P., "Slewing flexible spacecraft with deflection-limiting input shaping," *AIAA Journal of Guidance, Control, and Dynamics*, vol. 20, no. 2, pp. 291–298, 2009.

[108] SMITH, J. H., ALLEN, G. M., and VENSEL, D., "Design, fabrication, and flight test of the active arm external load stabilization system for cargo handling helicopters," Tech. Rep. D210-10638-1, Boeing Vertol Co., September 1973.

[109] SMITH, O. J. M., *Feedback Control Systems*. New York, NY: McGraw-Hill Book Co., Inc., 1958.

[110] SMITH, O. J. M., "Posicast control of damped oscillatory systems," *Proc. IRE*, vol. 45, pp. 1249–1255, Sep. 1957.

[111] SORENSEN, K. L., HEKMAN, K., and SINGHOSE, W. E., "Finite-state input shaping," *IEEE Transactions on Control Systems Technology*, vol. 18, no. 3, pp. 664–672, 2010.

[112] SORENSEN, K. L., SINGHOSE, W., and DICKERSON, S., "A controller enabling precise positioning and sway reduction in bridge and gantry cranes," *Control Engineering Practice*, vol. 15, pp. 825–837, Jul. 2007.

[113] SPILLANE, B. and FLINN, R., "Segway owner's death adds to safety, image challenges," 2010.

[114] STEPHENSON, A., "A new type of dynamic stability," *Proc. of the Manchester Literary and Philosophical Society*, 1908.

[115] STEPHENSON, A., "On induced stability," *Philosophical Magazine*, 1909.

[116] STEVENS, B. L. and LEWIS, F. L., "Modern design techniques," in *Aircraft Control and Simulation*, ch. 5, pp. 421–437, Hoboken, NJ: John Wiley & Sons, Inc., 1992.

[117] SZUSTAK, L. S. and JENNEY, D. S., "Control of large crane helicopters," *Journal of the American Helicopter Society*, vol. 16, pp. 11–22, July 1971.

[118] TISCHLER, M. B., "System identification requirements for high-bandwidth rotorcraft flight control system design," *AIAA Journal of Guidance, Control, and Dynamics*, vol. 13, no. 5, pp. 935–841, 1990.

[119] TRENTINI, M. and PIEPER, J. K., "Model-following control of a helicopter in hover," in *IEEE International Conference on Control Applications*, (Dearborn, MI), pp. 7–12, 15–18, September 1996.

[120] TUTTLE, T. and SEERING, W., "Experimental verification of vibration reduction in flexible spacecraft using input shaping," *AIAA Journal of Guidance, Control, and Dynamics*, vol. 20, pp. 658–664, Jul. 1997.

[121] TYLER JR., J., "The characteristics of model-following systems as synthesized by optimal control," *IEEE Transactions on Automatic Control*, vol. 9, no. 4, pp. 485–498, 1964.

[122] UK CIVIL AVIATION AUTHORITY SAFETY REGULATION GROUP, *Helicopter External Load Operations*. The Stationery Office, April 2006. CAP 426.

[123] ULLMAN, D. G., *The Mechanical Design Process*. New York, NY: McGraw-Hill, 3rd ed., 2002.

[124] UNITED STATES ARMY AVIATION AND MISSILE COMMAND, *Aeronautical Design Standard 33E: Handling Qualities Requirements for Military Rotorcraft*. Aviation Engineering Directorate, Redstone Arsenal, Alabama, 21 March 2000. ADS-33E-PRF.

[125] VAUGHAN, J., YANO, A., and SINGHOSE, W., "Comparison of robust input shapers," *Journal of Sound and Vibration*, vol. 315, pp. 797–815, Sep. 2008.

[126] VICON MOTION SYSTEMS, *Vicon MX Hardware System Reference*. Oxford, UK, 2007. Revision 1.6.

[127] VICON MOTION SYSTEMS, "Vicon | Products | Cameras | MX-3+." [Online]. Available: http://www.vicon.com/products/mx3.html, Date Accessed: 15 March 2012.

[128] WIE, B., SINHA, R., and LIU, Q., "Robust time-optimal control of uncertain structural dynamic systems," *AIAA Journal of Guidance, Control, and Dynamics*, vol. 15, no. 5, pp. 980–983, 1993.

[129] WIE, B., SINHA, R., SUNKEL, J., and COX, K., "Robust fuel- and time-optimal control of uncertain flexible space structures," in *AIAA Guidance, Navigation, and Control Conference*, (Monterey, CA), pp. 939–948, Aug. 1993.

[130] WINSOR, C. and ROY, R., "The application of specific optimal control to the design of desensitized model following control systems," *IEEE Transactions on Automatic Control*, vol. 15, no. 3, pp. 326–333, 1970. 10.1109/TAC.1970.1099453.

[131] XIANREN, K. and ZHENGXIAN, Y., "Combined feedback control and input shaping for vibration suppression of flexible spacecraft," in *2009 International Conference on Mechatronics and Automation*, (Changchun, China), pp. 3257–3262, IEEE, 2009.

[132] YAMAKAWA, T., "Stabilization of an inverted pendulum by a high-speed fuzzy-logic controller hardware system," *Fuzzy Sets and Systems*, vol. 32, no. 2, pp. 161–180, 1989.